The strain dependent critical current of high field superconductors for fusion energy applications

BRANCH, PAUL,OLIVER

The strain dependent critical current of high field superconductors for fusion energy applications

Paul Oliver Branch

Department of Physics
Durham University

A thesis submitted in partial fulfillment
of the requirements for the degree of
Doctor of Philosophy

June 2019

For my darling Bethany who despite all the late night experiments and stressful deadlines still married me!

Abstract

All superconductors in high field magnets operating above 12 T are brittle and subjected to large strains because of the differential thermal contraction between component parts on cool-down and the large Lorentz forces produced in operation. The continuous scientific requirement for higher magnetic fields in superconducting energy-efficient magnets, in applications such as fusion, means we must understand and control the high sensitivity of critical current density J_c to strain ε. This thesis presents detailed $J_c(B, T, \varepsilon, \theta)$ transport measurements as a function of field B, temperature T, strain ε and angle θ with respect to the applied magnetic field, on high field superconductors that include the very widely observed inverted parabolic dependence for $J_c(\varepsilon)$.

It is usually assumed that a coincidence occurs between the Fermi energy and a peak in the density of states in the unstrained state which leads to a peak in the superconducting properties in the unstrained state. The long-standing interpretation of $J_c(\varepsilon)$ data attributes the inverted parabolic strain behaviour to the averaged response of the underlying material. Features of the data in this work are identified in both HTS REBCO tape and LTS A15 wires which show that both of these assumptions are incorrect.

A new analysis is presented which shows the inverted parabolic nature of $J_c(\varepsilon)$ is the result of competition between domains with opposing strain dependencies and successfully accounts for the features of the data incompatible with standard assumptions. It is concluded that the origin of the competing domains in REBCO tape lies in twinned domains and in A15 wires is caused by percolative current flow across grain boundaries orientated in different directions which respond to an applied strain in different manners due to the Poisson effect. This work provides fresh insight into how improvements might be made to high field superconductors under strain.

Publications

P. Branch, Y. Tsui, K. Osamura and D. P. Hampshire. Weakly-Emergent Strain-Dependent Properties of High Field Superconductors. *Submitted Nature Scientific Reports*

P. Branch, Y. Tsui, K. Osamura and D. P. Hampshire. Multimodal strain dependence of the critical parameters in high and low temperature superconducting wires and tapes. *To be submitted to Superconductor Science and Technology*

P. Branch, K. Osamura and D. P. Hampshire. The critical current density in REBCO tape as a function of strain and angle. *To be submitted to Superconductor Science and Technology*

Conferences

(Oral) ASC 2016, 4th – 9th Sept. 2016, Denver, Colorado, USA

(Oral) Fusion Frontiers 2016, 25th – 29th April 2016, York, UK

(Oral) FuseNET Ph.D Event, 16th – 18th Nov. 2015, Prague, Czech Republic

(Invited oral) EuCAS 2015, 7th – 11th Sept. 2015, Lyon, France

(Oral, poster and orginiser) Fusion Frontiers 2015, 5th – 8th May 2015, York, UK

(Poster) JWPAS 2015, 12th 15th Apr. 2015, Cambridge, UK

(Poster) FuseNet Ph.D Event, 18th – 21st Nov. 2014, Lisbon, Portugal

(Poster) Fusion Frontiers 2014, 12th – 18th May 2014, York, UK

Declaration and copyright

I hereby declare that no part of the material offered in this thesis has previously been submitted by me for a degree in this or any other University. If material has been generated through joint work, my independent contribution has been clearly indicated. In all other cases material from the work of others has been acknowledged and quotations and paraphrases suitably indicated.

Paul Oliver Branch

June 2019

Acknowledgements

I would like to start by thanking my supervisor Professor Damian P. Hampshire for his support, guidance and scientific wisdom during this long journey. And I would like to thank all the members of the Durham Superconductivity Group I have known during my time here, Mark J. Raine, Prapaiwan (Bew) Sunwong, Yeekin Tsui, Peter Byrne, Guanmei (Mona) Wang, Thomas Lee, Andrea Dawson, Emily Roe, Michael McBreen, Matthew Plumb, Francis Ridgeon, Alexander Blair, Jack Greenwood, Andrew Smith, Simon Chislett-McDonald, Adel Nader and Charles Gurnham, for their friendship, many a debate about politics and occasionally helpful discussions about superconductivity. I would like to say a special thank you to Guanmei (Mona) Wang for her moral support and Mark J. Raine for his unwavering optimism (although he will deny ever being optimistic about anything!), I wouldn't have made it through without you both!

The experiments in this thesis needed many custom pieces of equipment which would not have been made into reality without the expertise and practical skills of the departmental mechanical and electronic workshops. I would like to thank Stephen Lishman, John Scott and the whole of their workshop teams; in particular I would would like to thank Andrew Davies for the weeks spent slaving away to make my temperature cup, without which this thesis wouldn't exist.

I would like to thank the long time collaborator of the Durham Superconductivity Group Professor Kozo Osamura for supplying the REBCO samples used in this thesis and for many helpful discussions and amusing stories about my supervisor!

On a personal note I would like to say a massive thank you to my wife Bethany Dix for believing in me even when I didn't, and for her constant support through all the stresses, and existential crises that inevitably come with doing a Ph.D; it means the world to me. To my parents, Yvonne and David Branch, for always enabling and encouraging me to pursue my passions, I wouldn't be here without them (figuratively and literally!). And to my best men, Daniel Trotter and my brother Jonathon Branch, for always being there to help unwind.

Table of contents

1 Introduction **1**

2 Fundamentals of superconductivity and fusion **7**

2.1 Introduction 7

2.2 Electrical and magnetic properties of a superconductor 8

2.3 Superconducting materials 12

2.4 London equations 15

2.5 Ginzburg - Landau theory (GL theory) 17

2.6 Anisotropic B_{c2} 22

2.6.1 Anisotropic GL theory in homogeneous materials 22

2.6.2 Layered superconductors 23

2.6.3 Lawrence – Doniach Theory (LD theory) 24

2.6.4 Tinkham's model for two dimensional thin films 26

2.6.5 Mineev's general expression for B_{c2} 27

2.7 BCS theory 28

2.7.1 Cooper pairs 29

2.7.2 The energy gap and results of BCS theory 30

2.8 Flux pinning 32

2.9 Nuclear fusion 35

2.9.1 The fusion reaction 35

2.9.2 Magnetic confinement 36

2.9.3 The fusion triple product 38

2.10 Concluding remarks 40

3 Superconducting conductors, their strain dependence and applications 41

3.1 Introduction 41

3.2 HTS materials 42

3.2.1 Properties and structure of REBCO and BiSCCO 43

3.2.2 The irreversibility field B_{irr} 44

3.2.3 The grain boundary 'problem' 46

3.3 Developments in high temperature superconducting wires and tapes . . 49

3.3.1 BiSCCO wires and tapes 50

3.3.2 REBCO tapes 54

3.4 Strain dependence of the critical current of LTS and HTS wires and tapes 68

3.4.1 Reversible strain effects in LTS conductors 70

3.4.2 Reversible strain effects in HTS conductors 72

3.5 The bimodal chain model for REBCO in zero field 73

3.6 Fusion reactor design 77

3.6.1 Tritium breeding 78

3.6.2 Neutron damage 80

3.6.3 Neutron irradiation of superconductors 85

3.7 Concluding remarks 87

4 Multimodal strain dependence in high field technological superconductors 89

4.1 Introduction 89

4.2 Experimental equipment and procedure 91

4.2.1 REBCO tape on a springboard 91

4.2.2 Bronze route Nb_3Sn on a Walters' spring 96

4.3 Transport measurements 97

4.3.1 REBCO measurements 97

4.3.2 Bronze route Nb_3Sn measurements on a Walters' spring 109

4.3.3 Internal tin Nb_3Sn and jelly roll Nb_3Al wire on a Walters' spring 109

4.3.4 A note on fitting methods 110

4.4 Engineering parameterisation of $J_c(B, T, \varepsilon_{app})$ 112

4.5 Flux pinning scaling 116

4.5.1 REBCO tape: Flux pinning scaling of $J_c(B, T, \varepsilon_{app})$ at $T \geq 60\,K$ 118

4.5.2 REBCO tape: Extending the flux pinning scaling to $T = 4.2, 20$ and $40\,K$ 122

4.5.3 REBCO tape: Temperature and strain scaling of $F_{p,max}$ with B^*_{c2} 125

4.5.4 Bronze route Nb_3Sn: Flux pinning scaling of $J_c(B, T, \varepsilon_{app})$ . . . 128

4.5.5 Internal tin Nb_3Sn and jelly roll Nb_3Al: Flux pinning scaling of $J_c(B, T, \varepsilon_{app})$ . . . 131

4.6 The bimodal chain model for REBCO . . . 133

4.6.1 Bimodal chain model for twinned domains in high magnetic fields 134

4.6.2 Numerical results of the bimodal chain model . . . 137

4.7 Estimating f and $\varepsilon_{J_{cA}=J_{cB}}$ . . . 145

4.8 Discussion . . . 153

4.8.1 Discussion of REBCO results . . . 155

4.8.2 Discussion of LTS results - polycrystalline materials . . . 162

4.9 Conclusions . . . 166

5 The strain and angular dependence of J_c in REBCO tape 169

5.1 Introduction . . . 169

5.2 Experimental procedures . . . 171

5.3 Results . . . 173

5.3.1 Angular dependence of the critical current density and index of transition . . . 173

5.3.2 Critical current density and index of transition . . . 176

5.3.3 Strain peak in the critical current density . . . 181

5.4 Functional form of $J_c(\theta)$ . . . 181

5.5 Flux pinning scaling curves and determination of $B^*_{c2}(\theta)$ . . . 185

5.6 Estimating f and $\varepsilon_{J_{cA}=J_{cB}}$ from $\varepsilon_{peak}(B, T, \theta)$ . . . 187

5.7 Discussion . . . 191

5.7.1 Angular dependence of B^*_{c2} 191

5.7.2 Flux pinning scaling curve 193

5.7.3 The chain model 193

5.7.4 Microstructure in REBCO tapes 195

5.7.5 Applications 196

5.8 Conclusions 198

6 Future work and concluding remarks **201**

References **211**

Chapter 1

Introduction

Power is the lifeblood of modern human society. Our homes, cities and infrastructure are dependent on uninterrupted supplies of electricity on truly enormous scales. In 2016 global electrical energy consumption averaged a rate of 3.33 TW, with an additional 15.16 TW of power used in non-electrical applications such as transport and heating; and 80 % of this power was produced via fossil fuels [1]. Independent of the seriousness of the effects of CO_2 on the global climate, an inescapable effect of our continued use of fossil fuels is the reduction in reserves, ultimately to the point where it will no longer be economically or physically feasible to extract further supply. Estimates on the amount of reserves accessible vary, however it is clear the timescale is of the order of a few generations and the issue must be addressed in the present to maintain future global stability. An acknowledgement of these issues over the past decade has led to large growth in renewable sources of energy such as wind and solar power. However such forms of energy production are intermittent and not suitable for providing

the continuous 24 hour supply demanded by the infrastructure of an economically developed country. Large scale energy storage is a possible solution to this issue but would require storage at currently unachievable and unprecedented densities. Nuclear fission is another way of providing uninterrupted supply with potential fuel reserves of hundreds of thousands of years, although the perception of nuclear power as unsafe and the possibility of advancing nuclear proliferation technologies present challenging political obstacles to its widespread global uptake.

In the early twentieth century Sir Arthur Stanley Eddington [2] said

> *'A star is drawing on some vast reservoir of energy by means unknown to us. This reservoir can scarcely be other than the subatomic energy which, it is known exists abundantly in all matter; we sometimes dream that man will one day learn how to release it and use it for his service. The store is well-nigh inexhaustible, if only it could be tapped.'*

Today we are close to 'tapping' this 'well-nigh inexhaustible' supply through nuclear fusion. Often referred to as the 'holy grail' of energy production, nuclear fusion is well on its way to providing clean, uninterrupted, safe energy in a time when we need it most. The most promising route to harnessing fusion power involves confining a hydrogen plasma using a very large magnetic field and heating the plasma to temperatures high enough for the hydrogen to fuse into helium.

There is a long running misconception regarding fusion which is that it is always 30 years away. The truth is, fusion is performed daily in experimental reactors around the world. In fact, the first reports of fusion reactions from a confined plasma are as early as 1953. Since then fusion has shown great progress with the performance of successive

fusion devices improving at a rate faster than Moore's law for transistor density in microprocessors [3]! However what is still yet to be achieved is the confinement of a stable plasma producing more fusion power than the power required to maintain the reaction, which is essential if fusion is to be used in power generation. The ITER reactor currently under construction is the largest experimental project in the world with operations due to start in $\sim$ 2025. It aims to be the first reactor to achieve this important milestone and show without doubt that fusion is a viable method of power production for the future by outputting a fusion power ten times that needed to maintain the reaction.

Fusion output scales as the fourth power of the magnetic field used to confine the plasma [4] so achieving the highest possible magnetic field is of paramount importance. Going to higher magnetic fields with copper magnets becomes increasingly prohibitive due to excessive Joule heating at the highest currents resulting in extremely high power and cooling requirements. The power needed to operate such conventional magnets far exceeds the potential fusion power output. In much the same way they enable technologies such as Magnetic Resonance Imaging (MRI), superconductors, with their ability to carry a lossless current density (zero resistance), are an enabling technology for fusion energy. The reduction in the magnet power requirements brought about by using superconducting magnets means more power can be produced by the fusion reaction than is needed in order to maintain it.

Currently low temperature superconductors (LTS) are the workhorse of all superconducting technologies. The maximum achievable field with these materials is

limited by their critical parameters. The relatively recent advent of high temperature superconductors (HTS) means there has been a significant improvement in maximum achievable field due to these materials being able to carry significantly higher current densities in high fields. However HTS magnets are still in research and development stages. The strength of the magnetic fields in current fusion magnets produce very large strains on the magnets themselves, and these strains become even larger when considering future higher field HTS magnets where the maximum achievable field can be so high it is limited by strength of the structural components rather than the critical parameters of the superconductor. These high strains have a significant effect on the amount of current that can be carried by the superconductor and cannot be overlooked in superconducting magnet design. High strains, both tensile and compressive, suppress the critical superconducting parameters, such as the critical temperature and the upper critical field, and in extreme cases can suppress superconductivity entirely. This in turn results in an often-significant reduction of the maximum current a superconductor can maintain, the critical current. So, unlike copper magnets where strain has little affect on conduction, when a superconductor is under strain in a magnet it can carry less current, meaning more turns (and more conductor) are required to achieve the desired field. Parameterisations of the critical superconducting parameters which include strain in addition to field and temperature are therefore essential when designing a superconducting magnet.

The polycrystalline superconducting conductors which are used in magnet production have complex microstructures with things such as superconducting filaments

embedded in copper matrices, grain boundaries and twinning to consider. While global parameterisations are essential, work into understanding the physics on a microscopic level which determine the macroscopic behaviour is equally as important in order to drive further improvements in the performance of superconducting conductors under strain.

With a focus on the HTS material (RE)$Ba_2Cu_3O_{7-\delta}$ (RE=Rare Earth) this work aims to understand how strain affects the performance of both LTS and HTS conductors on a fundamental level to help direct the future development of advanced conductors for use in high field fusion magnets and other high field applications.

Chapter 2 presents the fundamentals of superconductivity and fusion. Chapter 3 draws on work in the literature to discuss common technological superconducting conductors and the effects when strain is applied to these conductors, with a focus on HTS materials, some discussion of fusion reactor design is also presented. Chapter 4 details the first experimental campaign of this work on an HTS (RE)$Ba_2Cu_3O_{7-\delta}$ conductor (at fixed angle) and an LTS Nb_3Sn conductor, a field and temperature dependent bimodal chain model is introduced and used to describe features of the data which are incompatible with current models. Chapter 5 details the second experimental campaign of this work, expanding the parameter range for the same HTS (RE)$Ba_2Cu_3O_{7-\delta}$ conductor sample, the angular dependencies are discussed and the data are analysed using the bimodal chain model. Chapter 6 discusses future work to build on the results of this thesis which will further our understanding of the effects of strain on high field superconductors.

Chapter 2

Fundamentals of superconductivity and fusion

2.1 Introduction

Superconductivity is a property exhibited by certain materials where below some critical temperature they display the properties of zero DC electrical resistance and expulsion of an applied magnetic field from their bulk. Since its initial discovery in mercury by H. Kamerlingh Onnes in 1911 [5] hundreds of superconductors have been discovered including metals, alloys, metallic compounds and even non-metallic compounds (most of which have critical temperatures close to absolute zero). In 1986 the highest recorded critical temperature increased dramatically to $\sim 30\,\mathrm{K}$ with the discovery of superconductivity in cuprates [6]. Through the 1990s several cuprates were discovered with increasingly high critical temperatures, reaching values higher than the

boiling point of liquid nitrogen $\approx 77\,\mathrm{K}$. Currently the highest critical temperature at ambient pressure stands at 134 K [7] although critical temperatures as high as 203 K [8] have been achieved under extreme pressures.

This chapter introduces the basic principles and theories of superconductivity and nuclear fusion. Section 2.2 discusses the basic properties of superconductors, section 2.3 gives an overview of important superconducting materials, sections 2.4, and 2.5 cover the phenomenological London and Ginzburg–Landau theories of superconductivity respectively, section 2.6 covers theories of anisotropic upper critical field, and section 2.7 covers the microscopic BCS theory of superconductivity. Section 2.8 discusses flux pinning, section 2.9 describes the process of nuclear fusion and section 2.10 provides concluding remarks.

2.2 Electrical and magnetic properties of a superconductor

In zero field a superconducting material will enter the superconducting state below its critical temperature, T_c. The superconducting state is characterised by two unique properties: zero dc electrical resistance and the Meissner effect.

Proving a superconductor truly has zero dc electrical resistivity experimentally is limited by the sensitivity of the measurement techniques. Measurements of the decay of persistent current in superconducting rings have put an upper bound on the

resistivity of $7 \times 10^{-23}\,\Omega\,\mathrm{m}$ [9] (17 orders of magnitude lower than copper at cryogenic temperatures).

Discovered by Meissner in 1933 the Meissner effect is the exclusion of a small applied magnetic field from the bulk of the material [10]. Shielding currents flow in the surface layer of the material resulting in a magnetisation which exactly opposes the applied field (perfect diamagnetism). The Meissner effect that occurs in a superconductor differs from the magnetic response expected from a theoretical 'perfect conductor'. In a superconductor the exclusion of field from the bulk is not simply a consequence of the zero-resistance of the (super)electrons to the application of a magnetic field but is in fact an intrinsic property of the superconducting state. The distinction is demonstrated by considering the thought experiment of field-cooling a superconductor and a 'perfect conductor'. When a superconductor is field-cooled it will expel the applied field as it is cooled below its critical temperature whereas a 'perfect conductor' will maintain the field in its bulk and subsequently maintain that field in the bulk if the applied field is changed or removed. These ideas are depicted graphically in figure 2.1.

All superconductors exhibit the Meissner effect when the applied field is small and are said to be in the 'Meissner state'. As the magnetic field is increased two distinct categories of superconductor appear, Type I and Type II, determined by their response to the applied field.

In Type I superconductors the Meissner state is maintained until some critical field B_c is reached at which point superconductivity is destroyed and the material returns to the normal state.

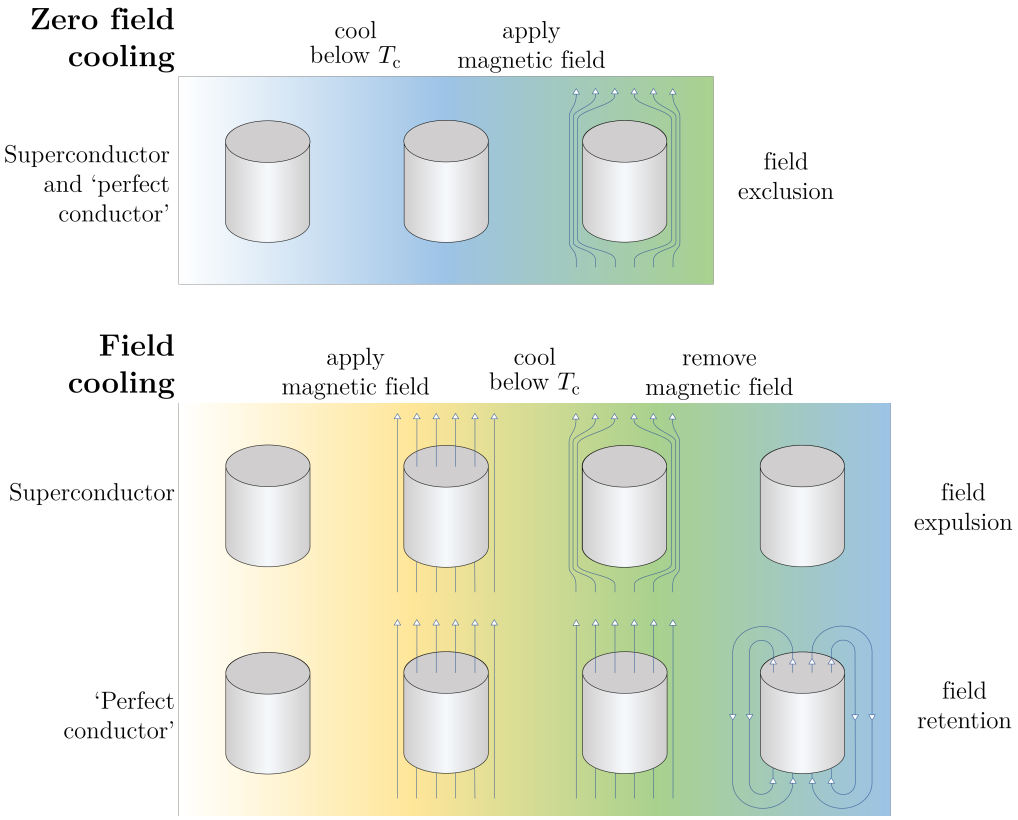

Figure 2.1. An illustration of the different responses of a superconductor and a theoretical 'perfect conductor' to a small applied magnetic field. A superconductor will work to exclude an applied field from the bulk when cooled below its critical temperature whereas a 'perfect conductor' will work to maintain the magnetic state it was in when it was cooled below its critical temperature.

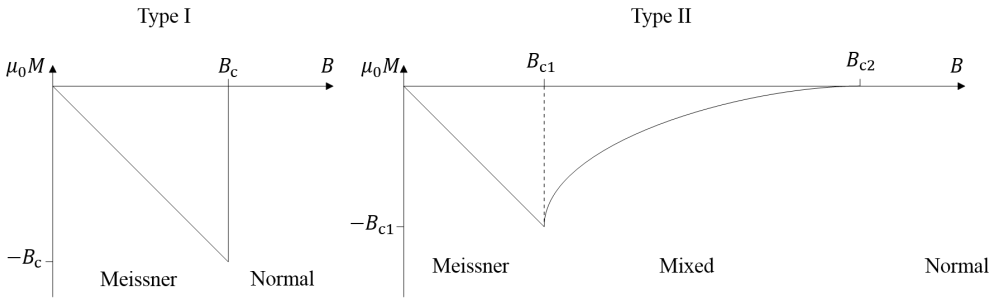

Figure 2.2. The magnetic responses of Type I and Type II superconductors to an applied field for a cylinder [11].

In Type II superconductors the Meissner state is maintained up to some lower critical field B_{c1}, above which the material enters the 'mixed state' and allows increasing amounts of the applied field into the bulk in the form of quantised flux vortices called fluxons which are discussed in greater detail in section 2.5. This continues until the upper critical field B_{c2}, is reached and the material returns to the normal state.

The magnetisation behaviours of Type I and Type II superconductors are shown in figure 2.2.

B_c, B_{c1} and B_{c2} all vary with temperature from a maximum at $T = 0\,\mathrm{K}$ to zero at $T = T_c$, as shown in figure 2.3. A theoretical understanding of how the upper critical field of Type II superconductors varies with temperature is given by W-H-H (Werthamer – Helfand – Hohenberg) theory [12] which includes temperature through microscopic BCS theory [13].

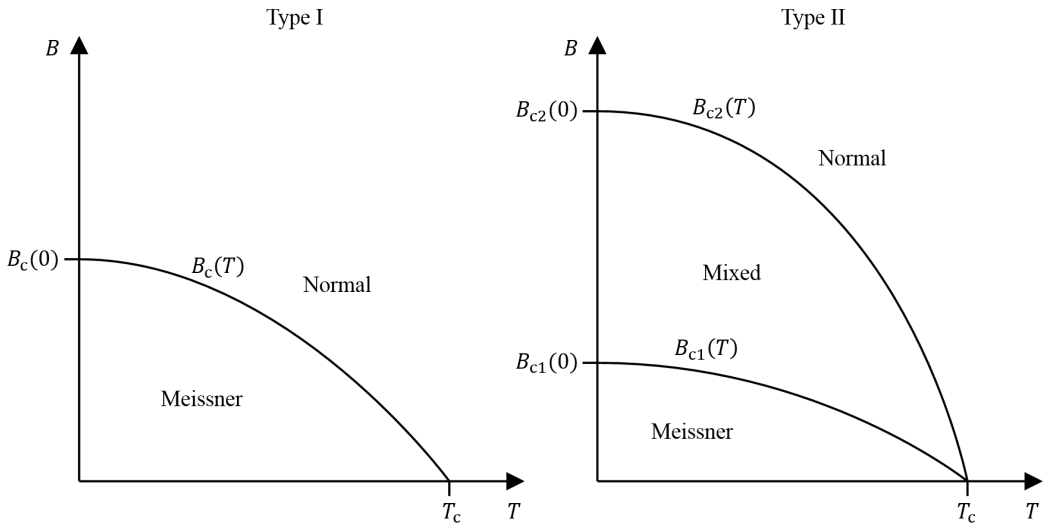

Figure 2.3. Variation of the critical fields of Type I and II superconductors with temperature.

2.3 Superconducting materials

Superconductivity appears in many types of materials. Generally most superconductors display Type II behaviour and Type I behaviour is observed primarily in elements. Some notable classes of material displaying superconductivity are listed below:

Elements are where superconductivity was first discovered. Many (but by no means all) are known to be superconducting at ambient pressures with more only showing superconductivity under pressure. Most of these elements are metals with only a few non-metals showing superconductivity under pressure. In general elemental superconductors display Type I behaviour and typically have transition temperatures of the order of 1 K and below. The most notable exception to this is niobium which displays Type II behaviour and has a critical temperature of 9.25 K, the highest of any element at ambient pressure. The

highest reported critical temperature of an element under pressure is in sulphur at 17 K under a pressure of 160 GPa [14].

Metallic alloys where at least one of the constitute elements is superconducting often also show superconductivity, sometimes with a critical temperature higher than any of the constituent elements. Currently the most used superconducting material is the alloy Nb–Ti. With a moderately high upper critical field at 4.2 K of about 13 T and a high current carrying capacity [7], it is a good material for making high field magnets. What sets Nb–Ti apart from other materials with higher upper critical fields and better current carrying capacities is the fact that it is a ductile alloy that is simple and cheap to draw into usable wire conductors. This fact has made Nb–Ti into the most widely used superconductor. Recent results under extreme pressures of up to 261.7 GPa have given Nb–Ti the record for the highest pressure where the superconducting state is known to survive as well as the highest known values of T_c and B_{c2} of the transition metal alloy superconductors [15].

Many types of intermetallic compound display superconductivity. Arguably the most important of these are the A15 materials such as Nb_3Sn and Nb_3Al. Nb_3Sn is the second most widely used superconducting material, with a higher upper critical than Nb-Ti. Due to the brittle nature of the compound, conductor manufacture is considerably more complicated. A Nb and bronze matrix is drawn into a malleable wire which is then wound into the desired shape before being heated in a furnace allowing the Sn to diffuse into the Nb

and react to form Nb_3Sn. After this reaction the wire is brittle and cannot be reshaped. Other important types of compound which display superconductivity are Chevrel phase materials with upper critical fields of up to $\sim 60\,\mathrm{T}$ [16], iron pnictide materials with critical temperatures of up to $\sim 55\,\mathrm{K}$ [17] and MgB_2 with respectable values of T_c and B_{c2}, and a low materials cost [18].

As the focus of this thesis, cuprate materials are deserving of special mention. The cuprates have a layered crystal structure where CuO_2 planes, responsible for the superconductivity, are separated by other layers. This layered structure leads to highly anisotropic superconducting properties. The two most important materials in this class are REBCO with the chemical formula $(RE)Ba_2Cu_3O_{7-\delta}$ (RE= Rare Earth) and BiSCCO with the general chemical formula $Bi_2Sr_2Ca_{n-1}Cu_nO_{4+2n}$ (n = 1,2 or 3). Cuprate materials can have critical temperatures in excess of the boiling point of liquid nitrogen (77 K), extremely high upper critical fields and carry very high current densities even in high field. At first glance their properties may make them seem like the ideal superconducting material, however problems transferring current across grain boundaries led to difficulties in producing usable conductors. In REBCO this has led to the development of conductors which are quasi-single crystal where only $\sim 1\,\%$ of the total cross sectional area of the conductor is the superconducting material. Due to the present high cost of these conductors they are not widely adopted for most superconducting applications, however they are the only conductors capable of operating at the very highest fields

and temperatures >77 K which accounts for a small but not insignificant proportion of the superconducting conductor market such as high field research magnets [19, 20], fault current limiters [21] and power transmission [22]. Their price is continually dropping as manufacturing techniques improve and they may one day become a competitive alternative in other areas of the superconducting market.

A summary of the critical parameters of a small selection of the most important superconducting materials for high field applications is shown in Table 2.1.

2.4 London equations

In 1935 F. and H. London developed a theory for superconductivity which describes the Meissner effect and describes how a supercurrent $\boldsymbol{J}_\mathrm{s}(\boldsymbol{r})$ flows [29]. At its core it consists of two equations,

$$\boldsymbol{E}(\boldsymbol{r}) = \mu_0 \lambda_\mathrm{L}^2 \frac{\mathrm{d}\boldsymbol{J}_\mathrm{s}(\boldsymbol{r})}{\mathrm{d}t}, \tag{2.1}$$

$$\boldsymbol{B}(\boldsymbol{r}) = \mu_0 \lambda_\mathrm{L}^2 \nabla \times \boldsymbol{J}_\mathrm{s}(\boldsymbol{r}), \tag{2.2}$$

where $\boldsymbol{E}$ is the electric field, $\boldsymbol{B}$ is the magnetic field, $\boldsymbol{r}$ is the position, μ_0 is the permeability of free space and λ_L is the London penetration depth. Eqn 2.1 shows that no electric field is required to maintain a persistent supercurrent (zero dc electrical resistance). Combining eqn 2.2 with Maxwell's equations we obtain expressions for the

Table 2.1. T_c and B_{c2} of a selection of technologically important superconductors.

Material	T_c (K)	$B_{c2}\,(T = 0\,\mathrm{K})$ (T)
Nb[a]	9.25	0.206
Hg[a]	4.15	0.0411[*]
$Pb_{38}Sn_{62}$[b]	7.3	0.30
$In_{52}Sn_{48}$[b]	6.4	0.34
$Bi_{49}Pb_{18}In_{21}Sn_{12}$[b] (Cerrolow 136)	6.4	3.3
Nb-Ti[c]	9.5	13.0
Nb_3Sn[c]	18.2	23.0
Nb_3Al[d]	18.6	32[**]
$PbMo_6S_8$[e]	13.7	56
$Ba\,(FeCo)_2\,As_2$[f]	25.8	56.4[†], 64.7[‡]
MgB_2[g]	31	34[†], 49[‡]
$YBa_2Cu_3O_{7-\delta}$[h]	90	120[†], 250[‡]
$Bi_2Sr_2CaCu_2O_8$[i]	84.4	231[†]
$Bi_2Sr_2Ca_2Cu_3O_{10}$[i]	108	297[†]
$HgBa_2Ca_2Cu_3O_8$[c]	131	190[†]

[*] $B_c\,(T = 0\,\mathrm{K})$, Type I superconductor

[**] $T = 4.2\,\mathrm{K}$

[†] $B \parallel c$, [‡] $B \perp c$

[a] Reference [23]

[b] Reference [24]

[c] Reference [7]

[d] Reference [25]

[e] Reference [16]

[f] Reference [26]

[g] Reference [18]

[h] Reference [27]

[i] Reference [28]

magnetic field and supercurrent,

$$\nabla^2 \boldsymbol{B}\left(\boldsymbol{r}\right) = \frac{\boldsymbol{B}\left(\boldsymbol{r}\right)}{\lambda_{\mathrm{L}}^2}, \tag{2.3}$$

$$\nabla^2 \boldsymbol{J}_{\mathrm{s}}\left(\boldsymbol{r}\right) = \frac{\boldsymbol{J}_{\mathrm{s}}\left(\boldsymbol{r}\right)}{\lambda_{\mathrm{L}}^2}, \tag{2.4}$$

which shows that the magnetic field decays exponentially inside the superconductor with a characteristic length λ_{L}, giving rise to the Meissner effect. The supercurrent has the same mathematical form as the magnetic field implying that supercurrent only flows in the thin layer near the surface of width $\sim \lambda_{\mathrm{L}}$. The London penetration depth is defined as,

$$\lambda_{\mathrm{L}}^2 = \frac{m_{\mathrm{e}}^*}{\mu_0 e^{*2} \left\langle n_{\mathrm{s}} \right\rangle}, \tag{2.5}$$

where m_{e}^*, e^* and $\langle n_{\mathrm{s}} \rangle$ are the effective mass, effective charge and average density of the supercurrent charge carriers respectively.

2.5 Ginzburg - Landau theory (GL theory)

Ginzburg-Landau (GL) theory was developed in 1950 [30] and is arguably the most powerful theory of superconductivity for describing properties in magnetic fields due to its applicability in a wide range of systems and its accurate prediction of the properties of a wide range of superconducting materials. It is a phenomenological theory which makes no assumptions regarding the underlying microscopic mechanisms causing superconductivity. Strictly only valid in the region $T \sim T_{\mathrm{c}}$, surprisingly its

results are often applicable over a large temperature range. Despite its accurate predictions the theory was not widely accepted until 1959 when it was shown its results are derivable from the microscopic BCS theory [31], discussed in section 2.7.

GL theory is an extension of the Landau theory of second order phase transitions [32]. A position dependent complex order parameter $\psi(\mathbf{r})$ is defined such that, $\psi(\mathbf{r}) = 0$ for $T > T_c$ and the modulus squared of the order parameter is equal to the local density of supercurrent charge carriers, $|\psi(\mathbf{r})|^2 = n_s$ for $T < T_c$. In the temperature region near T_c the Gibbs free energy density g_s is expanded in powers of $|\psi(\mathbf{r})|^2$ and $|\nabla\psi(\mathbf{r})|^2$, and a term to account for the magnetic energy density is included to give,

$$g_s = g_n + \alpha(T)|\psi|^2 + \frac{\beta(T)|\psi|^4}{2} + \frac{|(-i\hbar\nabla - e^*\boldsymbol{A})\psi|^2}{2m_e^*} + \frac{(\boldsymbol{B} - \mu_0\boldsymbol{H}_{app})^2}{2\mu_0}, \quad (2.6)$$

where g_n is the Gibbs free energy density in the normal state, $\alpha(T)$ and $\beta(T)$ are temperature dependent coefficients, $\boldsymbol{A}$ is the local magnetic vector potential, $\boldsymbol{B}$ is the local magnetic field and $\boldsymbol{H}_{app}$ is the applied magnetic field strength [33]. $\alpha(T)$ and $\beta(T)$ are expanded in powers of $(T_c - T) \propto (1 - T/T_c)$. In order to satisfy the condition that the free energy must have a single minimum at $\psi = 0$ for $T > T_c$ and a minimum at $\psi \neq 0$ for $T < T_c$, the temperature dependencies are taken to be $\alpha(T) \approx -\alpha_0(1 - T/T_c)$ and $\beta(T) \approx \beta_0$ to first order, where α_0 and β_0 are material dependent positive constants.

By minimising the Gibbs free energy with respect to variations in ψ and $\boldsymbol{A}$ the following coupled differential equations are obtained,

$$\frac{1}{2m_{\mathrm{e}}^{*}}\left(i\hbar\nabla + e^{*}\boldsymbol{A}\right)^{2}\psi + \alpha\psi + \beta\left|\psi\right|^{2}\psi = 0, \tag{2.7}$$

$$\boldsymbol{J}_{\mathrm{s}} = \frac{i\hbar e^{*}}{2m_{\mathrm{e}}^{*}}\left(\psi^{*}\nabla\psi - \nabla\psi^{*}\psi\right) - \frac{e^{*2}}{m_{\mathrm{e}}^{*}}\boldsymbol{A}\left|\psi\right|^{2}. \tag{2.8}$$

In general these equations cannot be solved analytically. However, by considering certain geometries many important results can be obtained. Considering eqn 2.7, for the zero field case of a semi-infinite superconductor in the x direction, the result,

$$\psi\left(x\right) = \psi_{\infty}\tanh\frac{x}{\sqrt{2}\xi}, \tag{2.9}$$

$$\left|\psi_{\infty}\right|^{2} = -\frac{\alpha}{\beta} = \frac{\alpha_{0}}{\beta_{0}}\left(1 - \frac{T}{T_{\mathrm{c}}}\right), \tag{2.10}$$

$$\xi^{2} = \frac{\hbar}{2m_{\mathrm{e}}^{*}\left|\alpha\right|}, \tag{2.11}$$

is obtained where x is the distance inside the superconductor from the surface, ψ_{∞} is the value of the order parameter deep inside the superconductor ($x \to \infty$) and ξ is the 'coherence length' which is the characteristic length scale over which the order parameter varies. Considering eqn 2.8 for the same geometry with an applied field in the z direction we obtain a differential equation for the magnetic vector potential,

$$\frac{\mathrm{d}^{2}}{\mathrm{d}x^{2}}A_{y}\left(x\right) = \frac{\mu_{0}e^{*2}\left|\psi\left(x\right)\right|^{2}}{m_{\mathrm{e}}^{*}}A_{y}\left(x\right). \tag{2.12}$$

From this equation we find that in the case of $x \gg \xi$ the applied field decays exponentially within the superconductor with a characteristic decay length of $\lambda_{\mathrm{L}}^2 = m_{\mathrm{e}}^*/\mu_0 e^{*2} \left|\psi_\infty\right|^2$ (i.e. the London penetration depth) in agreement with eqn 2.3. In the region close to the surface of the superconductor $x \sim \xi$ there is a small correction to the result obtained from the London equations which reduces the gradient of the decay near the boundary. In GL theory ξ and λ_{L} are the characteristic length scales which determine the properties of the superconductor.

The thermodynamic critical field B_{c} is obtained by considering the order parameter deep inside the superconductor ($\psi = \psi_\infty$), when the magnetic energy density equals the difference between the Gibbs free energy density in the normal and superconducting states,

$$\frac{B_{\mathrm{c}}^2}{2\mu_0} = g_{\mathrm{n}} - g_{\mathrm{s}} = -\alpha \left|\psi_\infty\right|^2 - \frac{1}{2}\beta \left|\psi_\infty\right|^4 = -\alpha\left(-\frac{\alpha}{\beta}\right) - \frac{1}{2}\beta\left(-\frac{\alpha}{\beta}\right)^2 = \frac{1}{2}\left(\frac{\alpha^2}{\beta}\right). \quad (2.13)$$

This corresponds to the critical field of any superconductor since it provides a thermodynamic critical field for Type II superconductors although it cannot be directly measured. In a Type II superconductor B_{c} is such that the area under the magnetisation curve is equal to the area under an imaginary Type I like magnetisation curve with a critical field of B_{c}.

There is a surface energy associated with forming a normal-superconducting boundary. It can be shown that this surface energy is positive for $\kappa = \lambda_{\mathrm{L}}/\xi < 1/\sqrt{2}$ (Type I behaviour) and negative for $\kappa > 1/\sqrt{2}$ (Type II behaviour), where κ is known as the

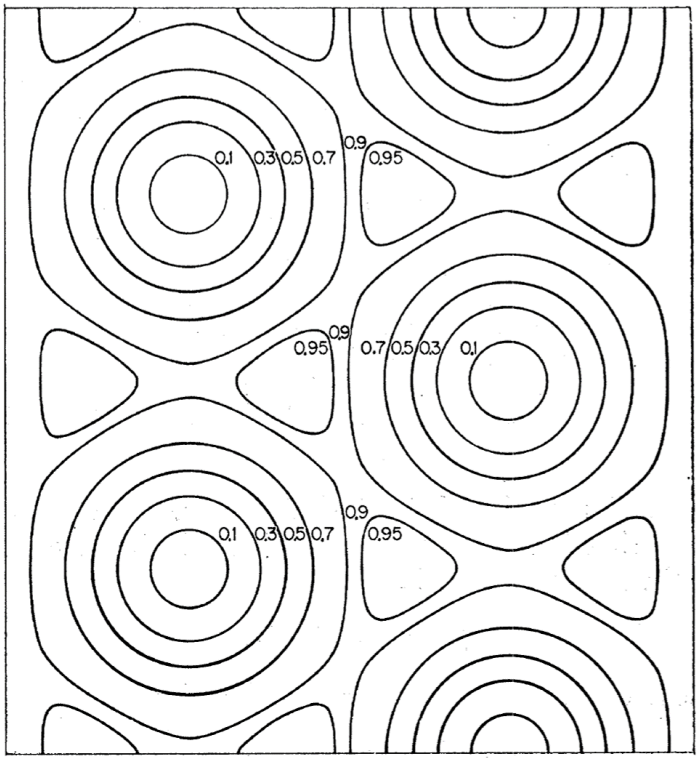

Figure 2.4. Contour plot of $|\psi_\infty|^2$ calculated from GL equations showing the triangular flux line lattice for an applied field just below B_{c2}, contours also represent contours of B and streamlines of the supercurrent [35].

GL parameter. The mixed state of Type II superconductors represents the formation of additional internal normal-superconducting boundaries, lowering the free energy of the system. Abrikosov [34] showed that these additional boundaries take the form of flux lines with a normal state core of radius $\sim \xi$, where each fluxon consists of a single quantum of magnetic flux, $\Phi_0 = h/e^* = 2.07 \times 10^{-15}\mathrm{T\,m^2}$. These fluxons penetrate the entire superconductor with supercurrent vortices flowing around them. The most stable arrangement for these flux lines is a triangular lattice (cf figure 2.4) [35]. This theoretical solution agrees with experimental results [36].

The upper critical field can be calculated from the GL equations by analogy with solutions for the quantum harmonic oscillator and is given by,

$$B_{c2} = \frac{\Phi_0}{2\pi\xi^2}. \tag{2.14}$$

The results of GL theory imply κ is temperature independent since ξ and λ_L have the same temperature dependence. This is only strictly true in the region of T_c and κ is in fact a function of temperature [37]. The theoretical treatment of the temperature dependence of κ is covered in section 4.4.

2.6 Anisotropic B_{c2}

2.6.1 Anisotropic GL theory in homogeneous materials

In a homogeneous anisotropic superconductor, the anisotropic properties can be accounted for using anisotropic GL theory. The effective mass term is replaced with an effective mass tensor. The effective masses in the principal crystallographic directions m_i, where i indicates the direction, are normalized by $(m_a m_b m_c)^{1/3}$ such that the product of the normalised effective masses $\widetilde{m_i}$ gives $\widetilde{m_a}\widetilde{m_b}\widetilde{m_c} = 1$. The coherence lengths ξ_i and penetration depths λ_i in the principal directions can then be written as,

$$\xi_i = \widehat{\xi}\,(\widetilde{m_i})^{-1/2}, \quad \text{where} \quad \widehat{\xi} = (\xi_a \xi_b \xi_c)^{1/3}, \tag{2.15}$$

$$\lambda_i = \widehat{\lambda}\,(\widetilde{m_i})^{1/2}, \quad \text{where} \quad \widehat{\lambda} = (\lambda_a \lambda_b \lambda_c)^{1/3}, \tag{2.16}$$

and the upper critical fields in the principal directions B_{c2}^{i} can be written as,

$$B_{c2}^{a} = \frac{\Phi_0}{2\pi\xi_b\xi_c}, \tag{2.17}$$

$$B_{c2}^{b} = \frac{\Phi_0}{2\pi\xi_a\xi_c}, \tag{2.18}$$

$$B_{c2}^{c} = \frac{\Phi_0}{2\pi\xi_a\xi_b}. \tag{2.19}$$

It is noted that λ_i relates to screening caused by supercurrents flowing in the ith direction and not the direction of the magnetic field being screened.

2.6.2 Layered superconductors

In most anisotropic superconductors, the anisotropy is the result of a layered structure at the microscopic level. These layered structures consist of alternate layers of superconducting material interspaced by non-superconducting (or weakly superconducting) material. This means the material is inhomogeneous at the microscopic level and anisotropic GL theory is not always applicable. If the material can be considered as three dimensional (i.e. the superconducting layers are strongly coupled) then anisotropic GL theory can be applied. However, if the material should be considered as stacked 2D layers (i.e. when the layers are weakly coupled or not coupled) then it must be dealt with in a different manner.

In layered superconductors it is common to define the c-axis as normal to the plane of the layers and for m_i in the plane of the layers to be independent of direction such that $m_a = m_b = m_{ab} = m_{\parallel} \neq m_c = m_{\perp}$, where $m_{\parallel}$ and $m_{\perp}$ are the effective masses

parallel and perpendicular to the plane of the superconducting layers respectively. It is convenient to define a dimensionless anisotropy parameter

$$\gamma \equiv \left(\frac{m_\perp}{m_\parallel}\right)^{\frac{1}{2}} = \frac{\lambda_\perp}{\lambda_\parallel} = \frac{\xi_\parallel}{\xi_\perp} = \frac{B_{c2}^\parallel}{B_{c2}^\perp}, \tag{2.20}$$

where $\parallel$ and $\perp$ indicate the values of the respective parameters in the direction parallel and perpendicular to the plane of the superconducting layers respectively.

2.6.3 Lawrence – Doniach Theory (LD theory)

Lawrence – Doniach (LD) theory gives a guide for determining how a layered superconducting material can be dealt with [38]. In LD theory a layered superconductor is considered as infinitesimally thin superconducting layers separated by insulating material of thickness s and additional terms are added to the GL free energy, eqn 2.6, to account for this.

LD theory shows that when $\xi_\perp > s/2$ the layers are strongly coupled, and the material can be considered as 3D. In this strong coupling limit the angular dependence of B_{c2} is calculated using anisotropic GL theory by taking an anisotropic generalisation of the quantum harmonic oscillator calculation used to calculate eqn 2.14 to give the result

$$\left(\frac{B_{c2}(\theta)\cos\theta}{B_{c2}^\perp}\right)^2 + \left(\frac{B_{c2}(\theta)\sin\theta}{B_{c2}^\parallel}\right)^2 = 1, \tag{2.21}$$

where θ is the angle between the direction perpendicular to the superconducting layers and the magnetic field [39]. The solutions of which are given by

$$B_{c2}(\theta) = \frac{B_{c2}^{\perp}}{\left(\cos^2\theta + \gamma^{-2}\sin^2\theta\right)^{1/2}}. \tag{2.22}$$

When $\xi_{\perp} < s/2$ the layers are considered weakly coupled resulting in 2D behaviour. In this situation B_{c2} is given by

$$B_{c2}^{\parallel} \approx \frac{\Phi_0}{2\pi s^2 \gamma \left[1 - \frac{s^2}{2\xi_{\parallel}^2}\right]^{\frac{1}{2}}}, \tag{2.23}$$

when the field is applied parallel to the superconducting layers and by

$$B_{c2}^{\perp} = \frac{\Phi_0}{2\pi\xi_{\parallel}^2}, \tag{2.24}$$

when the field is applied perpendicular to the superconducting layers [40]. LD theory does not give an angular dependence for B_{c2} in the weak coupling limit.

$\xi_{\perp}$ is a function of temperature and hence whether a layered superconducting material should be considered as 2D or 3D is also a function of temperature. The crossover temperature $T_{3D\to 2D}$ is determined when $\xi_{\perp} = s/2$ and is given by

$$T_{3D\to 2D} = T_c\left[1 - \frac{1}{\gamma^2}\left(\frac{2\xi_{\parallel}}{s}\right)^2\right]. \tag{2.25}$$

In BiSCCO and YBCO $T_{3D\to 2D}$ is approximately $(T_c - 0.1\,\mathrm{K})$ and 78 K respectively [39].

2.6.4 Tinkham's model for two dimensional thin films

In the limit of very weak coupling $s \gg \xi_\perp$ LD is no longer applicable. In this limit we can assume zero coupling between the superconducting layers and we consider them as individual layers. This contrasts with LD theory where the layers are considered to be infinitesimally thin.

Tinkham developed a model for the angular dependence of B_{c2} in an isolated 2D superconducting thin film of thickness d [41], this has also been shown to be applicable in layered superconductors with very weak coupling [42]. In this system it is the lower dimensionality of an otherwise isotropic material (or layer) which gives rise to the anisotropic behaviour. A superconducting thin film is considered 2D when $\xi > d$. Hence, when the field is applied parallel to the plane of the film the vortex size perpendicular to the plane is determined by the thickness of the film, not the coherence length. The free energy of the system is therefore reduced compared to if the vortices were limited in size by ξ, which in turn affects B_{c2}. By considering this modified free energy the angular dependence of B_{c2} is found to satisfy the equation

$$\frac{|B_{c2}(\theta)\cos\theta|}{B_{c2}^{\perp}} + \left(\frac{B_{c2}(\theta)\sin\theta}{B_{c2}^{\parallel}}\right)^2 = 1. \tag{2.26}$$

The solutions of which are given by

$$B_{c2}(\theta) = B_{c2}^{\perp}\gamma_{\text{Tink}}^2 \frac{\sqrt{\cos^2\theta + 4\sin^2\theta/\gamma_{\text{Tink}}^2} - |\cos\theta|}{2\sin^2\theta}, \tag{2.27}$$

where $\gamma_{\text{Tink}} = B_{c2}^{\parallel}/B_{c2}^{\perp} = \xi/d \propto (1 - T/T_c)^{-1/2}$ which differs from γ because $B_{c2}^{\parallel}$ has different temperature dependence.

2.6.5 Mineev's general expression for B_{c2}

In real materials there is no clear transition from 2D to 3D behaviour and in this transition region it is difficult to know which, if any, theory of anisotropic layered superconductors is applicable. In an attempt to address this, Mineev [43] considered superconducting layers of thickness d separated by insulating layers with interlayer spacing s, combining the ideas of LD theory and Tinkham thin film model, to derive a general expression for B_{c2} as a function of angle

$$\left(\frac{B_{c2}(\theta)\sin\theta}{\gamma^{\dagger}B_{c2}^{\perp}}\right)^2 + \frac{B_{c2}(\theta)}{B_{c2}^{\perp}}\left(\cos^2\theta + \gamma^{*-2}\sin^2\theta\right)^{\frac{1}{2}} = 1, \tag{2.28}$$

where $\gamma^* = \left(m_{\perp}/m_{\parallel}\right)^{1/2}$, $\gamma^{\dagger} = \left(B_{c2}^{\parallel}/B_{c2}^{\perp}\right)\left(1 - B_{c2}^{\parallel}/\gamma^* B_{c2}^{\perp}\right)^{-1/2} \propto (1 - T/T_c)^{-1/2}$. It is important to note that while γ^* plays a similar role to in the equation as γ in anisotropic GL theory, it is distinct as it does not represent the ratio of B_{c2} in orthogonal directions $\gamma^* \neq B_{c2}^{\parallel}/B_{c2}^{\perp}$.

A comparison of these three anisotropic models of B_{c2} is shown in figure 2.5. The anisotropic GL model gives a normalised B_{c2} which is independent of temperature, the Tinkham 2D thin film model is temperature dependent with a sharper peak at higher temperatures and a discontinuity in the first derivative at the peak, and the Mineev general expression shows a peak sharpness between the two extremes, temperature

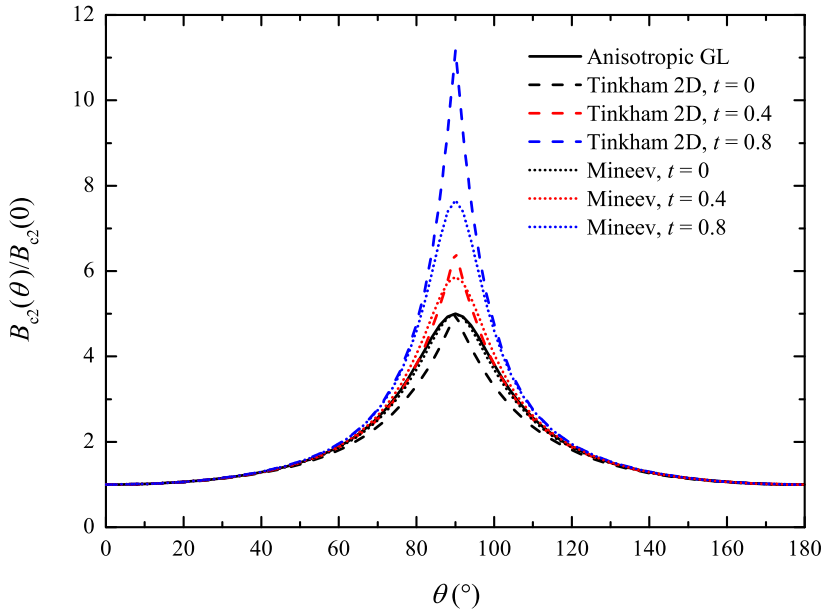

Figure 2.5. A comparison of the three anisotropic B_{c2} models presented in this section for three reduced temperatures $t = T/T_c$. The anisotropic GL model has $\gamma = 5$, the Tinkham 2D thin film model has $\gamma_{\text{Tink}}\,(T = 0\,\text{K}) = 5$ and the Mineev general expression has $B_{c2}^{\parallel}/B_{c2}^{\perp}\,(@T = 0\,\text{K}) = 5$ and $\gamma^* = 10$.

dependence and a continuous first derivative at the peak. The Mineev general expression can lie anywhere between the extremes of the anisotropic GL model and the Tinkham 2D thin film model depending on the values of $B_{c2}^{\parallel}/B_{c2}^{\perp}\,(@T = 0\,\text{K})$ and γ^*. It reduces to anisotropic GL when $B_{c2}^{\parallel}/B_{c2}^{\perp}\,(@T = 0\,\text{K}) = \gamma^*$ with $\gamma^* \equiv \gamma$ and to the Tinkham 2D thin film model when $\gamma^* \to \infty$ with $B_{c2}^{\parallel}/B_{c2}^{\perp} \equiv \gamma_{\text{Tink}}$.

2.7 BCS theory

Developed in 1957 by Bardeen, Cooper and Schrieffer, BCS theory [13] is a theory of the microscopic origins of superconductivity for conventional, low temperature superconductors. Without going into the detailed mathematical derivations, the

following section gives an overview of BCS theory and its results. References [44–46] give a more detailed description of the formulation of BCS theory and its results.

2.7.1 Cooper pairs

Fröhlich proposed there exists a coupling mechanism between two electrons (of pre-scattering momenta $\boldsymbol{k}$ and $-\boldsymbol{k}$) in a Fermi sea of electrons via the transfer of a phonon which produces an attractive potential $V(\boldsymbol{k}, \boldsymbol{k}')$ [47]. Later Cooper showed that for electronic states within $\hbar\omega_{\mathrm{D}}$ (where ω_{D} is the Debye frequency) of the Fermi surface this attractive potential is always greater than the Coulomb repulsion between the electrons and results in a bound state independent of how weak the attractive potential $V(\boldsymbol{k}, \boldsymbol{k}')$ is [48]. The interaction is maximised for states with opposing momenta $\boldsymbol{k}$ and $-\boldsymbol{k}$. Assuming an interaction potential

$$V(\boldsymbol{k}, \boldsymbol{k}') = \begin{cases} -V_0, & \text{if } |\varepsilon_{\boldsymbol{k}}| \text{ and } |\varepsilon_{\boldsymbol{k}'}| < \hbar\omega_{\mathrm{D}}, \\ 0, & \text{otherwise}, \end{cases} \tag{2.29}$$

where $\varepsilon_{\boldsymbol{k}}$ is the difference in energy between the electronic state and the Fermi surface, it can be shown the resulting binding energy between the two electrons E_{b} is given by

$$E_{\mathrm{b}} = 2\hbar\omega_{\mathrm{D}} \exp -\frac{2}{N(0)\, V_0}, \tag{2.30}$$

where IH: (in equation) italics removed from D in omega$_D$N(0) is the density of states (neglecting spin) at the Fermi surface for $T = 0\,\mathrm{K}$. It can also be shown the bound electrons have antiparallel spins. This bound state is known as a 'Cooper pair'.

While a phonon mediated interaction between two electrons is the basis of superconductivity in classical superconductors it is important to note that a phononic mechanism is not required to show superconductivity. Superconductivity follows within the framework of BCS theory for any pairing mechanism which produces an attractive interaction between two change carriers in states close to the Fermi surface.

2.7.2 The energy gap and results of BCS theory

BCS theory extends this interaction from a single pair of charge carriers to a whole system of charge carriers. It is found there is an energy gap $\Delta(T)$ at the Fermi level between the normal and superconducting states, implying that an excitation of energy 2Δ is required to break a Cooper pair. Conventional BCS theory assumes 'weak coupling', $|\Delta| \ll \hbar\omega_{\mathrm{D}} \ll \varepsilon_{\mathrm{F}}$, in this limit the zero-temperature energy gap is given by

$$\Delta(0) = 2\hbar\omega_{\mathrm{D}} \exp -\frac{1}{N(0)\,V_0}. \tag{2.31}$$

Figure 2.6 shows the temperature variation of the superconducting band gap.

BCS theory predicts that all Cooper pairs will have the same momentum, analogous to a Bose-Einstein condensate, because of this, scattering is prohibited and zero dc electrical resistivity results.

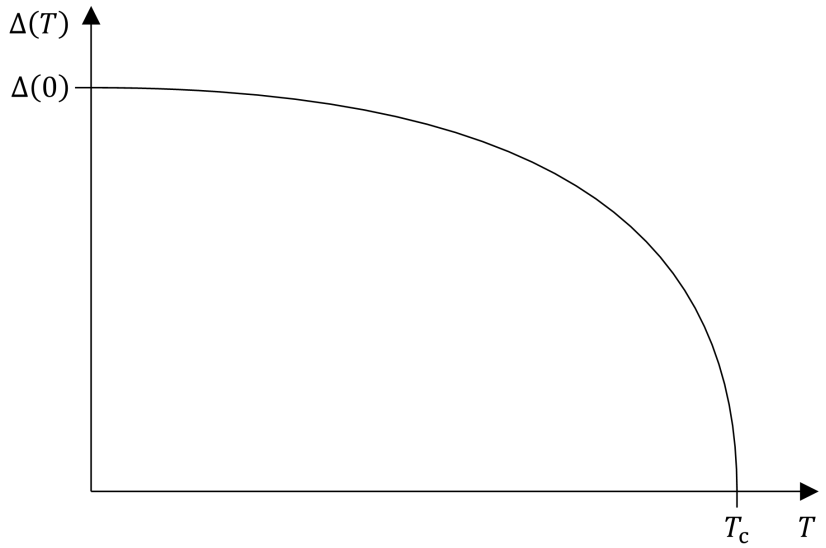

Figure 2.6. Plot of the variation of BCS energy gap with temperature.

The BCS critical temperature is defined as

$$k_{\mathrm{B}}T_{\mathrm{c}} = 1.14\hbar\omega_{\mathrm{D}} \exp -\frac{1}{N\left(0\right)V_0} = \frac{2\Delta\left(0\right)}{3.52}. \tag{2.32}$$

The 'isotope effect' is an important test of BSC theory that comes from this relation. The Debye frequency depends on the mass of the lattice ions M as $\omega_{\mathrm{D}}^{-1/2}$ hence $T_{\mathrm{c}} \propto M^{-1/2}$. Substituting the lattice ions with different isotopes will change M and therefore vary T_{c} with no effect on the electronic structure. Experimental confirmation of the isotope effect is one of the earliest successes of BCS theory and confirms conventional superconductivity is caused by a phonon mediated interaction [49].

Many superconductors do not follow the predictions of BCS theory and are known as unconventional superconductors, this is due to the breakdown of the assumptions of BCS theory such as: phonons mediating the attractive interaction, the simplified interaction potential and weak electron–phonon coupling.

2.8 Flux pinning

For a Type I superconductor it is clear the maximum transport current that can be carried without resistance is equal to the current for which the field at the surface is equal to H_c and the supercurrent flows in a thin layer near the surface of thickness $\sim \lambda_L$, as previously discussed in section 2.4.

When in the mixed state a Type II superconductor supports supercurrent flow throughout the bulk of the material, not just in the surface layer. The application of a transport current will result in a Lorentz type interaction between the fluxons and the transport current causing the fluxons to move, resulting in an electric field and dissipation. A perfect infinite bulk material of Type II superconductor in the mixed state cannot support a lossless transport current in high fields at all. This appears to be in contradiction with the large lossless transport currents found experimentally that make Type II superconductors so useful in high field applications. The apparent contradiction is reconciled by considering that no material is perfect. Fluxons lower their free energy by being located at inhomogeneities such as grain boundaries, precipitates and lattice defects. The Flux Line Lattice (FLL) distorts from the regular, periodic arrangement of the Abrikosov lattice (cf. figure 2.4) by allowing fluxons to pass through these inhomogeneities. These inhomogeneities are collectively known as 'pinning centres'. The critical current density $\boldsymbol{J}_c$ required to remove the FLL from its pinning centres and to start flux flow is defined by

$$\boldsymbol{F}_p = \boldsymbol{J}_c \times \boldsymbol{B}, \tag{2.33}$$

where $\boldsymbol{F}_\mathrm{p}$ is the flux pinning force density, a material property dependent on the type(s) of pinning centre present. $\boldsymbol{J}_\mathrm{c}$ represents the maximum current density for which a lossless current can flow and is the useful working limit for high field applications.

A complete understanding of the functional form of $\boldsymbol{F}_\mathrm{p}$ is a complex subject that requires understanding not only the behaviour of an individual type of pinning centre but also the effects of having numerous different types of pinning centre present in the same material, how the FLL distorts and how the fluxons interact with one another. A brief description of the most successful theories of flux pinning are covered below.

Most superconductors follow the same scaling law for F_p of the general form

$$F_\mathrm{p} \propto \frac{B_\mathrm{c2}^n}{\kappa^m} b^p \left(1-b\right)^q , \tag{2.34}$$

where n, m, p and q are constants and $b = B/B_\mathrm{c2}$ is the reduced field [50]. Two key features of this scaling law are: the temperature and strain independent universal curve behaviour found when $F_\mathrm{p}/F_\mathrm{p,max}$ is plotted against b, and that $F_\mathrm{p,max}$ scales with temperature and strain as $F_\mathrm{p,max} \propto B_\mathrm{c2}^n/\kappa^m$ [51].

Dew Hughes [52] considered pinning centres with different interaction types and geometries, and calculated scaling constants for them. The scaling constants p and q were found to be different half-integer values depending on the type of pinning centre, n was found to equal 2 for all types of pinning centre and m was found to be either 2 or 3 for the majority of types of pinning centre. Then by assuming the FLL can be considered as plastic and fluxons distort to match the arrangement of pinning centres

F_p can be considered as the elementary pinning force of a single pinning centre f_p multiplied by their density n_p. The physical consequence of this simple model is that all fluxons are 'depinned' simultaneously when the transport current reaches J_c.

A more realistic description of F_p for polycrystalline materials was introduced by Kramer [53] where the interaction between fluxons means the FLL must be considered as elastic and fluxons are not able to distort arbitrarily to match the arrangement of pinning centres. This results in some fluxons being strongly pinned by pinning centres while others are only weakly held in place due to the elasticity of the FLL. Here J_c is interpreted as the current where the Lorentz force overcomes the elasticity of the FLL causing the weakly held fluxons to flow around the strongly pinned ones. The scaling constants from this analysis give $n = 2.5$, $m = 2$, $p = 0.5$ and $q = 2$.

No one flux pinning model is suitable to describe all superconductors. For example Nb–Ti is best described using a plastic FLL with $p = 1$ and $q = 1$ indicating volume pins are the dominant pinning mechanism [52, 54]. Whereas Nb_3Sn is best described using an elastic FLL with $p = 0.5$ and $q = 2$, where above J_c flux flows along the grain boundaries [55, 56]. The general scaling law appears to be valid for most high field superconductors although the scaling constants p and q may not agree with any one theory.

2.9 Nuclear fusion

Fusion utilises the principle of mass-energy equivalence $E = mc^2$ to produce energy by fusing lighter nuclei together to produce heavier nuclei. Fusing two nuclei together is no small feat with temperatures of tens of millions of degrees required to overcome the Coulomb barrier wanting to keep the nuclei apart. The most 'well-known' place such extreme conditions exist is in the core of our Sun with temperatures of $\sim 15\,\text{million}\,\text{K}$, high enough to cause protons to fuse together into helium through the so-called p-p chain.

2.9.1 The fusion reaction

Unfortunately, the same p-p chain cannot be used for power generation here on Earth as the reaction rates are too low [57]. Instead a more favourable reaction must be selected, the reactions worth consideration are

$$
\begin{aligned}
{}^{2}_{1}\text{D} + {}^{2}_{1}\text{D} &\rightarrow {}^{3}_{1}\text{T} + {}^{1}_{1}\text{p} + 4.03\,\text{MeV},\\
{}^{2}_{1}\text{D} + {}^{2}_{1}\text{D} &\rightarrow {}^{3}_{2}\text{He} + {}^{0}_{1}\text{n} + 3.27\,\text{MeV},\\
{}^{3}_{2}\text{He} + {}^{2}_{1}\text{D} &\rightarrow {}^{4}_{2}\text{He} + {}^{1}_{1}\text{p} + 18.4\,\text{MeV},\\
{}^{2}_{1}\text{D} + {}^{3}_{1}\text{T} &\rightarrow {}^{4}_{2}\text{He} + {}^{0}_{1}\text{n} + 17.6\,\text{MeV}.
\end{aligned}
$$

The reaction rate per unit volume R is given by $R = n_1 n_2 \langle \sigma v \rangle$ where n_1 and n_2 are densities of the two reactants, and $\langle \sigma v \rangle$ is the thermal reactivity which is a strong function of temperature. Figure 2.7 shows the temperature dependence of $\langle \sigma v \rangle$ for

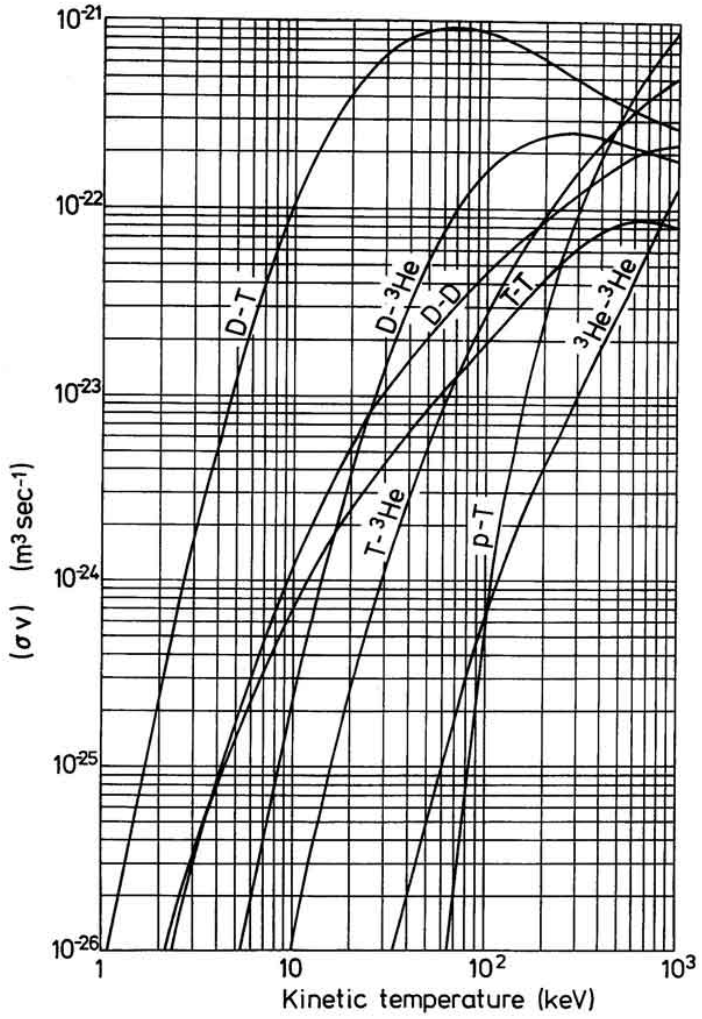

Figure 2.7. The thermal reactivity $\langle \sigma v \rangle$ of the important fusion reactions as a function of temperature [58], 1 keV = 11.6 million K.

these reactions (1 keV = 11.6 million K). The D–T reaction has a cross section two orders of magnitude higher than the other reactions making it the clear choice for maximising the fusion energy output.

2.9.2 Magnetic confinement

Temperatures in excess of 100 million K are required in order to achieve an appreciable reaction rate and unlike the Sun we do not have the luxury of a large gravitation

pressure to confine the hot D–T plasma. The leading method of achieving plasma confinement is Magnetic Confinement Fusion (MCF). A magnetic field $\boldsymbol{B}$ is applied to the plasma. This results in a Lorentz force exerted on the charged particles of the plasma causing them to gyrate around the field confining them in the direction $\perp \boldsymbol{B}$ although the particles are still free to travel $\parallel \boldsymbol{B}$. The radius of this gyration is the Larmor radius r_{L} and is given by the equation

$$r_{\mathrm{L}} = \frac{m v_{\perp}}{|e|\, B}, \tag{2.35}$$

where m is the particle mass, $v_{\perp}$ the particle velocity in the direction perpendicular to the magnetic field and e is the electrical charge of the particle. To achieve 3 dimensional confinement, the field lines are wrapped around into a toroidal shape so particles continually circulate around the torus. To keep the particles confined within a reasonable volume, the largest Larmor radius ($\sim$ cm) must be much smaller than the dimensions of the confined volume of plasma, requiring a magnetic field of $\sim 5\,\mathrm{T}$.

The toroidal geometry introduces significant particle drifts due to the curvature and gradient of $\boldsymbol{B}$ that cause confinement to be lost. These drifts are counteracted by adding a poloidal component to the magnetic geometry (cf. figure 2.8) which transposes the particle positions around the cross section of the torus. There are many ways of establishing this non-trivial magnetic geometry, the most developed of which is known as the tokamak and is the basis of the vast majority of currently operating fusion devices. In a tokamak the toroidal component of the field is produced using external

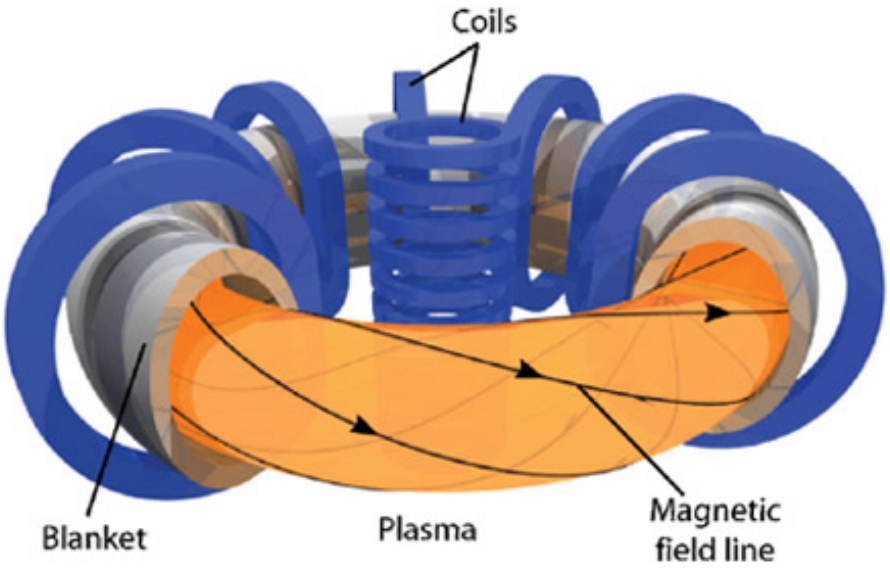

Figure 2.8. The magnetic geometry of a fusion tokamak [59].

magnets and the poloidal component is produced by inducing a large current in the plasma by ramping a central solenoid magnet.

Although this geometry produces good confinement, the plasma still slowly diffuses radially outward. At the edge of the plasma there is a thin layer known as the scrape-off layer. When particles enter this layer, they are quickly transported to the divertor at the bottom and/or top of the vessel and removed from the plasma. A cross section of a typical tokamak showing the scape-off layer and divertor is given in figure 2.9.

2.9.3 The fusion triple product

The fusion triple product is used to determine the 'performance' of a fusion plasma using the particle density n, the temperature T and the energy confinement time τ_{E} (the average time any single particle is confined before it leaves the system). Above a critical value of the fusion triple product, known as the 'Lawson criterion', the power

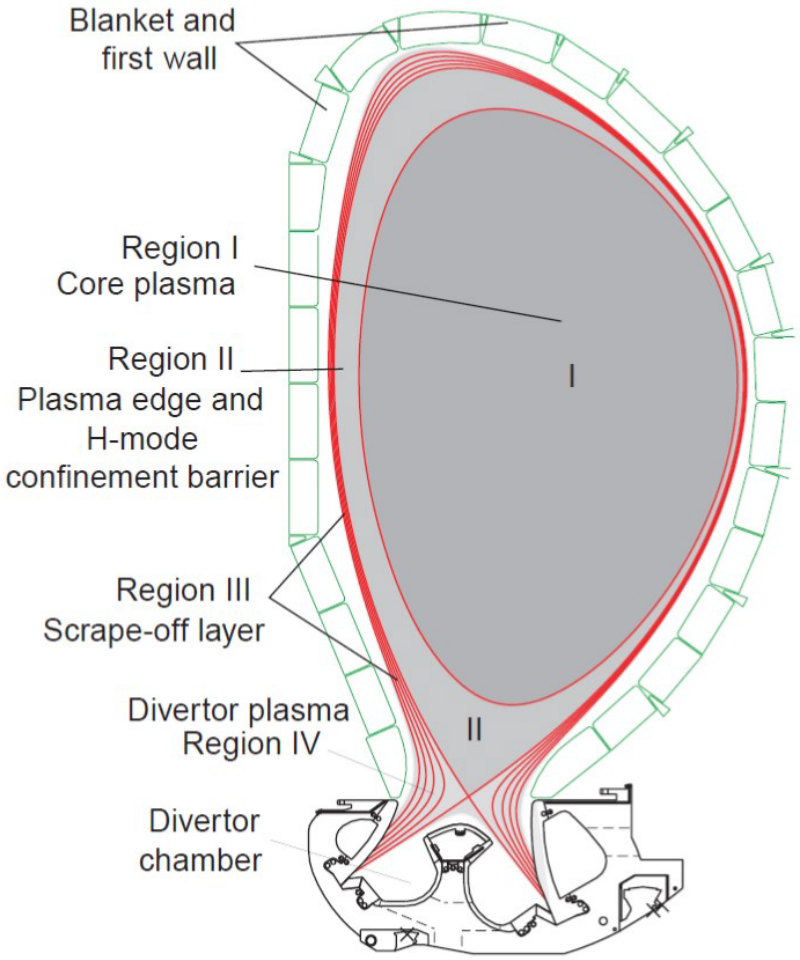

Figure 2.9. Cross section of the ITER reaction vessel, red lines represent magnetic flux surfaces [60].

released by the fusion reactions is enough to maintain the temperature of the plasma without external heating sources which is the key milestone for using fusion as an energy source. For a D–T fusion plasma this criterion is given by [61]

$$nT\tau_{\mathrm{E}} \geq 5 \times 10^{21}\,\mathrm{m}^{-3}\,\mathrm{s\,keV}. \tag{2.36}$$

A fusion plasma with a triple product higher than the Lawson criteria is said to have "ignited". In an idealised situation such a fusion plasma would be self sufficient so long as the density and energy confinement time are maintained. However, in reality the external heating systems can never be turned off completely as these systems also perform other functions such as injecting additional fuel, shaping the plasma and providing current to the plasma to maintain the poloidal magnetic field.

2.10 Concluding remarks

BCS theory is often thought of as the ultimate theory of superconductivity as it describes its origins on a microscopic level. However, for practical applications we find BCS theory is only applicable in a small number of systems. While giving no insight into the microscopic origins, the phenomenological GL theory can be used to describe the vast majority of superconductors in magnetic fields. When used together with theories of flux pinning, GL theory provides the basis for our understanding of most superconductors in magnetic fields which is one of the important considerations in this thesis.

Chapter 3

Superconducting conductors, their strain dependence and applications

3.1 Introduction

It is a common misconception outside of the superconductivity community that superconductors with the highest critical temperature are the best materials for making conductors capable of carrying large currents. However, this is not the case and issues such as low J_c in high fields, severe drops in J_c over grain boundaries and difficulties in forming the materials into traditional wire shapes are key issues in the development of usable HTS conductors. Such issues have now largely been overcome and while LTS conductors still dominate the market for most applications, superconducting devices using BiSCCO and REBCO conductors are becoming more widespread as costs continue to fall.

This chapter will review the manufacture and properties of common HTS conductors, and discuss design issues associated with magnetic confinement fusion reactors. Section 3.2 reviews the properties of HTS materials, section 3.3 reviews the architecture of different HTS conductors, section 3.4 reviews the strain dependence of LTS and HTS conductors, section 3.5 reviews a bimodal model which explains the strain dependence of REBCO tapes in zero field, section 3.6 reviews some selected aspects of fusion reactor design and section 3.7 provides concluding remarks.

3.2 HTS materials

Prior to the discovery of the cuprate superconductors, superconductivity was generally considered as a 'mature' field of science. The highest critical temperature under ambient conditions was 22.3 K found in Nb_3Ge [62], a conventional superconductor which can be understood through the framework of BCS theory and its extensions. In BCS theory T_c is linked to the vibrational frequency of the phonons exchanged between the electrons in a Cooper pair and it was thought this limited the maximum possible T_c under ambient pressure to approximately ~ 30 K [63]. So, the discovery of superconductivity in the cuprate materials at significantly higher temperatures, higher even than the boiling point of liquid nitrogen at 77 K, was entirely unexpected.

The initial discovery of superconductivity in the cuprate $Ba_xLa_{5-x}Cu_5O_y$ in 1986 with $T_c = 30$ K [6] earned its discoverers, J. Bednorz and K. Müller, the Nobel prize

in physics in 1987. In the years that followed several superconducting cuprates were discovered in quick succession with increasingly high T_c.

It was quickly established that cuprates cannot be described by conventional BCS theory, hence they are commonly referred to as 'unconventional' superconductors. They show a number of 'unconventional' properties including *d*-wave pairing symmetry [64,65] and the existence of a pseudogap at temperatures above T_c [66]. There are several competing theories regarding the origin of superconductivity in the cuprates such as: resonant valence bands [67], polaron-bipolaron [68] and spin fluctuations [69], and there is no clear evidence or consensus as to which of these theories holds the most, or any merit.

3.2.1 Properties and structure of REBCO and BiSCCO

The crystal structure of the cuprates consists of stacked CuO_2 planes interspaced by other ions/atoms, the unit cells are tetragonal or orthorhombic (close to tetragonal) and are highly anisotropic between the *ab*-plane and *c*-axis directions. Orthorhombic cuprates display twinning in the *ab*-plane along the $\langle 110 \rangle$ directions. The most important cuprates for applications are $Bi_2Sr_2CaCu_2O_8$ (Bi-2212), $Bi_2Sr_2Ca_2Cu_3O_{10}$ (Bi-2223) and (RE)$Ba_2Cu_3O_{7-\delta}$ where RE is a rare earth element such as Y, Sm, Eu, Gd or Nd (REBCO). Their crystal structures are shown in figure 3.1.

The superconductivity is caused by and to some extent is confined to the CuO_2 planes. The cuprates can essentially be considered as layered superconductors where there are alternating layers of superconducting and non-superconducting material lead-

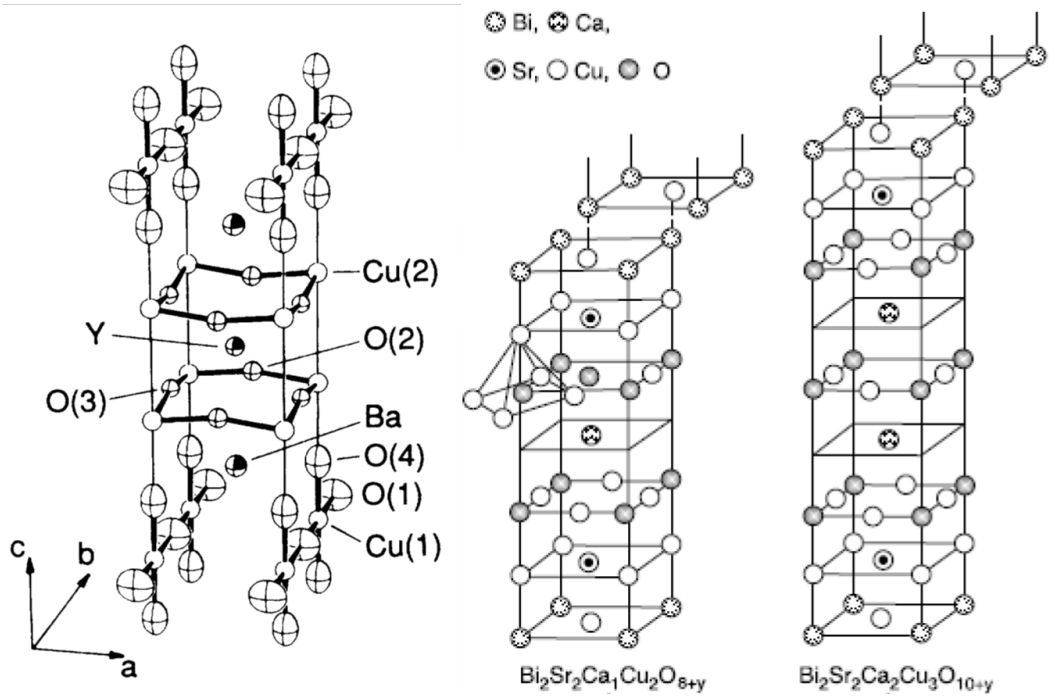

Figure 3.1. Crystal structures of REBCO [70], Bi-2212 and Bi-2223 [71].

ing to a high anisotropy of the superconducting properties. The coherence lengths ξ are short and the penetration depths λ are long compared to conventional superconductors, particularly in the direction of the c-axis. Some of the important superconducting parameters for REBCO, Bi-2212 and Bi-2223 are listed in table 3.1.

3.2.2 The irreversibility field B_{irr}

In conventional superconductors $J_{\mathrm{c}} \to 0$ as $B \to B_{\mathrm{c2}}$. However, in the cuprates there is an additional irreversibility field B_{irr} below B_{c2} above which $J_{\mathrm{c}} = 0\,\mathrm{A}$, despite still being in the superconducting state whereas B_{c2} delineates the superconducting and normal phases. The existence of B_{irr} is attributed to thermally activated flux jumps causing the fluxons to no longer be pinned above B_{irr} reducing the flux pinning force

Table 3.1. Some important properties of LTS and HTS materials used in commercially available conductors

Material	T_c (K)	$B_{c2}(0)$	$\lambda(0)$ (nm)	$\xi(0)$ (nm)	a (nm)	c (nm)
Nb-Ti	9.5[a]	13.0[a]	163[b]	3.4[c]	0.328[d]	-
Nb_3Sn	18.2[a]	23.0[a]	93.5[c]	2.73[c]	0.5289[e]	-
REBCO	90[f]	120[†f] 250[‡f]	894[†g] 135[‡g]	0.378[†c] 1.29[‡c]	0.3818[e]	1.1683[e]
Bi-2212	84.4[c]	231[†c]	3000[†h] 300[‡i]	0.324[†h] 3.24[‡c]	0.5410[e]	3.0930[e]
Bi-2223	108[c]	297[†c]	1160[†h] 165[‡j]	0.408[†h] 2.86[‡c]	0.539[e]	3.7[e]

[†] $B \parallel c$, [‡] $B \perp c$

[a] Reference [7]

[b] Reference [72]

[c] Reference [28]

[d] Reference [73]

[e] Reference [74]

[f] Reference [27]

[g] Reference [75]

[h] Reference [76]

[i] Reference [77]

[j] Reference [78]

to zero [79, 80]. For cuprates in the region near T_c, B_{irr} follows the power law relation

$$B_{irr} \approx a\,(1-t)^s\,, \tag{3.1}$$

where a and s are constants and $t = T/T_c$ is the reduced temperature [81]. For thin films $s \approx 1.2$ and for bulk crystals $s \approx 1.5$. B_{irr} also exists in conventional superconductors however it is usually so close to B_{c2} it becomes indistinguishable from it due to the transition width [39]. In magnetic measurements B_{irr} is generally determined by the field at which the magnetisation of a field cooled and zero field cooled sample deviate [81]. However, care must be taken when interpreting magnetic measurements depending on the measurement technique used. It has been shown that in vibrating sample magnetometry (VSM) the signal falls to zero when the effective AC field penetrates the whole sample before J_c falls to zero and this may be incorrectly interpreted as B_{irr} [82]. In transport measurements the point at which the resistance of the sample (measured using a small excitation current) is no longer zero is interpreted as B_{irr} and the point at which the resistance is equal to the normal state resistance is interpreted as B_{c2} [83].

3.2.3 The grain boundary 'problem'

Early experiments on cuprate single crystals showed it could support critical current densities at low temperatures far greater those attained in Nb–Ti and Nb_3Sn [84–86], raising hopes cuprates would quickly surpass conventional superconductors as the

material of choice for high field magnets. However, these hopes were quickly shattered when the critical current density of polycrystalline samples was found to be orders of magnitude lower [87].

It quickly became apparent that the critical current density across a grain boundary decreases rapidly with the misorientation angle θ_{gb} between the adjoining grains [88]. The twin boundaries in the *ab*-plane for orthorhombic cuprates have J_{c} comparable to the grains. So, for the purposes of grain boundary misorientation all cuprates can essentially be considered to have tetragonal symmetry.

There are three types of misorientation between grains known as [001] tilt, [100] tilt and [100] twist, the nature of which are summarised in figure 3.2. Experiments on bi-crystals show the critical current density falls approximately exponentially with increasing θ_{gb} of [001] tilt in nature [88–91] and further experiments found this behaviour to be independent of the nature of the grain boundary [90, 92], cf. figure 3.3.

Grain boundaries are not truly two dimensional but are in fact three dimensional with some finite width. The properties of the grain boundary region can differ significantly from that of the grains. The superconductivity is suppressed in the grain boundary region. This means a grain boundary can be considered as Josephson junction (superconducting-normal-superconducting junction) where the supercurrent has to quantum mechanically tunnel across the boundary [94]. J_{c} across the boundary is a strong function both of the width of the boundary and its normal state resistance [28, 76]. The grain boundaries in HTS materials have much higher resistivities than LTS grain boundaries so are much more sensitive to width. This explains why

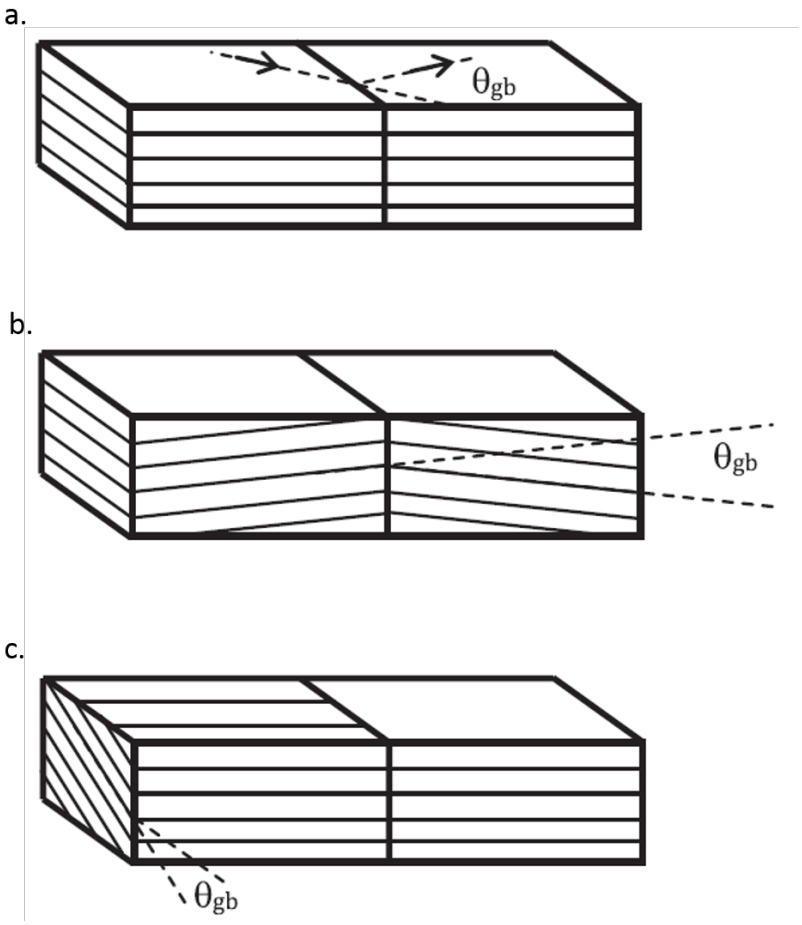

Figure 3.2. Sketches showing the nature of a) [001] tilt, b) [100] tilt and c) [100] twist grain boundary misorientation angles θ_{gb}. The planes in the sketches represent of the *ab*-planes. Reproduced from [93].

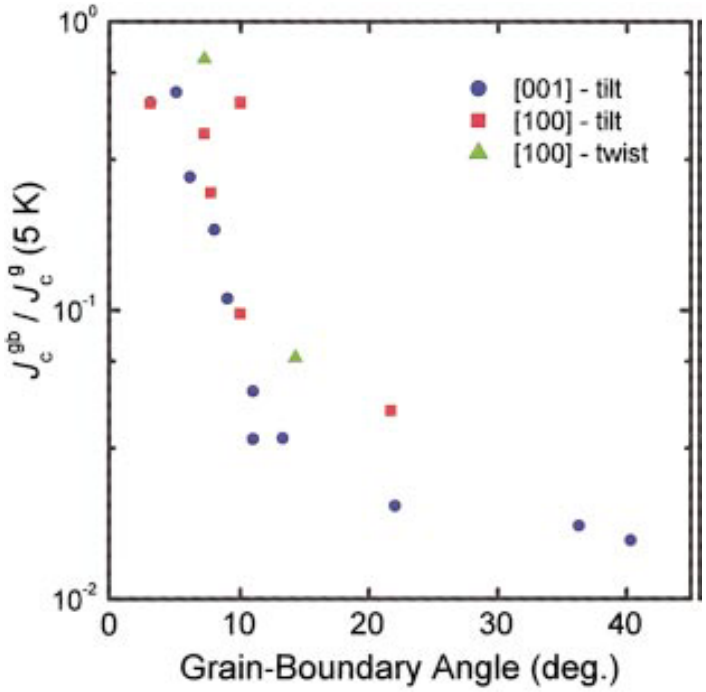

Figure 3.3. Normalised critical current density of grain boundaries as a function of misorientation angle showing similar behaviour for all three types of boundary. Figure reproduced from [90], data from [92].

thin, low angle grain boundaries are required to support high J_c in HTS materials, but not in LTS materials.

3.3 Developments in high temperature superconducting wires and tapes

Despite the difficulties arising from grain boundaries significant progress has been made toward producing competitive cuprate conductors. The following subsections will cover the architecture and properties of the three main cuprate conductors available: Bi-2212 round wire, Bi-2223 tape and REBCO tape. At low temperatures J_c of the

superconducting fraction of these conductors is far superior to their LTS counterparts (cf. figure 3.4a), however when the engineering critical current density J_{E} (the critical current density of the whole wire cross section) is considered they become comparable (cf. figure 3.4b). The relatively high cost of HTS conductors mean at present for applications < 20 T LTS conductors are still the material of choice, however in order to access fields > 20 T HTS conductors are the only option.

3.3.1 BiSCCO wires and tapes

BiSCCO was the first HTS material to be made into a useful conductor. Two types of BiSCCO conductor are available: Bi-2212 is available in the form of a round wire and Bi-2223 is available in a high aspect ratio tape geometry. Round wire geometries are generally preferable for magnet windings as they can easily be wound into arbitrary geometries.

Both Bi-2212 and Bi-2223 conductors are fabricated using the Powder-in-Tube (PIT) method [96]. In this process powdered superconducting material is poured into metal tubes which are drawn into wires, these wires are then stacked, and the stack is drawn further to produce a multifilamentary wire. This restacking may be repeated several times. The wire is then sintered in an overpressure process to densify the grains [97, 98]. Silver is used for the metal tubes as this encourages grain alignment, allows oxygen diffusion and does not react with the powders. Lower J_{c} values in Bi-2223 wires mean additional rolling and sintering steps are added to the process to improve the grain alignment, raising J_{c} and resulting in a final product which is tape-like with a

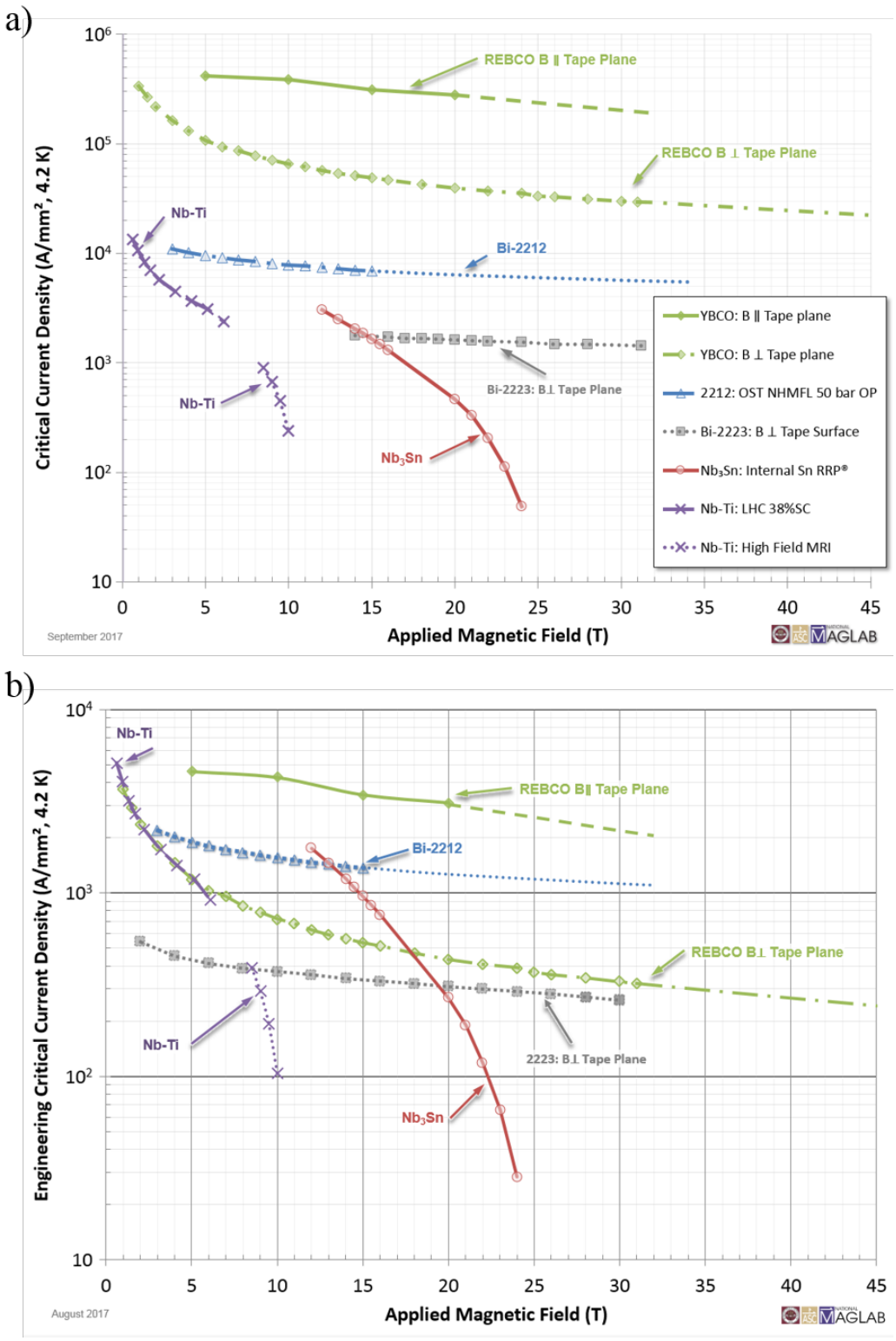

Figure 3.4. a) Critical current density J_c of the superconducting fraction and b) the engineering critical current density J_E of the whole wire cross section as a function of field for various commercial conductors. Adapted from [95].

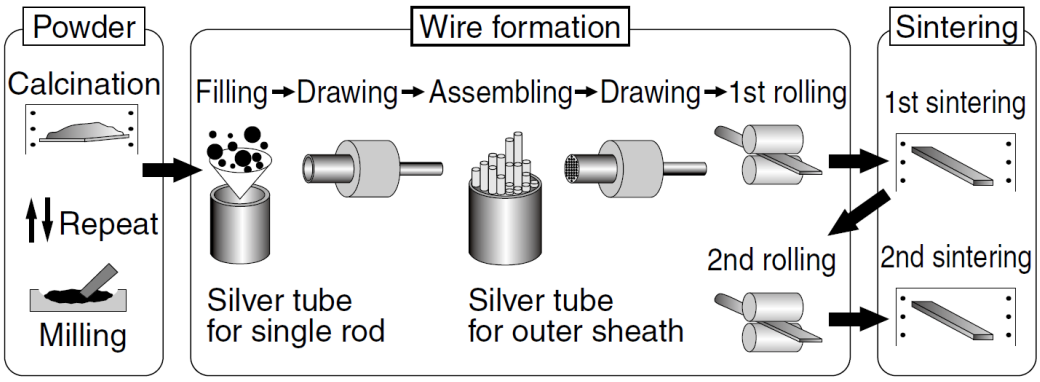

Figure 3.5. Manufacturing procedure for Bi-2223 multifilamentary tape conductors. For Bi-2212 multifilamentary round wires the rolling process is omitted from the procedure. Figure reproduced from [96].

high aspect ratio. The manufacturing procedure for Bi-2223 is summarised in figure 3.5. Cross sectional images for both conductors are shown in figure 3.6.

Bi-2212 wire is isotropic over long lengths whereas Bi-2223 tape is highly anisotropic with the c-axis in the direction normal to the tape surface and the ab-plane in the plane of the tape. Electron Backscatter Diffraction Orientation Imaging Microscopy has been used to look at the grain alignments within the filaments [101]. Counterintuitively, both Bi-2212 wire and Bi-2223 tape have good grain alignment, despite the isotropic nature of Bi-2212 wire. It was found that at a local level the grains in Bi-2212 wire showed a biaxial alignment with all three types of misorientation angle $< 15°$, the a-axis is aligned with the axis of the wire and the c-axis is orthogonal to it. Over length scales much larger than that of individual grains the direction of the c-axis rotates around the wire axis resulting in isotropic properties on macroscopic length scales. Bi-2223 tape has even better alignment and shows only uniaxial alignment, where the c-axis is aligned with the normal to the tape surface and grain orientations

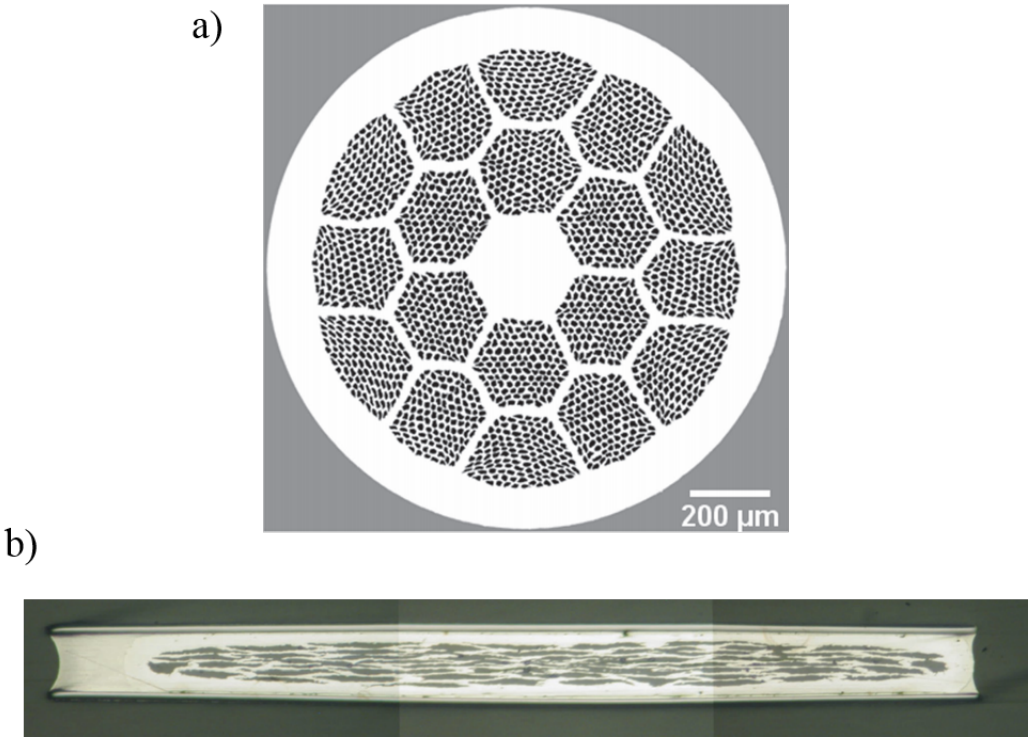

Figure 3.6. Cross sections of a) Bi-2212 wire (reproduced from [99]) and b) Bi-2223 tape (reproduced from [100]), showing the multifilamentary nature and differing geometries of the conductors.

in the *ab*-plane are random (i.e. the [100] tilt and twist grain boundaries are aligned to $< 15°$ and the [001] tilt grain boundaries are not aligned). The higher grain alignment in Bi-2212 wire explains why the wires currently have higher J_c values than the Bi-2223 tape.

Just as in LTS conductors the multifilamentary nature of BiSCCO conductors help reduce the a.c. losses caused when the field is cycled. In this regard, BiSCCO conductors have an advantage over REBCO tapes however the higher J_c values, larger usable temperature and field range, and comparable cost of REBCO means at present it has superseded BiSCCO in the majority of HTS applications.

3.3.2 REBCO tapes

Unlike BiSCCO, established manufacturing techniques in applied superconductivity were unable to achieve the grain alignment in REBCO required to achieve high J_c. Useful REBCO conductors came approximately a decade later than BiSCCO with the development of bespoke conductor manufacture processes. This subsection will look at the architecture, manufacture and properties of REBCO tapes.

REBCO tapes are composed of a thin layer of REBCO $\sim 1\,\mu m$ thick deposited on a textured substrate, this layer is topped with a thin layer of silver which alloys oxygen diffusion and does not react with the REBCO, and finally the tape is coated on all sides with copper to facilitate current transfer into the superconducting layer. A cut away schematic of a typical SuperPower REBCO tape, measured in this thesis, is shown in figure 3.7. The superconducting layer is biaxially textured with the *c*-axis of

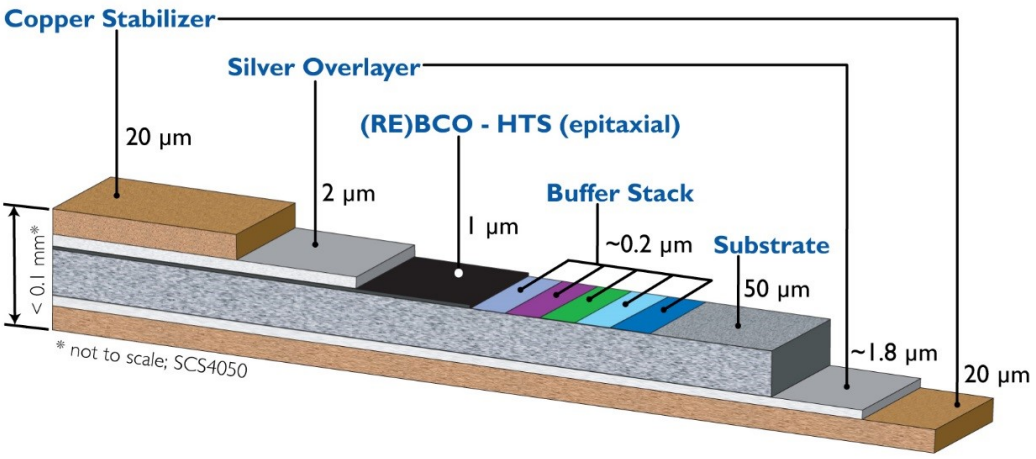

Figure 3.7. Schematic of a REBCO tape showing approximate thicknesses of the layers. Reproduced from [102].

the REBCO aligned in the direction normal to the surface of the tape and the a or b-axis is aligned with the direction along the length of the tape.

Tape manufacture processes

The substrate and buffer layers are responsible for imparting the grain alignment in the superconducting layer. There are three methods of producing the textured substrate:

- Ion Beam Assisted Deposition (IBAD)
- Inclined Substrate Deposition (ISD)
- Rolling-Assisted Biaxially Textured Substrate (RABiTS)

All three techniques begin with a metal substrate, most commonly the nickel alloy Hastelloy® C-276 [103]. In the IBAD technique the nickel alloy remains untextured. During buffer layer growth an ion beam is incident on the growth area, this preferentially removes growth which does not have a specific crystallographic orientation resulting in

a biaxially textured layer [104]. This is the manufacturing route used by SuperPower tapes [102], Fujikura [105], SuNam [106], SuperOx [107] and Bruker [108] (Bruker use a modified version of the IBAD process called 'alternating beam assisted deposition' ABAD on a stainless steel substrate).

The nickel alloy also remains untextured in the ISD technique but there is no additional ion beam. Instead the substrate is inclined so the buffer layers are deposited at an angle away from the surface normal [109]. This results in the growth of biaxially textured grains where the *ab*-plane is rotated by 45° so the [110] crystallographic direction is aligned with the direction of the tape and the *c*-axis is not perpendicular to the tape surface. The *c*-axis direction is inclined at some intermediate angle (typically $\sim 30°$) away from the surface normal to the tape. The ISD technique also results in a rough surface texture for the deposited layers. This is the fabrication route used by Theva [110].

In the RABiTS technique, texture is imparted directly into the nickel alloy via a rolling and recrystallisation process which gives a preferential grain alignment [111]. Numerous oxide 'buffer layers' are then deposited, these layers better match the unit cell size of the substrate to that of REBCO, further reduce the misorientation angles between adjacent grains and prevent the REBCO from reacting with the substrate. This is the fabrication route used by American Superconductor [112].

The important distinction between the 3 fabrication routes is that in the IBAD and ISD techniques the nickel alloy remains untextured and the texture is imparted

almost entirely by the buffer layers, in the RABiTS technique the texture is imparted on the superconducting layer both by the nickel alloy and the buffer layers.

The superconducting REBCO layer grows on the buffer layers with the same underlying texture. Methods of depositing the superconducting layer include:

- Pulsed Laser Deposition (PLD) [113, 114]
- Chemical Solution Deposition (CSD) [115–118]
- Metal Organic Chemical Vapor Deposition (MOCVD) [119, 120]
- Co-evaporation [121]

The deposition method has a strong influence on the grain size, the types and distribution of naturally occurring pinning sites and the speed of deposition. A comprehensive review of the different manufacturing techniques and how they affect the properties of the conductor can found in [93]. Finally, the silver and copper layers are added by either sputtering or electroplating.

Improving the critical current

The primary aim of research and development in conductor manufacture is to increase J_{E}. Currently the superconducting layer in a typical REBCO tape is $\sim 1\,\mu\mathrm{m}$ thick whereas the whole tape is $\sim 100\,\mu\mathrm{m}$ thick, so the superconducting layer accounts for only $\sim 1\,\%$ of the cross-sectional area. The easiest way to increase J_{E} is simply to increase the superconducting fraction by increasing the thickness of the superconducting layer. However, above a certain critical thickness tapes tend to lose their alignment

and change their growth orientation from c-axis aligned to a-axis aligned leading to a dramatic drop in J_c [122–124]. Some success has been made improving the thickness of the c-axis orientated growth [122, 125–127] but a-axis orientated growth is still a limiting factor for film thickness.

Improving the in-field J_c of a conductor is achieved through increasing the flux pinning force density F_p by increasing the number and/or strength of the pinning sites. For example, in Nb–Ti the density of α precipitates is increased and in Nb_3Sn the grain size is reduced to increase the density of grain boundary triple points. Improving J_c in this manner is always a balancing act between increasing F_p and the suppression of T_c and B_{c2} through the reduction of long range order.

In REBCO tapes F_p is improved through the addition of Artificial Pinning Sites (APCs), which are non-superconducting elements of a similar size to a vortex core embedded in the REBCO matrix. The two types of APC which are commonly included are nanorods and nanoparticles. Nanorods are elongated inclusions aligned parallel to the c-axis with a composition of either $BaZrO_3$, $BaHfO_3$ or $BaSnO_3$ (BZO, BHO and BSO respectively). Nanorods can be produced with the PLD [128–131] or MOCVD [132–134] deposition methods by altering the composition/ratios of the deposition materials. The nanorods self-assemble simultaneously with the REBCO making them ideal for large scale production. Nanoparticles are randomly distributed, approximately spherical, inclusions embedded in the REBCO matrix and can have many different compositions such as BZO, Y_2O_3, $BaCeO_3$ and Ba_2YTaO_4 [135] among others. They can be produced in the PLD [136] and CSD [135] deposition methods by altering

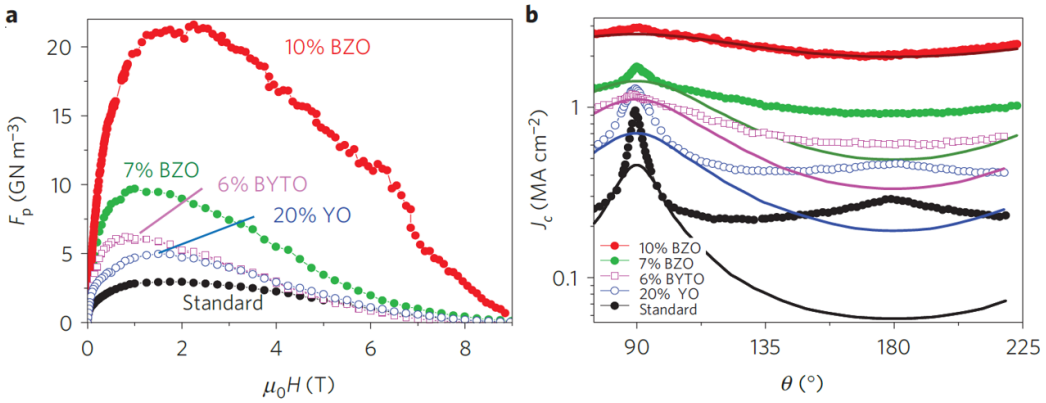

Figure 3.8. A comparison of a) F_p as a function of field and b) J_c as a function of angle θ (where $\theta = 90°$ is parallel to the *ab*-plane) at 77 K for REBCO thin films containing different APC nanoparticle inclusions with the field applied perpendicular to the tape surface. BZO, BYTO and YO are $BaZrO_3$, Ba_2YTaO_6 and Y_2O_3 respectively and the percentages relate to the molar quantity of inclusions. The solid lines indicate the theoretical contribution from point pins. Figure reproduced from [135].

the composition/ratios of the deposition materials and, as with the nanorods, they self-assemble alongside the REBCO during the deposition process. APCs can greatly increase J_c for $B \parallel c$ but tend to have less effect on J_c for $B \perp c$. Figure 3.8a show the increases in F_p for several samples with different APC inclusions and figure 3.8b shows the anisotropic J_c for some APC samples compared to a non-APC sample. Further discussion of the effect of APCs on anisotropy is covered in later in this section.

It is common for conductor manufacturers to quote J_c at 77 K under self-field conditions as a measure of tape quality. While this is reasonable for applications which replicate the test conditions, such as power transmission and fault current limiters, it is a poor measure for low temperature, high field applications such as MRI, particle accelerators and fusion magnets. It has been shown that the 77 K self-field properties of REBCO tapes show little or no correlation to their low temperature, high field properties so careful consideration must be given when comparing conductors from

different manufacturers for high field applications [137, 138]. However, their properties at 77 K under a low applied magnetic field correlate well with their low temperature, high-field properties and gives a much better measure of tape performance for these applications. This reflects that the APCs have little or no effect on the self-field properties of the samples.

Commercial REBCO conductors

Conductor manufacturers use different combinations of techniques, different buffer layer compositions and different APC inclusions. The continued development of the manufacturing process to improve J_c and manufacture speed/efficiency is an active area of research. At the time of writing no single manufacturing process is a clear 'front-runner' and the highly competitive nature of the industry mean the specifics of the manufacturing process used by each company are closely guarded commercial secrets.

Anisotropy of J_c in REBCO tape

The anisotropy of J_c in cuprates is complex and depends not only on the anisotropy of B_{c2} but also on the type, size and orientation of the pinning sites present in the material. The size of the vortex cores relative to the size of the pinning sites is one of the most important features in determining the angular dependence of J_c. The size of the vortex core is determined by the coherence lengths orthogonal to it. In anisotropic

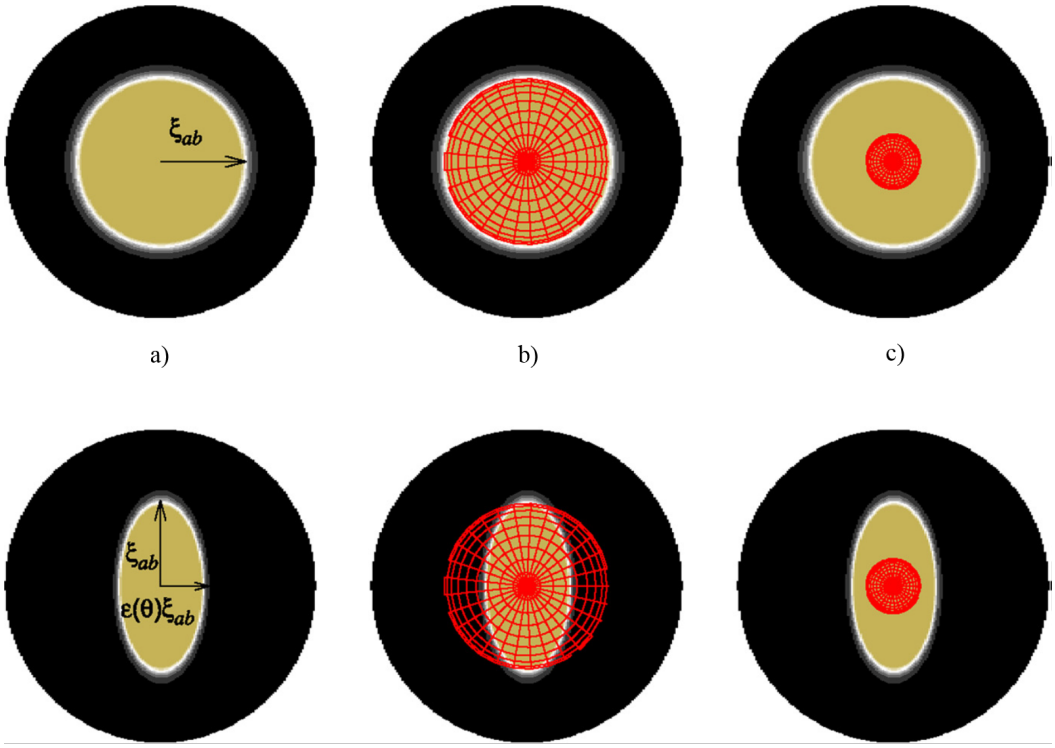

Figure 3.9. This figure illustrates how the interaction volume of a pinning site as a function of angle depends on the size of the vortex core relative to the size of the pinning site for point defects and precipitates/particles. The yellow area is the vortex core and the red mesh is the pinning site. a) and d) show how the size and shape of the vortex core change with angle. b) and e) show how for large pinning sites such as nanoparticles and precipitates the interaction volume changes as a function of angle. c) and f) show how for small point defects the interaction volume is independent of angle. Reproduced from [139].

GL theory, the angular dependence of ξ is given by

$$\xi(\theta) = \xi_{ab}\left(\cos^2\theta + \gamma^{-2}\sin^2\theta\right)^{\frac{1}{2}}, \tag{3.2}$$

where θ is the angle between the c-axis and the magnetic field [139]. Hence the size and shape of the vortex core is also a function of angle as shown in figure 3.9.

Pinning sites which are smaller than the vortex core size in all directions such as vacancies, interstitials and small precipitates are considered as random point defects. These defects are present in all REBCO thin films and tapes resulting from the manufacturing processes. Because the size of the pinning site is smaller than the vortex core in all directions the interaction volume between them does not change as a function of angle, as shown in figure 3.9. The flux pinning force of a single random point defect f_{p} in the low field limit can be approximated as follows [139–142]. A flux line has an energy per unit volume of E_{fl}, the reduction of the energy of a flux line passing through a pinning site E_{p} with an interaction volume V is therefore $E_{\mathrm{p}} \propto E_{\mathrm{fl}}V$. Since the defect is smaller than the vortex core in all directions V is independent of angle. The force required to remove the flux line from the pinning site is simply E_{p} divided by the distance required to remove it, which in this case is $\xi(\theta)$, hence $f_{\mathrm{p}} \propto E_{\mathrm{fl}}V/\xi(\theta)$. The resulting anisotropic f_{p} (and hence J_{c}) gives a peak when B is aligned parallel to the ab-planes and $J_{\mathrm{c}}^{ab}/J_{\mathrm{c}}^{c} = \gamma$, this is only true so long as the field dependencies of J_{c}^{ab} and J_{c}^{c} are the same which is not always the case in real systems. The anisotropic behaviour of point pins is shown in figure 3.10.

Stacking faults in the ab-plane are common in REBCO thin films and tapes depending on the manufacturing process [142]. The dislocation loop around the edge of a stacking fault acts as a linear pin with a cross section smaller than a vortex core for all angles [142, 143]. When the field is far from being parallel with the ab-plane they act in the same manner as random point defects. However, as the field approaches the ab-plane the flux lines will deform and align along the linear pins increasing their

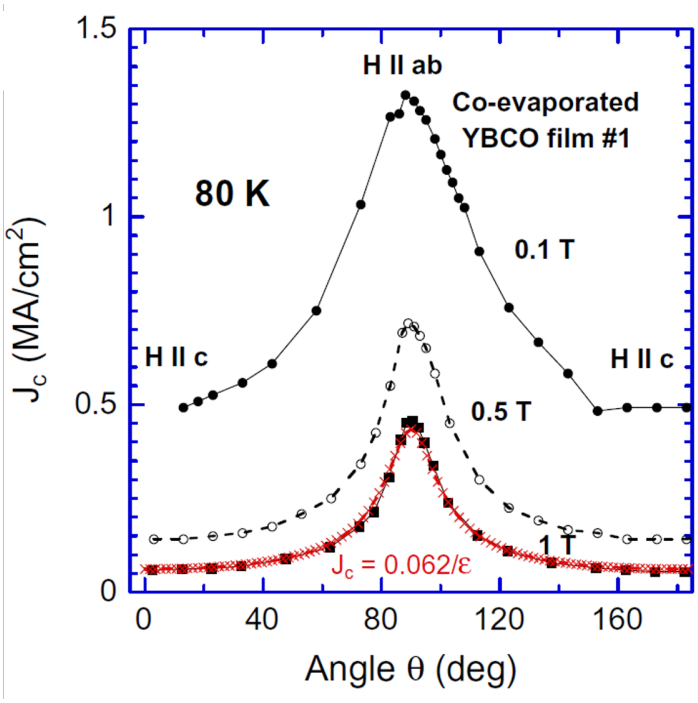

Figure 3.10. Anisotropic behaviour of a REBCO thin film showing the effect of point pins. The red crosses are the theoretical angular dependence for point pins at 1 T. Reproduced from [142].

interaction volume and their pinning force. The resultant behaviour is a larger, sharper peak in J_c about the *ab*-plane. Figure 3.11 shows the additional effect of the fluxons locking-in to *ab* pinning caused by the stacking faults – in the literature this can be called *ab*-correlated pinning.

ab pinning is also caused by the layered crystal structure of REBCO [144, 145]. The superconductivity is localised to the CuO_2 planes hence the superconducting order parameter varies periodically in the *c*-axis direction. This periodic variation acts to pin the flux lines when they are aligned with the *ab*-plane. The resulting behaviour is a very sharp peak in the angular dependence of J_c when the field is very close to being aligned with the *ab*-plane, superimposed on the usual angular dependence caused by

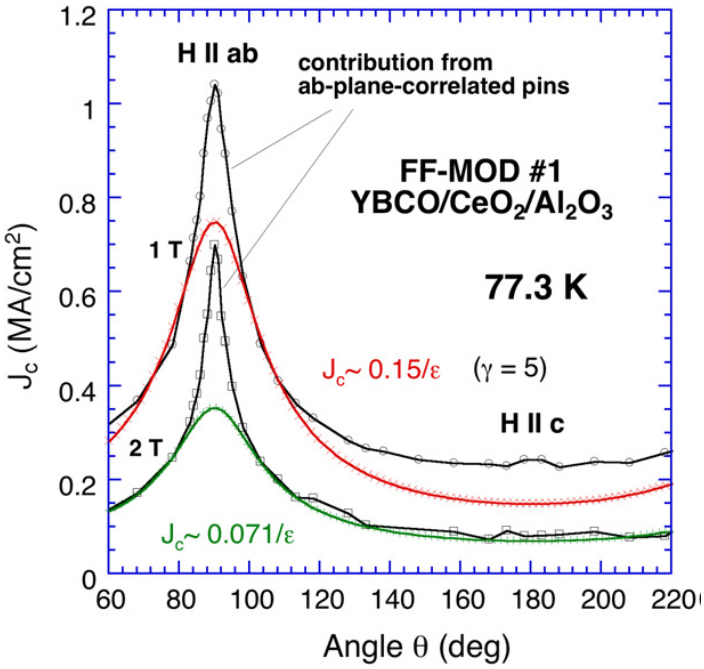

Figure 3.11. Anisotropic behaviour of a REBCO thin film with a high density of stacking faults. The red and green solid lines show the theoretical angular dependence for point pins. The peaks near the *ab*-plane are higher than that predicted by point pins displaying the effect of the pinning caused by the stacking faults. Reproduced from [143].

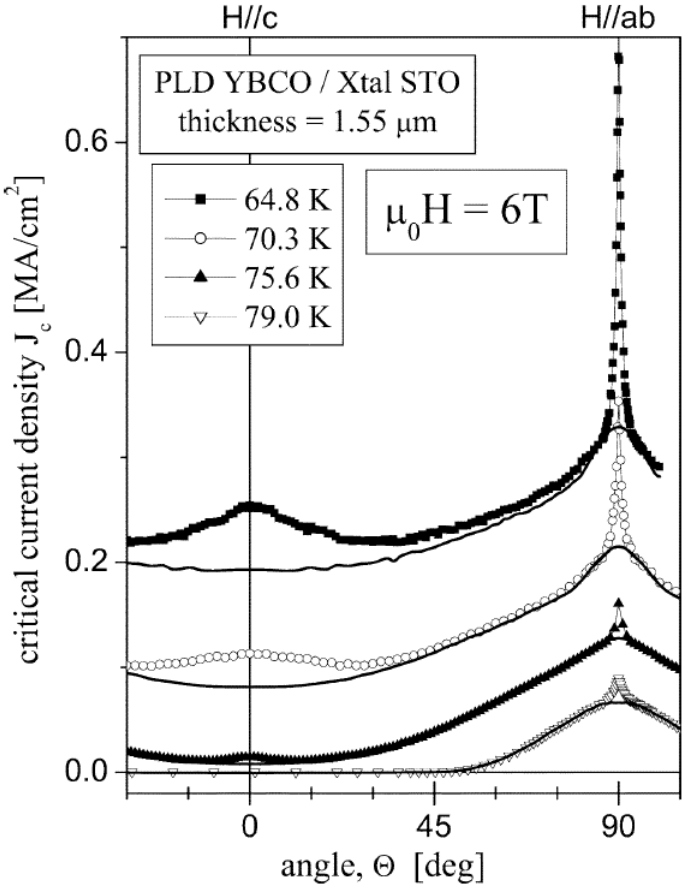

Figure 3.12. Anisotropic behaviour of a REBCO thin film with very low misorientation angles and low defect density. The solid lines show the contribution from point pins. The very sharp peak around the *ab*-plane is a result of correlated *ab*-pinning caused by the layered structure of REBCO. Reproduced from [140].

random point defects [140, 146] (cf. figure 3.12). This type of pinning is common to all REBCO thin films and tapes and can be considered as intrinsic. However, its strength relative to other types of pinning is small and the effect can be 'smeared out' by even small misorientation angles between grains. This means it is only observed in samples with very low defect densities and misorientation angles. The strength of this intrinsic pinning is much stronger at lower temperatures where the coherence length is smaller which results in a greater variation of the order parameter in the *c*-axis direction [146].

Although they can be engineered to a certain extent the afore mentioned types of pinning are generally all thought of as 'intrinsic' to REBCO and all result in a peak in F_p when the magnetic field is applied parallel to the *ab*-plane. Additional APCs in tapes are thought of as extrinsic pinning sites and show dramatically different anisotropic behaviour to intrinsic pinning sites. Nanoparticle APCs are approximately spherical and generally larger than the coherence length in all three dimensions. Since they are larger than the size of the vortex core, the interaction volume changes as a function of angle $V \propto \xi_{ab}\xi(\theta)$ as shown in figure 3.9. So, unlike small point pins, the reduction in energy of a flux line passing through a nanoparticle is a function of angle $E_\mathrm{p} \propto E_\mathrm{fl}\xi_{ab}\xi(\theta)$ [139, 141]. There is disagreement as to which length scale should be used for the distance required to remove the vortex core from its pinning site with experimental data to support both cases. Some suggest the vortex core minor axis $\xi(\theta)$ is the appropriate length scale [139] which gives $f_\mathrm{p} \propto E_\mathrm{fl}\xi_{ab}\xi(\theta)/\xi(\theta) = E_\mathrm{fl}\xi_{ab} = \text{const.}$ resulting in no angular dependence to f_p. Whereas others suggest the radius of the nanoparticle r_np is appropriate [141] which gives $f_\mathrm{p} \propto E_\mathrm{fl}\xi_{ab}\xi(\theta)/r_\mathrm{np}$ resulting in a broad peak in f_p around the *c*-axis (cf. figure 3.13). These disagreements suggest that this simplified model may not be adequate to fully describe the underlying physics of nanoparticle anisotropy however it is clear their angular dependence is very different to that of intrinsic pinning sites.

At angles away from the *c*-axis nanorods can be considered to act in a similar manner to nanoparticles. For angles approaching the *c*-axis the flux lines can align with the nanorods to produce strong pinning when the field is in the *c*-direction. This

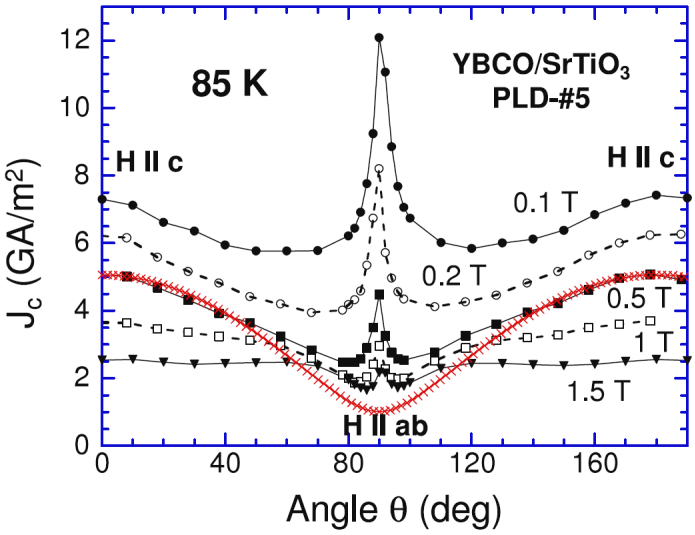

Figure 3.13. Anisotropic behaviour of a REBCO thin film with a high density of nanoparticles. The red crosses are the theoretical angular dependence for nanoparticles at 0.5 T. The peak in the *c*-axis direction is caused by the nanoparticles. Reproduced from [141].

behaviour is demonstrated nicely in [147] where linear defects (similar to nanorods) were introduced into a tape sample at various angles using heavy ion irradiation. Peaks in J_c were found at the irradiation angles (cf. figure 3.14).

Hence the anisotropic nature of a REBCO is a complex superposition of various anisotropic effects. This makes understanding the anisotropic behaviour of REBCO tapes an incredibly difficult task, made even more so by the different types of pinning site present in different conductors because of differences in the manufacturing technique and APC inclusions. No single theoretical description is currently able to completely describe the anisotropic behaviour as a function of field and temperature due to changing vortex size, the presence of numerous pinning sites, the lack of consideration of the elasticity of the FLL and the fact the anisotropic GL approximation is only valid in certain regimes.

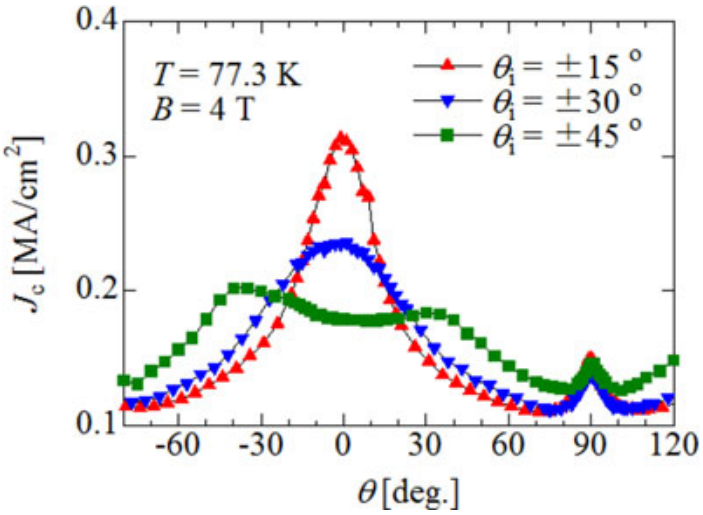

Figure 3.14. Anisotropic behaviour of REBCO tapes which have underwent heavy ion irradiation at various angles. θ is the angle between the magnetic field and the c-axis. The pinning caused by the ion irradiation is clear in the sample irradiated at an angle of 45°, showing peaks at 45° and −45°. Reproduced from [147].

3.4 Strain dependence of the critical current of LTS and HTS wires and tapes

In operation, high field superconducting magnets are under tremendous stress due to the differential thermal contraction of the components when cooling to cryogenic temperatures and the Lorentz forces generated when the magnet is energised. Hence, the effects of strain on the superconducting properties of the conductors are an important factor that cannot be ignored.

The immediately obvious effect of strain is cracking of the superconductor preventing current flow and rendering the conductor permanently degraded or even entirely unable to support a supercurrent. The effect is irreversible and is much more important in brittle A15 and HTS conductors than in alloys like Nb–Ti which are less likely

to undergo brittle fracture due to their ductility. The experimental signature of irreversible damage is that J_c does not return to its original value after an applied strain is relaxed [148–156]. The applied strain at which irreversible damage begins in known as ε_{irr}.

Damage to brittle samples is caused by crack propagation and in general is worse in tension because tensile cracks form close to perpendicular with the load axis whereas compressive cracks form close to parallel with the load axis [157–159] so are less disruptive to current flow. Also, a smaller strain is required to propagate cracks under tension.

In most high-performance Nb_3Sn conductors $\varepsilon_{irr} \sim 0.7\,\%$ [156, 160]. In REBCO conductors the Hastelloy substrate is also brittle and it is found irreversible damage is caused by cracks nucleated in the Hastelloy layer which propagate to the superconducting layer [161–163]. ε_{irr} is found to vary depending on the material of the stabilising layer [155] this is attributed to the different differential thermal contractions of the stabilising materials causing different strain states in the substrate and superconducting layers. For Cu stabilised tapes $\varepsilon_{irr} \sim 0.5\,\%$ [149, 150, 154]. In Bi-2212 wires $\varepsilon_{irr} \sim 0.2\,\%$ in tension and $\sim -0.3\,\%$ in compression [164]. In Bi-2223 tapes $\varepsilon_{irr} \sim 0.5\,\%$ in tension [151, 154] however they show irreversible damage under even the smallest compressions [165, 166]. This is attributed to the high porosity of Bi-2223 tapes and the low elastic moduli which result in buckling of the brittle filaments.

Before irreversible damage sets in, the critical properties of LTS and HTS conductors are reversible functions of strain (i.e. their properties return to their original values

when the strain is relaxed). The following two subsections will review the reversible effect of strain of LTS and HTS conductors respectively.

3.4.1 Reversible strain effects in LTS conductors

The effect of strain on Nb–Ti conductors is minimal compared to other high field conductors with changes in J_c of only a few percent even out to tensile strains of $\sim 3\,\%$ (far greater than the irreversible limit for brittle conductors) [167].

A15 conductors show an inverted parabolic strain dependence near the strain at which J_c is maximised ε_{peak} (cf. figure 3.15) [51, 168, 168–179]. In measurements on A15 wires the different components such as the Cu matrix, the superconducting filaments and sample holder, contract by different amounts on cooling to cryogenic temperatures [74, 180, 181]. This differential thermal contraction results in the intrinsic strain ε_{int} on the superconducting filaments differing from ε_{app}. Theoretical calculations of the thermal contraction [181, 182] and X-ray diffraction measurements [183] both show ε_{peak} occurs at approximately zero intrinsic strain. This leads to the common definition of intrinsic strain $\varepsilon_{int} = \varepsilon_{app} - \varepsilon_{peak}$. Further discussion of why ε_{peak} is so close to $\varepsilon_{int} = 0\,\%$ is contained in chapter 4.

The properties of the matrix materials must also be considered under cyclic loading and unloading of samples. The Nb_3Sn is brittle and therefore remains elastic over the whole strain region until it fractures. Some of the matrix materials, such as Cu, are however ductile, and will yield and undergo plastic deformation at strains lower than ε_{irr} [182]. The means that when returning to an applied strain of zero the intrinsic

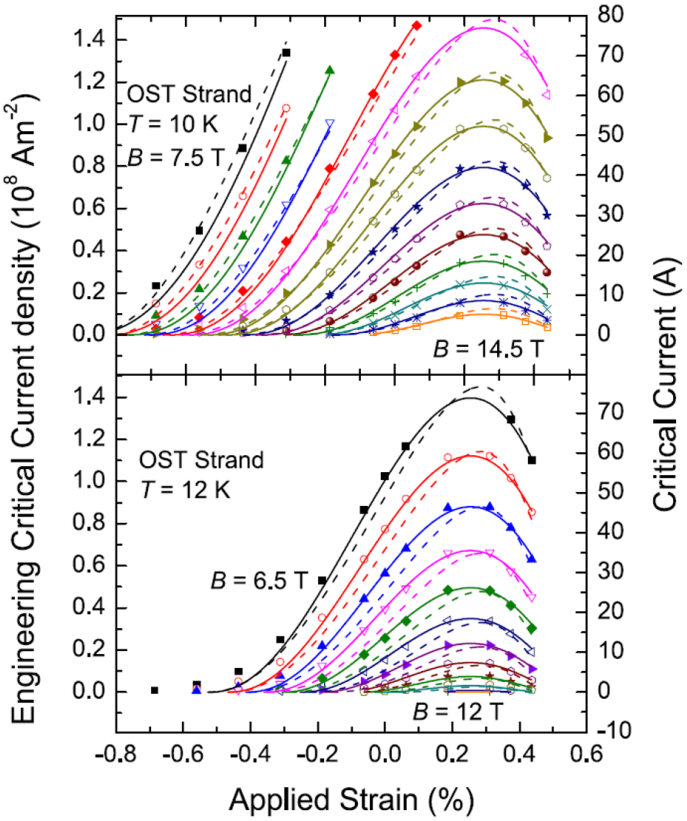

Figure 3.15. The strain dependence of the critical current density of an internal tin Nb_3Sn wire as a function of field at $T = 10\,\mathrm{K}$ (top) and $T = 12\,\mathrm{K}$ (bottom). The solid and dashed lines are parameterisations of the data as detailed in [179]. J_c shows an inverted parabolic relation with strain near ε_{peak}. Reproduced from [179].

strain on the superconductor will be slightly different [182, 184, 185]. Therefore, a repeat J_c measurement will give a slightly different result. When performing strain dependent measurements on composite wires and tapes, it is important to note that such a difference may not be indicative of irreversible fracture behaviour, typically the difference in J_c at zero applied strain caused by plastic deformation is $\sim 1\,\%$. Further repeat cycles to a maximum strain equal or less than the maximum strain in the first cycle will result in no further changes to J_c [185].

3.4.2 Reversible strain effects in HTS conductors

There are far fewer comprehensive studies on REBCO tapes under strain, largely due to the relative immaturity of techniques for measuring highly anisotropic HTS samples. There are many limited studies of the strain dependence of REBCO tapes under tensile strain as a function of temperature and field [148, 149, 152, 153, 155, 161, 162, 186–197]. However, it is difficult to interpret the data without also knowing how J_c behaves in compression. Studies in self-field that do show results in both tension and compression generally show an inverted parabolic dependence of the critical current with strain [198–205]. Fewer in-field data are reported. Some reports find, that the inverted parabolic behaviour persists at all fields [206, 207] (cf. Figure 3.16a). Whereas other studies report so-called 'double peak' behaviour in low fields, returning to inverted parabolic behaviour at higher fields [208, 209] (cf. Figure 3.16b). These differences in samples are likely caused by variations in the pinning properties.

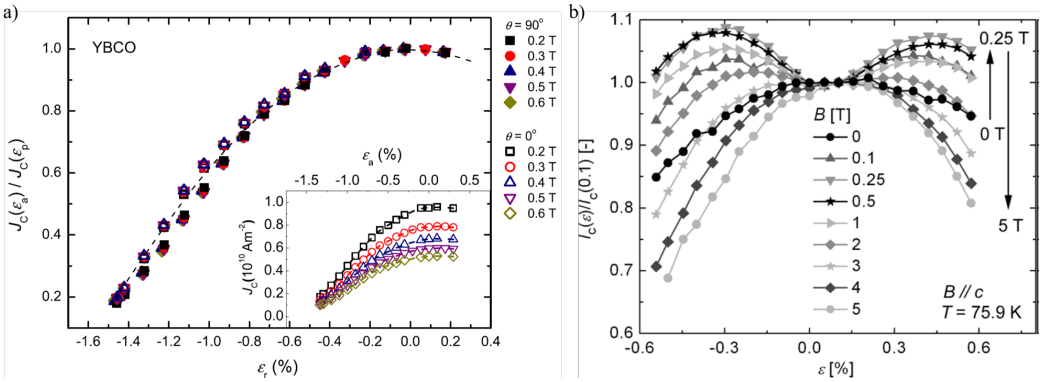

Figure 3.16. The normalised critical current as a function of applied strain from different studies on REBCO tapes at $T \approx 77\,\mathrm{K}$ showing a) inverted parabolic behaviour at all fields and b) double peak behaviour at low fields and inverted parabolic behaviour at higher fields. Reproduced from [207] and [209] respectively.

3.5 The bimodal chain model for REBCO in zero field

Single crystal measurements on REBCO show the strain dependence of the critical parameters T_c and B_{c2} are strongly anisotropic in the ab-plane [210, 211]. Figure 3.17 shows the anisotropy of the pressure (or equivalently strain) dependence of T_c. Tensile strain applied in the a-axis direction results in a linear increase in T_c, in the b-axis direction a linear decrease in T_c of the same order and close to zero change in T_c along the c-axis direction. These experiments show there is no inverted parabolic dependence of $T_c(\varepsilon)$ in single crystal REBCO. Since T_c is intrinsicly linked to the other superconducting parameters 2 and J_c we can see the inverted parabolic strain response of the tape cannot be directly related to the strain response of the underlying single crystal in zero field.

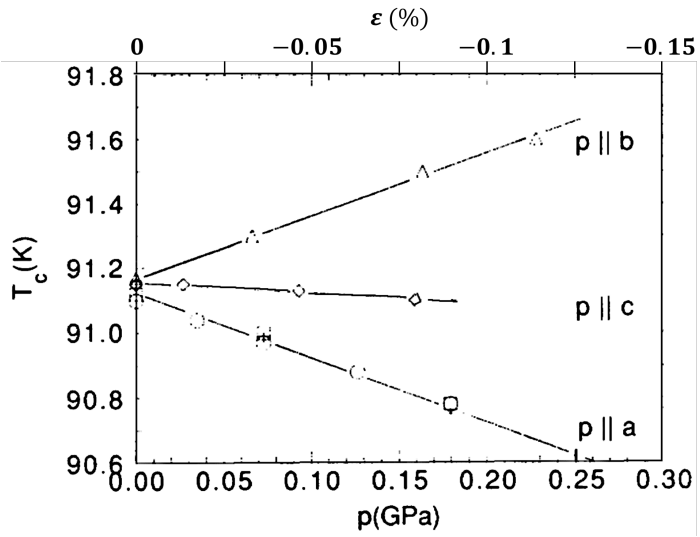

Figure 3.17. Anisotropy of the pressure dependence of T_c along the three crystal axis. Reproduced from [211].

In this section a bimodal chain model is outlined for the strain dependence of REBCO tapes in zero field which reconciles the apparent disagreement between the strain dependencies of single crystals and tapes [199]. It is a one-dimensional model in which strain is applied along the axis of the tape. In chapter 4 this model is extended to consider the role of magnetic field and temperature and discussed at length in the context of the data. In the tapes measured in this thesis, twinning in the REBCO layer results in some [100] domains aligned with the direction of applied strain (domain A) and other domains with [010] aligned with the direction of applied strain (domain B). In practice when applying strain, in some domains the critical parameters increase, whereas in other domains they decrease (i.e. a bimodal material).

Since there is no $\varepsilon_{\text{peak}}$ in the underlying single crystal, one cannot sensibly anchor data for a bimodal material at $\varepsilon_{\text{peak}}$. To avoid any confusion with the well-established definition of intrinsic strain, two new characteristic strains are defined. The first

characteristic strain is defined as the domain strain

$$\varepsilon_{\mathrm{JD}} = \varepsilon_{\mathrm{app}} - \varepsilon_{J_{\mathrm{cA}}=J_{\mathrm{cB}}} \tag{3.3}$$

where $\varepsilon_{\mathrm{JD}}$ is the domain strain and $\varepsilon_{J_{\mathrm{cA}}=J_{\mathrm{cB}}}$ is the applied strain at which the critical current density in both domains (A and B) are equal or equivalently, $\varepsilon_{\mathrm{JD}}$ is zero when the critical current density in both domains are equal. The magnitude of $\varepsilon_{J_{\mathrm{cA}}=J_{\mathrm{cB}}}$ is broadly determined by the differential thermal contraction produced by the sample holder and the matrix materials and hence to first order is constant for any particular experimental set-up because the strain at which $J_{\mathrm{cA}} = J_{\mathrm{cB}}$ will remain constant because the field and temperature dependence of J_{c} in both domains is the same. The second characteristic strain characterises the difference between $\varepsilon_{J_{\mathrm{cA}}=J_{\mathrm{cB}}}$ and the applied strain at which J_{c} reaches its maximum $\varepsilon_{\mathrm{peak}}$. By definition

$$\varepsilon_{\mathrm{p,JD}} = \varepsilon_{\mathrm{peak}} - \varepsilon_{J_{\mathrm{cA}}=J_{\mathrm{cB}}} \tag{3.4}$$

where $\varepsilon_{\mathrm{p,JD}}$ is the peak domain strain which (along with $\varepsilon_{\mathrm{peak}}$) can be field and temperature dependent and $\varepsilon_{J_{\mathrm{cA}}=J_{\mathrm{cB}}}$ is constant. Eqn 3.4 does not include the applied strain because it characterises the underlying behaviour of the superconducting material.

The two twinned domains A and B are present with domain fractions f and $(1-f)$ respectively. They are connected in series with one another. The central idea of the bimodal model, following the single crystal data, is that the effective critical

temperatures of each domain have opposing strain dependencies

$$T_{ci}^{*} = \begin{cases} T_{\mathrm{c}}^{*}(0) + \left|\frac{\mathrm{d}T_{\mathrm{cA}}^{*}}{\mathrm{d}\varepsilon_{\mathrm{JD}}}\right|_{\varepsilon_{\mathrm{JD}}=0\%} \varepsilon_{\mathrm{JD}}, & i = \mathrm{A}, \\ T_{\mathrm{c}}^{*}(0) - \left|\frac{\mathrm{d}T_{\mathrm{cB}}^{*}}{\mathrm{d}\varepsilon_{\mathrm{JD}}}\right|_{\varepsilon_{\mathrm{JD}}=0\%} \varepsilon_{\mathrm{JD}}, & i = \mathrm{B}, \end{cases} \tag{3.5}$$

where $T_{\mathrm{c}}^{*}(0)$ is the effective critical temperature at $\varepsilon_{\mathrm{JD}} = 0\,\%$. The parameter g_i, is introduced such that at strains close to $\varepsilon_{\mathrm{JD}} = 0\,\%$, the strain dependence of J_{ci} in each domain is linear and opposite,

$$J_{ci}(\varepsilon_{\mathrm{JD}}) = \begin{cases} J_{\mathrm{c}}(0)(1 + g_{\mathrm{A}}\varepsilon_{\mathrm{JD}}), & i = \mathrm{A}, \\ J_{\mathrm{c}}(0)(1 - g_{\mathrm{B}}\varepsilon_{\mathrm{JD}}), & i = \mathrm{B}, \end{cases} \tag{3.6}$$

where $g_i = (1/J_{\mathrm{c}}(0))\left|\partial J_{ci}/\partial\varepsilon_{\mathrm{JD}}\right|_{\varepsilon_{\mathrm{JD}}=0\%}$, J_{ci} is the critical current in domain i and $J_{\mathrm{c}}(0)$ is the critical current at $\varepsilon_{\mathrm{JD}} = 0\,\%$. Following the single crystal data, it was assumed $g_{\mathrm{A}} = g_{\mathrm{B}} = g$ and each domain is assumed to follow the same power law given by eqn. 2.34. The E-field generated by the chain is given by

$$E = E_{\mathrm{c}} f \left(\frac{J}{J_{\mathrm{cA}}}\right)^{N_{\mathrm{A}}} + E_{\mathrm{c}}(1 - f)\left(\frac{J}{J_{\mathrm{cB}}}\right)^{N_{\mathrm{B}}}, \tag{3.7}$$

where E_{c} is the E-field criterion. It was also assumed $N_{\mathrm{A}} = N_{\mathrm{B}} = N$. The critical current of the whole chain J_{cT} determined when $E = E_{\mathrm{c}}$ and $J = J_{\mathrm{cT}}$ is given by

$$J_{\mathrm{cT}} = J_{\mathrm{c}}(0)\left[f(1 + g\varepsilon_{\mathrm{JD}})^{-N} + (1 - f)(1 - g\varepsilon_{\mathrm{JD}})^{-N}\right]^{-\frac{1}{N}}. \tag{3.8}$$

By taking a second order Taylor series approximation about $\varepsilon_{\mathrm{JD}} = 0\,\%$ the following expression for $\varepsilon_{\mathrm{p,JD}}$ was found

$$\varepsilon_{\mathrm{p,JD}} = \frac{2f-1}{4f\,(1-f)}\frac{1}{g\,(N+1)}. \tag{3.9}$$

Hence when $f = 0.5$, $\varepsilon_{\mathrm{p,JD}} = 0\,\%$, which is field and temperature independent, when $f < 0.5$, $\varepsilon_{\mathrm{p,JD}} < 0\,\%$, and when $f > 0.5$, $\varepsilon_{\mathrm{p,JD}} > 0\,\%$. This model reconciles the disagreement between the linear strain dependence of single crystals with the strain dependence of tapes and shows the inverted parabolic nature of the strain dependence is emergent behaviour (i.e. unlike the behaviour of either domain) caused by competition between two domains with opposite strain dependencies.

3.6 Fusion reactor design

Inside a fusion reactor is one of the harshest environments on the planet. With the push toward ever more powerful reactors in the quest for fusion energy, the environment only gets more extreme. Heat loads $> 1\,\mathrm{MW\,m^{-2}}$ on the first wall and $> 10\,\mathrm{MW\,m^{-2}}$ in the divertor region (comparable to a rocket engine), highly energetic plasma incident on the in-vessel components, microstructural damage and transmutations caused by unmoderated, highly energetic, highly penetrating neutrons, and retention of highly regulated tritium fuel in the divertor are just a few examples of the extremes of the fusion reactor environment.

Many of the remaining challenges facing fusion energy relate not to the plasma science but to the materials science and engineering required to make a device capable of operating in this harsh environment for years (even decades) of continuous use. The following subsections will discuss a few select topics for fusion reactor technologies.

3.6.1 Tritium breeding

While one half of the fuel required for a fusion reactor, deuterium, can be found easily with an abundance of 156 ppm of the hydrogen in sea water, the other half, tritium, is considerably more difficult to come by. It has a half-life of only 12 years and so is not found naturally in any abundance. Currently the only civilian source of tritium is a by-product of heavy water fission reactors and supply is not high enough to support even a single fusion power plant. The solution is to breed tritium in the walls of the reactor through nuclear reactions of neutrons produced by the fusion reaction with lithium. This idea is known as a 'breeder blanket'. The stable isotopes of lithium undergo the following reactions with a neutron

$$^{6}_{3}\mathrm{Li} + ^{1}_{0}\mathrm{n} \rightarrow ^{3}_{1}\mathrm{T} + ^{4}_{2}\mathrm{He},$$

$$^{7}_{3}\mathrm{Li} + ^{1}_{0}\mathrm{n} \rightarrow ^{3}_{1}\mathrm{T} + ^{4}_{2}\mathrm{He} + ^{1}_{0}\mathrm{n}'.$$

The neutron released from the second reaction means there is the potential for a single fusion neutron to produce numerous tritium nuclei. However, the cross section of this reaction is much lower than that of the first reaction so the best strategy to improve

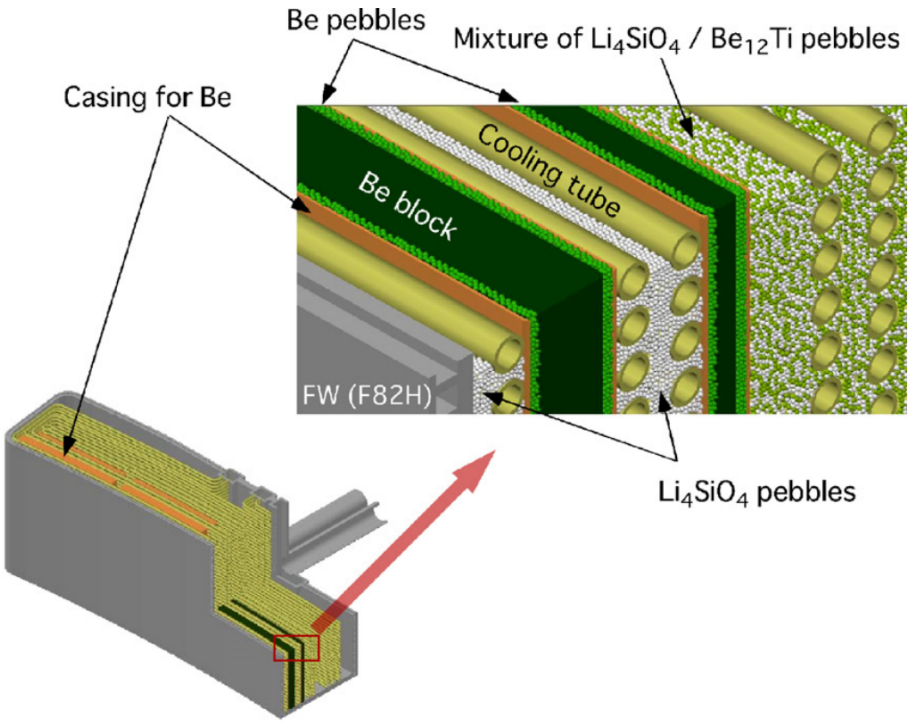

Figure 3.18. Schematic of a conceptual Li/Be pebble bed tritium breeding blanket design. Reproduced from [213].

the tritium yield is to enrich the lithium with ${}^{6}_{3}\mathrm{Li}$ and introduce neutron multipliers in close proximity to the lithium [212, 213]. Beryllium and lead are the most popular contenders for a neutron multiplier in breeder blanket designs. They undergo the following nuclear reactions

$$ {}^{9}_{4}\mathrm{Be} + {}^{1}_{0}\mathrm{n} \rightarrow 2\,{}^{4}_{2}\mathrm{He} + {}^{1}_{0}\mathrm{n}' + {}^{1}_{0}\mathrm{n}'', $$

$$ {}^{204}_{82}\mathrm{Pb} + {}^{1}_{0}\mathrm{n} \rightarrow {}^{203}_{82}\mathrm{Pb} + {}^{1}_{0}\mathrm{n}' + {}^{1}_{0}\mathrm{n}''. $$

Only one example of a Pb isotope is given here, however other isotopes of Pb also act as neutron multipliers. Figure 3.18 shows a conceptual tritium breeding blanket design known as a pebble bed which uses Be as the neutron multiplier.

For a fusion reactor to be self-sustaining it must produce at least as much tritium as it consumes and ideally slightly more, so a tritium reserve can be build up which can be used to commission new fusion power plants. A useful concept in this regard is the Tritium Breeding Ratio (TBR),

$$\mathrm{TBR} = \frac{\text{tritium produced}}{\text{tritium needed}} \geq 1. \tag{3.10}$$

When calculating the TBR one must consider all forms of losses: a fraction of the neutrons will pass straight through the blanket without reacting, a fraction of the chamber walls cannot be used for tritium breeding due to other reactor components (divertor, diagnostics, heating systems, etc.), as time goes on the tritium breeding/neutron multiplier materials will be depleted and unburnt tritium can be retained within the reaction vessel.

3.6.2 Neutron damage

The high energy and fluence of neutron irradiation in a fusion energy reactor can cause serious damage to the structural component materials of the reactor. Since neutrons are neutral they are very penetrating, $\sim 200\,\mathrm{mm}$ in iron, and maintain their energy until they undergo a collision. Most high energy neutron collisions with lattice nuclei result in an elastic collision. A high energy neutron colliding with a lattice nucleus will displace it from its lattice site. This initial displaced atom is known as the 'primary knock-on atom' (pka). This pka is charged and loses a considerable fraction of its

energy through electrostatic interaction with the lattice before undergoing an elastic collision with energy E_{k}, with another lattice atom displacing it. E_{k} is usually close to the energy at which the cross section of an elastic interaction becomes larger than that of an electrostatic interaction and is material dependent. Both atoms then displace two more atoms, and so on creating a localised collision cascade until the knock-on atoms no longer have enough energy to overcome the displacement energy of the lattice E_{d}. So, for every pka there can be a large amount of displacements and each fusion neutron produces numerous pka.

For example, consider a single fusion neutron incident on iron, assuming all atoms after the pka only interact through elastic collisions, the number of displacements produced by each primary knock on atom is $N_{\mathrm{displacements}} = E_{\mathrm{k}}/2E_{\mathrm{d}}$. For iron $E_{\mathrm{k}} = 56\,\mathrm{keV}$ and $E_{\mathrm{d}} = 25\,\mathrm{eV}$ giving $N_{\mathrm{displacements}} = 2,240$ per pka [214]. Each fusion neutron can produce ~ 35 pkas in iron. Hence the total number of displacements created by each fusion neutron is $\sim 76,000$. The damage is distributed into localized collision cascades $\sim 100\,\mathrm{nm}$ in radius separated by $\sim 20\,\mathrm{mm}$.

Each atomic displacement produces an interstitial and a vacancy (called a 'Frenkel pair') which diffuse independently through the lattice. If an interstitial and a vacancy come together they recombine repairing the damage. In alloys most Frenkel pairs will recombine almost immediately after the displacement event $\sim 10\,\mathrm{ps}$. Hence, even though an extremely large number of displacements occur with each fusion neutron only $\sim 5\,\%$ become long lived defects and contribute to the damage. Through diffusion

like types of point defect will combine to produce dislocation loops which contributes to embrittlement by hindering dislocation motion.

Other undesirable consequences of neutron radiation include swelling and voids [215]. Some interstitials will end up on the surface of the material or at a grain boundary because of diffusion. When this happens, the interstitial will bond to the free surface causing the material to swell and when vacancies cluster in large enough numbers they will cause voids.

Neutron dose is commonly quoted in dislocations per atom (dpa) which is the number of times, on average, each of the atoms in the material has been displaced from its lattice site. Currently the extent of our experimental expertise in neutron radiation damage is limited to $\sim 10\,\mathrm{dpa}$ for anything but the very smallest samples, whereas the predicted end of life damage of a fusion power plant will be $> 100\,\mathrm{dpa}$, at the moment we do not have suitable materials that can withstand this amount of damage.

Oxide dispersion strengthened steels

As with all large construction projects, steels form the backbone of the structure of a fusion reactor. Being the main structural component, it is extremely important to mitigate the detrimental effects of neutron irradiation of steel. A novel solution to neutron radiation damage is Oxide Dispersion Strengthened (ODS) steels. These steels have undergone mechanical alloying to introduce oxide nanoparticles, such as Y_2O_3 and TiO_2. The nanoparticles have been shown to act as sinks for defects reducing the

swelling and embrittlement effects [216, 217]. Tests on ODS steels have shown them to have higher yield stresses under irradiation than their normal counterparts.

Low activation steels

After losing energy through elastic collisions, high energy neutrons will become 'thermal' neutrons and will react with the atomic nuclei of the lattice causing transmutations, the products of which may be radioactive. The high neutron doses mean there is the possibility for significant amounts of long lived radioactive isotopes to build up in the structural steel components. This must be avoided to meet the long term, sustainability goal to produce zero high and medium level radioactive waste 100 years after plant operations have ceased.

Pure iron produces minimal levels of radioactive waste, it is the alloying elements of steels such as Mo, Nb and Ni which tend to transmute into long lived radioactive products. The solution is to develop steels where these alloying elements are replaced with elements such as Ta, W and V with shorter half-lives while maintaining the good metallurgical properties of standard steels [218–222]. Figure 3.19 shows the results of a simulation of the decay in radioactivity of various steels following the cessation of activities in a fusion power plant. Currently 'EUROFER' is the leading choice of structural steel, reaching low levels of radioactivity after 100 years and hands on levels after 500 years. While these timescales sound long, in comparison to the thousand-year time scales for fissile waste they are relatively short. These advanced alloys can also be integrated with ODS technologies [219, 220, 222].

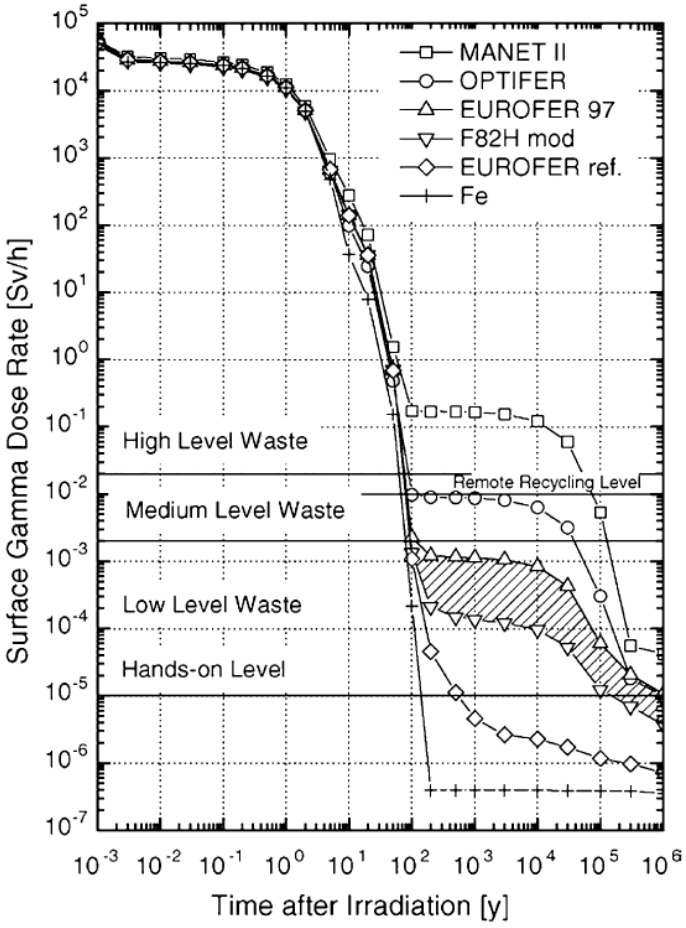

Figure 3.19. Activity of various steels as a function of time following an end of life neutron irradiation levels from a fusion power plant. Reproduced from [220].

3.6.3 Neutron irradiation of superconductors

The magnets are arguably the single most important system in a fusion reactor. With the fusion power scaling as the fourth power of the magnetic field [4], using the most powerful superconducting magnets is a necessity if fusion as an energy source is ever to make the transition from science fiction to a real-world technology. The magnets in a fusion reactor are not exposed to the extremely harsh environment of the reaction chamber itself however they can still be exposed to high levels of neutron irradiation. An understanding of how superconductors respond to high levels of neutron irradiation is essential for their use in fusion energy reactors.

High energy neutrons cause damage to superconductors in a similar manner as they do in steel, covered in section 3.6.2. An incoming neutron will displace a lattice atom turning it into a pka, the pka will lose energy through electronic interactions until at some energy E_{k} it will collide with another lattice atom causing a localised damage cascade. However, unlike in alloys such as steel, where lattice atom positions are interchangeable, the highly ordered nature of superconductors such as Nb_3Sn and REBCO mean the crystal structure does not recover after a damage cascade resulting in a region of amorphous material [223–225]. The damage cascades are approximately the size of vortex core, so they can act as pinning sites, increasing J_{c} at low fluences. At higher fluences there is a reduction in J_{c} which is the result of a significant reduction in T_{c} caused by the loss of long range order [226–240]. Figure 3.20 shows the influence neutron irradiation on the critical current of Nb_3Sn and REBCO, for comparison

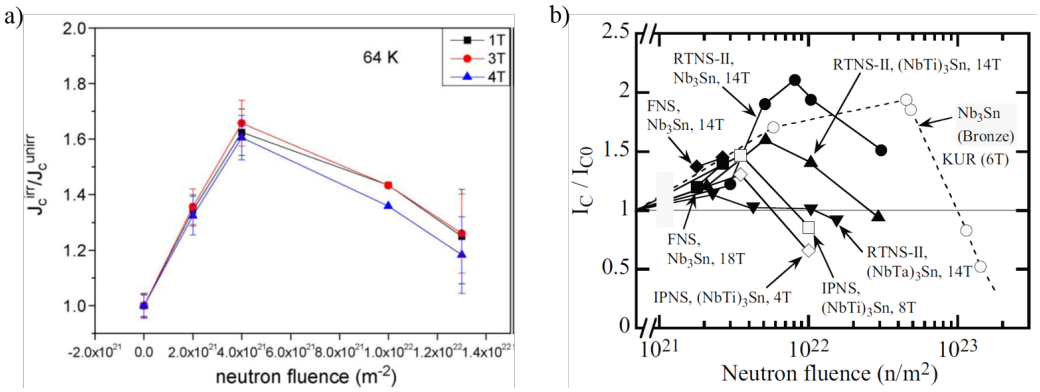

Figure 3.20. The influence of neutron irradiation on the critical current densities of a) an REBCO tape sample and b) various A15 wires. Reproduced from [229] and [225] respectively.

the end of life neutron fluence at the magnet location in ITER is expected to be $\sim 10^{22}\,\mathrm{m}^{-2}$ [234].

Transmutations appear to have minimal effect on the superconducting properties in comparison to the cascade damage with one notable exception, $GdBa_2Cu_3O_{7-\delta}$. ^{155}Gd and ^{157}Gd have very high neutron capture cross section for thermal and epi-thermal neutrons, ordinarily this would not have a significant effect on the superconducting properties. However, the products of these reactions, ^{156}Gd and ^{158}Gd, are unstable and both decay via gamma emissions with enough energy to displace the Gd from its lattice site. This rapidly deteriorates the superconducting properties even at low neutron fluences [241, 242]. REBCO tapes made with Gd are a very poor choice for use in fusion magnets.

3.7 Concluding remarks

There are many other considerations when producing a useful superconducting conductor than simply a high critical temperature. Many of these difficulties have now been largely overcome, and as prices of REBCO continues to fall they provide ever more competition to established LTS materials, particularly at $B > 20\,\mathrm{T}$. With fusion power scaling as a strong function of magnetic field, there is a clear drive toward HTS fusion magnets. Large, more powerful magnets will result in more strain on the superconducting components, so understanding how strain effects the superconducting properties is of paramount importance.

Chapter 4

Multimodal strain dependence of the critical parameters in high field technological superconductors

4.1 Introduction

In this chapter detailed measurements on two samples are presented. Detailed critical current density measurements as a function of field, temperature, and applied tensile and compressive uniaxial strain $J_c\left(B, T, \varepsilon_{app}\right)$ are presented for a 4 mm wide REBCO tape (Ref: SCS4050) manufactured by SuperPower [102]. The data were obtained with the magnetic field applied normal to the surface of the tape. The effective upper critical field was also measured resistively as a function of temperature and applied uniaxial strain $B_{c2}^{*\rho}\left(T, \varepsilon_{app}\right)$. The tape does not contain any artificial pinning centres (APC). It

is twinned along the (110) and $(1\bar{1}0)$ planes. This results in two types of domains such that a fraction f of the domains are aligned with the [100] direction along the principal axis of strain (i.e. a-axis domains) and the remaining fraction $(1-f)$ of domains have the [010] direction along the principle axis of strain [243]. Data from single crystals of REBCO show the strain dependence of the critical parameters T_c and B_{c2} is strongly anisotropic, monotonically increasing with tensile strain applied along the a-axis and monotonically decreasing with tensile strain applied along the b-axis [210, 211]. Hence in REBCO tape, there is a bimodal response from the domains to a uniaxial strain. Recently a chain model was developed, as discussed in section 3.5, that provides a straightforward explanation of how the inverted parabolic strain behaviour of the critical current in twinned REBCO tapes arises from this bimodal behaviour and shows that ε_{peak} is dependent on the domain fraction [199]. This explanation is quite different from the standard description for LTS where the peak in the strain dependence of the critical current is attributed to a peak in the intrinsic strain dependence of T_c and B_{c2} where all the grains show the same dependence (i.e. homogeneous behaviour). The chapter also includes detailed measurements and a bimodal analysis of $J_c(B, T, \varepsilon_{app})$ for a bronze route Nb_3Sn wire. Also analysed are $J_c(B, T, \varepsilon_{app})$ data for an internal tin Nb_3Sn wire and a Nb_3Al jelly roll wire that have been published previously [51, 176]. The evidence for domains with different strain dependencies (i.e. multimodal behaviour) in A15 compounds from single crystal measurements is considered [244, 245] and the role of grain boundaries is discussed.

In section 4.2, the experimental methods used to measure the REBCO tape and the bronze route Nb_3Sn wire are described. Section 4.3 details the critical current and the effective upper critical field results. Section 4.4 provides engineering parameterisations of the critical current density for all samples. Section 4.5 provides a comprehensive flux pinning scaling analysis for all samples. In section 4.6 the bimodal chain model is extended to include field and temperature. Section 4.7 uses the results of the chain model to investigate features of the data that cannot be accounted for in a homogeneous model and provides estimates for the domain fraction. Sections 4.8 and 4.9 give the discussion and the conclusions respectively.

4.2 Experimental equipment and procedure

4.2.1 REBCO tape on a springboard

Durham's 15 T, liquid helium cooled, 40 mm wet bore, superconducting split-pair horizontal magnet was used to perform transport critical current density J_c and resistive upper critical field measurements $B_{c2}^{*\rho}$ on the REBCO tape. The $J_c\left(B, T, \varepsilon_{app}, \theta\right)$ probe used to perform the measurements has been described in detail in ref. [246] (the inverted temperature cup has been redesigned for this work to improve the thermal efficiency and usability, the new inverted temperature cup is shown in figure 4.1).

The sample was soldered to the top of a CuBe springboard sample holder using standard 40Sn60Pb solder as shown in figure 4.1. Uniaxial tensile or compressive strain was applied by either pushing together or pulling apart the legs of the springboard. The

soldering temperature for 40Sn60Pb solder is ~ 240°C, which is above the maximum recommended soldering temperature for the tape of 200°C [102] hence delamination and/or degradation of the sample was a concern. Preliminary experiments at 77 K on samples attached to springboards with either SnPb solder or Bolton 136 (formerly Cerrolow 136) solder (composition 49Bi21In18Sn12Pb, melting point 58°C, soldering temperature 150°C) [247] showed similar strain dependent critical current properties over small strain ranges consistent with variations expected along the conductor length. This indicated that no or minimal delamination or degradation of the tape resulted from the relatively short period of high temperature soldering used for SnPb solder (less than one minute), consistent with results found in literature [248]. The SnPb solder was chosen for the main suite of measurements since the Bolton 136 solder was much more susceptible to unpredictable brittle fracture under high strains.

The strain was measured using a strain gauge attached to the middle of the springboard alongside the sample. The voltage taps were 13mm apart located in the centre of the sample. Temperature control of the sample is achieved through use of an inverted temperature cup [249, 250]. The cup is sealed at the top and has a vent in the bottom. Initially the cup fills with liquid cryogen. Three heaters attached to the underside of the sample holder are used to produce gas that drives the liquid cryogen out of the cup through the vent in the bottom leaving a gaseous environment inside. The temperature of the sample is controlled along its length using LakeShore 336 temperature controllers. There are three independent control loops for the three heaters and their associated field-calibrated Cernox$^{\text{TM}}$ resistance thermometers that

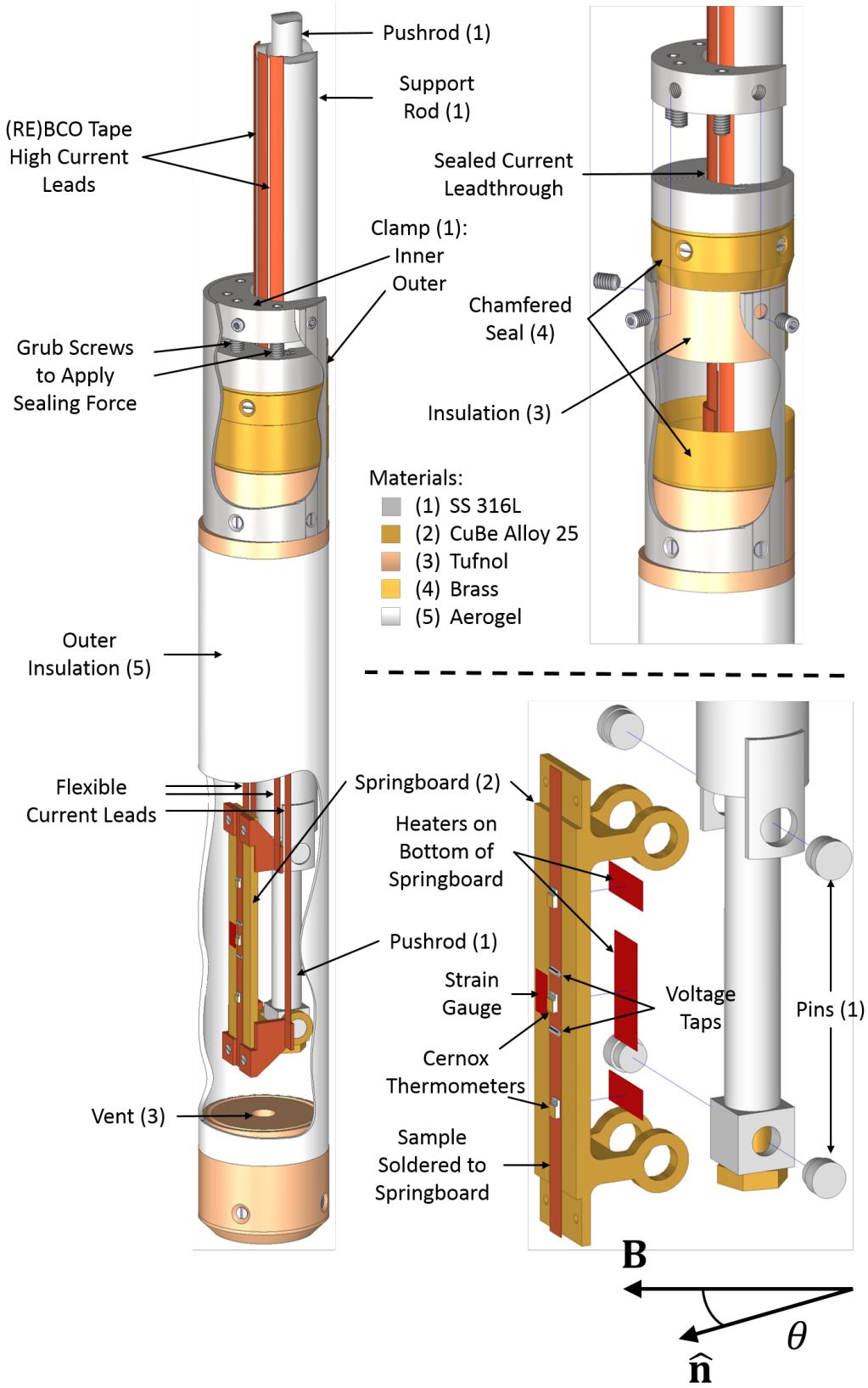

Figure 4.1. Schematic of the bottom of the $J_c\,(B, T, \varepsilon_{app}, \theta)$ measurement probe [246]. The numbers in brackets specify the material used to fabricate the component.

are directly in contact with the sample. The relatively small effect of magnetic field on the calibration of the Cernox^{TM} thermometers was corrected for, using data from the literature [251]. The calibration was first explicitly checked and confirmed at 4.2 K in fields up to 14 T and found to be independence of field angle at 0° and 90° and implemented over the whole field and temperature range of the measurements. A schematic of the end of the $J_c\,(B, T, \varepsilon_{app}, \theta)$ probe is shown in figure 4.1 and a diagram of the experimental setup is shown in figure 4.2. Water-filled bubblers were attached to the helium space to prevent a backflow of air. These were used in place of the more conventional one-way mechanical valves to minimise variations in pressure. The small differential pressures across bubblers gave more stable temperature control than mechanical valves. In order to reduce helium boil off, the probe has HTS tapes soldered along the length of the current leads. This makes turning the probe in-situ in the split-pair magnet very difficult at high fields because of the large magnetisation currents generated by the stray field of the magnet in the HTS current leads. In practice this meant the probe could only be rotated below 2 T.

Critical current transport measurements were performed by ramping up the current from 0 A at a constant rate such that each measurement took ~ 60 s. The current and voltage were measured continuously throughout the measurement. The strain gauge was also monitored and there was found to be no change in strain during the transport measurements. To begin with, measurements were made at zero applied strain. Then, a compressive strain of $\varepsilon_{app} = -1\,\%$ was applied to the sample at 4.2 K in zero magnetic field and the probe was mechanically locked. A complete set of

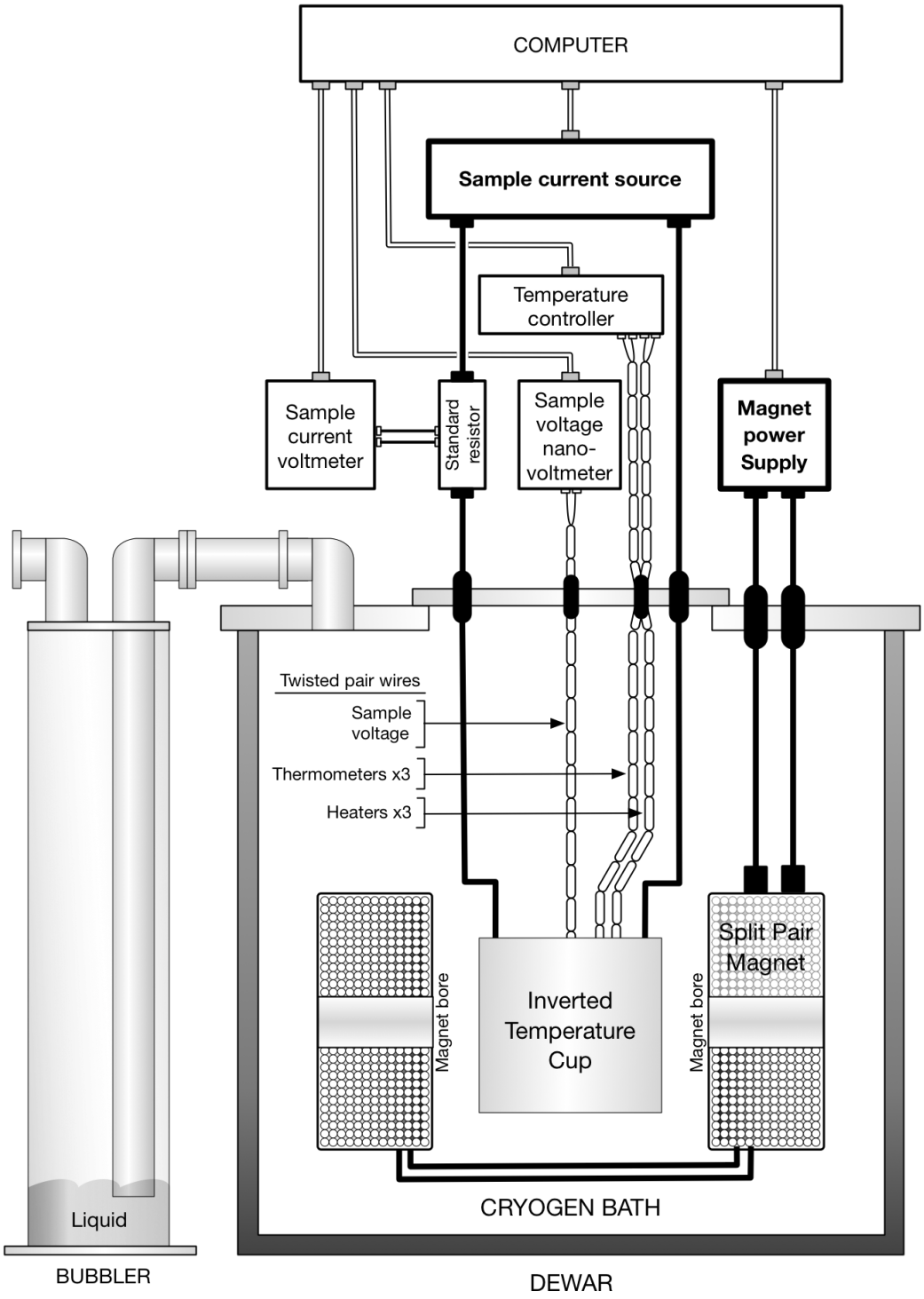

Figure 4.2. Schematic showing the experimental hardware setup for making critical current and resistivity measurements as a function of field, temperature and strain [252].

variable-field, variable-temperature measurements were taken. For $T = 4.2, 20, 40, 60\,\mathrm{K}$ measurements were taken at 2 T intervals from 14 to 2 T or until $I_\mathrm{c} > 250\,\mathrm{A}$ (the maximum achievable current of the probe). For $T = 68, 76, 84\,\mathrm{K}$ measurements were taken at 1 T intervals up to 14 T or until $B > B^*_{\mathrm{c}2}(T, \varepsilon_{\mathrm{app}})$. Alongside the critical current measurements, resistive measurements of the effective upper critical field were made. An excitation current of 100 mA was applied to the sample and the temperature was increased at a rate of $1\,\mathrm{K\,min^{-1}}$ while the voltage across the voltage taps and the temperature were monitored continuously. These resistivity measurements were completed in the range 14 to 0 T in 2 T intervals. Both critical current and effective upper critical field measurements were performed with the applied field normal to the tape surface. After the measurements at $\varepsilon_{\mathrm{app}} = -1\,\%$ were completed, the temperature was reduced to 4.2 K, the field reduced to zero and the applied strain changed to $-0.75\,\%$. Again the probe was locked and another complete set of critical current and resistivity measurements were made. In this way, measurements were performed at increasing strains at intervals of 0.25 % from $\varepsilon_{\mathrm{app}} = -1\,\%$ up to $+0.5\,\%$. Following the main suite of measurements, the strain was returned to $\varepsilon_{\mathrm{app}} = 0\,\%$, and critical current (at 2 T and 60 K) and effective upper critical field (at 2 T) measurements were taken to confirm the reversibility of the sample.

4.2.2 Bronze route Nb_3Sn on a Walters' spring

Detailed critical current density measurements on the bronze route Nb_3Sn wire were made in Durham's 17 T vertical solenoid magnet using the Durham $J_\mathrm{c}(B, T, \varepsilon_{\mathrm{app}})$

probe designed for strain measurements on superconducting wires [180]. A variable-temperature Walters' Spring design [253] was used to apply strain to the sample. Previous measurements using this equipment have been published extensively [51, 168, 175, 176, 178–180], although the data presented here are the most detailed to have been produced by the Durham group on a Nb_3Sn wire to date. The Nb_3Sn wire was manufactured by Bruker for use in the ITER fusion reactor [254]. The wire diameter was 0.82 mm with a Cu:nonCu ratio of approximately 60:40 and twist-pitch of 15 mm. The Nb_3Sn measurements were taken at strains from $\varepsilon_{\mathrm{app}} = -1.16\,\%$ to $\varepsilon_{\mathrm{app}} = +0.58\,\%$, at temperatures of $T = 4.2, 8, 10, 12, 14\,\mathrm{K}$ and various fields chosen such that typically eight in-field measurements were taken at each combination of temperature and strain. Y. Tsui was responsible for obtaining the data on the bronze route Nb_3Sn sample and for calculating J_c and N from the $E - J$ traces, P. Branch (the author) is responsible for the subsequent analysis.

4.3 Transport measurements

4.3.1 REBCO measurements

Figure 4.3 shows typical examples of $V - I$ (or equivalently $E - J$) traces as a function of magnetic field. Typical noise for the measurements was $\sim 30\,\mathrm{nV}$. The sample holder is in parallel with the sample and so acts as a resistive shunt for the current. Hence the total current measured I_{total} differs slightly from the current flowing though the

superconducting sample I_{SC} characterised by the relation

$$I_{\mathrm{SC}} = I_{\mathrm{total}} - \frac{V}{R_{\mathrm{shunt}}}, \tag{4.1}$$

where V is the measured voltage and R_{shunt} is the shunt resistance of the springboard. R_{shunt} was determined as a function of magnetic field and strain from the resistive measurements of the effective upper critical field. Typical shunt currents were $\sim 80\,\mathrm{mA}$ at $100\,\mu\mathrm{V\,m^{-1}}$. This correction was applied to all the $V - I$ traces before the critical current was determined at both the $10\,\mu\mathrm{V\,m^{-1}}$ and $100\,\mu\mathrm{V\,m^{-1}}$ criteria, and the index of transition N calculated by fitting the data between $10\,\mu\mathrm{V\,m^{-1}}$ and $100\,\mu\mathrm{V\,m^{-1}}$ using the definition of N given by

$$E = E_{\mathrm{c}} \left| \left(\frac{J}{J_{\mathrm{c}}} \right)^{N} \right|, \tag{4.2}$$

where E_{c} is the electric field criterion used to define J_{c}.

Measurements of the angular dependence of the critical current on the same sample are presented in chapter 5 and demonstrate that the critical parameters measured in this chapter (where the angle is defined to be 0° when the field is aligned normal to the tape surface) are broadly insensitive to the exact angle at which the field is applied. Figure 4.4 shows the full range of all of the critical current data for the REBCO tape at the $100\,\mu\mathrm{V\,m^{-1}}$ criterion on both a 2D and 3D plot. These data are consistent with the many reports in the literature that show the strain dependence of the critical current in REBCO tapes approximately follows an inverted parabola in the region about the peak in the critical current [153, 189, 195, 196, 199, 201, 202, 206, 208, 209, 243] and can

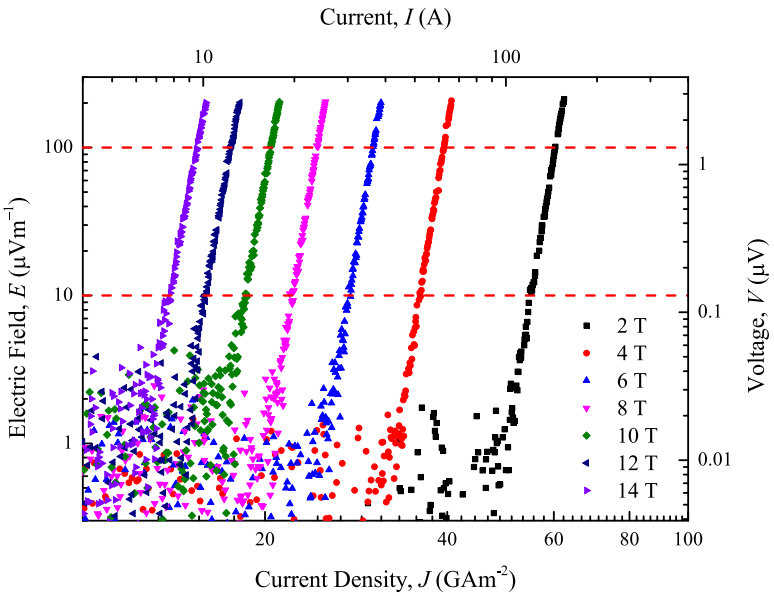

Figure 4.3. Field dependent $E - J$ traces for the REBCO tape at $T = 20\,\mathrm{K}$ and $\varepsilon_{\mathrm{app}} = 0\,\%$. The dashed lines indicate the $10\,\mu\mathrm{V\,m^{-1}}$ and $100\,\mu\mathrm{V\,m^{-1}}$ E-field criteria.

be characterised by

$$\frac{J_{\mathrm{c}}\left(\varepsilon_{\mathrm{app}}\right)}{J_{\mathrm{c}}\left(0\right)} = 1 - \beta\left(\varepsilon_{\mathrm{app}} - \varepsilon_{\mathrm{peak}}\right)^2 + \beta\varepsilon_{\mathrm{peak}}^2, \tag{4.3}$$

where $\varepsilon_{\mathrm{app}}$ is the applied strain, $\varepsilon_{\mathrm{peak}}$ is the applied strain at which the critical current is at its maximum value and β is a constant. In addition to the standard transport measurements, high field critical current values were also extracted from the resistive upper critical field traces. Linear interpolations of these critical current values found at various fields and temperatures were used to determine values coincident with the temperatures used in the transport measurements and good agreement is found between the two sources of data. Figure 4.5 shows inverse parabolic strain behaviour for the critical current density at $T = 68\,\mathrm{K}$. Figure 4.6 shows a similar inverse parabolic strain

dependence for the normalised critical current as a function of temperature at $B = 6\,\mathrm{T}$. $\varepsilon_{\mathrm{peak}}$ is extracted from the data by fitting eqn 4.3 to the inverted parabolic region, the results of this analysis are shown in figure 4.7. The most striking result, clearly shown in figures 4.6 and 4.7 is that $\varepsilon_{\mathrm{peak}}$ is a function of both field and temperature. It is noted that $\varepsilon_{\mathrm{peak}}$ is not a directly measured but is a fitted parameter and analysis of these results in both REBCO and Nb_3Sn is only possible due to a high SNR.

In LTS materials, the index of transition N can be parameterised using the critical current through a modified power law of the form

$$N = 1 - r_N J_{\mathrm{c}}^{S_N} \left(B, T, \varepsilon_{\mathrm{app}}\right), \tag{4.4}$$

where r_N and S_N are dimensionless constants [174, 175, 179, 255, 256]. The N-values for REBCO tape at all fields, temperatures and strains are shown in figure 4.8. The N-values at 4.2 K have been included for completeness, although they lie significantly above the overall trend at other temperatures, because of the heating that occurred at high E-fields (confirmed by the sample thermometry). Eqn 4.4 if fitted to the data at the $100\,\mu\mathrm{V\,m^{-1}}$ criterion (excluding the data at 4.2 K) to determine $S_N = 0.44$ and $r_N = 5.59$.

Figure 4.9 shows a typical resistive measurement of the effective upper critical field with the three different criteria considered in this work highlighted: extrapolated 0 % $\rho_{\mathrm{N}}\left(B_{\mathrm{c2}}^{ex.0\%}\right)$, 50 % $\rho_{\mathrm{N}}\left(B_{\mathrm{c2}}^{50\%}\right)$ and extrapolated 100 % $\rho_{\mathrm{N}}\left(B_{\mathrm{c2}}^{ex.100\%}\right)$, where ρ_{N} is the normal state resistivity. The inset shows the effect of varying the excitation current.

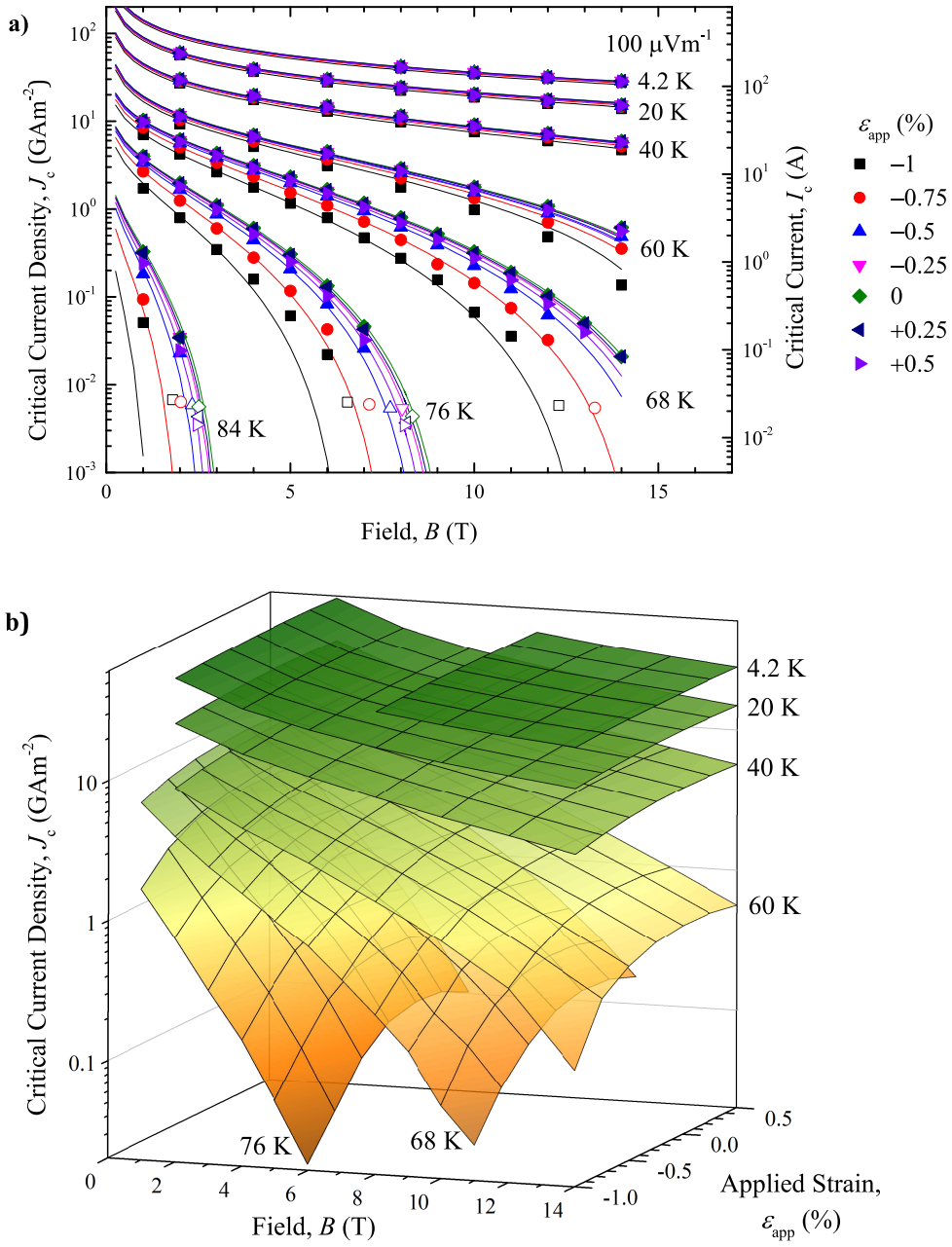

Figure 4.4. $J_c\,(B, T, \varepsilon_{app})$ for REBCO tape at the 100 μV m^{-1} E-field criterion in a) 2D and b) 3D plots. Open symbols indicate critical current values obtained from resistive upper critical field traces. Solid lines are an engineering scaling law parameterisation eqn 4.12 where the optimised parameters are given in table 4.2.

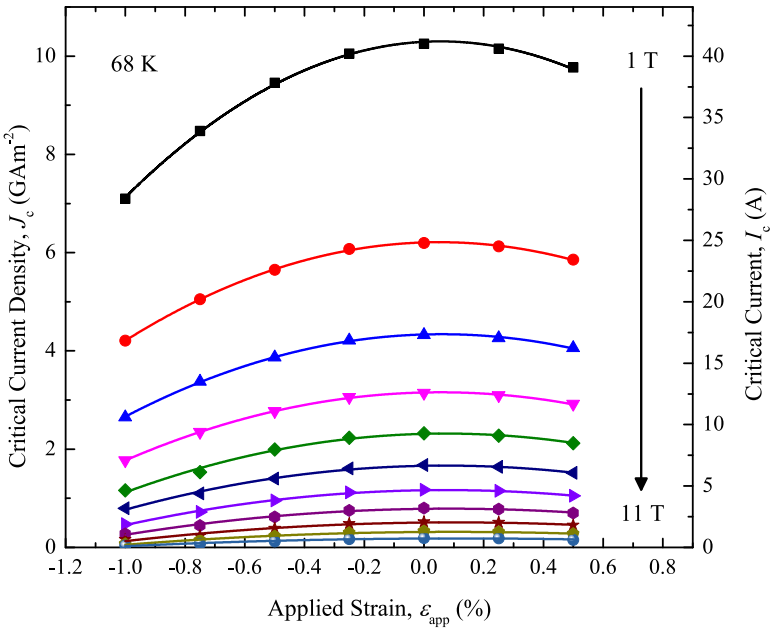

Figure 4.5. Strain dependence of the critical current density for REBCO tape at $T = 68\,\mathrm{K}$ and fields from 1 T to 11 T in increments of 1 T at the $100\,\mu\mathrm{V\,m^{-1}}$ criterion. Solid lines are parabolic fits to the data using eqn 4.3.

Higher current increases the signal to noise ratio of the measurement whereas using a lower current tends to avoid artefacts from flux flow dissipation. An excitation current of 100 mA was chosen across the whole measurement range. The degree to which the effective upper critical field should be considered similar to the thermodynamic upper critical field or the irreversibility field is discussed in section 4.8. Figure 4.10 shows typical $\rho - T$ traces as a function of field at zero applied strain. The reduction in the normal state resistance is associated with the magnetoresistive properties of the CuBe springboard. The 'bump' at the top of the transition at $B = 0\,\mathrm{T}$ is a consistent feature across all strains in zero field and is attributed to a non-uniform E-field across the width of the sample at $B = 0\,\mathrm{T}$. The temperature and strain dependence of the effective upper critical field have been parameterised using an equation for high

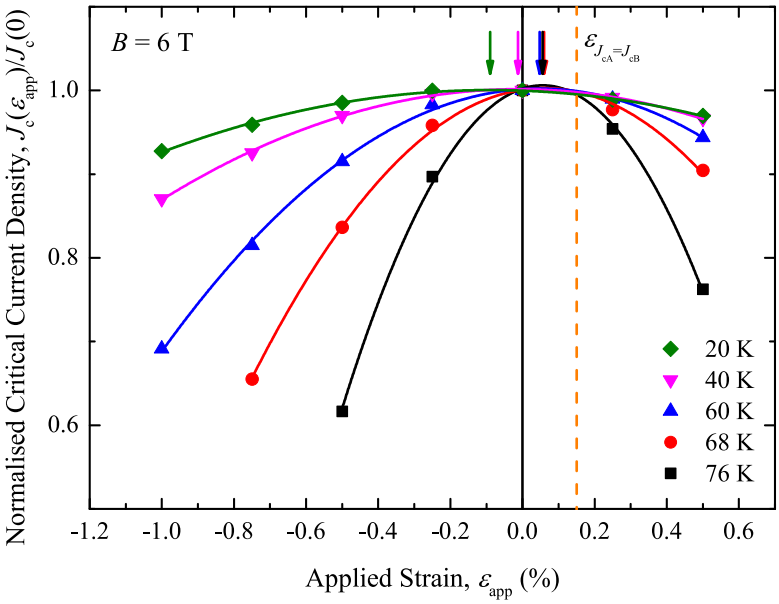

Figure 4.6. Strain dependence of the normalised critical current density for REBCO tape for various temperatures at $B = 6\,\mathrm{T}$ using the $100\,\mu\mathrm{V\,m^{-1}}$ criterion. Solid lines are parabolic fits to the data using eqn 4.3. Arrows indicate the position of $\varepsilon_{\mathrm{peak}}$. The values of $J_c\,(0)$ are $29.5, 14.9, 4.51, 1.66, 0.132\,\mathrm{Gm^2}$ at 20 K to 76 K respectively. The dashed line shows the position of $\varepsilon_{J_{cA}=J_{cB}}$ determined from an analysis of the temperature and field dependence of $\varepsilon_{\mathrm{peak}}$ detailed in section 4.7.

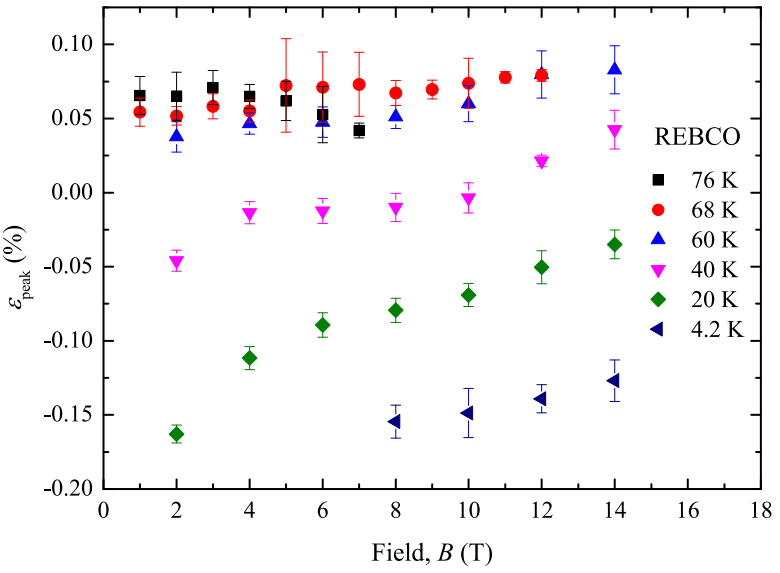

Figure 4.7. $\varepsilon_{\mathrm{peak}}$ as a function of field and temperature for the REBCO tape at the $100\,\mu\mathrm{V\,m^{-1}}$ criterion. The peak values of strain are obtained by fitting eqn 4.3 to the parabolic region of $J_c\,(\varepsilon_{\mathrm{app}})$ at each field and temperature.

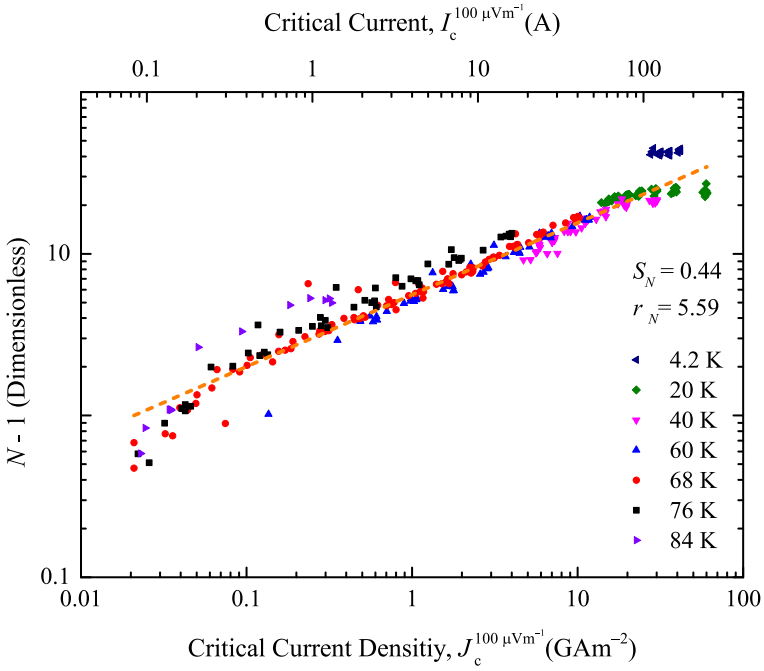

Figure 4.8. $N-1$ (where N is the index of transition) against the critical current on a log-log scale for the REBCO tape at the $100\,\mu V\,m^{-1}$ criterion. The 4.2 K data lie above the overall trend due to heating in the transition region. The dashed line is a linear fit to the data (excluding the 4.2 K data) and is used to extract the parameters S_N and r_N in eqn 4.4.

temperature superconductors of the form [257]

$$B^*_{c2}(T, \varepsilon_{app}) = B^*_{c2}(0, \varepsilon_{app}) \left(1 - \frac{T}{T^*_c(\varepsilon_{app})}\right)^s, \tag{4.5}$$

and [173]

$$\frac{T^*_c(\varepsilon_{app})}{T^*_c(0)} = 1 + c_1\varepsilon_{app} + c_2\varepsilon^2_{app} + c_3\varepsilon^3_{app} + c_4\varepsilon^4_{app}, \tag{4.6}$$

$$\frac{B^*_{c2}(\varepsilon_{app})}{B^*_{c2}(0)} = 1 + d_1\varepsilon_{app} + d_2\varepsilon^2_{app} + d_3\varepsilon^3_{app} + d_4\varepsilon^4_{app}, \tag{4.7}$$

where the c–values, the d–values, s, and the normalisation parameters $T^*_c(0)$ and $B^*_{c2}(0,0)$ are free parameter. Parameterisations were completed using only parabolic terms up to c_2 (and d_2) and are listed in table 4.1. When fitting data were weighted evenly as uncertainty on B^*_{c2} does not scale with its magnitude. In figure 4.11 the temperature and strain dependence of the entire $B^{ex.100\%}_{c2}$ dataset for the RE-BCO tape is shown. The data are replotted in figure 4.12 as a universal curve of $B^{ex.100\%}_{c2}(T, \varepsilon_{app}) / B^{ex.100\%}_{c2}(0, \varepsilon_{app})$ against the reduced temperature $t = T/T^{ex.100\%}_c(\varepsilon_{app})$ demonstrating the accuracy of the parameterisation. Figure 4.13 shows the variation of the transition width ΔT with field and applied strain which has been calculated by taking the difference between the extrapolated 100 % and 0 % criteria.

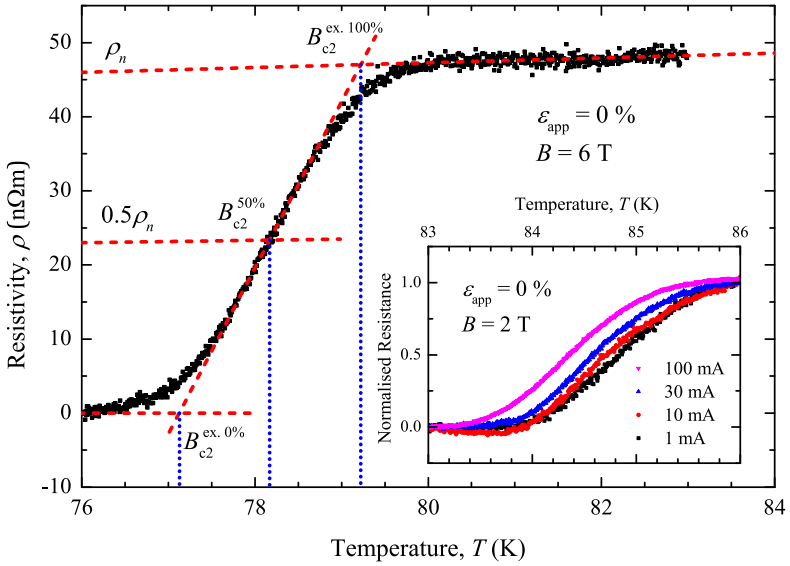

Figure 4.9. Typical resistive trace for the REBCO tape at $\varepsilon_{\text{app}} = 0\,\%$, $B = 6\,\text{T}$, for a 100 mA excitation current. The different criteria considered in this study are shown. Inset: Normalised resistive traces for the REBCO tape as a function of excitation current at $\varepsilon_{\text{app}} = 0\,\%$, $B = 2\,\text{T}$.

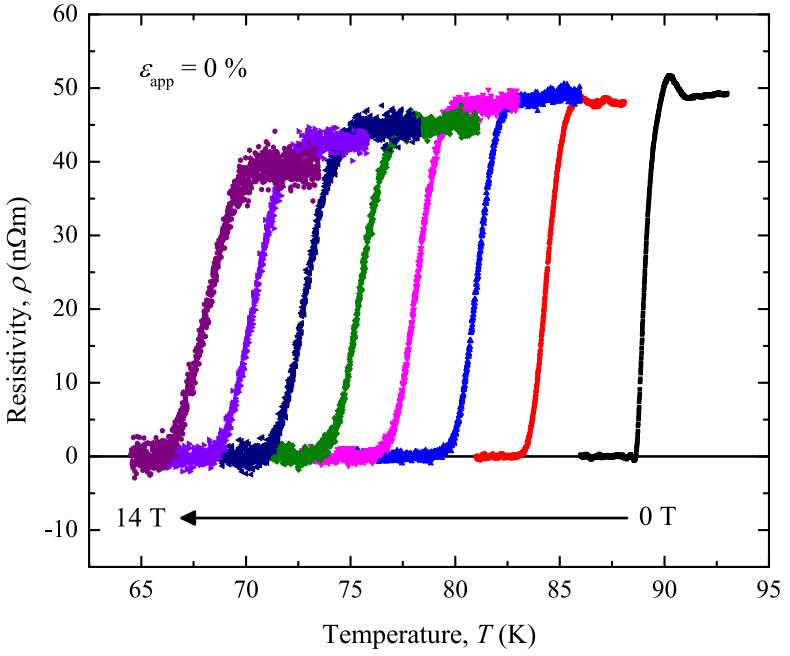

Figure 4.10. Resistive traces from 0 to 14 T in 2 T increments for the REBCO tape at $\varepsilon_{\text{app}} = 0\,\%$ with a 100 mA excitation current.

Table 4.1. Parameters of the $B_{c2}^{*\rho}$ parameterisation, eqn 4.5, for the REBCO resistive transport data at the three criteria considered in this study.

	$B_{c2}^{ex.0\%}$	$B_{c2}^{50\%}$	$B_{c2}^{ex.100\%}$
$T_c^{*\rho}(0)$ (K)	88.691	89.056	89.361
c_1 ($10^{-3}\%^{-1}$)	2.187	-0.4492	-2.786
c_2 ($10^{-3}\%^{-2}$)	-16.39	-12.04	-6.580
$B_{c2}^{*\rho}(0,0)$ (T)	86.06	90.49	94.64
d_1 ($10^{-3}\%^{-1}$)	22.34	31.68	36.30
d_2 ($10^{-3}\%^{-2}$)	-103.6	-108.6	-124.7
s	1.309	1.292	1.268
RMS Error of $B_{c2}^{*\rho}$ fit (mT)	59	44	60

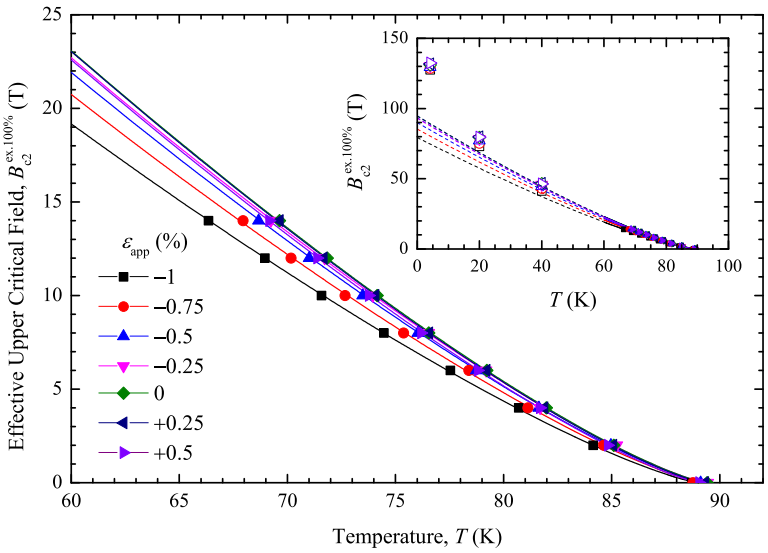

Figure 4.11. Effective upper critical field as a function of temperature and strain for the REBCO tape using the extrapolated 100 % criterion. Closed symbols are from resistivity measurements. Open symbols are from extrapolation of the flux pinning scaling curves as detailed in section 4.5. Solid lines are a parameterisation of the data using eqn 4.5 with the optimised parameters detailed in table 4.1 and the dashed lines are the extrapolation of this parameterisation to $T = 0\,\mathrm{K}$.

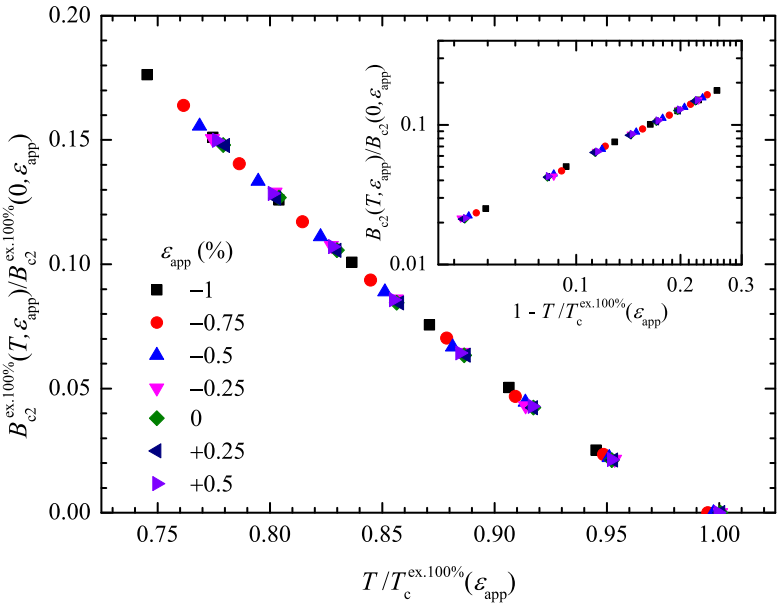

Figure 4.12. $B_{c2}^{ex.100\%}(T,\varepsilon_{app})/B_{c2}^{ex.100\%}(0,\varepsilon_{app})$ against reduced temperature for the REBCO tape. (inset) $B_{c2}^{ex.100\%}(T,\varepsilon_{app})/B_{c2}^{ex.100\%}(0,\varepsilon_{app})$ against one minus the reduced temperature.

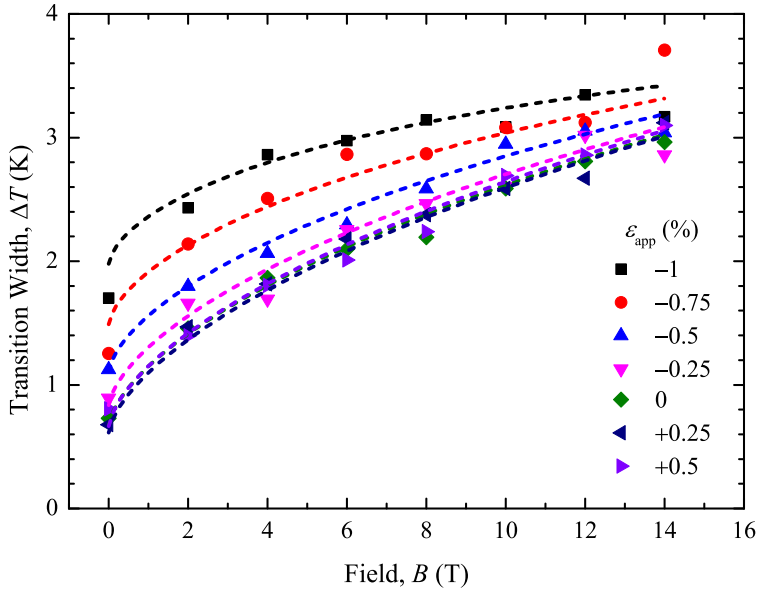

Figure 4.13. Variation of the transition width ΔT with field and applied strain for the REBCO tape. Dashed lines show ΔT obtained from the parameterisations of $B_{c2}^{*\rho}$ using eqn 4.5.

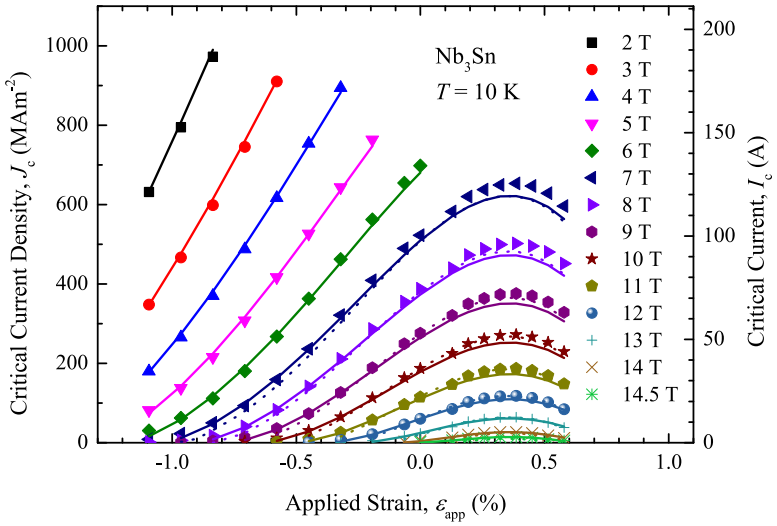

Figure 4.14. Critical current density of the bronze route Nb_3Sn wire at 10 K. Solid lines show the engineering parameterisation using eqn 4.12 where the values of the optimised parameters are given in table 4.2. Dotted lines show the parameterisation given in [258] fitted over a limited data range.

4.3.2 Bronze route Nb_3Sn measurements on a Walters' spring

Typical J_c data for the bronze route Nb_3Sn wire are shown in figure 4.14 at 10 K as a function of field and strain. When eqn 4.3 is fitted to the parabolic region of $J_c(\varepsilon_{app})$, ε_{peak} is a function of field and temperature as shown in figure 4.15 which provides evidence for multimodal behaviour.

4.3.3 Internal tin Nb_3Sn and jelly roll Nb_3Al wire on a Walters' spring

This section provides a reanalysis of similar measurements from two other LTS conductors, an internal tin Nb_3Sn wire and a jelly-roll Nb_3Al wire. The original experimental details of the measurements and the accompanying standard analysis can found in [176]

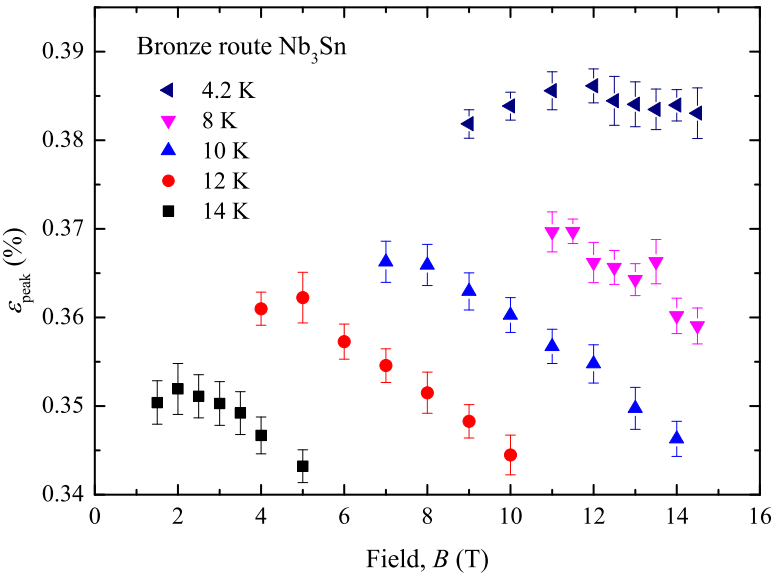

Figure 4.15. ε_{peak} as a function of field and temperature for the bronze route Nb_3Sn wire. ε_{peak} was obtained by fitting eqn 4.3 to the parabolic region of $J_c(\varepsilon_{app})$ at each field and temperature.

and [51] respectively. Figures 4.16 and 4.17 show ε_{peak} for the internal tin Nb_3Sn wire and the jelly-roll Nb_3Al wire.

4.3.4 A note on fitting methods

Throughout this thesis there are numerous fits made to data. Most fits are made by minimising Chi-squared with data weighted by Poisson statistics or by directly determined uncertainties in the y-axis variable where these were available. Where other fitting methods have been used, this is clearly stated.

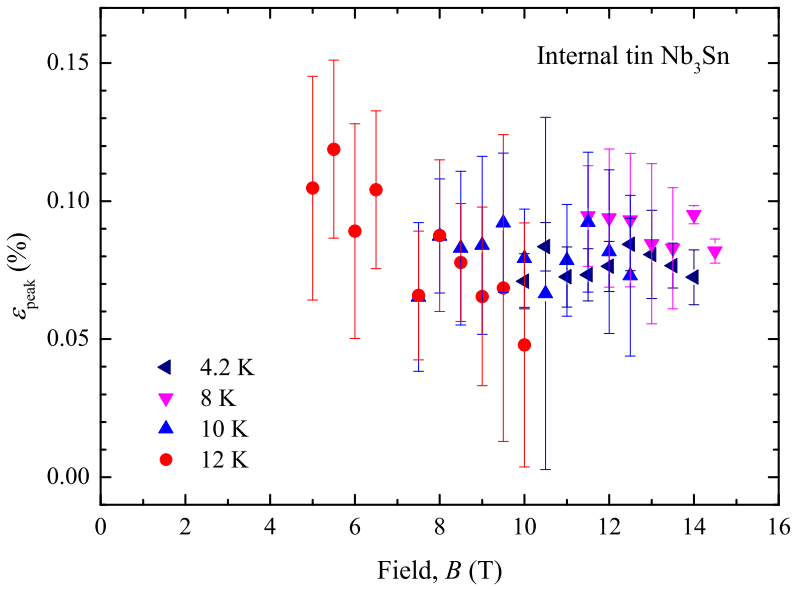

Figure 4.16. $\varepsilon_{\text{peak}}$ as a function of field and temperature for the internal tin Nb_3Sn wire. $\varepsilon_{\text{peak}}$ was obtained by fitting eqn 4.3 to the parabolic region of $J_c(\varepsilon_{\text{app}})$ at each field and temperature.

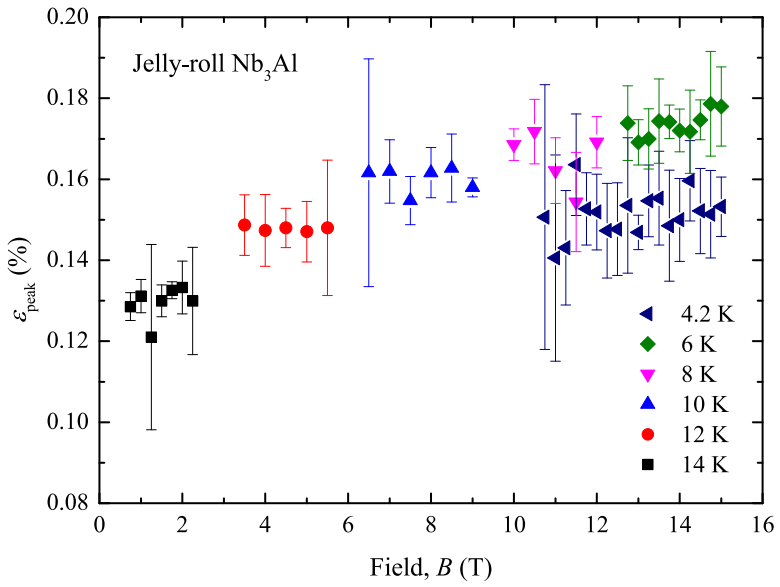

Figure 4.17. $\varepsilon_{\text{peak}}$ as a function of field and temperature for the jelly roll Nb_3Al wire. $\varepsilon_{\text{peak}}$ was obtained by fitting eqn 4.3 to the parabolic region of $J_c(\varepsilon_{\text{app}})$ at each field and temperature.

4.4 Engineering parameterisation of $\boldsymbol{J_c\left(B,T,\varepsilon_{app}\right)}$

Flux pinning scaling [52, 53, 55] is the standard way to describe the in-field critical current of Type II superconductors. As discussed in chapter 2, when the direction of current flow is perpendicular to the field, the general relation for the flux pinning force density F_p is given by

$$F_p = J_c B = C B^p \left(1-b\right)^q, \tag{4.8}$$

where C is a temperature and strain dependent factor, $b = B/B^*_{c2}\left(T,\varepsilon_{app}\right)$ is the reduced field, and p and q are constants. The underlying assumption for eqn 4.8 is that there is one mode, or one type, of pinning site. The values of p and q are an indication of the pinning mechanism where a change of 1/2 indicates a change in mechanism [52]. The prefactor C can be related to the maximum flux pinning force density $F_{p,max}$ through the relation

$$F_{p,max} = C\left(\frac{p}{p+q}\right)^p\left(1-\frac{p}{p+q}\right)^q. \tag{4.9}$$

In the standard flux pinning approach,

$$F_p = J_c B = A\frac{\left[B^*_{c2}\right]^n}{\left(2\pi\phi_0\right)^{1/2}\mu_0\left[\kappa_1^*\right]^m} b^p\left(1-b\right)^q, \tag{4.10}$$

where κ_1^* is the Ginzburg-Landau parameter, μ_0 is the vacuum permeability, ϕ_0 is the magnetic flux quantum and n, m, p, q and A are constants [52, 53, 55]. Technological high-field superconductors are designed to have as high J_c as possible and hence strong

pinning. This leads to them being complex and inhomogeneous, so we rarely find the integer and half-integer values of n, p and q given by simple flux pinning theory. This thesis does not add to the huge literature that considers the range of pinning mechanisms that operate in HTS and LTS materials. The scaling law and the derived parameters are simply used as a convenient way to accurately characterise the field, angle and temperature dependencies, but as this chapter outlines, not the strain.

It is well known that the correlations between these parameters can be significantly reduced if independent measurements of J_c and B^*_{c2} are made [51], as given in the current work. In early flux pinning work, only variable temperature data was available. It was assumed that κ_1^* was a constant and a value of n was extracted from the gradient of a $\log F_{p,max} - \log B^*_{c2}$ plot [50]. More detailed variable temperature and variable strain data followed on low temperature superconductors, and it was found that the temperature and strain dependence of κ_1^* needed to be included to accurately parameterise the $J_c\,(B, T, \varepsilon_{app})$ data [169, 259]. The temperature and strain dependence of κ_1^* is incorporated by taking the Ginzburg–Landau relation for the upper critical field $B_{c2}\left(T, \varepsilon\right) = \sqrt{2}\kappa_1^*\,(T, \varepsilon)\,B_c\,(T, \varepsilon)$ [260] along with the two-fluid model for the temperature dependence of the thermodynamic critical field $B_c\,(T, \varepsilon) = B_c\,(0, \varepsilon)\,(1 - t^2)$ [261] and the BCS equation for $B_c\,(0, \varepsilon) = (3\mu_0/2)^{1/2}\,(3.5/2\pi)\,\gamma^{1/2} T_c$ [260] where γ is the Sommerfeld constant, to give the equation [51]

$$\kappa_1^* = 924 \frac{B^*_{c2}}{\gamma^{1/2} T_c^*\,(1 - t^2)}. \tag{4.11}$$

Eqn 4.10 implies that the gradient of a $\log F_{\mathrm{p,max}} \left[\kappa_1^*\right]^m$ versus $\log B_{\mathrm{c2}}^*$ gives the value of the exponent n. Computational, experimental and analytic work led to setting m equal to 2 [53, 173, 259, 262] although different values of the exponent m have also been found useful for more limited datasets [74, 169–172]. For many Nb_3Sn [173, 178] and Nb_3Al [51] wires, F_{p} is given by eqn 4.10, with $n = 5/2$, $m = 2$, $p = 1/2$, $q = 2$ and A is a dimensionless constant $\sim 1/250$ for Nb_3Sn and $\sim 1/100$ for Nb_3Al. This has led to an engineering scaling law that has been successfully used to accurately parameterise the field, temperature and strain dependencies of many low temperature superconducting wires [173, 174, 177–179]

$$J_{\mathrm{c}}\left(B, T, \varepsilon_{\mathrm{app}}\right) = A^*\left(\varepsilon_{\mathrm{app}}\right)\left[T_{\mathrm{c}}^*\left(\varepsilon_{\mathrm{app}}\right)\left(1-t^2\right)\right]^2 \left[B_{\mathrm{c2}}^*\left(T, \varepsilon_{\mathrm{app}}\right)\right]^{n-3} b^{p-1}\left(1-b\right)^q, \quad (4.12)$$

where $A^*\left(\varepsilon_{\mathrm{app}}\right)$ can be taken as a strain dependent parameter to improve agreement with experimental results. $T_{\mathrm{c}}^*\left(\varepsilon_{\mathrm{app}}\right)$, $B_{\mathrm{c2}}^*\left(0, \varepsilon_{\mathrm{app}}\right)$ and $A^*\left(\varepsilon_{\mathrm{app}}\right)$ are related by the power laws,

$$\frac{T_{\mathrm{c}}^*\left(\varepsilon_{\mathrm{app}}\right)}{T_{\mathrm{c}}^*\left(0\right)} = \left(\frac{B_{\mathrm{c2}}^*\left(0, \varepsilon_{\mathrm{app}}\right)}{B_{\mathrm{c2}}^*\left(0,0\right)}\right)^{\frac{1}{w}} = \left(\frac{A^*\left(\varepsilon_{\mathrm{app}}\right)}{A^*\left(0\right)}\right)^{\frac{1}{u}}, \quad (4.13)$$

where w and u are constants, and $T_{\mathrm{c}}^*\left(\varepsilon_{\mathrm{app}}\right)/T_{\mathrm{c}}^*\left(0\right)$ is given by the fourth order polynomial in eqn 4.6. There are in principle 13 free parameters in this parameterisation: $T_{\mathrm{c}}^*\left(0\right)$, $B_{\mathrm{c2}}^*\left(0,0\right)$, $A^*\left(0\right)$, s, w, u, n, p, q, c_1, c_2, c_3 and c_4. Following the work in [178,179] w and u were fixed at $w = 2.2$ and $u = 0$. It is noted that small data sets can be parameterised, with some limited loss of accuracy, using just six free parameters [177].

Accurate engineering parameterisations across field, temperature and strain are extremely important for technological applications of superconductors, for example in the large high field magnets such as those used in magnetic confinement fusion that undergo enormous stresses. Although it is shown in this chapter that the REBCO tape is bimodal so the standard (homogeneous) scaling law, eqn 4.10, is not physically justifiable, nevertheless, a useful engineering parameterisation can be provided by applying eqn 4.12 to the critical current data. This provides useful parameterisations for magnet design engineers using HTS and LTS materials.

The importance of using the correct weighting procedures when applying fitting procedures to critical current data is noted. Here each fit to the data minimises Chi-squared with Poisson statistics [263]. This approach ensures the fitting parameters remain independent of whether J_c or F_p data are fitted.

For the REBCO tape, a reasonably accurate parameterisation useful for engineering applications, without using the resistively measured values of B^*_{c2}, was found after splitting the data into two temperature regimes: a) $T \leq 60\,\mathrm{K}$ and b) $T \geq 68\,\mathrm{K}$ where eqn 4.5 gives the functional form of B^*_{c2}. The free parameters obtained for the $100\,\mu\mathrm{V\,m^{-1}}$ criterion are given in table 4.2 and shown graphically in figure 4.4a. In the low temperature region the engineering scaling law parameterisations includes unphysical constants as has been reported previously [264]. For the LTS materials, the constants found for the parameterisation were obtained without applying shunt

corrections and the functional form of B^*_{c2} was taken to be

$$B^*_{c2}(T, \varepsilon_{app}) = B^*_{c2}(0, \varepsilon_{app}) \left(1 - \left(\frac{T}{T^*_c(\varepsilon_{app})}\right)^{\nu}\right), \tag{4.14}$$

where ν is a free parameter. The free parameters obtained are also listed in table 4.2 and are shown graphically for the bronze route wire in figure 4.14. Also shown in figure 4.14 is a similar parameterisation with parameters taken from a F4E report [258] where the fit was performed over a smaller data range to improve its accuracy in the region of interest for that report, resulting in a reduction of the RMS error from 4.8 A to 2.5 A.

4.5 Flux pinning scaling

The strategy for a detailed analysis of flux pinning behaviour first requires consideration of eqn 4.8. Using the resistively measured values of B^*_{c2}, it is first determined which combinations of B^*_{c2} and E-field criteria give temperature and strain independent values of p and q and hence show universal scaling behaviour. The universal scaling curve is then extended to lower temperatures where direct measurements of B^*_{c2} are not available. It is then determined how $F_{p,max}$ scales with B^*_{c2} via a $\log F_{p,max}\left[\kappa^*_1\right]^m - \log B^*_{c2}$ plot. This approach makes no *a priori* assumptions about the relationship between $F_{p,max}$ and B^*_{c2} [51].

Table 4.2. Parameters for the engineering parameterisation, eqn 4.12, for all samples investigated. The parameters in bold were taken to be fixed [178].

Parameter	REBCO		Bronze route	Internal tin	Jelly roll
	$T \leq 60\,\mathrm{K}$	$T \geq 68\,\mathrm{K}$	Nb_3Sn	Nb_3Sn	Nb_3Al
$A\,(0)$ ($\mathrm{MA\,m^{-2}\,K^{-2}\,T^{3-n}}$)	0.0625	6.55	45.8	113	66.3
$T_c^*\,(0)$ (K)	185.0	90.1	16.5	16.6	15.6
$B_{c2}^*\,(0,0)$ (T)	139.0	98.7	30.7	33.3	26.9
c_1 ($\%^{-1}$)	0.00224	0.00139	0.107	0.0671	0.0156
c_2 ($\%^{-2}$)	-0.0198	-0.0294	-0.0972	-0.316	-0.0515
c_3 ($\%^{-3}$)	0.00391	0.0104	-0.0806	-0.300	-0.00302
c_4 ($\%^{-4}$)	0.00103	0.00520	-0.0291	-0.126	0.00664
w	**2.2**	**2.2**	**2.2**	**2.2**	**2.2**
u	**0**	**0**	**0**	**0**	**0**
s	5.27	1.26			
ν			1.28	1.35	1.30
n	3.33	2.66	2.44	2.40	2.65
p	0.451	0.581	0.526	0.926	0.702
q	1.44	2.86	1.74	2.82	2.78
r_N	5.59		1.44	1.78	0.775
S_N	0.44		0.50	0.36	0.621
RMS Error of J_c fit in $\mathrm{MA\,m^{-2}}$ (or equivalently I_c in A, I_c Error in brackets)	600 (2.4)	50 (0.20)	23 (4.8)	11 (2.3)	4.9 (1.0)

4.5.1 REBCO tape: Flux pinning scaling of $\boldsymbol{J_c}(\boldsymbol{B}, \boldsymbol{T}, \boldsymbol{\varepsilon_{app}})$ at $\boldsymbol{T \geq 60\,K}$

The parameters p, q and B^*_{c2} are quite strongly correlated so a wide range of parameter combinations give acceptable agreement with the data [51]. Resistively measured values of the effective upper critical field are used to minimise the effect of this correlation in the temperature region where such measurements are available ($T \geq 60\,\mathrm{K}$). Figure 4.18 shows flux pinning curves for the REBCO tape at $T = 68\,\mathrm{K}$ and $\varepsilon_{app} = 0\,\%$ at the $100\,\mu\mathrm{V\,m^{-1}}$ criterion for each of the three B^*_{c2} criteria considered in this study. First inspection suggests the extrapolated $100\,\%$ criterion is the most appropriate as the other criteria give non-zero values of J_c at B^*_{c2}. However, this simple interpretation does not account for distributions in the critical parameters, or the percolative path and current shunting at low values of critical current.

Below it is investigated which combination(s) of E-field and B^*_{c2} criteria show consistent scaling of the flux pinning curve: eqn 4.8 is fitted to the data in the region where direct measurements of the resistive upper critical field are available ($T = 60, 68$ and $76\,\mathrm{K}$), $B^{*\rho}_{c2}(T, \varepsilon_{app})$ is used to calculate the reduced field b and $F_{p,max}$ is an unconstrained temperature and strain dependent free parameter. The data were fitted using all combinations of E-field and $B^{*\rho}_{c2}$ criteria. Four different fitting procedures are used to investigate fully the temperature and strain scaling of the parameters p and q: in procedure 1 p and q are unconstrained temperature and strain dependent free parameters, in 2, p and q are free parameters constrained to

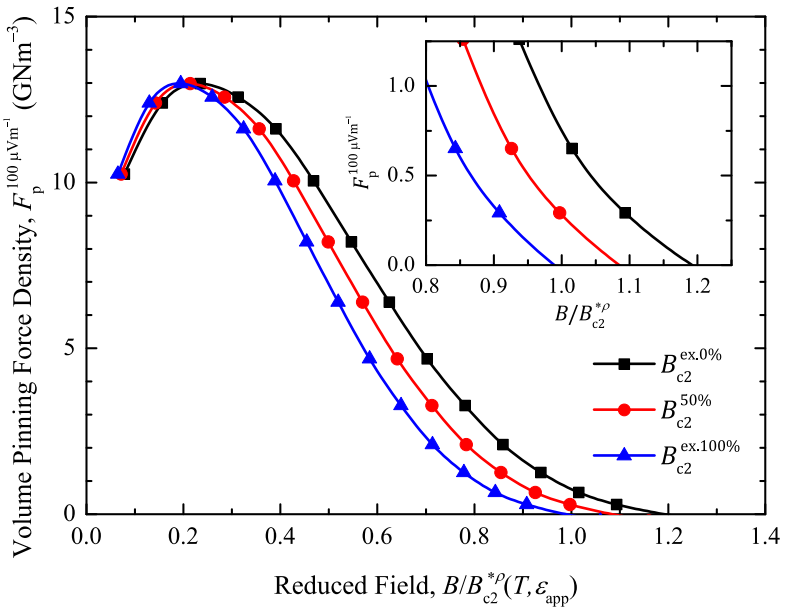

Figure 4.18. Volume pinning force versus reduced field for the REBCO tape at $T = 68\,\mathrm{K}$, $\varepsilon_{app} = 0\,\%$ with an E-field criterion of $100\,\mu\mathrm{V\,m^{-1}}$ for the three $B_{c2}^{*\rho}$ criteria. Solid lines are guides for the eye. B_{c2}^{*} values are $\approx 14\,\mathrm{T}$.

be independent of strain but unconstrained in temperature, in 3, p is a global free parameter independent of both temperature and strain and q is a free parameter constrained to be independent of strain but unconstrained in temperature, in 4, both p and q are global free parameters independent of temperature and strain. The results of fitting procedures 2 - 4 are summarised in table 4.3 for all combinations of criteria and results of all fitting procedures are presented graphically in figure 4.19 for a limited selection of criteria combinations.

The results of using fitting procedure 1 provide the data points in figure 4.19, which are temperature and strain dependent, are similar to the results obtained using fitting procedure 2 (solid lines in figure 4.19), which are temperature dependent only for all combinations of criteria. This shows there is no strain dependence to p and q.

Table 4.3. Results of fitting the $J_c\,(B, T, \varepsilon_{app})$ data at $T = 60, 68, 76\,\mathrm{K}$ for REBCO tape to eqn 4.8 for all combinations of E-field and $B^{*\rho}_{c2}$ criteria. Data are shown for fitting procedures 2 - 4: 2) p and q are free parameters constrained to be independent of strain but unconstrained in temperature, 3) p is a global free parameter independent of both temperature and strain and q is a free parameter constrained to be independent of strain but unconstrained in temperature, 4) both p and q are global free parameters independent of temperature and strain.

Fitting procedure	T (K)	$B^{ex.0\%}_{c2}$				$B^{50\%}_{c2}$				$B^{ex.100\%}_{c2}$			
		$10\,\mu\mathrm{V\,m^{-1}}$		$100\,\mu\mathrm{V\,m^{-1}}$		$10\,\mu\mathrm{V\,m^{-1}}$		$100\,\mu\mathrm{V\,m^{-1}}$		$10\,\mu\mathrm{V\,m^{-1}}$		$100\,\mu\mathrm{V\,m^{-1}}$	
		p	q	p	q	p	q	p	q	p	q	p	q
2	60	0.52	2.09	0.51	1.78	0.59	2.56	0.57	2.19	0.64	3.06	0.62	2.63
	68	0.37	1.64	0.36	1.35	0.45	2.16	0.44	1.83	0.57	2.89	0.54	2.42
	76	0.11	1.17	0.11	0.91	0.24	1.74	0.20	1.34	0.47	2.71	0.36	2.04
3	60	↑	1.93	↑	1.62	↑	2.38	↑	2.03	↑	2.95	↑	2.50
	68	0.43	1.74	0.42	1.44	0.50	2.24	0.49	1.90	0.60	2.94	0.55	2.47
	76	↓	1.56	↓	1.25	↓	2.10	↓	1.73	↓	2.93	↓	2.37
4	All T	0.42	1.82	0.40	1.50	0.48	2.28	0.47	1.93	0.59	2.94	0.56	2.47

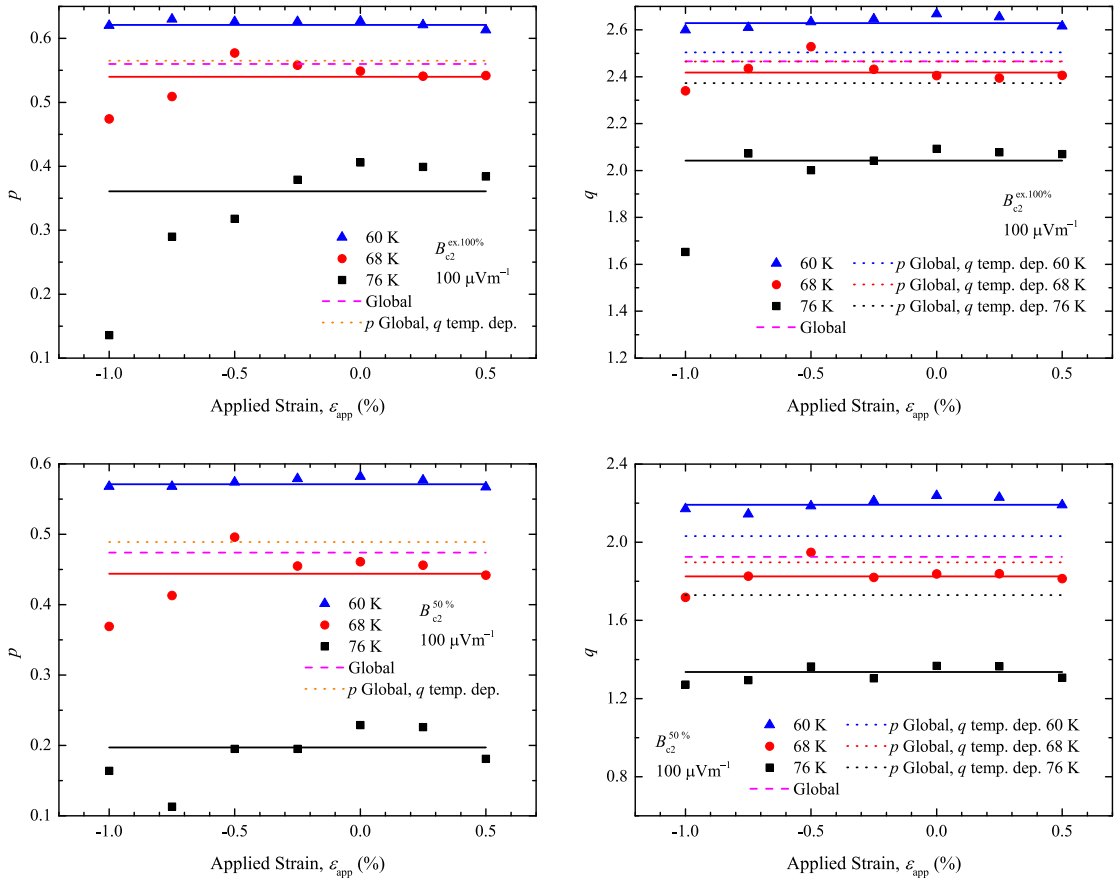

Figure 4.19. The values of p and q obtained from the fitting of volume pinning force curves for the REBCO tape at $T = 60, 68, 76\,\mathrm{K}$ at the $100\,\mu\mathrm{V\,m^{-1}}$ E-field criterion. $B_{c2}^{*\rho}(T, \varepsilon_{app})$. The upper pair of panels were calculated at the extrapolated 100 % criterion to determine B_{c2}^{*}, whereas the lower panels were calculated using the 50 % criterion. Points show the results of fitting proceedure 1) where p and q are unconstrained temperature and strain dependent free parameters. Solid lines show the results of fitting proceedure 2) where p and q are free parameters constrained to be independent of strain but unconstrained in temperature. Short dashed lines show the results of fitting proceedure 3) where p is a global free parameter independent of both temperature and strain and q is a free parameter constrained to be independent of strain but unconstrained in temperature. Long dashed lines show the results of fitting proceedure 4) where both p and q are global free parameters independent of temperature and strain.

Procedure 2 shows a relatively strong temperature dependence and can be compared to procedure 3 (dotted lines in figure 4.19) which makes p a global free parameter independent of temperature and strain. Procedure 3 has a significant reduction in the temperature dependence for q, which can be associated with uncertainties in the determination of p because of limited data at low reduced field and the strong correlation between p and q. The results of fitting procedure 3 at all temperatures are within the uncertainties of fitting procedure 4 (dashed lines in figure 4.19), where both p and q are global free parameters independent of temperature and strain, for the $B_{c2}^{ex.100\%}$ criterion at both E-field criteria. It is concluded that the $B_{c2}^{ex.100\%}$ criterion gives consistent, temperature and strain independent universal scaling in the high temperature region for both E-field criteria. Hereafter only values at the $B_{c2}^{ex.100\%}$ and $100\,\mu V\,m^{-1}$ criteria are reported.

4.5.2 REBCO tape: Extending the flux pinning scaling to $T = 4.2, 20$ and $40\,K$

Direct measurements of $B_{c2}^{ex.100\%}$ were not possible at low temperatures ($T = 4.2, 20, 40\,K$) because the magnet system is limited to 15 T. In addition, extrapolating the B_{c2}^{*} parameterisation (cf. eqn 4.5) is found to not provide reliable values. Hence, at low temperatures the effective upper critical field, $B_{c2}^{*Low\,T}$ and $F_{p,max}$ were determined by fitting eqn 4.8 to the J_c data with p and q fixed at the values obtained for $T \geq 60\,K$ ($p = 0.56$ and $q = 2.47$). $F_{p,max}$ was taken to be an unconstrained temperature and strain dependent free parameter, and $B_{c2}^{*Low\,T}$ was characterised as a temperature and

Table 4.4. Results of determining $B_{c2}^{*\mathrm{Low}\,T}$ at $T = 4.2, 20, 40\,\mathrm{K}$ for REBCO tape at the $100\,\mu\mathrm{V\,m^{-1}}$ E-field criterion. The flux pinning curve, eqn 4.8, is fitted to the J_c data with $p = 0.56$ and $q = 2.47$ (the values obtained from the flux pinning analysis at $T = 60, 68, 76\,\mathrm{K}$). $B_{c2}^{*\mathrm{Low}\,T}$ is a temperature and strain dependent free parameter, unconstrained in temperature and constrained in strain by a second order polynomial given by eqn 4.7 where $d_3 = d_4 = 0$.

T (K)	$B_{c2}^{*\mathrm{Low}\,T}(0)$ (T)	d_1 ($10^{-3}\,\%^{-1}$)	d_2 ($10^{-3}\,\%^{-2}$)
4.2	131	22	-5
20	79	31	-48
40	46.5	31	-80

strain dependent free parameter, unconstrained in temperature and constrained in strain by a second order polynomial given by eqn 4.7 where the normalisation constant is denoted by $B_{c2}^{*\mathrm{Low}\,T}(\varepsilon_{\mathrm{app}} = 0\,\%)$ and $d_3 = d_4 = 0$. The high values of $B_{c2}^{*\mathrm{Low}\,T}$ mean only the initial part of the F_p curve is available at these temperatures, the high gradient of the curve in this region leads to solutions with unphysical results where the location of $F_{p,\mathrm{max}}$ is clearly incorrect. To account for this in a consistent manner, the fitting procedure was weighted by F_pB so the data near $F_{p,\mathrm{max}}$ are preferentially weighted resulting in physically reasonable results.

The free parameters describing $B_{c2}^{*\mathrm{Low}\,T}$ obtained from this analysis are summarised in table 4.4 and are included alongside the direct measurements of B_{c2}^{*} at high temperatures in the inset of figure 4.11. The $B_{c2}^{*\mathrm{Low}\,T}$ values are considerably higher than suggested by the parameterisation at high temperature (cf. eqn 4.5) and have a lower strain dependence. Figure 4.20 shows the universal scaling of the flux pinning curves at all temperatures and strains.

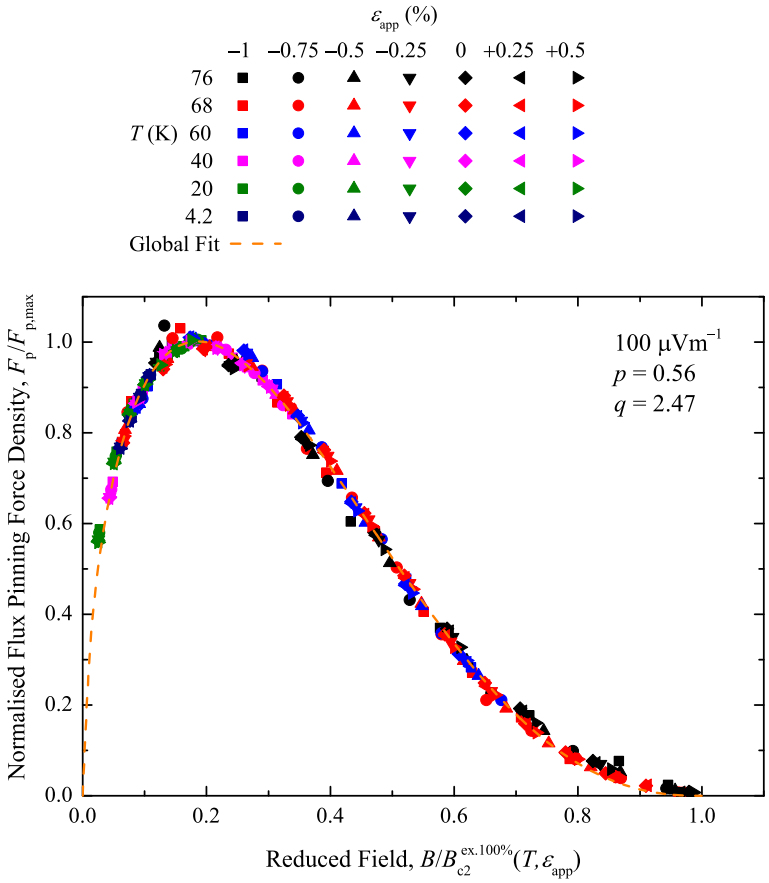

Figure 4.20. Universal scaling of F_p at all temperatures and strains using the $B_{c2}^{ex.100\%}$ and $100\,\mu V\,m^{-1}$ criteria. The global fit was determined by the method outlined in section 4.5.

4.5.3 REBCO tape: Temperature and strain scaling of $F_{p,max}$ with B^*_{c2}

In sections 4.5.1 and 4.5.2, B^*_{c2} and $F_{p,max}$ were determined from the universal scaling of the flux pinning curve. B^*_{c2} was characterised using eqn 4.5 for the $B^{ex.100\%}_{c2}$ criterion at $T = 60, 68, 76\,\mathrm{K}$, and eqns 4.7 and 4.8 at $T = 4.2, 20, 40\,\mathrm{K}$, $F_{p,max}$ was an unconstrained temperature and strain dependent free parameter. Figure 4.21 shows $F_{p,max}$ as a function of B^*_{c2} on a log-log scale. The parameter n (cf. eqn 4.10) extracted from this graph is a function of temperature. At all temperatures $F_{p,max}$ shows double valued behaviour as a function of B^*_{c2}, where the compressive data has higher values of $F_{p,max}$ than the tensile data at all temperatures. It was investigated whether including the temperature and strain dependence of κ_1^* as given by eqn 4.11 produces a single universal value for the exponent n. Figure 4.22 shows $F_{p,max}\left[\kappa_1^*\right]^m$ against B^*_{c2} on a log-log scale. Although the range of n values was significantly reduced for a value of $m = 2$, n are still found to be a function of temperature and double valued behaviour of $F_{p,max}$ as a function of B^*_{c2} are still present. Other values of m were investigated and strain dependent values of γ (or equivalently A) were considered [51, 74, 169–172, 177–179] but none were found to be significantly better than $m = 2$ with a strain independent γ.

By performing the scaling with no *a priori* assumptions made about the dependence of $F_{p,max}$ on B^*_{c2}, the identification of the double valued behaviour of $F_{p,max}\left[\kappa_1^*\right]^2$ versus B^*_{c2} and a temperature dependence for the exponent n is made possible. These features cannot be identified from using the engineering parameterisation (cf. table 4.2) because

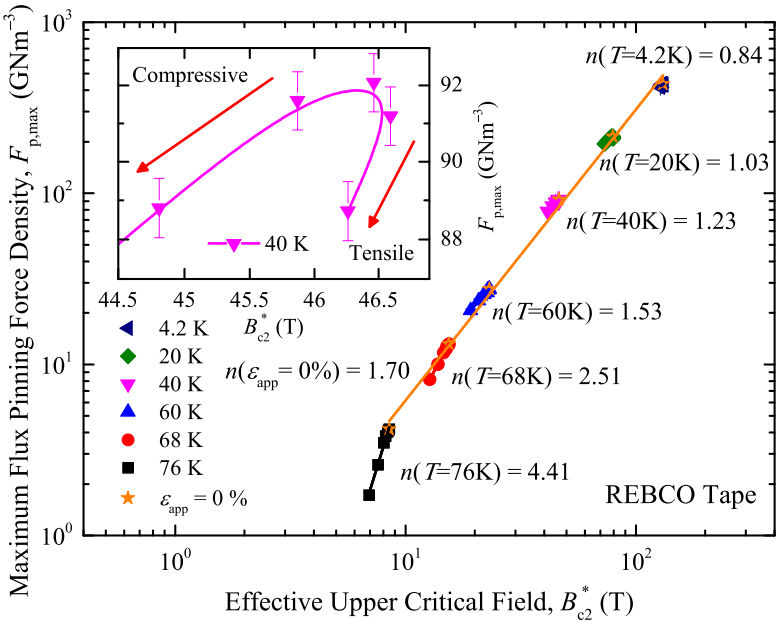

Figure 4.21. Maximum flux pinning force density against the effective upper critical field on a log-log scale for the REBCO tape at the 100 µV m^{-1} E-field criterion and extrapolated 100 % B^*_{c2} criterion. B^*_{c2} is determined using eqn 4.5 at $T = 60, 68, 76$ K, and eqns 4.7 and 4.8 at $T = 4.2, 20, 40$ K, as detailed in sections 4.5.1 and 4.5.1. The solid lines are linear fits at each temperature, the dashed line is a linear fit at $\varepsilon_{app} = 0$ % (the associated exponents n are also shown). (inset) Detail of data at 40 K showing double valued behaviour of $F_{p,max}$. The solid line is a guide for the eye.

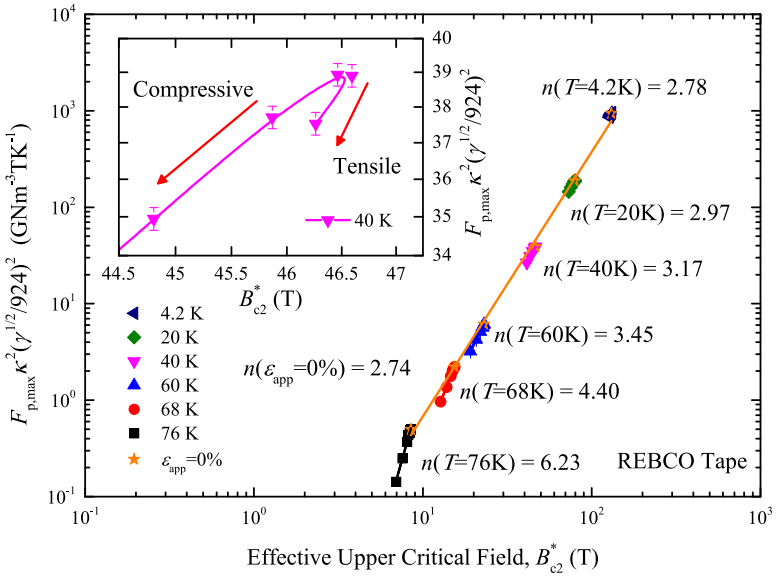

Figure 4.22. Maximum flux pinning force density multiplied by the square of the Ginzburg–Landau parameter κ_1^* against the effective upper critical field on a log-log scale for the REBCO tape at the 100 µV m^{-1} E-field criterion and extrapolated 100 % B_{c2}^* criterion. B_{c2}^* is determined using eqn 4.5 at $T = 60, 68, 76$ K, and eqns 4.7 and 4.8 at $T = 4.2, 20, 40$ K, as detailed in sections 4.5.1 and 4.5.2. The solid lines are linear fits at each temperature, the dashed line is a linear fit at $\varepsilon_{app} = 0$ % (the associated exponents n are also shown). (inset) Detail of the data at 40 K showing double valued behaviour of $F_{p,max}$. The solid line is a guide to the eye.

it assumes $F_{\mathrm{p,max}}$ is a single-valued function B^*_{c2} and n is temperature independent. It is also noted that the engineering parameterisation assumes that $\varepsilon_{\mathrm{peak}}$ is independent of magnetic field and temperature in contradiction with the experimental data in figure 4.7.

4.5.4 Bronze route Nb_3Sn: Flux pinning scaling of $J_c(B, T, \varepsilon_{app})$

The comprehensive $J_c(B, T, \varepsilon_{app})$ data obtained for the bronze route Nb_3Sn wire were analysed in a similar manner using eqn 4.8 where p and q were global free parameters independent of temperature and strain, $F_{\mathrm{p,max}}$ was an unconstrained temperature and strain dependent free parameter. $B^*_{c2}(T, \varepsilon_{app})$ was parameterised using eqn 4.14 where ν is a free parameter and, $T_c(\varepsilon_{app})$ and $B^*_{c2}(0, \varepsilon_{app})$ are fourth order functions of strain given by eqns 4.6 and 4.7 respectively. The free parameters are provided in table 4.5. Again, no *a priori* assumptions are made about the dependence of $F_{\mathrm{p,max}}$ on B^*_{c2}. Universal behaviour was found for $F_p(b)$ confirming temperature and strain scaling and providing global values for p and q. In figure 4.23 $F_{\mathrm{p,max}}[\kappa^*_1]^2$ is plotted as function of B^*_{c2} on a log-log scale. As with the REBCO tape it is found that including the $[\kappa^*_1]^2$ factor improves the agreement between the variable temperature and the variable strain scaling of n [169, 259]. However, there is not a single exponent for n that fits all the data. It is also found that $F_{\mathrm{p,max}}[\kappa^*_1]^2$ is a double valued function of B^*_{c2}, where the tensile $F_{\mathrm{p,max}}$ data are consistently higher than the compressive data at all temperatures.

Table 4.5. Results of the detailed flux pinning analysis, eqn 4.8 for the Nb_3Sn and Nb_3Al wires, where p and q are global free parameters independent of temperature and strain, $F_{p,max}$ is an unconstrained temperature and strain dependent free parameter, B^*_{c2} is given by eqn 4.14, and $T^*_c(\varepsilon_{app})$ and $B^*_{c2}(0, \varepsilon_{app})$ are fourth order polynomials given by eqns 4.6 and 4.7 respectively.

Bronze route Nb_3Sn	p	0.611	q	1.99
	ν	1.26		
	$T^*_c(0)$ (K)	16.3	$B^*_{c2}(0,0)$ (T)	32.8
	c_1 ($\%^{-1}$)	0.0928	d_1 ($\%^{-1}$)	0.238
	c_2 ($\%^{-2}$)	-0.0565	d_2 ($\%^{-2}$)	-0.250
	c_3 ($\%^{-3}$)	-0.125	d_3 ($\%^{-3}$)	-0.138
	c_4 ($\%^{-4}$)	-0.0722	d_4 ($\%^{-4}$)	0.00846
Internal tin Nb_3Sn	p	0.870	q	2.67
	ν	1.34		
	$T^*_c(0)$ (K)	16.8	$B^*_{c2}(0,0)$ (T)	32.5
	c_1 ($\%^{-1}$)	0.0925	d_1 ($\%^{-1}$)	0.135
	c_2 ($\%^{-2}$)	-0.261	d_2 ($\%^{-2}$)	-0.689
	c_3 ($\%^{-3}$)	-0.448	d_3 ($\%^{-3}$)	-0.520
	c_4 ($\%^{-4}$)	-0.287	d_4 ($\%^{-4}$)	-0.0807
Jelly roll Nb_3Al	p	0.668	q	2.51
	ν	1.37		
	$T^*_c(0)$ (K)	15.5	$B^*_{c2}(0,0)$ (T)	25.6
	c_1 ($\%^{-1}$)	0.0146	d_1 ($\%^{-1}$)	0.0405
	c_2 ($\%^{-2}$)	-0.0488	d_2 ($\%^{-2}$)	-0.119
	c_3 ($\%^{-3}$)	-0.00257	d_3 ($\%^{-3}$)	-0.0143
	c_4 ($\%^{-4}$)	-0.00430	d_4 ($\%^{-4}$)	0.0446

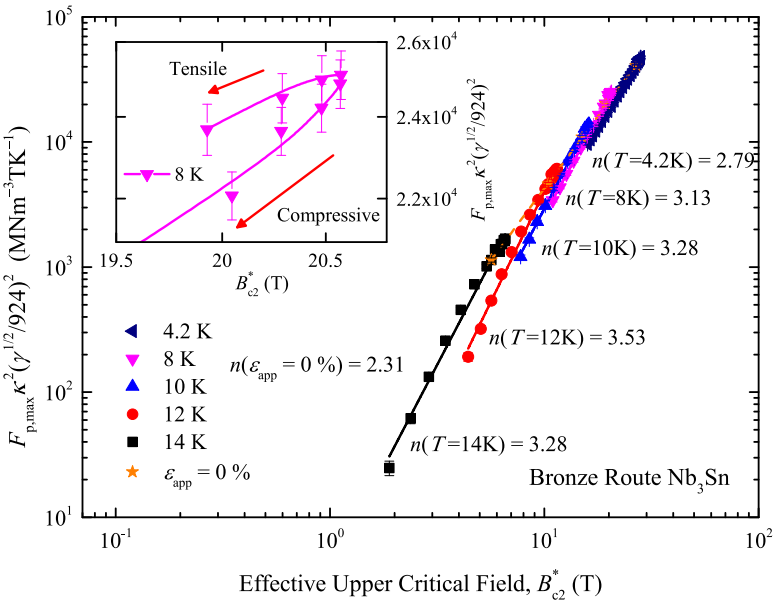

Figure 4.23. Maximum flux pinning force density multiplied by the square of the Ginzburg–Landau parameter κ_1^* against the effective upper critical field on a log-log scale for the bronze route Nb_3Sn wire. The solid lines are linear fits at each temperature, the dashed line is a linear fit at $\varepsilon_{app} = 0\,\%$ (the associated exponents n are also shown). (inset) Detail of the data at 8 K showing double valued behaviour. The solid line is a guide to the eye.

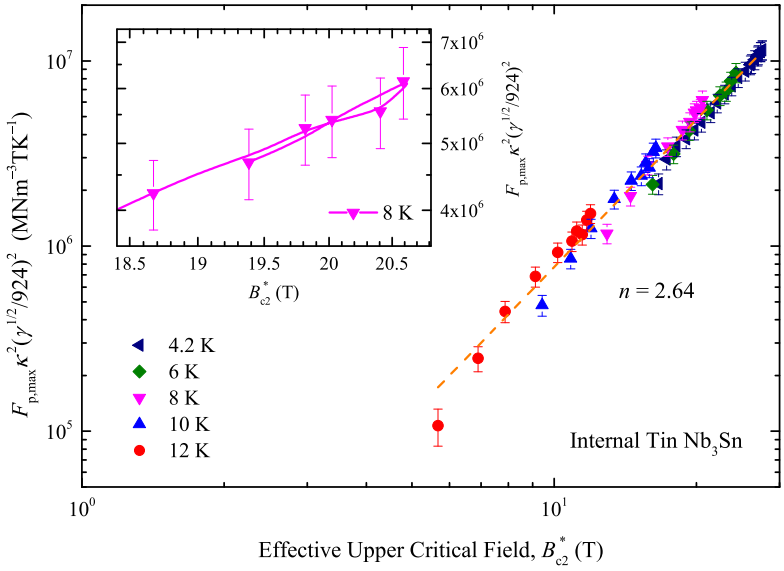

Figure 4.24. Maximum flux pinning force density multiplied by the square of the Ginzburg–Landau parameter κ_1^* against the effective upper critical field on a log-log scale for the internal tin Nb_3Sn wire. The dashed line is a linear fit at all temperatures and strains (the associated exponent n is also shown). (inset) Detail of the data at 8 K. The solid line is a guide to the eye.

4.5.5 Internal tin Nb_3Sn and jelly roll Nb_3Al: Flux pinning scaling of $J_c(B, T, \varepsilon_{app})$

In figures 4.24 and 4.25 the results of the same analysis for internal tin Nb_3Sn and jelly roll Nb_3Al respectively are shown. In contrast to the REBCO tape and the bronze route Nb_3Sn wire, a single temperature and strain independent value of the exponent n is found to describe the data reasonably well for both materials when the $[\kappa_1^*]^2$ factor is included in the scaling law, and $F_{p,max}[\kappa_1^*]^2$ is a weakly double valued or single valued function of B_{c2}^* to within the experimental uncertainties.

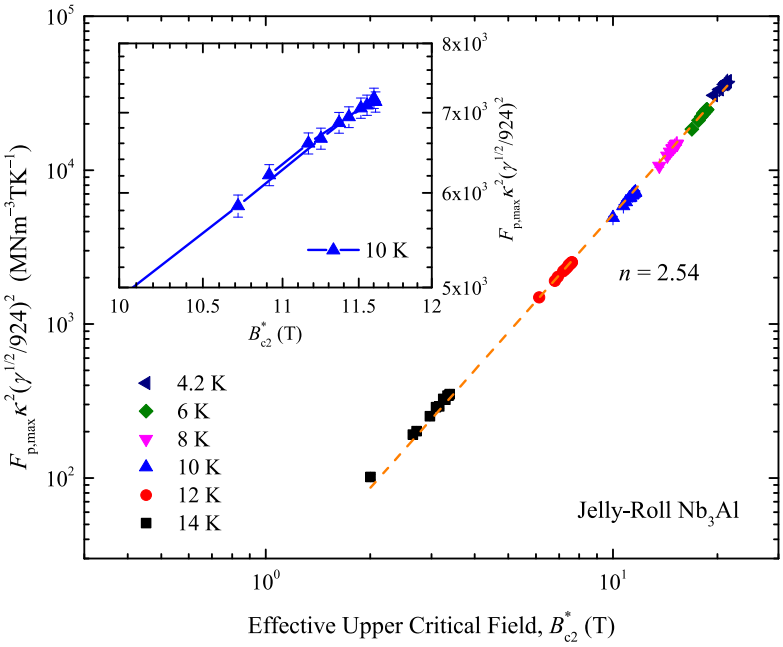

Figure 4.25. Maximum flux pinning force density multiplied by the square of the Ginzburg–Landau parameter κ_1^* against the effective upper critical field on a log-log scale for Nb_3Al wire. The dashed line is a linear fit at all temperatures and strains (the associated exponents n is also shown). (inset) Detail of the data at 10 K. The solid line is a guide to the eye.

4.6 The bimodal chain model for REBCO

To date, when flux pinning scaling laws are used in the literature to describe LTS materials, it is assumed the material is close to homogenous so all the grains respond in broadly the same manner and the critical parameters, T_c^*, B_{c2}^* and J_c have a similar response to uniaxial strain. More specifically, it is generally assumed that the peak of all these critical parameters occur when the intrinsic strain on the superconducting component itself is close to zero. This has led the community to anchor J_c versus strain data at this strain ε_{peak}, by defining a characteristic strain called the intrinsic strain $\varepsilon_{int} = \varepsilon_{app} - \varepsilon_{peak}$ where ε_{peak} is the applied strain at which $J_c(\varepsilon_{app})$ is maximised or equivalently, ε_{int} is zero at the peak. The values of ε_{peak} found experimentally then have their origin in the differential thermal contraction of the matrix materials and sample holder exerting a prestrain on the superconducting component of the conductor and are independent of temperature and field [181, 183].

In section 3.5 it was shown that such a description of the effects of strain is incompatible with REBCO tapes when single crystal measurements and the microstructure are considered. A simple bimodal model for the uniaxial strain dependence of REBCO tapes in zero field was also reviewed [199]. A key consequence of this model is that ε_{peak} cannot be assumed to occur at $\varepsilon_{int} = 0\,\%$ or to be independent of field and temperature. As such, to avoid any confusion with the well-established definition of ε_{int} two new characteristic strains were introduced: the domain stain $\varepsilon_{JD} = \varepsilon_{app} - \varepsilon_{J_{cA}=J_{cB}}$ where $\varepsilon_{J_{cA}=J_{cB}}$ is the applied strain at which the critical current in both domains are equal, and the peak domain strain $\varepsilon_{p,JD} = \varepsilon_{peak} - \varepsilon_{J_{cA}=J_{cB}}$ which is the domain strain at

which J_c is maximised. In the next section the bimodal model is extended to include the field and temperature dependencies.

4.6.1 Bimodal chain model for twinned domains in high magnetic fields

The parameter α_{J_c} is introduced which accounts for different strain sensitivity in the A- and B- domains and is defined by

$$\alpha_{J_c} = \left|\frac{\mathrm{d}J_{\mathrm{cB}}}{\mathrm{d}\varepsilon_{\mathrm{JD}}}\right|_{\varepsilon_{\mathrm{JD}}=0\%} \Bigg/ \left|\frac{\mathrm{d}J_{\mathrm{cA}}}{\mathrm{d}\varepsilon_{\mathrm{JD}}}\right|_{\varepsilon_{\mathrm{JD}}=0\%} = \frac{g_{\mathrm{B}}}{g_{\mathrm{A}}}, \tag{4.15}$$

where an equivalent definition for α_{T_c} in terms of the derivatives of T^*_{cA} and T^*_{cB} can also be written down. By setting the condition $E = E_c$ in eqn 3.7, it is found,

$$1 = f\left(\frac{J_{\mathrm{cT}}}{J_{\mathrm{cA}}}\right)^{N_{\mathrm{A}}} + (1-f)\left(\frac{J_{\mathrm{cT}}}{J_{\mathrm{cB}}}\right)^{N_{\mathrm{B}}}, \tag{4.16}$$

where N_{A} and N_{B} are functions of J_{cA} and J_{cB} respectively defined through eqn 4.4. The transcendental nature of J_{cT} in eqn 4.16 rules out simple analytic solutions. Nevertheless, to develop insight into the field and temperature dependence of $\varepsilon_{\mathrm{peak}}$, an approximate analytic expression for $\varepsilon_{\mathrm{p,JD}}$ is derived. Using a second order Taylor expansion for J_{cT} about $\varepsilon_{\mathrm{JD}} = 0\,\%$, and comparing the coefficients to eqn 4.3, an analytic expression is found for the peak domain strain $\varepsilon_{\mathrm{p,JD}}$ as a function of f, α_{J_c}

and g_{A}, given by

$$\varepsilon_{\mathrm{peak}} - \varepsilon_{J_{\mathrm{cA}}=J_{\mathrm{cB}}} = -\left(\frac{\mathrm{d}J_{\mathrm{cT}}}{\mathrm{d}\varepsilon_{\mathrm{JD}}}\right)_{\varepsilon_{\mathrm{JD}}=0\%} \Bigg/ \left(\frac{\mathrm{d}^2 J_{\mathrm{cT}}}{\mathrm{d}\varepsilon_{\mathrm{JD}}^2}\right)_{\varepsilon_{\mathrm{JD}}=0\%} = \frac{f - \alpha_{J_{\mathrm{c}}}/\left(1+\alpha_{J_{\mathrm{c}}}\right)}{f\left(1-f\right)\left(1+\alpha_{J_{\mathrm{c}}}\right)} \frac{F\left(N_0, S_N\right)}{g_{\mathrm{A}}\left(B,T\right)}, \quad (4.17)$$

where the parameter $F\left(N_0, S_N\right) = N_0/\left(N_0\left(N_0+1\right) - 2S_N\left(N_0-1\right)\right)$, N_0 is the index of transition at $\varepsilon_{\mathrm{JD}} = 0\,\%$, S_N is defined in eqn 4.4 and g_{A} contains the temperature and field dependencies. It is noted that in the limit where $\alpha_{J_{\mathrm{c}}} = 1$ and $N_0\left(N_0+1\right) \gg 2S_N\left(N_0-1\right)$ (cf. typical values for S_N and N_0 are 0.4 and 10 respectively), $F\left(N_0\right) \approx 1/\left(N_0+1\right)$ and eqn 4.17 reduces to eqn 3.9.

Eqn 4.17 requires an explicit evaluation of g_{A} which is calculated as follows: $J_{\mathrm{c}i}$ in each domain is assumed to follow the scaling law given by eqn 4.10 and is approximated to be linear in the region of $\varepsilon_{\mathrm{JD}} = 0\,\%$, as with the derivation of eqn 3.9. Taking the derivative of eqn 4.10 and comparing the result to eqn 3.6, g_i is found to be given by

$$g_i = \left|\frac{\mathrm{d}T_{\mathrm{c}i}^*}{\mathrm{d}\varepsilon_{\mathrm{JD}}}\right|_{\varepsilon_{\mathrm{JD}}=0\%} \left[\frac{2}{T_{\mathrm{c}}\left(0\right)} \frac{1+t^2\left(0\right)}{1-t^2\left(0\right)}\right] + \left[B_{\mathrm{c}2}^{*\,-1}\left(T,0\right) \frac{\mathrm{d}}{\mathrm{d}\varepsilon_{\mathrm{JD}}}\left(B_{\mathrm{c}2}^*\left(T,\varepsilon_{\mathrm{JD}}\right)\right)\Big|_{\varepsilon_{\mathrm{JD}}=0\%} \left(\frac{qb\left(0\right)}{1-b\left(0\right)} + n - p - m\right)\right], \quad (4.18)$$

where $t\left(\varepsilon_{\mathrm{JD}} = 0\,\%\right) = T/T_{\mathrm{c}}^*\left(0\right)$ and $b\left(\varepsilon_{\mathrm{JD}} = 0\,\%\right) = B/B_{\mathrm{c}2}^*\left(T,0\right)$ are the reduced temperature and field at $\varepsilon_{\mathrm{JD}} = 0\,\%$ respectively. If the HTS parameterisation of $B_{\mathrm{c}2i}^*\left(T,\varepsilon_{\mathrm{JD}}\right)$

(cf. eqn 4.5) is taken, the following expression is obtained

$$g_{i,\mathrm{HTS}} = \left|\frac{\mathrm{d}T^*_{ci}}{\mathrm{d}\varepsilon_{\mathrm{JD}}}\right|_{\varepsilon_{\mathrm{JD}}=0\%} \frac{1}{T_{\mathrm{c}}(0)} \left[2\frac{1+t^2(0)}{1-t^2(0)} + \left(\frac{st(0)}{1-t(0)} + w\right)\left(\frac{qb(0)}{1-b(0)} + n - p - m\right)\right]. \quad (4.19)$$

And if the LTS parameterisation of $B^*_{\mathrm{c2}i}(T, \varepsilon_{\mathrm{JD}})$ (cf. eqn 4.14) is taken, then the expression becomes

$$g_{i,\mathrm{LTS}} = \left|\frac{\mathrm{d}T^*_{ci}}{\mathrm{d}\varepsilon_{\mathrm{JD}}}\right|_{\varepsilon_{\mathrm{JD}}=0\%} \frac{1}{T_{\mathrm{c}}(0)} \left[2\frac{1+t^2(0)}{1-t^2(0)} + \left(\frac{\nu t(0)}{1-t^{\nu}(0)} + w\right)\left(\frac{qb(0)}{1-b(0)} + n - p - m\right)\right]. \quad (4.20)$$

Eqns 4.19 and 4.20 show that g_i is proportional to $|\mathrm{d}T^*_{ci}/\mathrm{d}\varepsilon_{\mathrm{JD}}|_{\varepsilon_{\mathrm{JD}}=0\%}$ which implies that for both the HTS and LTS functional forms considered here $\alpha_{J_{\mathrm{c}}} = \alpha_{T_{\mathrm{c}}} = \alpha$.

In general the index of transition in each domain N_i is field, temperature and strain dependent. It is parameterised as a function of the critical current given by eqn 4.4. Hence the $E - J$ relation of the whole chain, eqn 3.7, no longer strictly obeys the simple power law. However, an approximate expression for index of transition for the whole chain N_{T} can be determined by replacing the left hand side of eqn 3.7 with $E_{\mathrm{c}}(J/J_{\mathrm{cT}})^{N_{\mathrm{T}}}$, differentiating with respect to J and setting $J = J_{\mathrm{cT}}$. This gives

$$N_{\mathrm{T}} \approx f N_{\mathrm{A}} \left(\frac{J_{\mathrm{cT}}}{J_{\mathrm{cA}}}\right)^{N_{\mathrm{A}}} + (1-f) N_{\mathrm{B}} \left(\frac{J_{\mathrm{cT}}}{J_{\mathrm{cB}}}\right)^{N_{\mathrm{B}}}, \quad (4.21)$$

from which approximate values of N_{T} for the chain model can be calculated.

4.6.2 Numerical results of the bimodal chain model

In this section the predictions of the in-field behaviour of the bimodal chain model are calculated. They are presented through the parameters J_{cT} and N_{T} by solving the transcendental eqn 4.16 numerically. The critical current in each domain $J_{\mathrm{c}i}$ is defined using the generalised flux pinning scaling relation of the form of eqn 4.10 where $T^*_{\mathrm{c}i}$ and $B^*_{\mathrm{c}2i}$ are unique to each domain and the strain dependence is constrained by a linear strain dependence for $T^*_{\mathrm{c}i}$ given by eqn 3.5. Table 4.6 provides the free parameter values used in the calculation: $T^*_{\mathrm{c}}(0)$, $B^*_{\mathrm{c}2}(0,0)$, s and S_N are taken as approximations of the experimental parameters, n, p and q are taken as the Kramer values [53], A and r_N are chosen such that N-values are in agreement with experiment, $\mathrm{d}T^*_{\mathrm{cA}}/\mathrm{d}\varepsilon_{\mathrm{JD}}|_{\varepsilon_{\mathrm{JD}}=0\%}$ is taken to be $2.5\,\mathrm{K}\,\%^{-1}$ (cf. table 4.6), and w is taken to be 3 [171]. Eqn 4.16 is solved numerically for J_{cT}.

In figures 4.26 - 4.30, the simplest case, $\alpha_{J_{\mathrm{c}}} = \alpha_{T_{\mathrm{c}}} = \alpha = 1$, is considered. Figure 4.26 shows J_{cT} normalised at zero domain strain as a function of domain strain for $\alpha = 1$ at 5 T for different temperatures and two values of f. Figure 4.27 shows how different domain fractions (different values of f) affect the field and temperature dependence of $\varepsilon_{\mathrm{p,JD}}$ for $\alpha = 1$. It is found that the strain at which J_{cT} reaches its peak value is a function of field and temperature. For $\alpha = 1$:

- for the special case of $f = 0.5$, the bimodal model predicts behaviour similar to homogeneous models;

Table 4.6. Parameters used in the numerical calculation of the 1D chain model.

Parameter	Value
A	10
$T_{\mathrm{c}}^{*}\,(0)$ (K)	90
$B_{\mathrm{c2}}^{*}\,(0,0)$ (T)	100
$\mathrm{d}T_{\mathrm{cA}}^{*}/\mathrm{d}\varepsilon_{\mathrm{JD}}\vert_{\varepsilon_{\mathrm{JD}}=0\%}$ (K %$^{-1}$)	2.5
w	3
s	1.25
n	2.5
m	2.0
p	0.5
q	2
r_N	90
S_N	0.4

- when $f < 0.5$, $\varepsilon_{\mathrm{p,JD}} < 0\,\%$;
- when $f > 0.5$, $\varepsilon_{\mathrm{p,JD}} > 0\,\%$.

The magnitude of $\varepsilon_{\mathrm{p,JD}}$ increases as the difference in the relative domain fractions increases (i.e. for larger values of $|f - 0.5|$).

Figure 4.28 shows $N_{\mathrm{T}} - 1$ against J_{cT} as a function of temperature and domain strain determined by solving eqn 4.21 for $\alpha = 1$. N_{T} is always lower than N_i of a single domain for any non-zero domain strain for all f including 0.5 and for $f \neq 0.5$ double valued behaviour of N_{T} appears. When:

- $f = 0.5$, $N_{\mathrm{T}} < N_i$ and N_{T} is single valued;
- $f < 0.5$, $N_{\mathrm{T}} < N_i$ and N_{T} is higher under tension than compression;
- $f > 0.5$, $N_{\mathrm{T}} < N_i$ and N_{T} is higher under compression than tension.

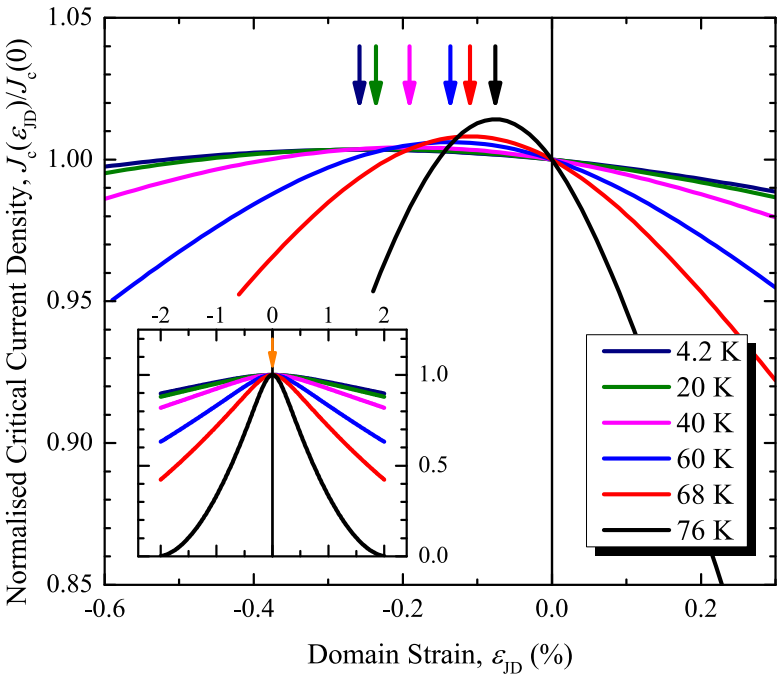

Figure 4.26. Numerical results of the bimodal chain model using the values in table 4.6 showing the variation of the normalised critical current density with domain strain at various temperatures for $B = 5\,\mathrm{T}$, $f = 0.3$ and $\alpha = 1$. The arrows show the peak position $\varepsilon_{\mathrm{p,JD}}$. (inset) Results for $f = 0.5$ and $\alpha = 1$ showing behaviour similar to a homogeneous model.

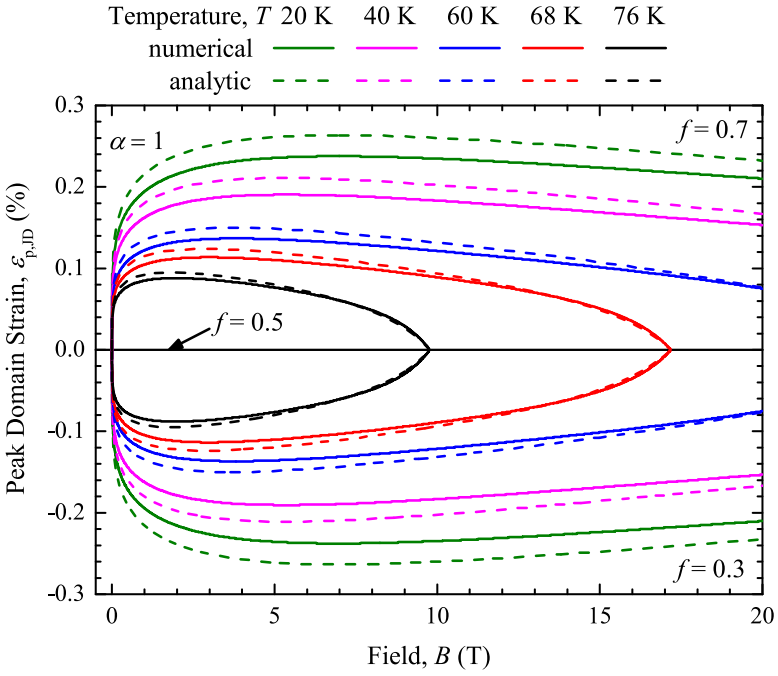

Figure 4.27. Numerical results for the peak domain strain $\varepsilon_{\mathrm{p,JD}}$ as a function of field and temperature from the 1D chain model for $f = 0.3$ (bottom half of the panel), 0.5 (horizontal line) and 0.7 (top half of the panel), using the values in table 4.6 with $\alpha = 1$. Also shown are the results of the analytically derived equation for $\varepsilon_{\mathrm{p,JD}}$ given by eqn 4.17 using the same parameters.

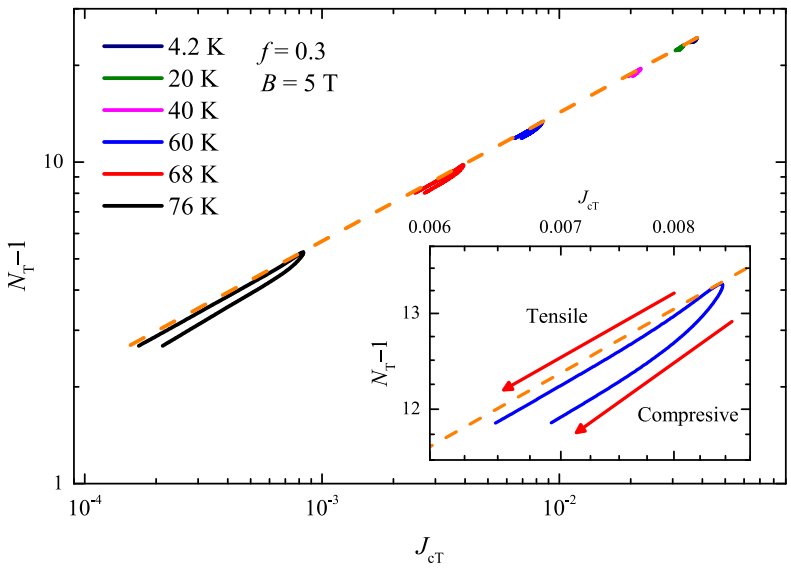

Figure 4.28. Results for $N_\mathrm{T} - 1$ calculated using eqn 4.21 against J_cT calculated numerically in the range $-1\,\% \leq \varepsilon_\mathrm{JD} \leq +1\,\%$ at $B = 5\,\mathrm{T}$ when $f = 0.3$ and $\alpha = 1$. The dashed line shows $N_i - 1$ for a single domain. (inset) Detail of the results at 60 K.

The predicted double valued behaviour of N_T is much smaller than the scatter on the experimental N-values and hence was not observed in the experimental data.

Figure 4.29 shows $\log F_\mathrm{p,max}\,[\kappa_1^*]^2$ versus $\log B_\mathrm{c2}^*$ as a function of temperature and domain strain with $f = 0.3$ and $\alpha = 1$. For $f \neq 0.5$ and $\alpha = 1$ double valued behaviour of $F_\mathrm{p,max}$ appears as shown in the inset. For:

- $f = 0.5$, $F_\mathrm{p,max}$ shows single-valued behaviour with B_c2^* comparable to scaling models for homogeneous materials;
- $f < 0.5$, $F_\mathrm{p,max}$ is higher in compression than in tension for the same value of B_c2^*;
- $f > 0.5$,$F_\mathrm{p,max}$ is higher in tension than in compression for the same value of B_c2^*.

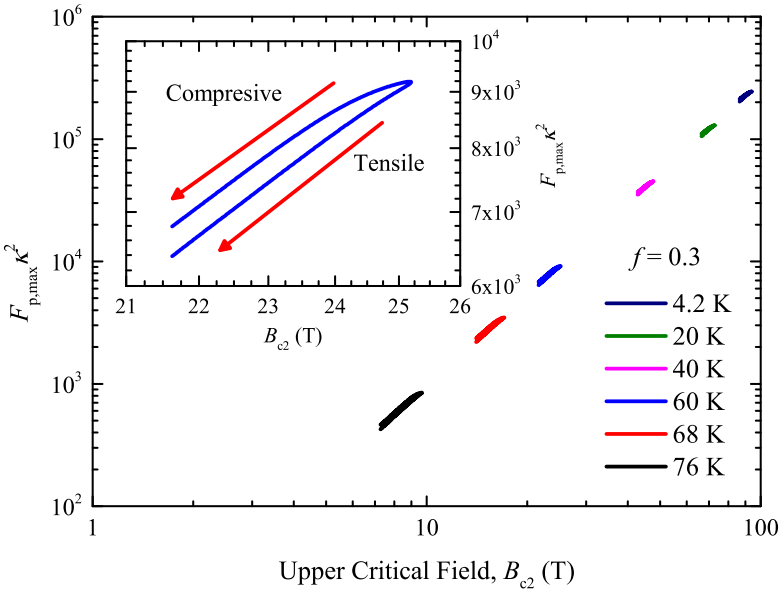

Figure 4.29. Numerical results of the bimodal chain model in the range $-1\,\% \leq \varepsilon_{JD} \leq +1\,\%$ showing $F_{p,max}$ against B^*_{c2} on a log-log scale using the values in table 4.6 for $f = 0.3$ and $\alpha = 1$. (inset) Detail of the results at 60 K.

Eqn 4.16 shows B^*_{c2} of the system (defined mathematically as the lowest field at which $J_{cT} = 0$) is entirely determined by B^*_{c2i} of the domain with the lowest J_{ci} independent of the domain fraction and α (assuming $f \neq 0 \vee 1$ and $\alpha \neq 0 \vee \infty$). For $\alpha = 1$, B^*_{c2i} is the same in each domain when the domain strain is equal and opposite independent of the value of f, hence $B^*_{c2}(+\varepsilon_{JD}) = B^*_{c2}(-\varepsilon_{JD})$. However this is not the case for $J_c(\varepsilon_{JD})$ which is asymmetric for $f \neq 0.5$ and hence $F_{p,max}(+\varepsilon_{JD}) \neq F_{p,max}(-\varepsilon_{JD})$. The result of this is double valued behaviour of $F_{p,max}$ with B^*_{c2}. The inset in figure 4.30 shows the relative magnitude of the difference between the tensile and compressive data, $(F_{p,max}(T,-\varepsilon_{JD}) - F_{p,max}(T,+\varepsilon_{JD}))/F_{p,max}(T,+\varepsilon_{JD}) = \Delta F_{p,max}(T,\pm\varepsilon_{JD})/F_{p,max}(T,+\varepsilon_{JD})$, increases and then saturates as the strain increases. The model breaks down as $\varepsilon_{JD} \to \pm\infty\,\%$ because one domain is completely suppressed

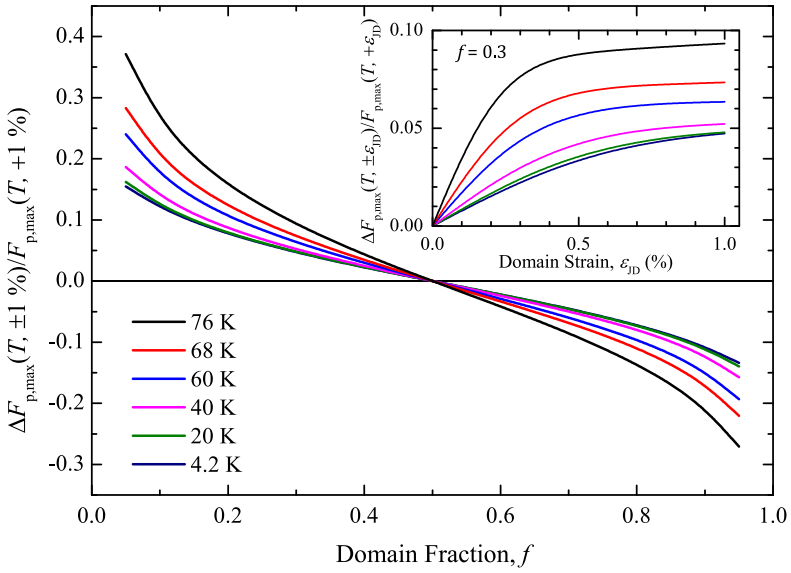

Figure 4.30. Numerical results of the bimodal chain model showing the normalised difference in the double valued behaviour of $F_{\mathrm{p,max}}$ as a function of temperature and f using the values in table 4.6 for $\varepsilon_{\mathrm{JD}} = \pm 1\,\%$ and $\alpha = 1$, and (inset) as a function of $\pm\varepsilon_{\mathrm{JD}}$ and temperature for $f = 0.3$ and $\alpha = 1$.

while the other has infinite critical current. So it was chosen to characterise this difference at $\varepsilon_{\mathrm{JD}} = \pm 1\,\%$ because this is large enough to be in the saturated region but not unphysically large. Figure 4.30 shows $\Delta F_{\mathrm{p,max}}\left(T, \pm\varepsilon_{\mathrm{JD}}\right) / F_{\mathrm{p,max}}\left(T, +\varepsilon_{\mathrm{JD}}\right)$ as a function of domain fraction at different temperatures for $\varepsilon_{\mathrm{JD}} = \pm 1\,\%$.

It is now considered how $\alpha \neq 1$ affects $\varepsilon_{\mathrm{p,JD}}$. Figure 4.31 shows how different values of f and α affect the field dependence of $\varepsilon_{\mathrm{p,JD}}$. When:

- $f = \alpha/\left(1+\alpha\right)$, $\varepsilon_{\mathrm{p,JD}} = 0\,\%$;
- $f < \alpha/\left(1+\alpha\right)$, $\varepsilon_{\mathrm{p,JD}} < 0\,\%$;
- $f > \alpha/\left(1+\alpha\right)$, $\varepsilon_{\mathrm{p,JD}} > 0\,\%$;

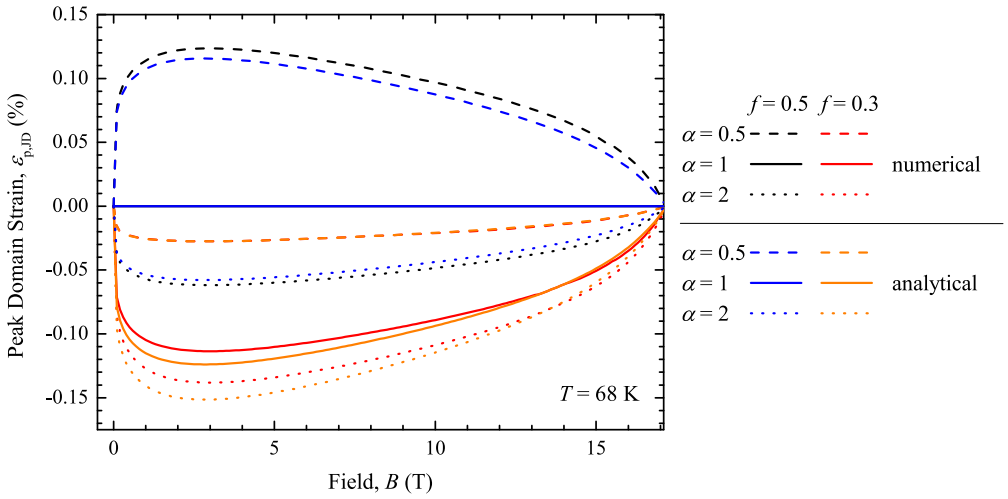

Figure 4.31. Numerical results of the bimodal chain model for the peak domain strain $\varepsilon_{\mathrm{p,JD}}$ at $T = 68\,\mathrm{K}$ as a function of field and α for $f = 0.3$ and 0.5 using the values given in Table 6. Also shown are the results of an analytically derived equation for $\varepsilon_{\mathrm{p,JD}}$ given by eqn 4.17 using the same parameters.

When $\alpha \neq 1$, $B^*_{\mathrm{c2}}(+\varepsilon^*_{\mathrm{JD}}) \neq B^*_{\mathrm{c2}}(-\varepsilon^*_{\mathrm{JD}})$ which leads to a more complex relation between B^*_{c2} and $F_{\mathrm{p,max}}$. No mathematical condition could be found where $F_{\mathrm{p,max}}$ was not a double-valued function of B^*_{c2} for $\alpha \neq 1$.

J_{cT} is dominated by the domain with the lowest $J_{\mathrm{c}i}$. Conceptually the dependence of $\varepsilon_{\mathrm{p,JD}}$ on f and/or α can be understood by considering that the E-field generated by one domain is not the same as that generated by the other at equal and opposite strain hence the function is not symmetric and $\varepsilon_{\mathrm{p,JD}} \neq 0\,\%$. Increasing f or decreasing α for any given strain results in an increase in the ratio of the E-field generated by domain A relative to domain B. This means a greater tensile strain is required before domain B (which has lower $J_{\mathrm{c}i}$ in tension than domain A) becomes dominant, resulting in $\varepsilon_{\mathrm{p,JD}}$ shifting in the tensile direction. The opposite is true for decreasing f or increasing α. The greater the relative difference between J_{cA} and J_{cB} the greater the degree to which

J_{cT} is dominated by the weaker domain. The field and temperature dependence of $\varepsilon_{\mathrm{p,JD}}$ is caused by variation of $\mathrm{d}J_{ci}\left(\varepsilon_{\mathrm{JD}}\right)/\mathrm{d}\varepsilon_{\mathrm{JD}}$ with field and temperature. At lower fields and temperatures, the magnitude of $\mathrm{d}J_{ci}\left(\varepsilon_{\mathrm{JD}}\right)/\mathrm{d}\varepsilon_{\mathrm{JD}}$ is lower meaning more strain is required to achieve the same relative difference between J_{cA} and J_{cB}. Hence a lower magnitude of $\mathrm{d}J_{ci}\left(\varepsilon_{\mathrm{JD}}\right)/\mathrm{d}\varepsilon_{\mathrm{JD}}$ means the peak moves to higher compressive or tensile strain (depending on whether $f < \alpha/\left(1+\alpha\right)$ or $f > \alpha/\left(1+\alpha\right)$ respectively). The analytical expression for $\varepsilon_{\mathrm{peak}}$, eqn 4.17, is also compared to the numerical results in figures 4.27 and 4.31 showing the expression is a reasonably good approximation with a typical error of $\sim 10\,\%$.

4.7 Estimating the domain fraction f and the applied strain at which J_{c} is the same in both domains $\varepsilon_{J_{\mathrm{cA}}=J_{\mathrm{cB}}}$

In this section the experimental results for the REBCO tape, bronze route and internal tin Nb_3Sn, and jelly-roll Nb_3Al wire are compared to the numerical and analytic results derived from the chain model.

Eqn 4.17 shows $\varepsilon_{\text{peak}}$ plotted against $\mathrm{d}T^*_{\text{cA}}/\mathrm{d}\varepsilon_{\text{JD}}|_{\varepsilon_{\text{JD}}=0\%}\, F\left(N_0, S_N\right)/g_{\text{A}}\left(B,T\right)$ should give a liner relation with

$$\text{gradient} = \frac{f-\alpha_{J_{\text{c}}}/\left(1+\alpha_{J_{\text{c}}}\right)}{f\left(1-f\right)\left(1+\alpha_{J_{\text{c}}}\right)}\Bigg/\left|\frac{\mathrm{d}T^*_{\text{cA}}}{\mathrm{d}\varepsilon_{\text{JD}}}\right|_{\varepsilon_{\text{JD}}=0\%}, \tag{4.22}$$

$$\text{intercept} = \varepsilon_{J_{\text{cA}}=J_{\text{cB}}}. \tag{4.23}$$

For REBCO, $\varepsilon_{\text{peak}}$ is plotted against $\mathrm{d}T^*_{\text{cA}}/\mathrm{d}\varepsilon_{\text{JD}}|_{\varepsilon_{\text{JD}}=0\%}\, F\left(N_0, S_N\right)/g_{\text{A,HTS}}\left(B,T\right)$ in figure 4.32 where $\mathrm{d}T^*_{\text{cA}}/\mathrm{d}\varepsilon_{\text{JD}}|_{\varepsilon_{\text{JD}}=0\%}/g_{\text{A,HTS}}$ is given by a rearrangement of eqn 4.19. To calculate F and $\mathrm{d}T^*_{\text{cA}}/\mathrm{d}\varepsilon_{\text{JD}}|_{\varepsilon_{\text{JD}}=0\%}/g_{\text{A,HTS}}$, strictly the input parameters, $B^*_{\text{c2}}\left(T, \varepsilon_{\text{JD}}=0\,\%\right)$, n, p, q and $T^*_{\text{c}}\left(\varepsilon_{\text{JD}}=0\,\%\right)$ for an applied strain when $\varepsilon_{\text{JD}}=0\,\%$ (i.e. $\varepsilon_{\text{app}}=\varepsilon_{J_{\text{cA}}=J_{\text{cB}}}$) are required. It is initially assumed $\varepsilon_{\text{app}}=0\,\%$ when $\varepsilon_{\text{JD}}=0\,\%$ and the input parameters are taken from the detailed flux pinning scaling analysis (cf. section 4.5). N_0 values were taken to be their experimental values and w was taken to be the standard value of 2.2 [178]. The data at 4.2 K were not included in the analysis due to the systematic inconsistencies in the N-values, discussed in section 4.3.1. Preliminary values of the intercept and gradient ($\varepsilon_{J_{\text{cA}}=J_{\text{cB}}}$ and $\left(\mathrm{d}T^*_{\text{cA}}/\mathrm{d}\varepsilon_{\text{JD}}|_{\varepsilon_{\text{JD}}=0\%}\right)^{-1}\left[f-\alpha/\left(1+\alpha\right)\right]/\left[f\left(1-f\right)\left(1+\alpha\right)\right]$ respectively) were then extracted from a linear fit to the data (cf. figure 4.32). New values of F and $\mathrm{d}T^*_{\text{cA}}/\mathrm{d}\varepsilon_{\text{JD}}|_{\varepsilon_{\text{JD}}=0\%}/g_{\text{A,HTS}}$ were calculated with the new value for $\varepsilon_{J_{\text{cA}}=J_{\text{cB}}}$. After iterating this process, the data in figure 4.32 were obtained and the final gradient and intercept values obtained are presented in table 4.7. It is noted that the data shown in figure 4.32 are broadly insensitive to the iteration process because the input parameters are predominantly determined by the magnetic field

and temperature, and are insensitive to small changes in $\varepsilon_{J_{\mathrm{cA}}=J_{\mathrm{cB}}}$. Single crystal values of $\mathrm{d}T^*_{\mathrm{cA}}/\mathrm{d}\varepsilon_{\mathrm{JD}}|_{\varepsilon_{\mathrm{JD}}=0\%}$ and α are required to calculate an estimate of f from the gradient. Data from the literature for $\mathrm{d}T^*_{\mathrm{cA}}/\mathrm{d}\varepsilon_{\mathrm{JD}}|_{\varepsilon_{\mathrm{JD}}=0\%}$ and α are listed in table 4.8 and are used to calculate values of f. Also shown on figure 4.32 is a linear fit including additional data as a function of angle (presented in chapter 5) where $\varepsilon_{J_{\mathrm{cA}}=J_{\mathrm{cB}}} = 0.19\,\%$ and $\left(\mathrm{d}T^*_{\mathrm{cA}}/\mathrm{d}\varepsilon_{\mathrm{JD}}|_{\varepsilon_{\mathrm{JD}}=0\%}\right)^{-1}\left[f-\alpha/\left(1+\alpha\right)\right]/\left[f\left(1-f\right)\left(1+\alpha\right)\right] = -0.27$. The relative difference in the double valued behaviour of $F_{\mathrm{p,max}}$ was also measured and the results compared to the numerical bimodal chain model results given in figure 4.30. Given that the compressive data is higher than the tensile data, it is expected that $f < 0.5$. Qualitatively the same saturation of the normalised difference in $F_{\mathrm{p,max}}$ as a function of strain predicted by the model is found and from the magnitude of $\Delta F_{\mathrm{p,max}}\left(T,\pm\varepsilon_{\mathrm{JD}}\right)/F_{\mathrm{p,max}}\left(T,+\varepsilon_{\mathrm{JD}}\right)$ an estimate of $f \sim 0.42$ for $\left(\mathrm{d}T^*_{\mathrm{cA}}/\mathrm{d}\varepsilon_{\mathrm{JD}}|_{\varepsilon_{\mathrm{JD}}=0\%}\right)^{-1} = 2.5\,\mathrm{K}\,\%^{-1}$ and $\alpha = 1$ is obtained.

A similar analysis was performed on the bronze route and internal tin Nb_3Sn, and jelly-roll Nb_3Al wires, shown in figures 4.33, 4.34 and 4.35 respectively. The free parameters were taken from the detailed flux pinning scaling analysis (cf. section 4.5). The parameter w was taken to be the standard value for a LTS material of 2.2 [178] . An estimate of $\mathrm{d}T^*_{\mathrm{cA}}/\mathrm{d}\varepsilon_{\mathrm{JD}}|_{\varepsilon_{\mathrm{JD}}=0\%}$ for Nb_3Sn was obtained from data available in literature. Magnetic measurements on single crystals give $\mathrm{d}T^*_{c\langle 100\rangle}/\mathrm{d}\varepsilon_{\mathrm{JD}}\,|_{\varepsilon_{\mathrm{JD}}=0\%}$ values along the $\langle 100\rangle$ directions that vary by an order of magnitude depending on whether a full screening criterion or an onset criterion was used [265]. A value of $\mathrm{d}T^*_{c\langle 100\rangle}/\mathrm{d}\varepsilon_{\mathrm{JD}}\,|_{\varepsilon_{\mathrm{JD}}=0\%}$ of $1.63\,\mathrm{K}\,\%^{-1}$ characteristic of about 30 % screening is chosen,

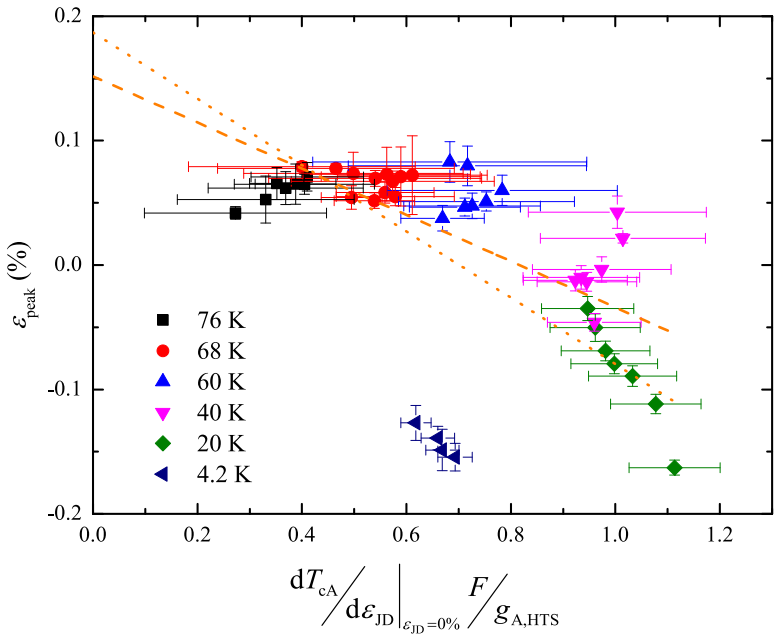

Figure 4.32. $\varepsilon_{\text{peak}}$ versus $\mathrm{d}T^*_{\mathrm{cA}}/\mathrm{d}\varepsilon_{\mathrm{JD}}|_{\varepsilon_{\mathrm{JD}}=0\%}/g_{\mathrm{A,HTS}}$ for the REBCO tape. The dashed line is a linear fit to the data, excluding $T = 4.2\,\mathrm{K}$, with parameters shown in table 4.7. The dotted line is a linear fit including additional data as a function of angle (presented in chapter 5) The parameter $F = N_0/\left(N_0\left(N_0+1\right) - 2S_N\left(N_0-1\right)\right)$ and $\mathrm{d}T^*_{\mathrm{cA}}/\mathrm{d}\varepsilon_{\mathrm{JD}}|_{\varepsilon_{\mathrm{JD}}=0\%}/g_{\mathrm{A,HTS}}$ is given by a rearrangement of eqn 4.19.

Table 4.7. Results of fitting eqn 4.17 to the ε_{peak} data for REBCO tape, bronze route and internal tin Nb_3Sn, and jelly roll Nb_3Al wires. $dT^*_{cA}/d\varepsilon_{JD}|_{\varepsilon_{JD}=0\%}$ is coupled with the domain fraction f which is calculated using values of $dT^*_{cA}/d\varepsilon_{JD}|_{\varepsilon_{JD}=0\%}$ obtained from litterature as discussed in the body of the text. For these LTS, it has been assumed that $\alpha = 1$.

	REBCO tape	Bronze route Nb_3Sn	Internal tin Nb_3Sn	Jelly-roll Nb_3Al
$\varepsilon_{J_{cA}=J_{cB}}$	0.15 ± 0.02	0.32 ± 0.03	0.089 ± 0.006	0.079 ± 0.007
$\frac{f-\alpha/(1+\alpha)}{f(1-f)(1+\alpha)}\left(\frac{dT^*_{cA}}{d\varepsilon_{JD}}\Big\|_{\varepsilon_{JD}=0\%}\right)^{-1}$	-0.19 ± 0.02	1.16 ± 0.07	-0.09 ± 0.08	2.0 ± 0.2
f	See table 4.8	0.69	0.48	~ 0.5 or 0.67
$\frac{dT^*_{cA}}{d\varepsilon_{JD}}\Big\|_{\varepsilon_{JD}=0\%}$ (K %$^{-1}$)		0.39 [265]	0.39 [265]	0.19
Hysteretic $F_{p,max}\left[\kappa^*_1\right]^2$	Yes $f < 0.5$	Yes $f > 0.5$	No	No

Table 4.8. Values of the domain fraction f determined using various experimental values of $\mathrm{d}T^*_{ci}/\mathrm{d}\varepsilon$ from literature. The results of Welp *et al.* [211] and Fietz *et al.* [210] are converted from stress to strain using Young's moduli of 162.7 GPa along the a-axis and 178.1 GPa along the b-axis [266].

	$\mathrm{d}T^*_{\mathrm{cA}}/\mathrm{d}\varepsilon_{\mathrm{JD}}$ (K %$^{-1}$)	$\mathrm{d}T^*_{\mathrm{cB}}/\mathrm{d}\varepsilon_{\mathrm{JD}}$ (K %$^{-1}$)	α	f
Suzuki et. al. [267]	$+4.09 \pm 0.02$	-2.09 ± 0.01	0.51	0.17
Fietz et. al. [210]	$+1.6 \pm 0.1$	-2.1 ± 0.1	1.31	0.40
Welp et. al. [211]	$+3.3 \pm 0.3$	-3.4 ± 0.4	1.03	0.26

using a Young's modulus of 165 GPa [268] to make the stress-strain conversion. This is an upper-bound value along the $\langle 100 \rangle$ direction in which the strain dependence is greatest. The random orientation of the grains in Nb_3Sn wires will result in the average value of $\mathrm{d}T^*_{\mathrm{cA}}/\mathrm{d}\varepsilon_{\mathrm{JD}}|_{\varepsilon_{\mathrm{JD}}=0\%}$ being lower. An approximate average over all solid angles is taken to obtain $\mathrm{d}T^*_{\mathrm{cA}}/\mathrm{d}\varepsilon_{\mathrm{JD}}|_{\varepsilon_{\mathrm{JD}}=0\%} = 0.24 \times \mathrm{d}T^*_{c\langle 100\rangle}/\mathrm{d}\varepsilon_{\mathrm{JD}}\,|_{\varepsilon_{\mathrm{JD}}=0\%} = 0.39\,\mathrm{K}\,\%^{-1}$ [244]. Single crystal data for Nb_3Al is not available. Since the strain dependence of the critical parameters of Nb_3Al measured in polycrystalline composite wires is approximately half that of Nb_3Sn, it is assumed $\mathrm{d}T^*_{\mathrm{cA}}/\mathrm{d}\varepsilon_{\mathrm{JD}}|_{\varepsilon_{\mathrm{JD}}=0\%} = 0.19\,\mathrm{K}\,\%^{-1}$. The nature of competing domains in A15 wires is unclear and is the subject of discussion in section 4.8.2, so for simplicity, a value of $\alpha = 1$ is assumed. The initial values of $\varepsilon_{J_{\mathrm{cA}}=J_{\mathrm{cB}}}$ were taken be 0.39 %, 0.14 % and 0.12 % for bronze route and internal tin Nb_3Sn, and jelly-roll Nb_3Al and the values of f and numbers obtained after iteration are listed in table 4.7. For the bronze route Nb_3Sn, the data at 4.2 K is again omitted from the analysis because there was heating at high currents that caused deviation of the $E - J$ traces from power law behaviour for high E-fields.

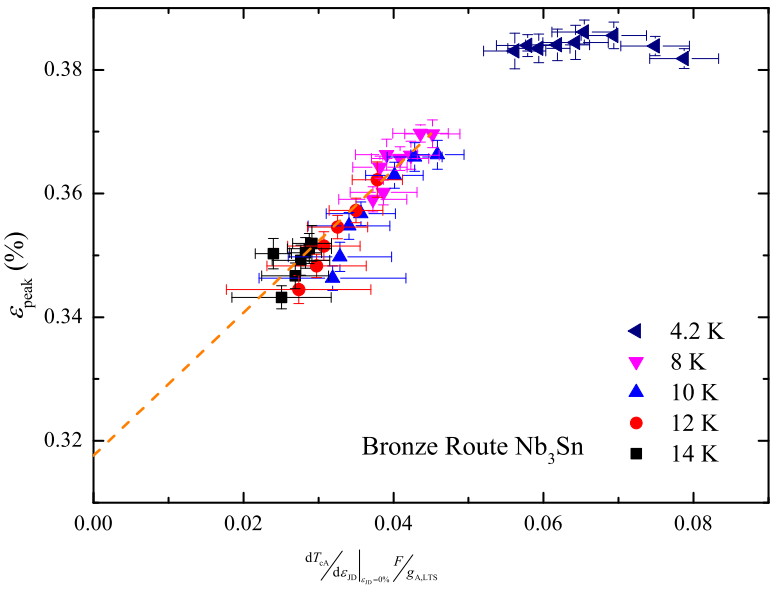

Figure 4.33. $\varepsilon_{\mathrm{peak}}$ versus $\mathrm{d}T^*_{\mathrm{cA}}/\mathrm{d}\varepsilon_{\mathrm{JD}}|_{\varepsilon_{\mathrm{JD}}=0\%}\, F/g_{\mathrm{A,LTS}}$ for the bronze route Nb_3Sn wire. The dashed line is a linear fit to the data, excluding $T = 4.2\,\mathrm{K}$, with parameters shown in table 4.7. The parameter $F = N_0/\left(N_0\left(N_0+1\right) - 2S_N\left(N_0-1\right)\right)$ and $\mathrm{d}T^*_{\mathrm{cA}}/\mathrm{d}\varepsilon_{\mathrm{JD}}|_{\varepsilon_{\mathrm{JD}}=0\%}\,/g_{\mathrm{A,LTS}}$ is given by a rearrangement of eqn 4.20. The linear fit has been performed by minimising Chi-squared with data weighted by the uncertianties in $\mathrm{d}T^*_{\mathrm{cA}}/\mathrm{d}\varepsilon_{\mathrm{JD}}|_{\varepsilon_{\mathrm{JD}}=0\%}\, F/g_{\mathrm{A,LTS}}$ as these uncertianties are signifigantly larger than those in $\varepsilon_{\mathrm{peak}}$.

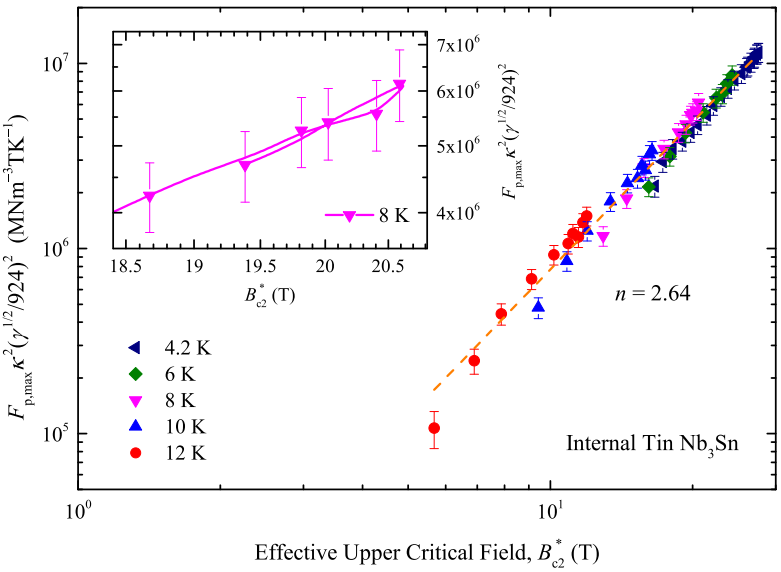

Figure 4.34. $\varepsilon_{\text{peak}}$ versus $\mathrm{d}T^*_{\text{cA}}/\mathrm{d}\varepsilon_{\text{JD}}|_{\varepsilon_{\text{JD}}=0\%}\, F/g_{\text{A,LTS}}$ for the internal tin Nb_3Sn wire. The dashed line is a linear fit to the data with parameters shown in table 4.7. The parameter $F = N_0/\left(N_0\left(N_0+1\right)-2S_N\left(N_0-1\right)\right)$ and $\mathrm{d}T^*_{\text{cA}}/\mathrm{d}\varepsilon_{\text{JD}}|_{\varepsilon_{\text{JD}}=0\%}/g_{\text{A,LTS}}$ is given by a rearrangement of eqn 4.20.

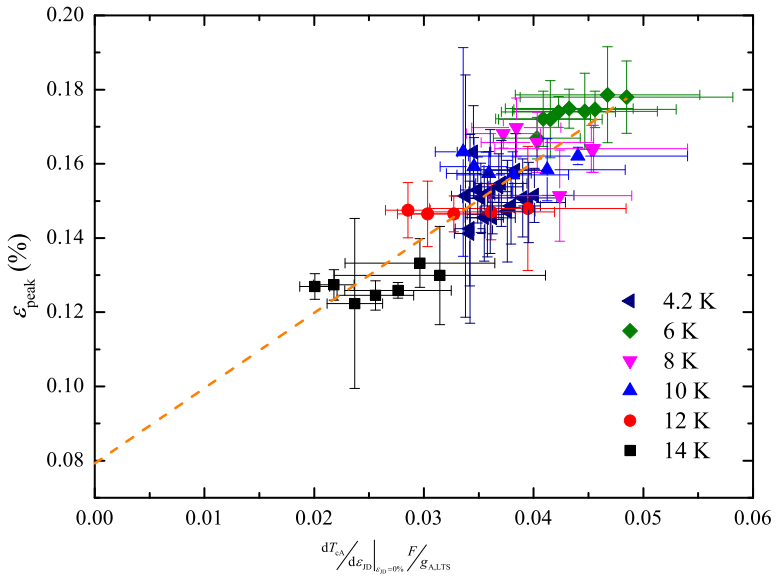

Figure 4.35. $\varepsilon_{\text{peak}}$ versus $\mathrm{d}T^*_{\text{cA}}/\mathrm{d}\varepsilon_{\text{JD}}|_{\varepsilon_{\text{JD}}=0\%}\, F/g_{\text{A,LTS}}$ for the jelly-roll Nb_3AlPB: Added missing Nb3Al wire. The dashed line is a linear fit to the data with parameters shown in table 4.7. The parameter $F = N_0/\left(N_0\left(N_0+1\right)-2S_N\left(N_0-1\right)\right)$ and $\mathrm{d}T^*_{\text{cA}}/\mathrm{d}\varepsilon_{\text{JD}}|_{\varepsilon_{\text{JD}}=0\%}/g_{\text{A,LTS}}$ is given by a rearrangement of eqn 4.20.

A similar analysis of $\Delta F_{\mathrm{p,max}}\left(T, \pm\varepsilon_{\mathrm{JD}}\right)/F_{\mathrm{p,max}}\left(T, +\varepsilon_{\mathrm{JD}}\right)$ was completed for the bronze route Nb_3Sn wire using $\mathrm{d}T^{*}_{\mathrm{cA}}/\mathrm{d}\varepsilon_{\mathrm{JD}}|_{\varepsilon_{\mathrm{JD}}=0\%} = 0.39\,\mathrm{K}\,\%^{-1}$ and $\alpha = 1$. Again, saturation of the normalised difference in $F_{\mathrm{p,max}}$ as a function of strain is found, and is consistent with $f > 0.5$ with the tensile data being higher than the compressive data as shown in figure 4.23. The experimental results for $\Delta F_{\mathrm{p,max}}\left(T, \pm\varepsilon_{\mathrm{JD}}\right)/F_{\mathrm{p,max}}\left(T, +\varepsilon_{\mathrm{JD}}\right)$ are approximately an order of magnitude higher than the largest numerical results. This is attributed to the limitations of applying the chain model to LTS polycrystalline materials discussed in section 4.8. The internal tin Nb_3Sn and jelly-roll Nb_3Al wire did not show double valued behaviour of $F_{\mathrm{p,max}}$ to within the uncertainties of the measurements.

In conclusion the field and temperature dependence of $\varepsilon_{\mathrm{peak}}$ is found to be similar to the predictions of the chain model. For the REBCO tape $f < 0.5$, for the bronze route Nb_3Sn wire $f > 0.5$, and for the internal tin Nb_3Sn wire $f = 0.5$. The jelly-roll Nb_3Al wire has contradictory results, the field and temperature dependence of $\varepsilon_{\mathrm{peak}}$ gives $f = 0.67$ whereas the single-valued behaviour of $F_{\mathrm{p,max}}$ suggests $f \sim 0.5$, it is noted that that considering the field dependence of $\varepsilon_{\mathrm{peak}}$ alone also leads to $f \sim 0.5$.

4.8 Discussion

For many decades, the magnetic field and temperature dependence of J_{c} has been measured as part of understanding and increasing J_{c} for technological applications. More recently, measurements on the strain dependence of J_{c} have become important

because of the large differential strains that occur on cool-down, and the large Lorentz forces that can occur in large scale systems such as CERN [269] or ITER [270]. Given that the critical superconducting properties of polycrystalline Nb_3Sn are reduced either in compression or tension, historically, it was not unreasonable to make the general assumptions that: i) the material has, by chance, optimal superconducting properties when unstrained and ii) it can quite accurately be described using scaling laws that describe the material as broadly homogeneous under strain. Neither of these assumptions are valid for twinned REBCO tapes. The supply of high-quality single crystals of REBCO has underpinned extensive data that describe the anisotropic properties of REBCO in-field and under strain including the monotonic and anisotropic strain dependence for T_c for the 2 domains in a REBCO tape. Hence the inverted parabolic strain dependence of J_c (cf. figures 4.6 and 4.7) is associated with competing bimodal behaviour and cannot be associated with a fortuitous optimisation of the superconducting properties of REBCO at zero strain. This chapter has developed the chain model to explain and identify the broad features of REBCO tapes, including the marked field and temperature dependence of ε_{peak} [195, 207, 209], that cannot be explained with the standard historical assumptions for LTS materials. The clear collapse of these assumptions for REBCO, following extensive single crystal data, naturally begs the question whether the standard interpretation of the strain dependence of J_c in LTS is in fact correct. As discussed below, it is found that despite the widespread industrial use of A15 materials to provide the critical superconducting component in applications above 10 T, there is actually very little data on the anisotropic strain properties of

single crystal material. It is argued that although the two historical assumptions about LTS materials can help provide scaling laws (cf. table 4.2) that are useful for optimising magnet design, they are fundamentally wrong and a bi- or multimodal approach is required to understand A15 materials properly. More specifically, it is suggested that in Nb_3Sn and Nb_3Al polycrystalline materials, because grain boundaries are critical in determining J_c, the peak in the strain dependence of J_c is associated with a bimodal grain boundary behaviour such that on applying strain the local critical current density increases across some grain boundaries and decreases for others. In this section, the general approach is discussed, the HTS results are considered in detail, including their strengths and weaknesses, and finally the LTS results are discussed.

4.8.1 Discussion of REBCO results

In this thesis, a REBCO tape with a simple microstructure and relatively high J_c has been investigated. Tapes with higher J_c (for example those that include artificial pinning centres) have been avoided because such materials with multiple types of pinning site of differing geometries leads to many mechanisms, each with their own field, temperature and strain dependencies that make it extremely difficult to deconvolve the underlying science. The universal flux pinning curve in figure 4.20SC, IH and PB: Added missing figure ref provides strong evidence that for the REBCO tape chosen, it is reasonable to assume a single pinning mechanism determines J_c at the fixed angle chosen.

A combination of phenomenological equations and microscopic equations have been used to characterise J_c and equated the irreversibility field B_{irr} found in flux pinning equations, and the upper critical field B_{c2}, to the effective upper critical field B^*_{c2} measured in this chapter. The irreversibility field is a field below the upper critical field above which $J_c = 0$, despite still being in the superconducting state associated with the onset of bulk flux flow [79, 80], whereas the upper critical field is a thermodynamic property which delineates the superconducting and normal phases. In figure 4.36 the resistive transport results are compared to upper critical field and irreversibility field results from literature. RF measurements [27] on a single crystal follow the well-known WHH-like behaviour for B_{c2} found in LTS across the entire temperature range. Magnetic [12, 271] and resistive [83] measurements of B_{c2} on single crystals also show WHH-like behaviour, whereas B_{irr} follows the empirical relation $B_{irr}(T) = B(0)(1 - T/T_c)^s$. The resistive measurements performed on the tape sample in this study show behaviour consistent with B_{irr} at both the extrapolated 0 % criterion (associated with B_{irr} for single crystals) and the extrapolated 100 % criterion (associated with B_{c2} for single crystals). This behaviour is attributed to the architecture of tape samples where the silver and copper stabilising layers, and the sample holder are electrically in parallel with the superconducting layer. When the resistance, caused by dissipation of the flux lines (i.e. in the vortex liquid state), is greater than the parallel resistance the current will shunt through the stabilising metallic layers as well as flowing in the superconducting layer. The measured voltage is then predominantly determined by the current through the shunt. It is concluded that the effective upper critical fields

presented in this work are best associated with B_{irr} rather than B_{c2} for all criteria investigated. A comprehensive analysis would include measurements of B_{c2} and B_{irr} on the same sample. However, this is a formidable challenge, since ideally one would require local probes operating on the scale of the coherence length because these two critical fields vary spatially in high J_c materials, and also a much better understanding than is currently available would be required to extract the characteristic fields for the scaling laws from such measurements.

A temperature dependence for the exponent n (cf. eqn 4.10) is observed in the pinning scaling behaviour of REBCO tape and bronze route Nb_3Sn where $f \neq \alpha/(\alpha+1)$ but is not observed in the internal tin Nb_3Sn sample and the jelly-roll Nb_3Al samples where $f \sim \alpha/(\alpha+1)$. (cf. figures 4.22 - 4.25). This suggests that the temperature dependence of n may be due to bimodal strain dependence but is not accounted for by the chain model in its current implementation. Extensions to the model which could account for this behaviour include: distributions of T_c^* in each domain, introducing two or three dimensional percolative current flow and including the effect of current shunting through the sample holder and matrix materials. Distributions of T_c^* were implemented into the model (data not shown), but this was found to make little difference to the results and did not explain the temperature variation of n. Extending the chain model to two or three dimensions to allow for percolative flow and current shunting may explain the observed behaviour but such extensions are beyond the scope of this thesis.

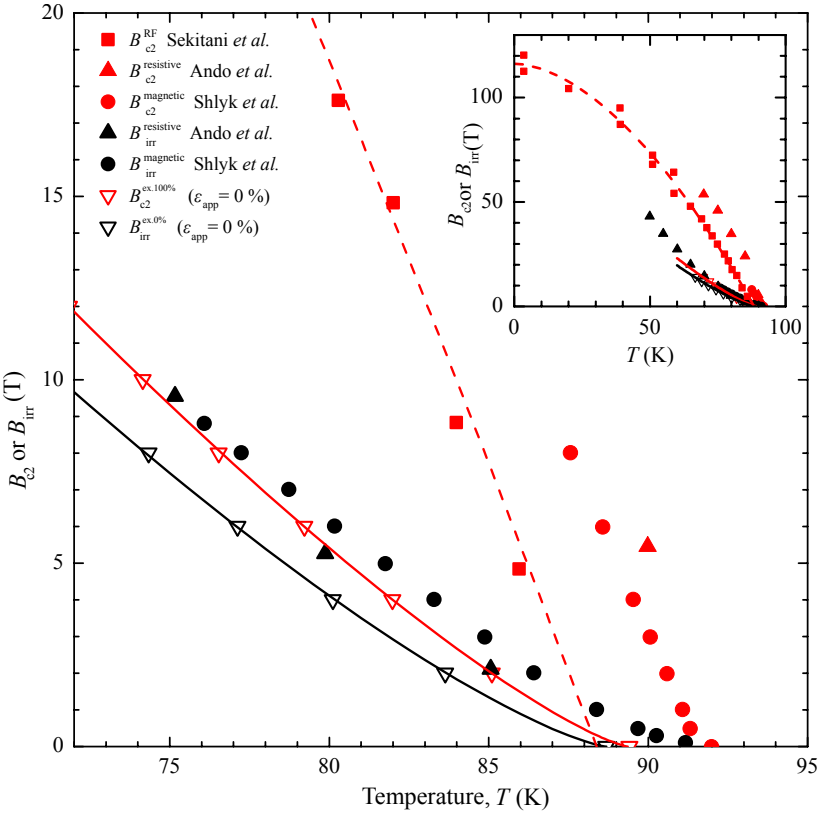

Figure 4.36. Resistive upper critical field data at $\varepsilon_{app} = 0\,\%$ for REBCO tape using the extrapolated 0 % and 100 % criteria plotted with upper critical field and irreversibility field data from the literature obtained using a variety of techniques on both single crystal and tape samples from Sekitani *et al.* [27], Ando *et al.* [83] and Shlyk *et al.* [271]. Closed symbols are for single crystal and open symbols are for tape. Red and black symbols denote measurement techniques which, for a single crystal, give B_{c2} and B_{irr} respectively. The solid lines are parameterisations of the extrapolated 0 % and 100 % data using eqn 4.5, the dashed line is a guide for the eye for the [27] data. (inset) Extended temperature range.

One of the central results in this thesis is the observation that the value of $\varepsilon_{\mathrm{peak}}$ varies with field and temperature in the REBCO tape. It is considered here whether this result could be an experimental artefact or a product of the analysis: the change in $\varepsilon_{\mathrm{peak}}$ observed experimentally as a function of temperature is much larger than the differential thermal expansion between 4.2 K and 77 K for CuBe which is $\sim 0.018\,\%$ [74] and therefore the temperature dependence of $\varepsilon_{\mathrm{peak}}$ cannot be associated with the differential thermal contraction between the sample and the spring board sample holder. One can explain the temperature dependence of $\varepsilon_{\mathrm{peak}}$ using the standard flux pinning framework for a homogeneous material by setting aside the experimental parameterisation of B^*_{c2} where the relationship between $B^*_{\mathrm{c2}}(0, \varepsilon_{\mathrm{app}})$ and $T^*_{\mathrm{c}}(\varepsilon_{\mathrm{app}})$ is constrained through the exponent w and allow $B^*_{\mathrm{c2}}(0, \varepsilon_{\mathrm{app}})$ to be a maximised at a different strain to $T^*_{\mathrm{c}}(\varepsilon_{\mathrm{app}})$ [51]. However, there is no equivalent way to explain the field dependence of $\varepsilon_{\mathrm{peak}}$ either as an artefact of the experiment or within the standard flux pinning model. It is considered highly unlikely the field and temperature dependence of $\varepsilon_{\mathrm{peak}}$ is an experimental artefact or can result from a homogeneous sample where all domains respond to strain in broadly the same manner.

The broad features predicted by the chain model can be reproduced as long as there is competition between two components of the material that determine J_{c}. The simple linear strain dependence of T^*_{c} in each domain is sufficient to explain both the parabolic behaviour of $J_{\mathrm{c}}(\varepsilon)$ at low strains as well as the non-parabolic behaviour of $J_{\mathrm{c}}(\varepsilon)$ at high strains (i.e. the 'tails' at high strains in figure 4.26) that have been observed experimentally [200, 204, 206]. In contrast, in a homogeneous model higher

order strain dependent terms in T_c^* are arbitrarily added to explain this behaviour. Nevertheless, there are some limitations to the parameterisation used to describe the in-field behaviour of J_c. Figure 4.27 shows that at low fields $\varepsilon_{p,JD}$ rapidly converges to $\varepsilon_{JD} = 0\,\%$ as $B \to 0\,\mathrm{T}$. This is a result of the unphysical way in which the flux pinning relation eqn 4.10 predicts $\lim_{B\to 0\,\mathrm{T}} J_{ci} = \infty$ when $p < 1$ and therefore through eqn 4.4 $\lim_{B\to 0\,\mathrm{T}} N_0 = \infty$. A more physical low-field parameterisation of J_{ci} will result in ε_{peak} tending to a finite values as $B \to 0\,\mathrm{T}$. The chain model also leads to a non-physical discontinuity in the gradient of the strain dependence for the critical parameters T_c^* and B_{c2}^* at $\varepsilon_{J_{cA}=J_{cB}}$ because they follow that of the domain with lowest values. This discontinuity is not seen in the data and this discrepancy is expected to diminish if the chain model is extended to 2D or 3D and include the role of percolation and current shunting.

Experimental values of $\mathrm{d}T_{ci}^*/\mathrm{d}\varepsilon_{p,JD}|_{\varepsilon_{JD}=0\%}$ from the literature for REBCO single crystals [210, 211] and detwinned tapes [267] are summarised in table 4.8 and used to calculate a range of f values. The range of $\mathrm{d}T_{ci}^*/\mathrm{d}\varepsilon_{JD}|_{\varepsilon_{JD}=0\%}$ values reported in the literature is attributed to differences in the doping and stoichiometry of the samples measured. Although there is no agreement about the value of α or $\mathrm{d}T_{ci}^*/\mathrm{d}\varepsilon_{JD}|_{\varepsilon_{JD}=0\%}$ in the region of $\varepsilon_{JD} = 0\,\%$, there is general agreement that $\mathrm{d}T_{ci}^*/\mathrm{d}\varepsilon_{JD}|_{\varepsilon_{JD}=0\%}$ have opposite signs in the two domains which is the central requirement for the chain model. The high temperature parameterisation of $B_{c2i}^*(T, \varepsilon_{JD})$ has been used for the analytic derivation of $g_{A,HTS}$ at high temperatures. At low temperatures, cf section 4.5, $B_{c2i}^*(T, \varepsilon_{JD})$ was determined from the flux pinning scaling which gives higher values and a smaller strain

dependence than an extrapolation of the high temperature parameterisation, as shown in the inset of figure 4.11. This leads to lower $g_{\mathrm{A,HTS}}$ at low temperatures and higher f. It is noted this higher value of f is consistent with that determined from the magnitude of the double valued behaviour of $F_{\mathrm{p,max}}$.

The temperature dependence of $\varepsilon_{\mathrm{peak}}$ has been reported in literature under self-field conditions [208] and also as a function of field [195, 207, 209]. These results can be described using the bimodal chain model with a value of $f < \alpha/(\alpha+1)$ for references [207–209] and $f > \alpha/(\alpha+1)$ for reference [195]. Osamura *et al.* found values of f ranging from 0.36 to 0.65 for a number of lengths of tape assuming $\alpha = 1$ [199]. Analysis of XRD measurements [267] on SuperPower samples with no artificial pinning centres also gives an estimate of the domain fraction to be $f \approx 0.45$. These data show that the values of f in table 4.8 are reasonable. Inclined Substrate Deposition (ISD) produces tapes with grains aligned 45° from other deposition methods. With this alignment one would expect a homogeneous response of the domains to a uniaxial strain applied along the tape axis. Measurements on ISD [161, 162, 201] and 'detwinned' [267, 272] tapes show a linear dependence of T_{c}^{*} and J_{c} to an applied strain indicative of the homogeneous behaviour that is expected in both cases from the chain model. It is noted that annealing a single tape sample under different stresses in oxygen [267,272] would lead to a broad range of f values which the chain model predicts would lead to large changes in $\varepsilon_{\mathrm{peak}}$ that could not be explained by the differential thermal contraction used for LTS [182] and suggests that such experiments provide a stringent test of the chain model.

4.8.2 Discussion of LTS results - polycrystalline materials

Most of the theoretical work on the band structure of Nb_3Sn dates back to a time when A15 materials claimed the record for the superconducting material with the highest critical temperature. It was widely believed that 30 K was the theoretical limit for T_c for a BCS superconductor [13,63] and the 'high' critical temperatures of 18 K for Nb_3Sn and 23 K for $Nb_3(Al_{1-x}Ge_x)$ were due to a near coincidence between the Fermi energy and the peak in the density of states (DoS) when the material is in an unstrained state [273–276]. However, A15 compounds undergo a cubic-tetragonal distortion below ~ 40 K under certain conditions [277–279] and show highly anisotropic behaviour [244,245,265]. And no experimental evidence for parabolic behaviour of T_c^* under strain for Nb_3Sn from data on single crystals could be found. Along the $\langle 100 \rangle$ direction the strain dependence of T_c^* is found to be linear with $dT_c^*/d\varepsilon_{\langle 100 \rangle} \approx +1.63\,\mathrm{K}\,\%^{-1}$ [265]. For V_3Si, along $\langle 100 \rangle$ direction $dT_c^*/d\varepsilon_{\langle 100 \rangle} \approx +10.6\,\mathrm{K}\,\%^{-1}$ whereas the opposite behaviour is found along $\langle 111 \rangle$ direction where $dT_c^*/d\varepsilon_{\langle 111 \rangle} \approx -0.62\,\mathrm{K}\,\%^{-1}$ (using a Young's modulus of 233 GPa [280] to make the stress-strain conversion). These results open the possibility that the strain dependence of A15 materials can be considered as multimodal: the critical parameters of some grains increase while others decrease, but with a range of sensitivities to strain that depends on the orientation of each grain to the direction of the applied strain. Without much very detailed single crystal anisotropic strain data on A15 materials, it is not possible to characterise the multimodal behaviour in detail. Nevertheless, even for multimodal materials, the bimodal chain model may still be useful as a proxy model, an approximation where each of the two modes in the model

parameterises the average of those grains with increasing critical parameters and those with decreasing critical parameters.

It has long been known that grain boundaries are the dominant pinning mechanism in polycrystalline A15 materials [55, 56]. At J_c, fluxons flow along grain boundary channels with the fluxons in the grains strongly pinned and stationary [262]. Given that the current density in high fields for most polycrystalline materials is typically less than just a few percent of the depairing current density [28, 76], one can consider them as granular to a good approximation. The grain boundaries are complex structures but it is reasonable to assume that they act as a barrier through which the supercurrent quantum mechanically tunnels [94] and include a central region of low T_c and/or higher normal state resistivity where the superconducting order parameter and the (transport) current density that can cross the grain boundary are severely depressed. In polycrystalline materials, Time Dependent Ginzburg–Landau theory (TDGL) shows that large current densities circulate within and around the edge of the grains [262] with some (transport) current density crossing the grain boundaries. In granular materials, one can therefore expect the transport current density to be percolative, consistent with the relatively small ratio of 2 – 3 for J_c when measured in longitudinal and transverse orientation of the applied field with respect to the macroscopic current flow in polycrystalline materials [281, 282] and hence all grain boundaries, both those orthogonal and parallel to the macroscopic current flow direction, contribute to J_c. Given that the critical current through a grain boundary is strongly affected by the tunnelling of superelectrons through the thickness of the boundary, it can be expected

that small changes in thickness to produce significant changes in J_c [283]. Consideration of the role of Poisson's ratio leads to competing behaviour from grain boundaries at different orientations to direction of applied strain. Boundaries orthogonal to an applied tensile strain get wider whereas those parallel to a tensile strain narrow causing J_c to decrease or increase respectively. Hence, applying either tensile or compressive strain always results in J_c across some grain boundaries to decrease and to increase across others. In the context of the chain model and grain boundaries that are highly sensitive to strain, the peak in critical properties is expected to be predominantly associated with the grain boundaries and occur at strains close to the unstrained state in polycrystalline materials. These simple considerations also explain the commonly observed experimental asymmetry in the strain dependence of J_c, because Poisson's ratio is lower than unity, the fact polycrystalline materials are not completely percolative and the nature of the (non-linear) exponential tunnelling mechanism, all lead to J_c reducing more under tensile strain than an equivalent magnitude of compressive strain. It is concluded that polycrystalline superconductors are not best described as homogeneous materials, but as multimodal percolative materials. Whether tension or compression is applied to the material, it consists of competing grains and grain boundary components where some grain boundaries widen and others narrow depending upon their orientation relative to the direction of the applied strain.

The bronze route Nb_3Sn wire shows similar features to REBCO - namely temperature and field dependence of ε_{peak} (figures 4.15 and 4.7 respectively) and double valued behaviour of $F_{p,max}$ (figures 4.23 and 4.22 respectively). Unfortunately there are very

few other sufficiently comprehensive datasets in the literature that provide detailed measurements of the field and temperature dependence of $\varepsilon_{\text{peak}}$ for bronze route wires. To within the accuracy of the data, the $\varepsilon_{\text{peak}}$ data in figure 4.16 for the internal tin conductor shows little or no field and temperature dependence and figure 4.24 shows no double valued behaviour of $F_{\text{p,max}}$. These results are consistent with a value of $f \approx 0.5$ for $\alpha = 1$. A single detailed enough dataset for $\varepsilon_{\text{peak}}$ in an A15 conductor was found in the literature for an internal tin Nb_3Sn conductor and shows similar behaviour with $f \approx 0.5$ for $\alpha = 1$ [284] (WST sample, data available at [285]). However double valued behaviour of $F_{\text{p,max}}$ has also been observed in literature [156] for two jelly roll internal tin Nb_3Sn wires suggesting $f > 0.5$ for $\alpha = 1$. We suggest that as with REBCO the composition and manufacturing process affect the relative domain fractions f of the competing components in Nb_3Sn. The Nb_3Al data appears to show some contradictory behaviour but it is also noted that it is the material for which there is almost no variable-strain single crystal data. Figure 4.16 shows a clear temperature dependence for $\varepsilon_{\text{peak}}$ but only a weak field dependence at each temperature. This is in contrast to the bronze route Nb_3Sn data in figure 4.15, where the same value of f is found whether variable temperature or variable field data are taken. It is noted that the field dependent behaviour of $\varepsilon_{\text{peak}}$, is only dependent on the accuracy of the universal scaling law (section 4.5), whereas the temperature dependence is also dependent on the parameterisation of $B^*_{c2i}(0, \varepsilon_{\text{app}})$ with $T^*_{ci}(\varepsilon_{\text{app}})$ through the exponent w. A lack of single crystal data means the $B^*_{c2i}(0, \varepsilon_{\text{app}})$ parameterisation of each component is unknown. For example if the possibility that w is anisotropic is allowed, it could lead to

a temperature dependence of $\varepsilon_{\text{peak}}$ with minimal field dependence for $f \sim 0.5$ and $\alpha = 1$ which is consistent with the lack of any double valued behaviour of $F_{\text{p,max}}$ observed in figure 4.25. We note that if the variable field data are considered alone (cf. figure 4.17), Nb_3Al is described by the chain model with $f \sim 0.5$ for $\alpha = 1$. If both the field and temperature data are considered (cf. figure 4.35) then $f \sim 0.67$ for $\alpha = 1$ as shown in table 4.7. It is noted that the changes in $\varepsilon_{\text{peak}}$ for A15 materials as a function of field and temperature are much smaller than those observed in REBCO. This is due to the higher N-values in A15 materials, which acts to decrease the magnitude of the changes in $\varepsilon_{\text{p,JD}}$ through eqn 4.17. Also, differences between $\varepsilon_{\text{peak}}$ and $\varepsilon_{J_{\text{cA}}=J_{\text{cB}}}$ similar to those observed in this work have been measured using XRD [183] and these can be better understood in the framework of the chain model.

4.9 Conclusions

Transport $J_{\text{c}}(B, T, \varepsilon_{\text{app}})$ measurements on samples of REBCO tape, bronze route Nb_3Sn wire are performed alongside a reanalysis of previously published measurements on internal tin Nb_3Sn and jelly-roll Nb_3Al wires over an extensive range of fields ($B \perp$ tape surface for REBCO), temperatures and uniaxial strains. For REBCO tape, transport measurements of the effective upper critical field were performed and parameterised. Engineering parameterisations for J_{c} were also obtained for all four materials. Features that cannot be described by standard flux pinning scaling with a homogeneous strain response were observed for REBCO and bronze route Nb_3Sn:

the field and temperature dependence of the strain at which J_c is maximised ε_{peak} and the double valued behaviour of $F_{p,max}$ as a function of B^*_{c2}. These features were not observed in the internal tin Nb_3Sn and temperature dependence of ε_{peak} was observed in jelly-roll Nb_3Al wire but field dependence and double valued behaviour of $F_{p,max}$ were not.

The bimodal chain model has been developed to account for the inverted parabolic behaviour of the $J_c(\varepsilon_{app})$ in REBCO. It is found that the temperature and field dependence of ε_{peak} and double valued behaviour of $F_{p,max}$ are natural results of this model. The model is based on two domains with opposing strain dependencies of the critical parameters of relative magnitude and relative domain fractions of f and $1-f$. It is found that the position of ε_{peak} is not determined by a peak in the critical parameters but by the combination of the strain responses from the two competing domains. For $f < \alpha/(\alpha+1)$ it is found ε_{peak} moves further into compression as the field or temperature is lowered, and for $f > \alpha/(\alpha+1)$ moves further into tension. For $\alpha = 1$, it is found $F_{p,max}$ is higher in compression than in tension for the same value of B^*_{c2} when $f < 0.5$, and is higher in tension than in compression when $f > 0.5$. It is found ε_{peak} is not a function of field and temperature for $f = \alpha/(\alpha+1)$, whereas $F_{p,max}$ is a single valued function of B^*_{c2} only for the specific case $f = 0.5$ and $\alpha = 1$. An analytic equation for the field, temperature and domain fraction dependence of ε_{peak} is also derived,

$$\varepsilon_{peak} = \frac{f - \alpha/(1+\alpha)}{f(1-f)(1+\alpha)} \frac{F(N_0, S_N)}{g_A(B,T)} + \varepsilon_{J_{cA}=J_{cB}}, \tag{4.24}$$

where

$$F\left(N_0, S_N\right) = \frac{N_0}{N_0\left(N_0+1\right) - 2S_N\left(N_0-1\right)}, \tag{4.25}$$

and the factor g_{A} is a function containing the temperature and field dependencies.

Whilst the chain model was developed for REBCO, it has also been discussed in the context of the role of grain boundaries in LTS materials. It is concluded: the two historical assumptions about the properties of polycrystalline Nb_3Sn (there is a fortuitous coincidence between the Fermi-level and a peak in the DoS in the unstrained state and the grains respond in a broadly homogeneous manner to an applied strain) are both incorrect; the field and temperature dependence of $\varepsilon_{\mathrm{peak}}$ and the double valued behaviour of $F_{\mathrm{p,max}}$ with B^*_{c2} show that bronze route Nb_3Sn superconductors are bi- or multimodal materials and cannot accurately be described using a homogeneous strain dependence for their critical parameters. The internal tin Nb_3Sn and (probably) jelly-roll Nb_3Al conductors are multimodal with $f = \alpha/\left(\alpha+1\right)$. The (unimodal) LTS scaling laws for homogeneous materials can usefully parameterise their behaviour but do not provide a very good physical description of the mechanisms determining J_{c} as a function of strain.

Chapter 5

The strain and angular dependence of the critical current density in REBCO tape

5.1 Introduction

Chapter 4 provided strong evidence that while universal scaling laws can provide excellent parameterisations of $J_c(B, T, \varepsilon_{app})$ the underlying physical assumptions are incorrect. The strain dependence is in fact an emergent behaviour arising from competing contributions of grains and/or grain boundaries with opposing strain dependencies.

Magnets made with REBCO tape can achieve fields $> 20\,\mathrm{T}$ inaccessible to their LTS counterparts. The anisotropy of these tapes adds another dimension to the $J_c(B, T, \varepsilon_{app}, \theta)$ phase space where θ is the angle between B and the normal to the

tape surface [140, 142, 143, 146, 286–289]. There are relatively few studies which look at the strain dependence of REBCO in both tension and compression [198–207, 290, 291] (which is required for a complete understanding of the behaviour), and most of these concentrate on $\theta = 0°$. Investigations into the combined strain and angular response of J_c in coated conductors in the literature are limited [191, 192, 241]. In fact the author could only find reports with only tensile applied strain and $B < 1.5\,\mathrm{T}$. This chapter reports on the second experimental campaign on the exactly the same piece of material used in chapter 4. It increases the data we have and our understanding of the angular dependent region of phase space. We investigate if the bimodal chain model remains valid as a function of angle.

In this chapter variable field, temperature, strain and angle data are presented. In-depth flux pinning analysis of the data is performed, and these results are used to inform detailed discussion of the angular dependencies of J_c, the index of transition N and the effective upper critical field B^*_{c2}. The field and temperature dependence of ε_{peak} is identified as a function of angle and it is shown that the results are consistent with the bimodal model. Sections 5.2 and 5.3 detail the experimental procedures and present the results respectively. In section 5.4 the critical current density as a function of angle is analysed. In section 5.5 an in-depth flux pinning analysis is performed. In section 5.6 the field, temperature and angular dependence of ε_{peak} is used to estimate values of $\varepsilon_{J_{cA}=J_{cB}}$ and f. Sections 5.7 and 5.8 provide the discussion and conclusion respectively.

5.2 Experimental procedures

In this chapter the phase space has been expanded to include the angular dependence of J_c at the cost of reducing the density of points obtained as function of temperature and field. The custom-built probe used in chapter 4 was again used in Durham's in-house 15 T liquid helium cooled, 40 mm wet bore, superconducting, split-pair magnet to perform the measurements. Descriptions of the setup and experimental procedure can be found in chapter 4. The entire field, temperature, strain and angle phase space was too large to investigate comprehensively in a single experimental campaign. To maximise the range of angular phase space measured, the experiment was split into two distinct parts: dense angular dependent measurements at $\varepsilon_{app} \approx 0\,\%$ and $\varepsilon_{app} \approx -1\,\%$, and in-depth field, temperature and strain dependent measurements at selected angles. In the bimodal chain model analysis completed in this chapter, results from chapter 4 for $\theta = 0°$ are also included. Relaxation of the experimental probe after thermal cycling between the two experimental campaigns means there was a slight difference in the initial unstrained state as measured using the strain gauge. The unstrained state in this campaign was 0.024 % higher (i.e. in tension) than in the previous campaign (cf. chapter 4). It was chosen not to force the zero applied strain state to be equivalent to the previous experiment as, for ease, the initial measurements are taken without attaching the screw jack (required to vary the applied strain) to the probe and since the difference is known it does not affect the results. The strain values quoted in this chapter are consistent with those quoted in chapter 4.

Dense J_c measurements were then taken as a function of θ at $T = 20, 40$ and $60\,\mathrm{K}$, $B = 2$ and $4\,\mathrm{T}$ and $\varepsilon_{app} = 0.024\,\%$. $\theta = 0°$ was fixed when the B-field was normal to the surface of the tape using a Hall probe mounted on the tape surface. The strain was then taken to $\varepsilon_{app} = -0.976\,\%$ and a second set of dense angular measurements were obtained at the same temperatures and fields. The peak in $J_c(\theta)$ associated with the *ab*-plane occurred at $\theta = 87.5°$. Using the dense angular measurements four angles were selected $\theta = 47.5°$, $77.5°$, $82.5°$ and $87.5°$ which cover a large range in J_c values. At these angles, in depth field, temperature and strain dependent J_c measurements were taken. Starting at $\varepsilon_{app} = -0.976\,\%$, J_c measurements were obtained, at temperatures of $20, 40$ and $60\,\mathrm{K}$ and fields from 14 to $2\,\mathrm{T}$ in intervals of $2\,\mathrm{T}$ or until $J_c > 250\,\mathrm{A}$. The angle was then changed to the next angle and the measurement set repeated until measurements were obtained for all angles. The strain was then increased in intervals of $0.25\,\%$ up to $+0.524\,\%$ and held at each strain where another B, T and θ dependent dataset was obtained. The strain was then relaxed to $\varepsilon_{app} = 0.024\,\%$ and measurements of J_c taken to confirm the reversibility of the sample. These results were found to agree with the results taken at the start of the experiment, showing the sample remained reversible and undamaged. J_c was determined at the $100\,\mu\mathrm{V\,m^{-1}}$ criterion. The shunt current through the sample holder and stabilising materials was corrected for using the known field and strain dependent resistance of the shunt in the same manner as chapter 4. The index of transition N was determined by fitting the relation $E/E_c = (J/J_c)^N$ to the shunt corrected data in the transition region between $10\,\mu\mathrm{V\,m^{-1}}$ and $100\,\mu\mathrm{V\,m^{-1}}$.

It was considered whether small uncertainties $\sim 1°$ in the angle caused by not returning the probe to the exact same angle at each applied strain could have caused significant additional uncertainty in the J_c measurements due to the strong angular dependence of J_c. To test this; after the main suite of measurements and reversibility checks, the probe was moved to $\theta = 87.5°$, the strain cycle from $\varepsilon_{app} = -0.976\,\%$ to $\varepsilon_{app} = +0.524\,\%$ was repeated without changing the angle between measurements at different strains. At each strain J_c measurements were taken at $B = 4, 10$ and $14\,\mathrm{T}$, and $T = 40$ and $60\,\mathrm{K}$. The results were compared to results from the main suite of measurements and were found to be in good agreement.

5.3 Results

5.3.1 Angular dependence of the critical current density and index of transition

Figure 5.1 shows dense angular measurements of J_c as a function of field and temperature at $\varepsilon_{app} = 0.024\,\%$ and $\varepsilon_{app} = -0.976\,\%$. The peak in $J_c(\theta)$ occurs when the field is nearly parallel to the *ab*-planes. Figure 5.2 shows these results normalised to the peak $J_c(\theta)$ value determined by fitting a double Lorentzian to the $J_c(\theta)$ data. The positions of the angular peaks experimental uncertainties of 87.5° for all fields and temperatures. This shows the *ab*-planes of the REBCO are slightly offset from the plane of the tape. In figure 5.2 we see that the peak becomes more pronounced at higher fields and lower temperatures. Changing the strain from $0.024\,\%$ to $-0.976\,\%$ does not change the angular

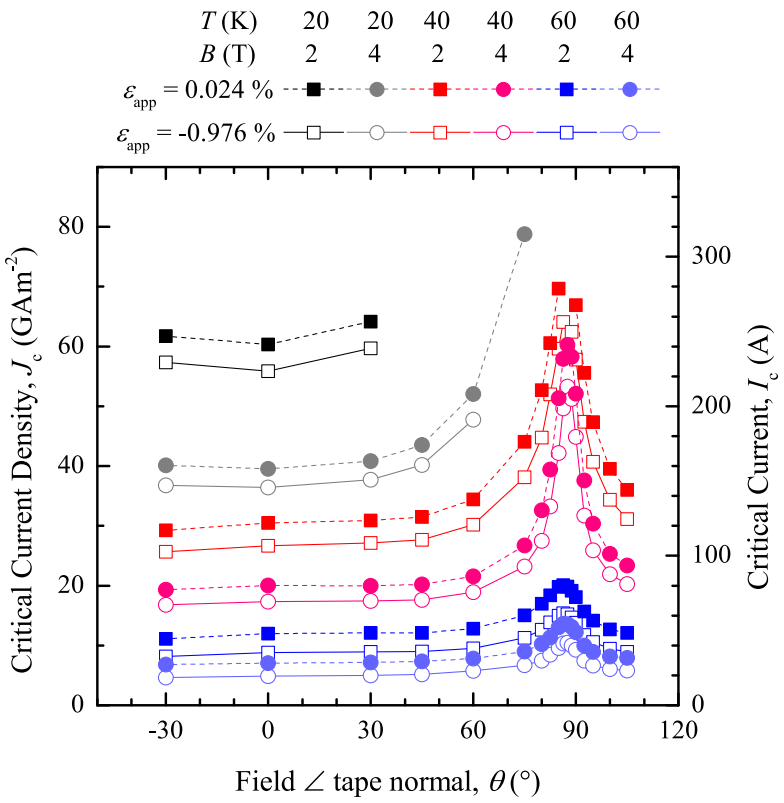

Figure 5.1. Critical current density as a function of angle at $\varepsilon_{\text{app}} = 0.024\,\%$ and $-0.976\,\%$.

position and shape of the angular peaks. Figure 5.3 shows the dense angular dependent results when normalised to $J_c\,(B, T, \varepsilon_{\text{app}} = 0.024\,\%, \theta)$. Figures 5.2 and 5.3 show that the field and angular dependence of the ratio $J_c\,(B, T, -0.976\,\%, \theta)/J_c\,(B, T, 0.024\,\%, \theta)$ is low, $\leq 5\,\%$, for all combinations of field and temperature investigated except for $B = 4$ T, $T = 60$ K where this rises to $\sim 10\,\%$. Figure 5.4 shows the dense angular dependent results for the index of transition N as a function of B and T at $\varepsilon_{\text{app}} = 0.024\,\%$ and $\varepsilon_{\text{app}} = -0.976\,\%$. The N-values decrease at angles where the magnetic field is close to parallel to the *ab*-plane.

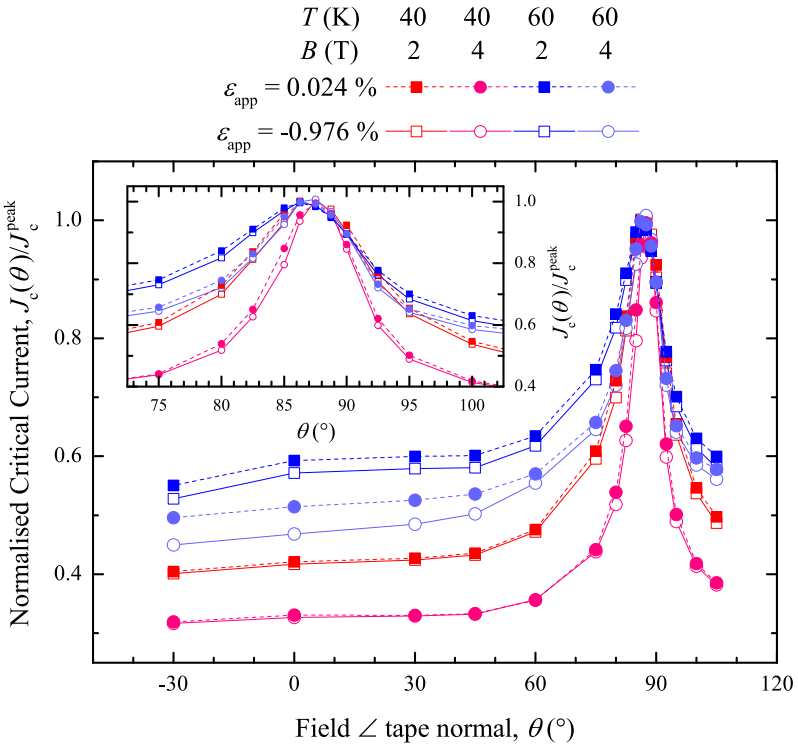

Figure 5.2. Normalised critical current as a function of angle at $\varepsilon_{\mathrm{app}} = 0.024\,\%$ and $-0.976\,\%$. Values are normalised to the maximum J_{c} value determined by fitting a double Lorentzian to the angular J_{c} data at and around the peak. (inset) Detail around the peak.

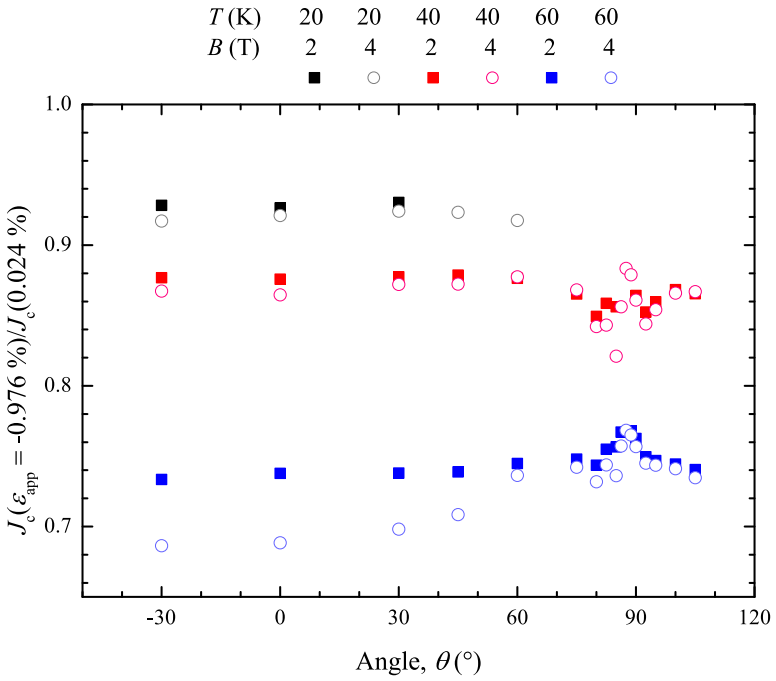

Figure 5.3. $J_c\,(\varepsilon_{app} = -0.976\,\%)\,/\,J_c\,(\varepsilon_{app} = 0.024\,\%)$ as a function of angle at different fields and temperatures.

5.3.2 Critical current density and index of transition

Figure 5.5 shows an overview of all the in-depth J_c measurements at selected angles and figure 5.6 shows $N-1$ as a function of J_c on a log-log plot. At $\theta = 0°$, N can be characterised as a function of J_c using eqn 4.4. At the higher angles investigated in this study no single combination of r_N and S_N can describe all the data. It is found that r_N and S_N must be temperature and angular dependent to parameterise our data; the values of S_N are summarised in table 5.1 and shown graphically in figure 5.7. There was insufficient data at $\theta = 82.5°$ and $T = 20\,\mathrm{K}$ to perform a fit so S_N has been set to be zero.

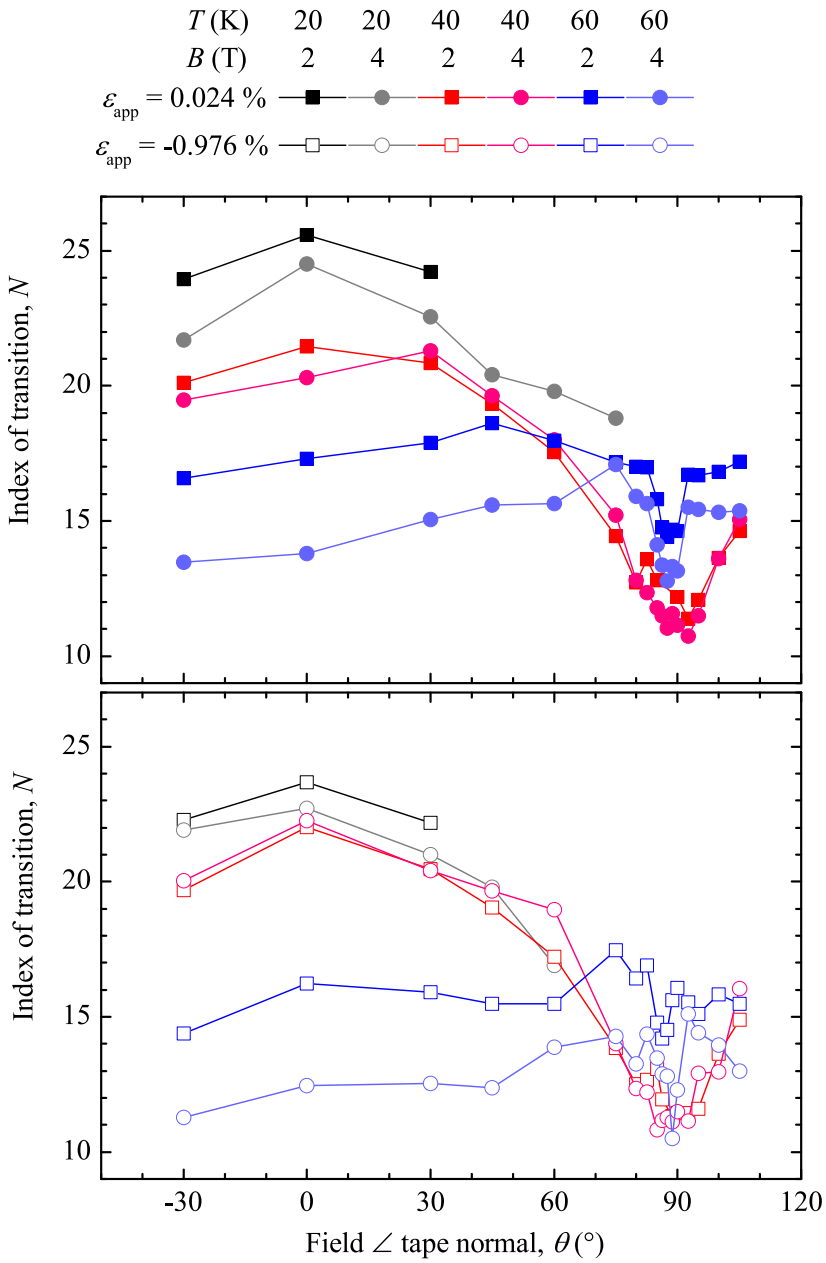

Figure 5.4. Angular dependence of the index of transition N at $\varepsilon_{\mathrm{app}} = 0.024\,\%$ and $-0.976\,\%$ at different temperatures and fields.

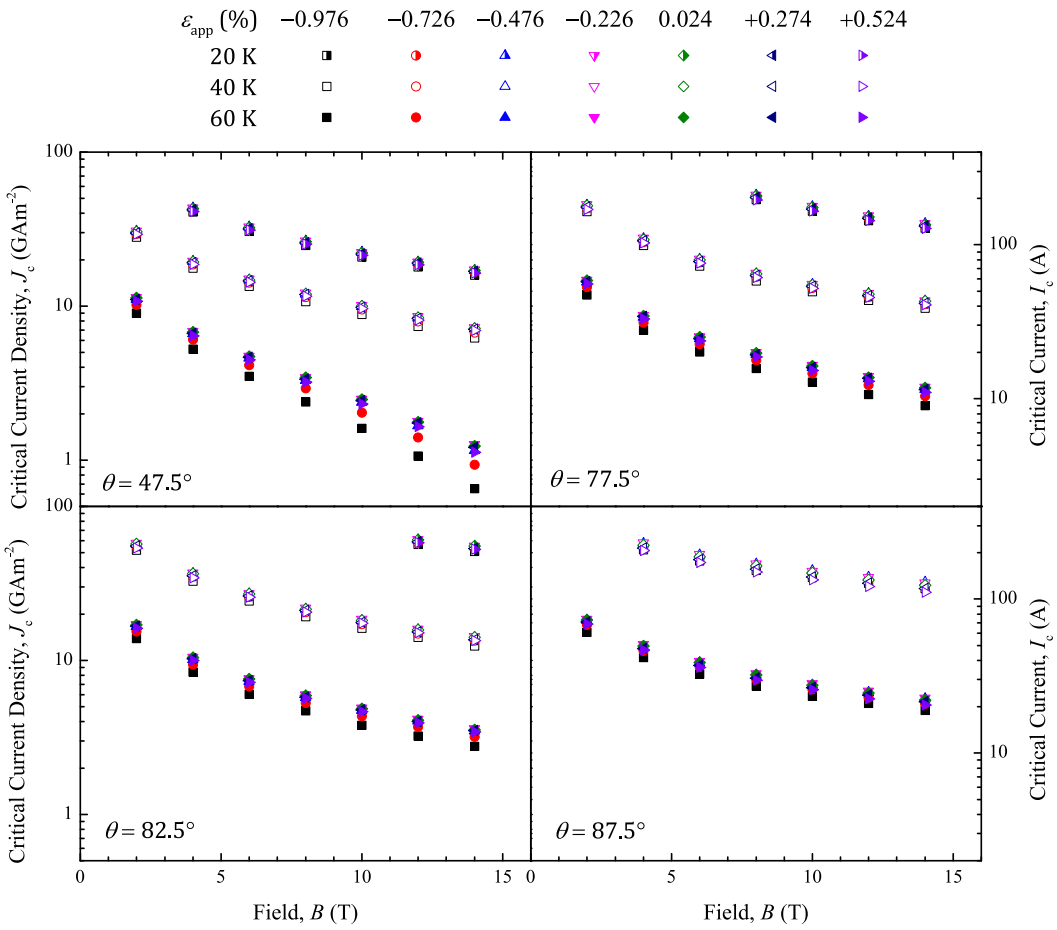

Figure 5.5. Field, temperature and strain dependence of the critical current density at four different angles θ.

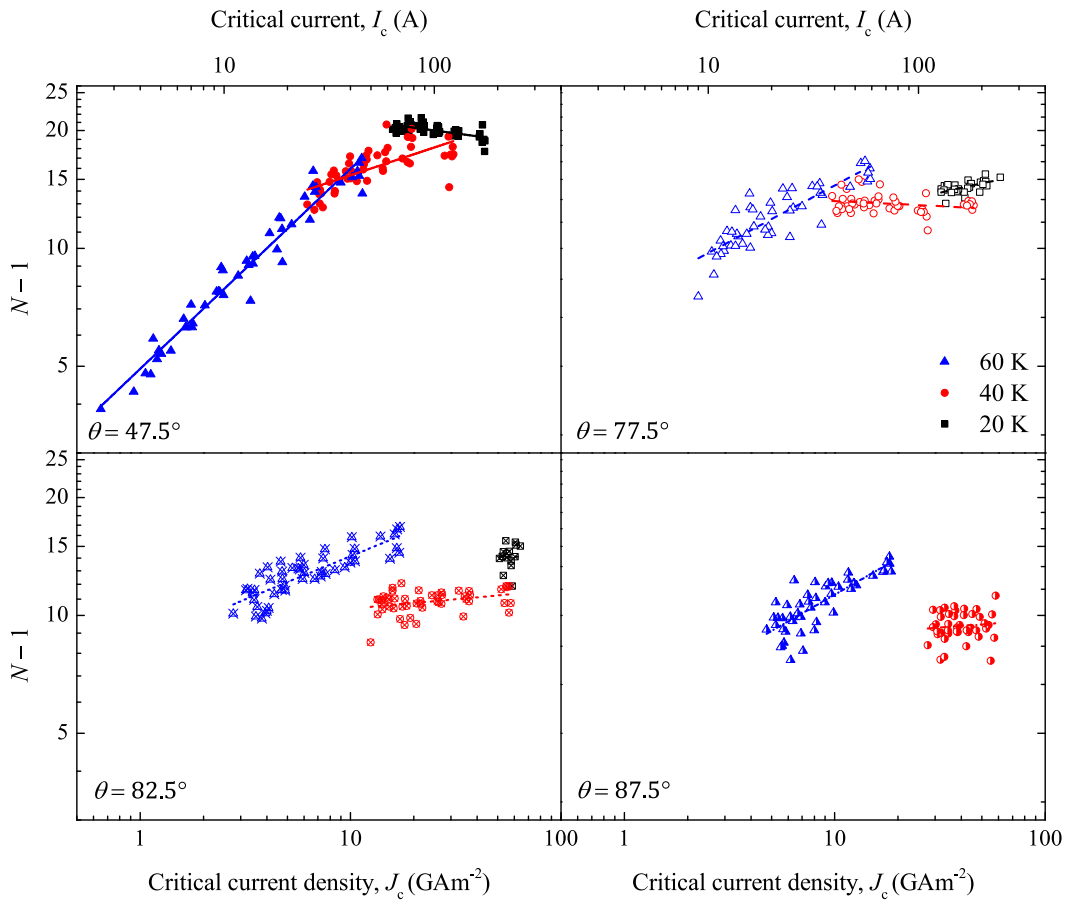

Figure 5.6. $N-1$ as a function of J_c at four different angles.

Table 5.1. The temperature and angular dependent values of S_N derived from fits to the data. There was insufficient data at $\theta = 82.5°$ and $T = 20\,\mathrm{K}$ to perform a fit so S_N has been set to be zero.

θ (°)	T (K)	S_N
47.5	20	-0.07 ± 0.01
	40	0.18 ± 0.03
	60	0.51 ± 0.02
77.5	20	0.12 ± 0.03
	40	-0.03 ± 0.02
	60	0.29 ± 0.02
82.5	20	0
	40	0.04 ± 0.02
	60	0.22 ± 0.02
87.5	40	0.04 ± 0.06
	60	0.31 ± 0.03

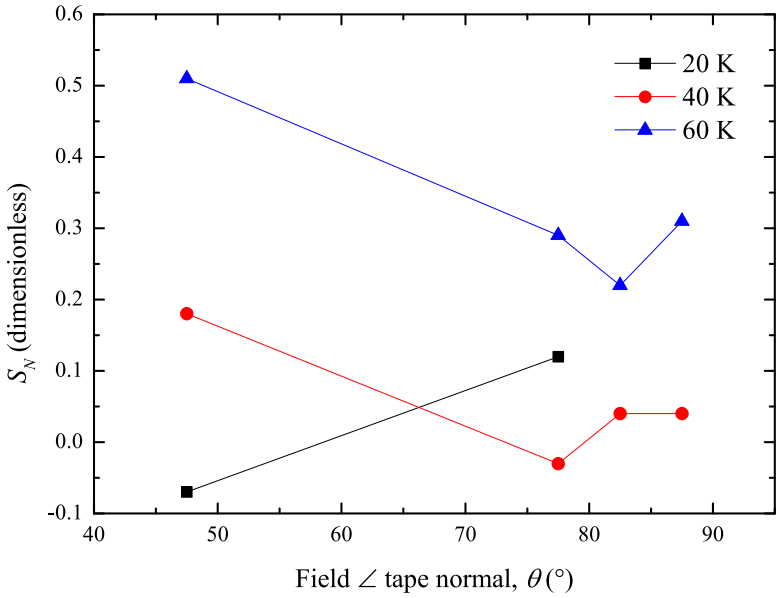

Figure 5.7. S_N as a function of angle at different temperatures.

5.3.3 Strain peak in the critical current density

The strain at which J_c is maximised ε_{peak} is determined as a function of field, temperature and angle by fitting the inverted parabola eqn 4.3. Figure 5.8 shows some examples of the inverted parabolic nature of $J_c(\varepsilon_{app})$ at $\theta = 87.5°$. Also, shown as open symbols, are the results of fixing the angle at $\theta = 87.5°$ before performing a strain cycle where the angle remained fixed. Comparison between these datasets would show any errors introduced by cycling the angle between different sets of strain measurements, during the main suite of measurements. We conclude that the procedure we used to set the angles quoted here did not cause significant uncertainty in J_c and did not affect the values of ε_{peak} obtained to within the experimental uncertainties. Figure 5.9 shows a summary of ε_{peak} as a function of field, temperature and angle. The uncertainties in ε_{peak} are taken directly from the fitting procedure for the inverted parabolas. There is a strong temperature, and angular dependence to ε_{peak} and almost no measureable field dependence.

5.4 Functional form of $J_c(\theta)$

The measurements presented here are at low temperatures and high angles and therefore are in the low reduced field limit $b \ll 1$. Using the scaling law, eqn 4.10, with $m = 2$ in this limit, the ratio of the critical current density at arbitrary applied strains ε_1 and

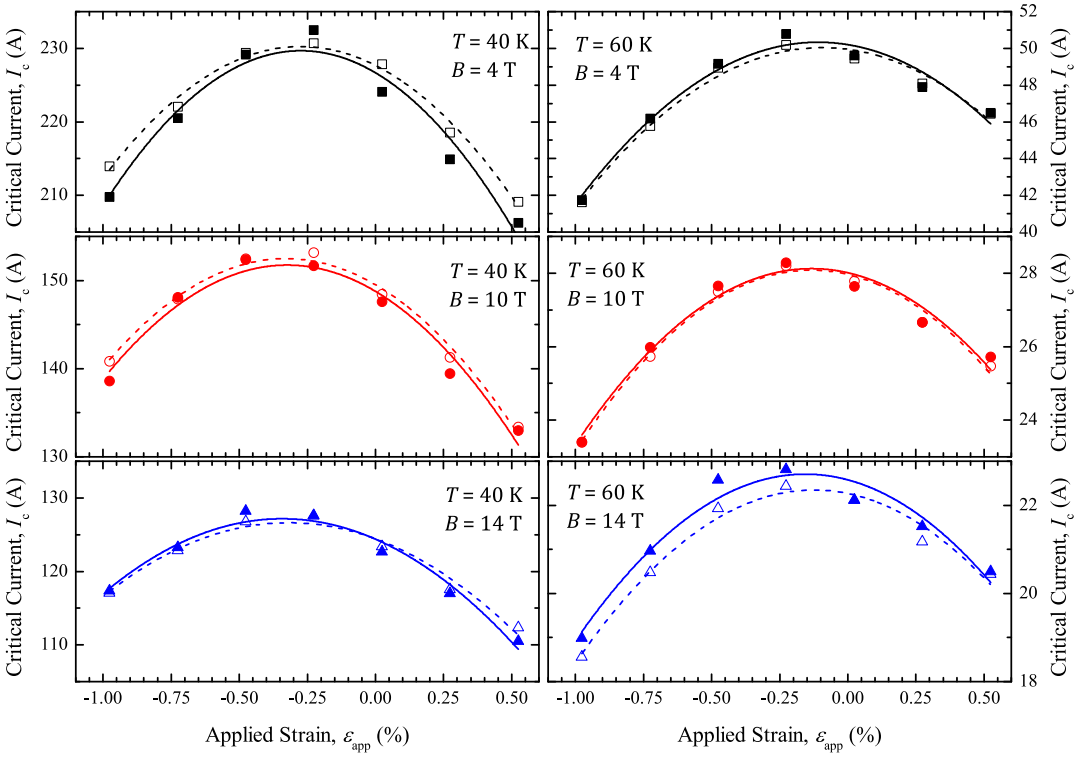

Figure 5.8. Parabolic fits to the strain dependent critical current data at an angle of $\theta = 87.5°$. Each of the closed symbols (and solid lines) were generated at each strains after the angle between the magnet field and the tape had been cycled. In contrast, the open symbols (and dashed lines) were all generated while the angle between the magnet field and the tape was held fixed.

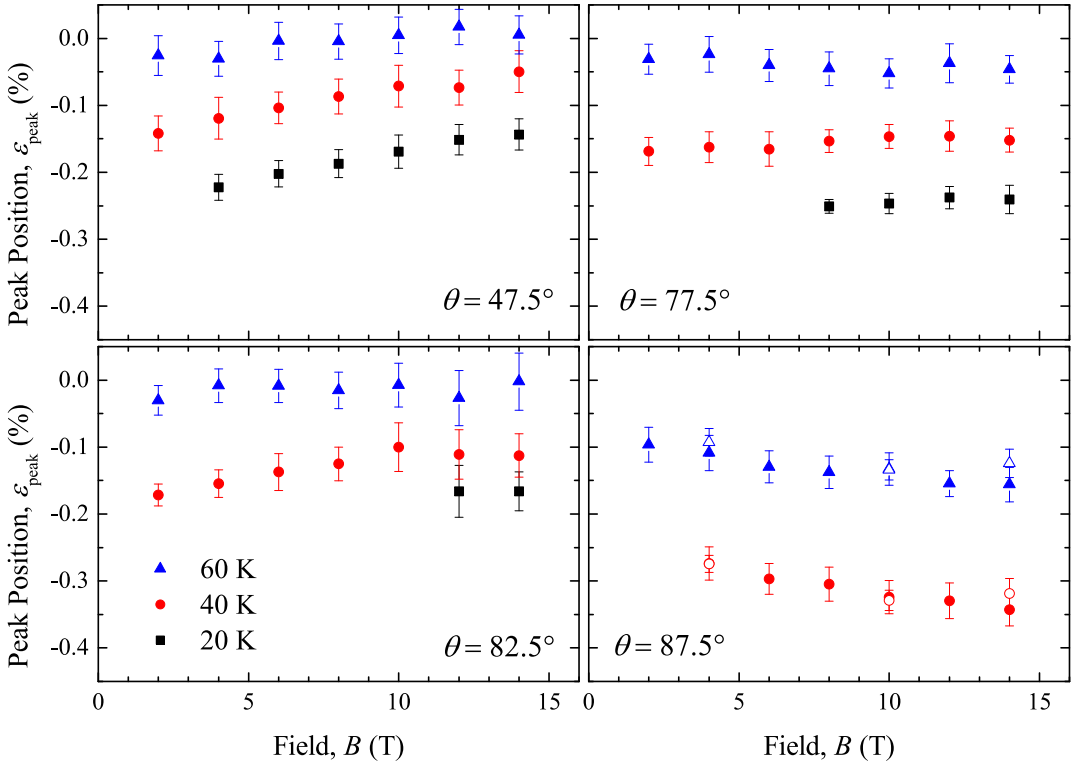

Figure 5.9. Field, temperature and angular dependence of ε_{peak} determined using parabolic fits to the strain dependent data for: (closed symbols) the main data set, where the angle was changed between varying the strain; and (open symbols) the fixed angle data set at $\theta = 87.5°$, where the angle was not changed between varying the strain.

ε_2, $J_c(B,T,\varepsilon_1,\theta)/J_c(B,T,\varepsilon_2,\theta)$ is given by

$$\frac{J_c(B,T,\varepsilon_1,\theta)}{J_c(B,T,\varepsilon_2,\theta)} = \frac{A}{A}\left[\frac{T_c^*(\varepsilon_1)\left(1-\left(\frac{T}{T_c^*(\varepsilon_1)}\right)^2\right)}{T_c^*(\varepsilon_2)\left(1-\left(\frac{T}{T_c^*(\varepsilon_2)}\right)^2\right)}\right]^2 \left(\frac{B_{c2}^*(T,\varepsilon_1,\theta)}{B_{c2}^*(T,\varepsilon_2,\theta)}\right)^{n-p-2}. \quad (5.1)$$

We have assumed that the effective upper critical field $B_{c2}^*(T,\varepsilon_{app},\theta)$ is separated into a component describing the functional form $f_{B_{c2}^*}(T,\varepsilon_{app},\theta)$ and a normalisation constant $B_{c2}^*(0,\varepsilon_{app},\theta)$ of the form $B_{c2}^*\left(T,\varepsilon_{app},\theta\right) = B_{c2}^*(0,\varepsilon_{app},\theta)\, f_{B_{c2}^*}(T,\varepsilon_{app},\theta)$. This leads to

$$\frac{J_c(B,T,\varepsilon_1,\theta)}{J_c(B,T,\varepsilon_2,\theta)} = \left(\frac{T_c^*(\varepsilon_1)}{T_c^*(\varepsilon_2)}\right)^2 \left(\frac{1-t^2(\varepsilon_1)}{1-t^2(\varepsilon_2)}\right)^2 \left(\frac{B_{c2}^*(0,\varepsilon_1,\theta)\, f_{B_{c2}^*}(T,\varepsilon_1,\theta)}{B_{c2}^*(0,\varepsilon_2,\theta)\, f_{B_{c2}^*}(T,\varepsilon_2,\theta)}\right)^{n-p-2}. \quad (5.2)$$

Using the relation $B_{c2}^*(0,\varepsilon_1,\theta)/B_{c2}^*(0,\varepsilon_2,\theta) = \left(T_c^*(\varepsilon_1)/T_c^*(\varepsilon_2)\right)^w$ where w is a constant [178, 179] the following equation is obtained

$$\frac{J_c(B,T,\varepsilon_1,\theta)}{J_c(B,T,\varepsilon_2,\theta)} = \left(\frac{T_c^*(\varepsilon_1)}{T_c^*(\varepsilon_2)}\right)^2 \left(\frac{1-t^2(\varepsilon_1)}{1-t^2(\varepsilon_2)}\right)^2 \left(\left(\frac{T_c^*(\varepsilon_1)}{T_c^*(\varepsilon_2)}\right)^w \frac{f_{B_{c2}^*}(T,\varepsilon_1,\theta)}{f_{B_{c2}^*}(T,\varepsilon_2,\theta)}\right)^{n-p-2}. \quad (5.3)$$

This equation shows there is no field dependence for the ratio $J_c(B,T,\varepsilon_1,\theta)/J_c(B,T,\varepsilon_2,\theta)$ in the low reduced field limit but there is a temperature dependence. These predictions are in agreement with the experimental data shown in figures 5.2 and 5.3. The data also show no angular dependence for the ratio $J_c(B,T,\varepsilon_1,\theta)/J_c(B,T,\varepsilon_2,\theta)$. In the context of eqn 5.3 we suggest this means $f_{B_{c2}^*}(T,\varepsilon_{app},\theta) \to f_{B_{c2}^*}(T,\varepsilon_{app})$, and that the

parameters w, n, p are independent of angle. The arguments break down at $B = 4\,\mathrm{T}$, $T = 60\,\mathrm{K}$ and $\theta \not\approx 90°$, which is attributed to the low reduced field limit not being applicable.

At temperatures close to T_c, $f_{B^*_{c2}}(T, \varepsilon_{app})$ is commonly given by $f_{B^*_{c2}}(T, \varepsilon_{app}) = (1 - T/T^*_c(\varepsilon_{app}))^s$ for HTS materials [257], however at lower temperatures it is known to deviate from this relation as discussed in chapter 4 [264]. The functional form of $f_{B^*_{c2}}(T, \varepsilon_{app})$ over the whole temperature range is unknown since measurements of B^*_{c2} are lacking due to its extremely large value at low temperature. It has already been shown in chapter 4 that the field, temperature, strain and angular scaling of REBCO tapes cannot be parameterised using a simple global scaling law at fixed angle. Unsurprisingly attempts to apply a global fitting procedure to the angular data in this chapter also proved unsuccessful.

5.5 Flux pinning scaling curves and determination of $B^*_{c2}(\theta)$

Here a method similar to that in chapter 4 is again used, which decouples $F_{p,max}$ from B^*_{c2}, to produce the universal flux pinning scaling curve (cf. figure 5.10), without making any assumptions about their temperature and angular dependencies or their relation to each other. The high B^*_{c2} values associated with the fields, temperatures and angles chosen to make measurements in this chapter were too high to be measured directly. The values of $p = 0.56$ and $q = 2.47$ were fixed at their values obtained at

$\theta = 0°$ from chapter 4 where direct measurements of B^*_{c2} were available and the flux pinning scaling equation, eqn 4.8 was fitted to produce a universal scaling curve with $F_{p,max}$ as an unconstrained temperature, strain and angular dependent free parameter, and B^*_{c2} is constrained through the following equation

$$B^*_{c2}(T, \varepsilon_{app}, \theta) = h(T, \theta)\, B^*_{c2}(T, \varepsilon_{app}, \theta = 0°). \tag{5.4}$$

where $h(T, \theta)$ is a function of temperature and angle and $B^*_{c2}(T, \varepsilon_{app}, \theta = 0°)$ is constrained by the measurements in chapter 4.

One of the most important features of a flux pinning scaling curve is the location of $F_{p,max}$, which for a universal scaling curve occurs at the same value of b independent of temperature, strain and angle. Most of the data obtained in this study are at fields that are even below that at which $F_{p,max}$ occurs. Because the turning point in F_p at $F_{p,max}$ is only captured at the lowest angle, fitting procedures using standard weighting techniques lead to F_p curves which are clearly erroneous on visual inspection, often with unphysical values of $F_{p,max}$ and B^*_{c2}. The high gradient of the F_p curve at very low reduced field and the small reduced field region over which the data are fitted are responsible for this, making the results of the fitting relatively insensitive to large variations in the effective upper critical field. To lower the impact of this, the data was weighted by $F_p \times B$ forcing the fitting procedure to weight data closer to $F_{p,max}$ more heavily which resulted in more physically reasonable scaling curves. Figure 5.10 shows the universal flux pinning scaling curve obtained. Figure 5.11 shows the values of

$B^*_{c2}(T,\varepsilon_{app},\theta)/B^*_{c2}(T,\varepsilon_{app},\theta=0°)$ together with the predicted forms from anisotropic Ginzburg-Landau theory [140, 142, 143, 146] and the extreme theoretical case of the 2D Tinkham model [41] for thin films. The data in figure 5.11 do not show a consistent temperature dependence at all angles. The insets of figure 5.10 and 5.11 show the results when the author imposed a consistent temperature dependence at all angles for $h(T,\theta)$ which also give physically reasonable F_p scaling curves and values of B^*_{c2}. The results show that physically reasonable values for the fitting parameters can be found but are obscured by other values that fit equally well to the limited dataset.

Figure 5.12 shows the results of $F_{p,max}[\kappa^*_1]^2$ vs B^*_{c2} on a log-log plot for the variable angle data including the data at $\theta = 0°$ from chapter 4. The solid line is a linear fit to the data at $\varepsilon_{app} = 0\,\%$ which gives a value of $n = 2.85$.

5.6 Estimating f and $\varepsilon_{J_{cA}=J_{cB}}$ from $\varepsilon_{peak}(B,T,\theta)$

In this section we consider whether the bimodal chain model can be extended to include angle. Following the method outlined in chapter 4, eqn 4.17 shows that plotting ε_{peak} against $dT^*_{cA}/d\varepsilon_{JD}|_{\varepsilon_{JD}=0\%}\,F/g_{A,HTS}$ should give a linear relationship where the intercept gives $\varepsilon_{J_{cA}=J_{cB}}$ and the gradient can be used to calculate f for given values of $dT^*_{cA}/d\varepsilon_{JD}|_{\varepsilon_{JD}=0\%}$ and α. Figure 5.13 shows this plot for the angular data obtained on this sample as well as the data at $\theta = 0°$ from chapter 4. The values of S_N are taken from table 5.1. As was found in chapter 4, although there are relatively large uncertainties in the values of S_N they have little impact on the final results. N_0 is

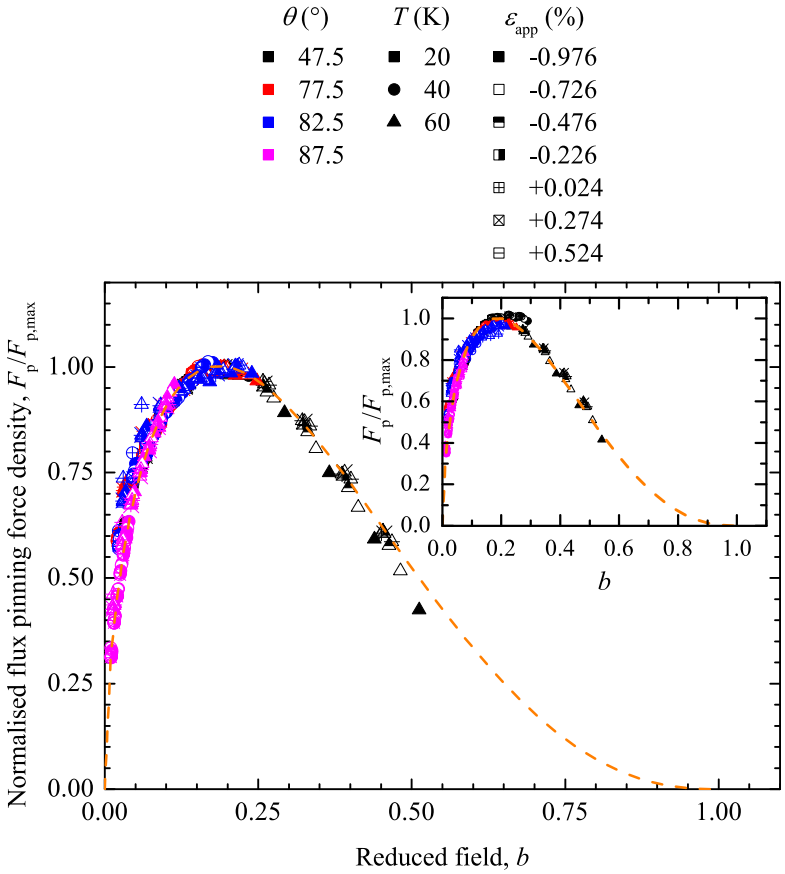

Figure 5.10. Normalised flux pinning scaling curve obtained from the fitting process described in section 5.5. Eqn 4.8 was fitted by fixing the parameters $p = 0.56$ and $q = 2.47$ to their values determined at $\theta = 0°$. $F_{\mathrm{p,max}}$ is an unconstrained temperature, strain and angular dependent free parameter. B^*_{c2} is constrained through eqn 5.4 where $h\,(T, \theta)$ is an unconstrained temperature and angular dependent free parameter and $B^*_{\mathrm{c2}}\,(\varepsilon_{\mathrm{app}}, \theta = 0°)$ is constrained by the values obtained in chapter 4. The values of B^*_{c2} obtained are summarised in figure 5.11. The data are weighted by $F_{\mathrm{p}} \times B$. (inset) The results when $h\,(T, \theta)$ is determined manually to give a reasonable flux pinning scaling curve and have a systematic temperature dependence as a function of angle.

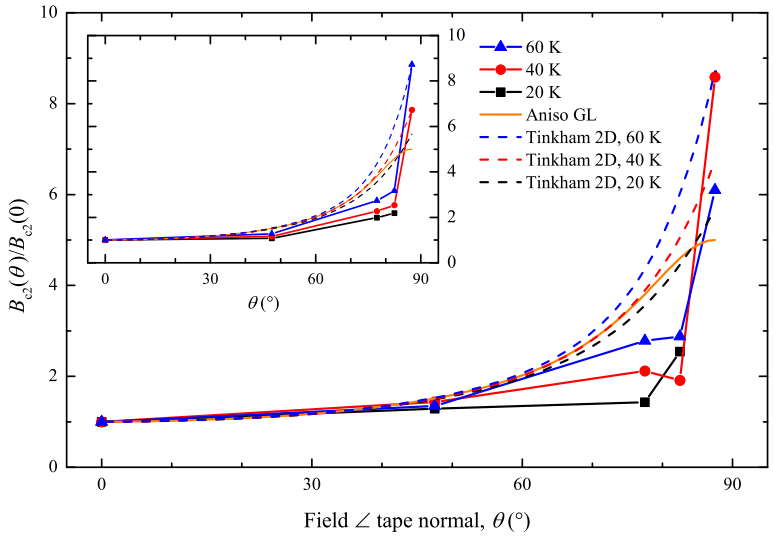

Figure 5.11. $B^*_{c2}(\theta)/B^*_{c2}(0)$ as a function of angle and temperature - the ratio was determined by fitting F_p curves to the data where F_p is given by eqn 4.8, the parameters $p = 0.56$ and $q = 2.47$ are given by their values determined at $\theta = 0°$. $F_{p,max}$ is an unconstrained temperature, strain and angular dependent free parameter. B^*_{c2} is constrained through eqn 5.4 where $h(T,\theta)$ is an unconstrained temperature and angular dependent free parameter and $B^*_{c2}(\varepsilon_{app}, \theta = 0°)$ is constrained by the values obtained in chapter 4. The data are weighted by $F_p \times B$. (inset) $h(T,\theta)$ is determined manually to give a reasonable flux pinning scaling curve and have a systematic temperature dependence as a function of angle.

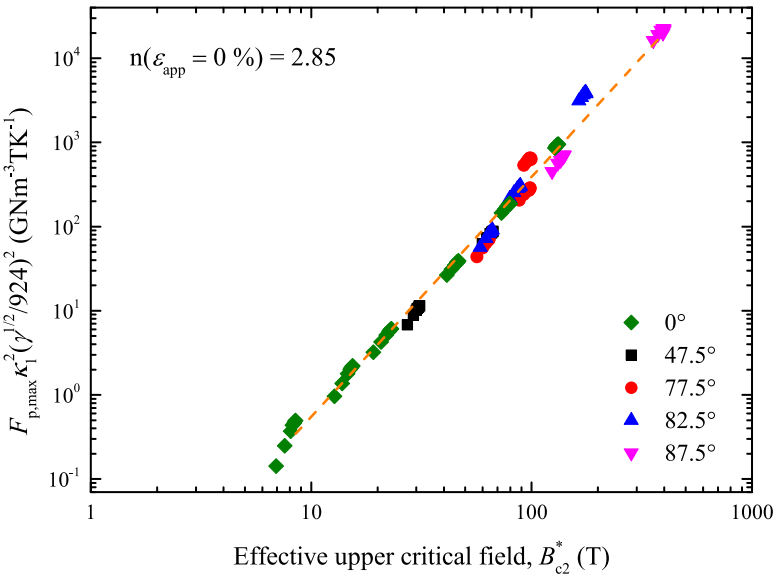

Figure 5.12. $F_{p,max}[\kappa^*_1]^2$ against B^*_{c2} on a log-log scale including the data at 0° from chapter 4. The dashed line is a linear fit to the data at $\varepsilon_{app} = 0\,\%$.

obtained from the experimental data. The parameter w was taken to be independent of angle and equal to the value used in chapter 4 (i.e. 2.2). This is equivalent to assuming eqn 4.13 in chapter 4 can be generalised to an equation of the form

$$B^*_{c2i}\left(\varepsilon_{app},\theta\right)/B^*_{c2i}\left(0,\theta\right)=\left[T^*_{ci}\left(\varepsilon_{app}\right)/T^*_{ci}\left(0\right)\right]^w, \tag{5.5}$$

s and $T^*_c\left(\varepsilon_{JD}=0\,\%\right)$ are taken from results of direct measurements of B^*_{c2} obtained in chapter 4 and $B^*_{c2}\left(T,\varepsilon_{JD}=0\,\%\right)$ is taken from the results of flux pinning scaling analysis (cf. figure 5.10), linear interpolation was used to determine the values of n, N_0, T^*_c and B^*_{c2} at $\varepsilon_{JD}=0\,\%$. The value of $\varepsilon_{J_{cA}=J_{cB}}$ is unknown at the beginning of the analysis however it is needed to determine values for n, N_0, $T^*_c\left(\varepsilon_{JD}=0\,\%\right)$ and $B^*_{c2}\left(T,\varepsilon_{JD}=0\,\%\right)$ hence the iterative process was again used with the initial assumption $\varepsilon_{J_{cA}=J_{cB}}=0\,\%$. The change in $\varepsilon_{J_{cA}=J_{cB}}$ and gradient after just one iteration was well below its uncertainty. The uncertainties in ε_{peak} shown in figure 5.13 are associated with uncertainties that follow from the inverted parabola fitting procedure, and the uncertainty in $\mathrm{d}T^*_{cA}/\mathrm{d}\varepsilon_{JD}|_{\varepsilon_{JD}=0\%}\,F/g_{A,HTS}$ is dominated by uncertainties in N_0 which were estimated from the standard deviation of N about the fits shown in figure 5.6. The data in figure 5.13 show a straight-line fit with an intercept at $\varepsilon_{J_{cA}=J_{cB}}=0.19\pm0.01\,\%$ and a gradient of -0.27 ± 0.01. The chain model analysis was repeated with the results from the insets in figures 5.10 and 5.11 and makes little change to the results. As discussed in chapter 4 value of f depends on $\mathrm{d}T^*_{cA}/\mathrm{d}\varepsilon_{JD}|_{\varepsilon_{JD}=0\%}$ and α, and there are large variations in the values of these parameters in literature. Table 5.2 provides

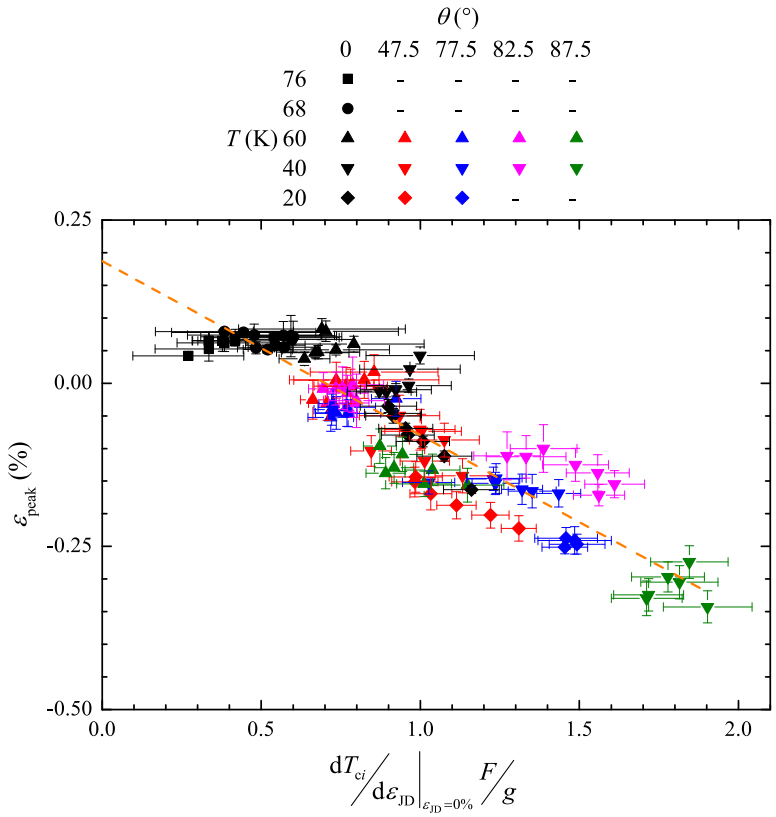

Figure 5.13. $\varepsilon_{\text{peak}}$ verses $\mathrm{d}T^*_{\text{cA}}/\mathrm{d}\varepsilon_{\text{JD}}|_{\varepsilon_{\text{JD}}=0\%}\, F/g_{\text{A,HTS}}$ including the $\theta = 0°$ data from chapter 4. The dashed line is a linear fit to the data. The uncertainties in $\varepsilon_{\text{peak}}$ are taken directly from the fitting procedure and the uncertainties in $\mathrm{d}T^*_{\text{cA}}/\mathrm{d}\varepsilon_{\text{JD}}|_{\varepsilon_{\text{JD}}=0\%}\, F/g_{\text{A,HTS}}$ are propagated from the uncertainty in F (the dominant source of uncertainty).

different values of f obtained when using the different values of $\mathrm{d}T^*_{\text{cA}}/\mathrm{d}\varepsilon_{\text{JD}}|_{\varepsilon_{\text{JD}}=0\%}$ and α from three different sources in the literature.

5.7 Discussion

5.7.1 Angular dependence of B^*_{c2}

The effective upper critical field B^*_{c2} determined in this work is the field at which J_{c} drops to zero and can be associated with the irreversibility field B_{irr} for REBCO tape

Table 5.2. Values of the domain fraction f determined using various experimental values of $\mathrm{d}T^*_{ci}/\mathrm{d}\varepsilon_{\mathrm{JD}}|_{\varepsilon_{\mathrm{JD}}=0\%}$ from literature, allong with a speculative result for $\alpha = 1$ and $\mathrm{d}T^*_{ci}/\mathrm{d}\varepsilon_{\mathrm{JD}}|_{\varepsilon_{\mathrm{JD}}=0\%} = 1.6\,\mathrm{K}\,\%^{-1}$. The results of Welp *et al.* [211] and Fietz *et al.* [210] are converted from stress to strain using Young's moduli of 162.7 GPa along the a-axis and 178.1 GPa along the b-axis [266].

	$\mathrm{d}T^*_{\mathrm{cA}}/\mathrm{d}\varepsilon_{\mathrm{JD}}$ ($\mathrm{K}\,\%^{-1}$)	$\mathrm{d}T^*_{\mathrm{cB}}/\mathrm{d}\varepsilon_{\mathrm{JD}}$ ($\mathrm{K}\,\%^{-1}$)	α	f
Suzuki et. al. [267]	$+4.09 \pm 0.02$	-2.09 ± 0.01	0.51	0.13
Fietz et. al. [210]	$+1.6 \pm 0.1$	-2.1 ± 0.1	1.31	0.34
Welp et. al. [211]	$+3.3 \pm 0.3$	-3.4 ± 0.4	1.03	0.21
	$+1.6$	-1.6	1	0.32

as shown in chapter 4. Figure 5.11 shows the functional form of B^*_{c2} is even sharper than the Tinkham 2D thin film model. This work provides experimental results to help increase the limited current understanding of B_{irr} as a function of angle. Single crystal measurements of B_{c2} and B_{irr} as a function of angle at low temperatures would greatly increase the ability to parameterise and understand the angular dependence of J_c. It is also unclear whether surface effects caused by the silver/copper/oxides/Hastalloy mean B_{c2} and B_{irr} values obtained from single crystals differ from that obtained on tapes. Experiments to determine the precise nature of the temperature and angular dependence (even in the absence of strain) would need to be extensive and would be difficult due to the extremely high fields involved. Although such experiments are necessary if J_c in REBCO tapes is to be fully understood to the same extent as LTS materials such as Nb_3Sn.

5.7.2 Flux pinning scaling curve

The data in figure 5.10 show that the values of p and q (0.56 and 2.47 respectively) can be taken to be independent of angle over the limited range of fields, temperatures and angles we have measured. This suggests the pinning mechanism(s) active are independent of angle. The data in figure 5.14 have been extracted from figure 5.12. The global value of $n = 2.85$ (cf figure 5.12) is similar to the value obtained using only the data at 60 K. Hence, the angular dependence of B^*_{c2} from figure 5.11, when included in the scaling law, leads to a reasonable approximation of the angular dependence of J_c. However, figure 5.14 shows as the temperature is reduced the value of n increases showing that the sharpness of the angular dependence of B^*_{c2} alone is insufficient to describe the sharpness of the $J_c(\theta)$ peaks. We conclude that there is a stronger angular dependence to $F_{p,max}$ at low temperatures than expected from the scaling law alone and will discuss a possible microstructural origin for this in section 5.7.4.

5.7.3 The chain model

In chapter 4 it was shown the chain model provides a good explanation for the parabolic strain dependence of J_c in REBCO tapes at $\theta = 0°$. The parabolic nature of the strain dependence of J_c is emergent behaviour (i.e. the parabolic behaviour of the tape is unlike the linear behaviour of the underlying domains) caused by competing domains with opposing strain dependencies. Figure 5.13 provides the combined data from chapters 4 and 5. The addition of this angular dataset to the previous one, increases our confidence that the model provides a good description of REBCO tape. It has

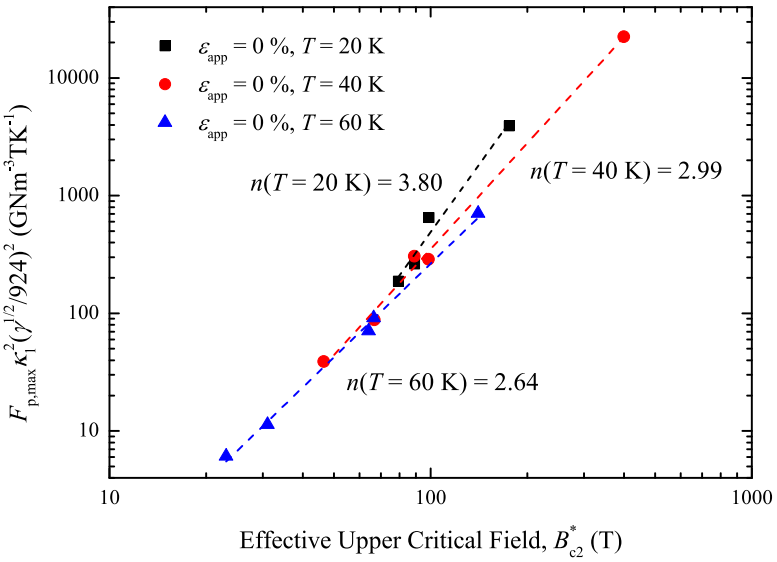

Figure 5.14. $F_{\mathrm{p,max}}\left[\kappa_1^*\right]^2$ against B_{c2}^* on a log-log scale showing only data at $\varepsilon_{\mathrm{app}} = 0\,\%$ including the data at 0° from chapter 4. The dashed lines are linear fits to the data as a function of temperature.

extended the range of $\varepsilon_{\mathrm{peak}}$ values because we have made measurements at lower reduced field. The values of f in table 5.2 are quite far from the equilibrium value of $f = 0.5$. As discussed in chapter 4, this is probably in part because of uncertainties associated with the values of $g_{\mathrm{A,HTS}}$ derived from the functional form of B_{c2}^* at temperatures close to T_c^* and extrapolated to low temperatures. In addition, there is uncertainty in the values of $\mathrm{d}T_{\mathrm{cA}}^*/\mathrm{d}\varepsilon_{\mathrm{JD}}|_{\varepsilon_{\mathrm{JD}}=0\%}$ (cf. table 5.2) required to calculate f [210, 211, 267]. Nevertheless figure 5.13 provides strong evidence that the chain model not only explains the field and temperature dependence of $\varepsilon_{\mathrm{peak}}$ (as shown in chapter 4) but also explains the angular dependence.

5.7.4 Microstructure in REBCO tapes

Stacking faults in the *ab*-plane are a common feature of high J_c REBCO tapes. It has been shown that the dislocation loops associated with the stacking faults produce a strong additional pinning component when the applied field is increasingly close to being parallel to the *ab*-plane [142]. At low angles ($\theta \approx 0°$) the flux lines are orthogonal to the dislocation loops and only provide weak pinning. The rigidity of the FLL prevents the fluxons from deforming to follow the dislocation loop, so the interaction volume of the fluxon is not extended along its length. However, at higher angles approaching $\theta = 90°$, where the field is aligned with the *ab*-planes and the direction of the dislocations, the FLL can distort and it becomes more energetically favourable for fluxons to follow the dislocation loops over an extended portions of their length. This greatly increases the interaction volume and hence F_p [142]. We have found that the peak in J_c when the direction of the applied field is parallel to *ab*-plane is more pronounced for higher fields and lower temperatures, consistent with the literature for staking faults [141–143]. Literature for samples containing high densities of stacking faults [142,143] suggests that weak point pinning operates at all fields and temperatures and that the strong pinning provided by stacking faults preferentially operates when $B \parallel ab$-planes.

Associated with the strong angular dependence of J_c when $B \parallel ab$-planes in high fields and low temperatures, we have found a marked reduction in N (cf. figure 5.4). This reduction is not consistent with the empirical relation $N = r_N J_c^{S_N} + 1$. The results at $\varepsilon_{app} = 0.024\,\%$ and $\varepsilon_{app} = -0.976\,\%$ show that strain has little effect on

this reduction. We have not found other reports of the reduction of N as a function of angle for high J_c samples. However, a similar drop in N at high angles, despite increases in J_c, has been observed [146] associated with intrinsic pinning caused by the modulation of the superconducting order parameter in the c-axis direction due to the superconductivity being localised to the CuO_2 planes. Such intrinsic pinning results in a very sharp peak about the ab-plane only a few degrees in width and is not observed in the high J_c samples investigated here, where other sources of pinning dominate over this weak effect and as expected for these high J_c samples that are not perfect single crystals with perfect alignment of the ab-planes between grains. Civale et al [146] working on pulsed laser deposition films on single-crystal $SrTiO_3$ substrate argue that the reduction in N at low temperatures is caused by thermally activated, intrinsic pinning associated, staircase behaviour in the FLL when the direction of field is close to the ab-plane [292]. They attribute the weaker suppression of N at higher temperature, independent of field, to the decreasing importance from intrinsic pinning to the overall pinning. We suggest that the arguments Civale et al use for intrinsic pinning can also be applied to stacking fault pinning to explain the the reduction of N observed in this work.

5.7.5 Applications

The suppression of N close to the ab-plane has implications for the use of REBCO tapes in magnet windings. Simple pancake windings are often considered optimal for REBCO wound magnets as the maximum deviation of the field angle away from the

ab-plane is minimised so higher operational J_c's can be achieved compared with other winding geometries (such as using Cable On Round Conductor). However, optimal magnet design also requires high values of N to ensure the stability of the magnet. N is often overlooked in studies of REBCO tapes. This work shows one cannot assume that a high J_c guarantees a high N and that that more attention must be paid to the N-values when testing REBCO tapes for use in magnets.

There is a strong focus in studies on REBCO tapes to increasing J_c by whatever means, and that achieving a high J_c is the only objective and metric by which the quality of a tape judged, often using only one field orientation. This study has identified that such a strategy will often overlook other vital metrics and may hinder a deeper scientific understanding of how these materials behave. While achieving high J_c values is vital for high performance tapes, we suggest more effort should be put into more complete characterisations of high performance tapes and into creating a more complete understanding of the fundamentals underpinning REBCO tapes to better inform us in how to optimise tapes for their intended application. The increasingly complex architectures and stoichiometry of REBCO tapes mean it is often impossible to deconvolve the various effects and mechanisms at play and determine which are responsible for the high performance. An increased focus on the underlying science may help increase the rate at which further improvements in high performance REBCO tapes can be driven forward.

5.8 Conclusions

An extensive survey of the $J_c(B, T, \varepsilon_{app}, \theta)$ phase space on a sample of REBCO tape without artificial pinning sites has been performed. The peak in $J_c(\theta)$ around the *ab*-plane is too sharp to solely be attributed to the rise in B^*_{c2} near the *ab*-plane for any model of $B^*_{c2}(\theta)$ or the directly determined values values of B^*_{c2}. The presence of stacking faults as pinning sites can explain the depression in the index of transition N as well as the enhancement in J_c when $B \parallel$ to the *ab*-plane. To the authors knowledge this is the first time this behaviour has been identified in a high J_c sample.

A single normalised F_p curve was found to describe the field dependence of the data at all temperatures, strains and angles, indicating the same pinning mechanism is active over all the phase space under investigation. It was also shown that the magnitude and shape of normalised angular dependent J_c curve is independent of strain. This observation was used to support the argument that, in the low reduced field limit, there is no change in pinning mechanism across the phase space. The method of determining the normalised F_p curve allowed for the independent evaluation of $F_{p,max}$ and B^*_{c2} as a function of temperature and angle. The angular dependence of B^*_{c2} was found to be sharper than predicted by any theoretical model.

The parabolic nature of the strain dependence of J_c is shown to be emergent behaviour caused by the interaction of two domains, one of which increases J_c with applied strain and one of which decreases. This bimodal model predicts a field, temperature and angular dependence of the strain at which J_c is maximised ε_{peak}. Field, temperature and angular dependence of ε_{peak} is shown to be present in the data and that

it is consistent with the predictions of this model. A value of $\varepsilon_{J_{\mathrm{cA}}=J_{\mathrm{cB}}} = 0.19 \pm 0.01\,\%$ is estimated from the data and various estimates of f are given, obtained using different experimental results reported for the single crystal anisotropic strain dependence. Such a field temperature and angular dependence of $\varepsilon_{\mathrm{peak}}$ cannot be satisfactorily incorporated into homogeneous models where all portions of the material respond to strain in broadly the same manner.

Chapter 6

Future work and concluding remarks

This thesis has highlighted that the current understanding of how strain affects superconducting conductors is fundamentally flawed. It has shown polycrystalline superconductors have a bimodal (or multimodal) response to an applied strain. This intrinsically changes the approach to driving further improvements in superconducting conductors for use in high field magnets under strain (such as fusion magnets). In this chapter experiments designed to further improve the understanding of polycrystalline superconducting conductors under strain and a direction for driving future improvements in conductor technology is outlined.

This thesis has focused on studying REBCO tape without additional pinning centres (APCs) so the additional effects caused by these were not confused with or mistaken for effects caused by the underlying REBCO. For applications tapes with APCs will

be used due to their higher performance. Similar experiments to those performed in this thesis should now be performed on tapes including APCs, and in fact work on this is already being carried out by others in the Durham Superconductivity Group with input from the author. It should now be possible to use the results of this thesis to deconvolve any additional effects arising from the APCs from those caused by the underlying REBCO. Another objective of this experiment is to investigate the angular dependence of B^*_{c2} in these APC tapes. There is an improvement in J_c when the applied magnetic field is normal to the tape surface compared to tapes without APCs. It is often assumed that this is simply due to an increase in the pinning strength caused the geometry of APCs. However, there is also the possibility that the improvement in J_c could be caused (at least in part) by an associated improvement in B^*_{c2}. Understanding how APCs affect B^*_{c2} is important for understanding scaling in these materials as well as the nature of B^*_{c2}.

One of the most logical extensions to the bimodal model for REBCO tapes is to include the effect of a two-dimensional applied strain which allows for further tests of the predictions made by the model and work in this area has already begun [293]. An example prediction that can be made by extending the model into two dimensions, is that it should be possible to keep J_c constant by applying (tensile or compressive) strain in both the principle directions orthogonal to the c-axis, and the ratio of these strains needed to keep J_c constant can be used to make an estimate of the parameter α. Careful consideration of the role of Poisson's ratio is needed in the analysis two-dimensional strain data, as the effective Poisson's ratio is largely determined by the

sample holder and matrix materials, this will vary from that of a single crystal and will depend on the measurement setup and sample type.

The measurements in this thesis have shown that the exponent n, from the flux pinning scaling relation $F_{\mathrm{p,max}} \left[\kappa_1^*\right]^2 \propto \left[B_{\mathrm{c2}}^*\right]^n$ is a function of both temperature, strain and angle. In the bimodal chain model as it currently stands, distributions in the critical superconducting parameters (T_{c}^*, B_{c2}^* and J_{c}) across different grains, the effects of percolative current flow, and current shunting through the matrix materials and sample holder are ignored. It may be that at higher temperatures, approaching T_{c}^*, parts of the material belonging to either the weaker domain or both domains are in the normal state, but this is not picked up as a transition due to percolative current flow allowing for the current to find a path around the affected areas. It will nevertheless result in a reduction of J_{c} (and also $F_{\mathrm{p,max}}$) due to a reduction in the effective cross-sectional area. Since the critical superconducting parameters in each domain are also a function of strain, the interplay of these effects could lead to the observed variations in n. This represents a significant increase in the complexity of the model and it is difficult to predict what the effect on the results would be without performing the study. It would be interesting to see if extending the bimodal to include distributions in the critical superconducting parameters among the grains, and either two or three dimensional percolative current flow, reproduces the measured behaviour for $F_{\mathrm{p,max}} \left[\kappa_1^*\right]^2 - \log B_{\mathrm{c2}}^*$, confirming whether the behaviour is the result of the bimodal behaviour or whether it is an additional mechanism at play which has not been considered.

This thesis has restricted the analysis of data using the bimodal model to the field, temperature and angular dependence of $\varepsilon_{\mathrm{peak}}$, for which approximate analytic solutions can be obtained. However, there are other predictions made by the model, such as how quickly the critical current density falls off away from $\varepsilon_{\mathrm{peak}}$, the non-parabolic 'tails' of $J_{\mathrm{c}}\left(\varepsilon_{\mathrm{JD}}\right)$ at high strains and the asymmetric nature of $J_{\mathrm{c}}\left(\varepsilon_{\mathrm{JD}}\right)$. These features could form the basis of future analysis of the data presented here or new data. For example, an attempt to fit the model to the entire dataset (or a subset of strain dependent data) could be performed which would allow for an estimation of the parameters α, $\mathrm{d}T^{*}_{\mathrm{cA}}/\mathrm{d}\varepsilon_{\mathrm{JD}}|_{\varepsilon_{\mathrm{JD}}=0\%}$ and the domain fraction f without independent single domain measurements on single crystals or thin films. Such a fitting procedure would, however, prove difficult to implement in practice due to the transindential nature of the equations and the confidence in the results may be questionable due to large number and strongly correlated nature the fitting parameters. Also, very low uncertainties on the measurements and a very high confidence in the assumptions made in the model about the specific functional forms of how changes the strain dependence of T_{c} relates to J_{c} in each domain would be required for the results of such an analysis to be convincing. An analysis of the rate at which the critical current density falls off away from $\varepsilon_{\mathrm{peak}}$ or the asymmetric nature of $J_{\mathrm{c}}\left(\varepsilon_{\mathrm{JD}}\right)$ could also allow for similar estimations of α, $\mathrm{d}T^{*}_{\mathrm{cA}}/\mathrm{d}\varepsilon_{\mathrm{JD}}|_{\varepsilon_{\mathrm{JD}}=0\%}$ and f to be made.

In LTS materials the terms upper critical field and irreversibility field can often be used interchangeably as they are generally almost identical. However, in HTS materials this is not the case and the upper critical field and irreversibility field have very

different functional forms. There is conflict in literature as to whether the irreversibility field should be considered a thermodynamic phase transition in an HTS high field superconductor. This work has shown the advantage on having direct measurements of B_{irr} when analysing J_{c} data. However, there is next to no B_{irr} data except close to T_{c}^{*} in literature, and data as a function of angle is especially lacking, due to its extremely high value at low temperature. Direct measurements of B_{irr} above 20 T using very high field and pulsed field magnet systems at international facilities will help to develop a better understanding of B_{irr} in HTS materials. It will be no small feat to perform such measurements, especially for composite tapes with metallic components, however they are required in order to incorporate B_{irr} into the scaling laws self-consistently.

One of the issues with the analysis of the REBCO data has been the wide variety of values found in the literature for the intrinsic strain dependent properties of each domain on what are nominally the same materials. Our current understanding of what affects this is lacking, both experimentally and theoretically, suggesting further study is required in this area to understand how variables such as oxygen content, rare earth element composition and whether we are looking at a thin film or a bulk sample affect the intrinsic strain dependent properties of the domains. Also, our current understanding of the intrinsic strain dependent properties of A15 materials is also lacking. This thesis clearly identifies that the strain dependence of polycrystalline Nb_3Sn is the result of competing domains, although there is not enough information in the literature to make firm conclusions about the nature of these domains. The competing domains could be due to grain boundaries where Poisson's ratio causes some grain boundaries to

widen and other to contract (as suggested in this thesis), however it is still entirely possible that the source of the competing domains has its origins in different crystal alignments of the grains themselves, or it could be that the strain dependence of the grain boundaries is primarily determined by the strain dependence of the adjacent grains rather than the boundary thickness. In order to investigate this fully, studies on single crystals and on single grain boundaries of A15 materials under strain are required. While such measurements will be extensive and demanding, particularly on individual grain boundaries in A15 materials, they will give unique insight into the underlying causes of the strain dependence of polycrystalline superconducting conductors. It may also be possible to perform limited investigations of this using commercial wires without the need and effort of single crystal investigations using experimental equipment similar to that used in this investigation. While the Nb_3Sn grains in the bronze-route wire reported here are nearly randomly oriented [294], in Restacked Rod Processed (RRP) and Powder In Tube (PIT) Nb_3Sn wires, partial texturing in the $\langle 100 \rangle$ and $\langle 110 \rangle$ directions respectively occur along the filaments [295]. Fabricating conductors that are strongly textured will give a preferential crystal direction that the strain is applied in and measuring wires with different twist pitches would go some way to providing some control over this direction.

The bimodal model gives some clear insights into how the strain tolerance of superconducting conductors can be improved. The challenge for conductor manufacture is developing these insights into workable, cost effective solutions which can be implemented into the production process. For REBCO conductors experiments into

tuning the domain fractions of conductors are already underway [267, 272, 296] and conductors with the [110] manufactured using the ISD technique are already in production [161, 162, 201]. The ability to tune the domain fraction where the performance of a tape improves under an applied strain provides a clear advantage over ISD tapes with a flat strain response, however currently tuning the domain fraction is only possible on short lengths of tape whereas ISD is an established manufacturing procedure. Another possibility for improving the properties of REBCO tape under strain would be to apply a strain in the direction orthogonal to the axis of the tape during operation. Experiments applying strain in two dimensions have already been discussed and the results of such experiments could help inform and drive forward advanced magnet designs capable of applying an orthogonal strain during operation. For A15 materials grain boundaries were identified as the likely source of the competing domains, with the competition being caused by Poisson's ratio and percolative current flow. One potential way to improve the properties of A15 conductors under strain would be to change Poisson's ratio effectively changing α, while it is obviously impossible to change the intrinsic Poisson's ratio of the superconductor the effective Poisson's ratio of the composite conductor could be changed by changing the matrix materials and conductor architecture. However, there are many considerations when choosing matrix materials which restrict the choices and since all metals have similar Poisson's ratios it is unlikely such a strategy would lead to significant improvements in performance under strain. While changing the matrix materials may not be an effective strategy for improving performance of commercial conductors, it could be useful to experiment on

such conductors in the context of the bimodal model to better understand the nature of the competing domains. Grain boundary engineering also has the potential to improve the properties of A15 conductors under strain. Thinner grain boundaries should result in increases in J_c across all of phase space and may lead to a reduction in the strain sensitivity of J_c across grain boundaries.

Conventional fusion reactors are designed at the limit of what is achievable with LTS magnet technologies so giant fusion reactors are required to have any chance of achieving break even. In fact, the only conventional LTS reactor with the chance of achieving this goal is the gigantic ITER reactor currently under construction and over a decade away from achieving its stated goal of producing at least five times more fusion energy out than is required to maintain the reaction. As the largest experimental scientific project in the world both in terms of investment and international cooperation, ITER is a one time only reactor and for a long time has been a critical stepping stone on the road to commercial fusion energy, the failure of which could lead to end of the fusion dream. However, improvements in the critical current densities of HTS tapes are set to usher in a new age of fusion technologies. With fusion power scaling as the forth power of the magnetic field the very high field magnets made possible by HTS conductors have shattered the conventional wisdom that a fusion reactor needs to be a behemoth to achieve a net energy gain. New designs of much smaller reactors using HTS magnets, with the same aims as ITER, are now appearing [297, 298]. Their small size meaning they are far cheaper with timescales of the order of years not decades. The plasma physics is not as certain in these very high field regimes as it is for ITER,

however the high reward and comparatively cheap price tag have meant investors have not been discouraged. And the lower cost shorter time frames also stimulate development through a willingness to fund higher risk investments. Very high field HTS fusion magnets will produce enormous strains on the superconductor so understanding the effects of strain are critical for the success of fusion (and other applications) using HTS magnets. Fuelled by constantly improving HTS conductors, the next decade will be an exciting time for both fusion and other very high field magnet technologies.

We currently stand on the cusp of a potentially bleak looking energy future; could high temperature superconductivity be the key to producing a star on Earth which will shine our way to a brighter future?

References

[1] Shell. World energy model: a view to 2100. *https://www.shell.com/energy-and-innovation/the-energy-future/scenarios/shell-scenarios-energy-models/world-energy-model/_jcr_content/par/textimage.stream/1510344160326/d62f12b8fe88e85dc3349c38b1ca5e44cc22c5ccc6f70beed634020cfb527c82/shell-world-energy-model.pdf*, 2017.

[2] A S Eddington. The internal constitution of the stars. *The Observatory*, 43(557):341–358, 1920.

[3] G T Hoang and J Jacquinot. Controlled fusion: the next step. *Physics World, https://physicsworld.com/a/controlled-fusion-the-next-step/*, January 2004.

[4] A E Costley. On the fusion triple product and fusion power gain of tokamak pilot plants and reactors. *Nuclear Fusion*, 56(6):066003, 2016.

[5] H K Onnes. The resistance of pure mercury at helium temperatures. *Commun. Phys. Lab. Univ. Leiden*, 12:120, 1911.

[6] J G Bednorz and K A Müller. Possible high T_c superconductivity in the Ba − La − Cu − O system. *Zeitschrift für Physik B Condensed Matter*, 64(2):189–193, 1986.

[7] C P Poole, H A Farach, and R J Creswick. *Type II Superconductivity*, pages 337 – 384. Dover Publications, New York, 2007.

[8] A P Drozdov, M I Eremets, I A Troyan, V Ksenofontov, and S I Shylin. Conventional superconductivity at 203 kelvin at high pressures in the sulfur hydride system. *Nature*, 525(7567):73–76, 2015.

[9] F J Kedves, S Mészáros, K Vad, G Halász, B Keszei, and L Mihály. Estimation of maximum electrical resistivity of high T_c superconducting ceramics by the meissner effect. *Solid State Communications*, 63(11):991–992, 1987.

[10] W Meissner and R Ochsenfeld. Ein neuer effekt bei eintritt der supraleitfähigkeit. *Naturwissenschaften*, 21:787–788, 1933.

[11] J R Waldram. *Superconducting States with Internal Magnetic Flux*, book section 5, pages 61–91. IOP Publishing Ltd., London, 1996.

[12] N R Werthamer, E Helfand, and P C Hohenberg. Temperature and purity dependence of the superconducting critical field, H_{c2}. III. electron spin and spin-orbit effects. *Physical Review*, 147(1):295–302, 1966.

[13] J Bardeen, L N Cooper, and J R Schrieffer. Theory of superconductivity. *Physical Review*, 108(5):1175–1204, 1957.

[14] V V Struzhkin, R J hemley, H Mao, and Y A Timofeev. Superconductivity at $10 - 17$ K in compressed sulphur. *Nature*, 390:382–384, 1997.

[15] J Guo, G Lin, S Cai, C Xi, C Zhang, W Sun, Q Wang, K Yang, A Li, Q Wu, Y Zhang, T Xiang, R J Cava, and L Sun. The extraordinary superconductivity of commercial niobium-titanium wire at extreme pressures. *https://arxiv.org/ftp/arxiv/papers/1808/1808.07215.pdf*, 2018.

[16] D N Zheng, H D Ramsbottom, and D P Hampshire. Reversible and irreversible magnetization of the Chevrel-phase superconductor $PbMo_6S_8$. *Physical Review B*, 52(17):12931–12938, 1995.

[17] Z Ren, G Che, X Dong, J Yang, W Lu, W Yi, X Shen, Z Li, L Sun, F Zhou, and Z Zhao. Superconductivity and phase diagram in iron-based arsenic-oxides $ReFeAsO_{1-\delta}$ (RE = rare-earth metal) without fluorine doping. *EPL*, 83:17002, 2008.

[18] A Gurevich, S Patnaik, V Braccini, K H Kim, C Mielke, X Song, L D Cooley, S D Bu, D M Kim, J H Choi, L J Belenky, J Giencke, M K Lee, W Tian, X Q Pan, A Siri, E E Hellstrom, C B Eom, and D C Larbalestier. Very high upper critical fields in MgB_2 produced by selective tuning of impurity scattering. *Superconductor Science Technology*, 17(2):278–286, 2004.

[19] H W Weijers, W D Markiewicz, A J Voran, S R Gundlach, W R Sheppard, B Jarvis, Z L Johnson, P D Noyes, J Lu, H Kandel, H Bai, A V Gavrilin, Y L Viouchkov, D C Larbalestier, and D V Abraimov. Progress in the development of a superconducting 32 T magnet with REBCO high field coils. *IEEE Transactions on Applied Superconductivity*, 24(3):5, 2014.

[20] S Yoon, J Kim, K Cheon, H Lee, S Hahn, and S-H Moon. 26 T 35 mm all-$GdBa_2Cu_3O_{7-x}$ multi-width no-insulation superconducting magnet. *Superconductor Science and Technology*, 29(4):1–6.

[21] L Martini, M Bocchi, M Ascade, A Valzasina, V Rossi, C Ravetta, and G Angeli. The first italian superconducting fault current limiter: Results of the field testing experience after one year operation. *Journal of Physics: Conference Series*, 507(3):032003, 2014.

[22] H Thomas, A Marian, A Chervyakov, S Stückrad, D Salmieri, and C Rubbia. Superconducting transmission lines - sustainable electric energy transfer with higher public acceptance? *Renewable and Sustainable Energy Reviews*, 55, 2016.

[23] *CRC Handbook of Chemistry and Physics*. CRC Press, 93 edition, 2012.

[24] Y Tsui, R Mahmoud, E Surrey, and D P Hampshire. Superconducting and mechanical properties of low-temperature solders for joints. *IEEE Transaction on Applied Superconductivity*, 26(3):6900204, 2016.

[25] T Takeuchi. Nb_3Al conductors for high-field applications. *Superconductor Science and Technology*, 13(9):R101–R119, 2000.

[26] Jens Hänisch, Kazumasa Iida, Fritz Kurth, Elke Reich, Chiara Tarantini, Jan Jaroszynski, Tobias Förster, Günther Fuchs, Ruben Hühne, Vadim Grinenko, Ludwig Schultz, and Bernhard Holzapfel. High field superconducting properties of $Ba\left(Fe_{1x}Co_x\right)_2 As_2$ thin films. *Scientific Reports*, 5:17363, 2015.

[27] T Sekitani, N Miura, S Ikeda, Y H Matsuda, and Y Shiohara. Upper critical field for optimally-doped $YBa_2Cu_3O_{7-\delta}$. *Physica B: Condensed Matter*, 346–347:319–324, 2004.

[28] G Wang, M J Raine, and D P Hampshire. How resistive must grain-boundaries be to limit J_c in polycrystalline superconductors? *Superconductor Science and Technology*, 30(10):104001, 2017.

[29] F London and H London. The electromagnetic equations of the supraconductor. *Proceedings of the Royal Society A*, A149:71–88, 1935.

[30] V L Ginzburg and L D Landau. On the theory of superconductivity. *Zhurnal Eksperimentalnoj i Teoreticheskoj Fiziki*, 20:1064–1082, 1950.

[31] L P Gor'kov. Microscopic derivation of the Ginzburg-Landau equations in the theory of superconductors. *Soviet Physics JETP*, 9(6):1364–1367, 1959.

[32] L D Landau. Zur theorie der phasenumwandlungen II. *Physikalische Zeitschrift der Sowjetunion*, 11:545 – 555, 1937.

[33] D R Tilley and J Tilley. *Ginzburg-Landau Theory*, pages 296–302. IOP publishing Ltd., Bristol, 3rd edition, 1990.

[34] A A Abrikosov. On the magnetic properties of superconductors of the second group. *Soviet Physics JETP*, 5(6):1174–1182, 1957.

[35] W H Kleiner, L M Roth, and S H Autler. Bulk solution of Ginzburg-Landau equations for Type II superconductors: Upper critical field region. *Physical Review*, 133(5A):A1226–A1227, 1964.

[36] H F Hess, R B Robinson, R C Dynes, J M Valles Jr, and J V Waszczak. Scanning-tunneling-microscope observation of the abrikosov flux lattice and the density of states near and inside a fluxoid. *Physical Review Letters*, 62(2):214–216, 1989.

[37] K Maki. The magnetic properties of superconducting alloys I. *Physics*, 1(1):21–30, 1964.

[38] W E Lawrence and S Doniach. Theory of layer structure superconductors. In E Kanda, editor, *Proceedings of the twelfth international conference on low temperature physics*, page 361. Academic press of Japan.

[39] M Tinkham. *The High-Temperature Superconductors*. McGraw-Hill Book Co., Singapore, 1996.

[40] R A Klemm, A Luther, and M R Beasley. Theory of the upper critical field in layered superconductors. *Physical Review B*, 12(2):877–891, 1975.

[41] M Tinkham. Effect of fluxoid quantization on transitions of superconducting films. *Physical Review*, 129(6):2413–2422, 1963.

[42] R Fastampa, S Sarti, E Silva, and E Milani. Scaling in the angular dependence of the critical current and temperature-dependent anisotropy ratio in $Bi_2Sr_2CaCu_2O_8$. *Physical Review B*, 49(22):15959–15964, 1994.

[43] V P Mineev. General expression for the angular dependence of the critical field in layered superconductors. *Physical Review B*, 65(1):012508, 2001.

[44] C P Poole, H A Farach, and R J Creswick. *BCS Theory*, page 64. Dover Publications, New York, 2007.

[45] D R Tilley and J Tilley. *Microscopic Theory of Superconductivity*, pages 119–122. IOP Publishing Ltd, Bristol, 1990.

[46] M Tinkham. *The BCS Theory*, page 64. Dover Publications, New York, 1996.

[47] H Fröhlich. Theory of the superconducting state. i. the ground state at the absolute zero of temperature. *Physical Review*, 79(5):845–856, 1950.

[48] L N Cooper. Bound electron pairs in a degenerate fermi gas. *Physical Review*, 104(4):1189 –1190, 1956.

[49] C A Reynolds, B Serin, W H Wright, and L B Nesbitt. Superconductivity of isotopes of mercury. *Physical Review*, 78(4):487, 1950.

[50] W A Fietz and W W Webb. Hysteresis in superconducting alloys - temperature and field dependence of dislocation pinning in niobium alloys. *Physical Review*, 178(2):657–667, 1969.

[51] S A Keys, N Koizumi, and D P Hampshire. The strain and temperature scaling law for the critical current density of a jelly-roll Nb_3Al strand in high magnetic fields. *Superconductor Science and Technology*, 15:991–1010, 2002.

[52] D Dew-Hughes. Flux pinning mechanisms in Type II superconductors. *Philosophical Magazine*, 30(2):293–305, 1974.

[53] E J Kramer. Scaling laws for flux pinning in hard superconductors. *Journal of Applied Physics*, 44(3):1360–1370, 1973.

[54] I Pong, A Vostner, B Bordini, M Jewell, F Long, Y Wu, L Bottura, A Devred, D Bessette, and N Mitchell. Current sharing temperature of NbTi SULTAN samples compared to prediction using a single pinning mechanism parametrization for NbTi strand. *Superconductor Science and Technology*, 25(5):054011, Apr 2012.

[55] D Dew-Hughes. The role of grain boundaries in determining j_c in high-field high-current superconductors. *Philosophical Magazine B*, 55(4):459–479, 1987.

[56] W Schauer and W Schelb. Improvement of nb3sn high field critical current by a two-stage reaction. *IEEE Transactions on Magnetics*, 17:374–377, 1981.

[57] E E Salpeter. The reaction rate of the proton-proton chain. , 116:649–650, Nov 1952.

[58] *Tables of Physical Chemical Constants (16th edition 1995). 4.7.4 Nuclear fusion.* Kaye Laby Online, 16 edition, 2005.

[59] Fusion for Energy. Understanding fusion, accessed on 24/11/2017. *http://fusionforenergy.europa.eu/understandingfusion/*, 2015.

[60] ITER Physics Basis Editors, ITER Physics Expert Group Chairs, Chairs Co, ITER Joint Central Team, and Unit Physics Integration. Chapter 1: Overview and summary. *Nuclear Fusion*, 39(12):2137, 1999.

[61] J D Lawson. Some criteria for a power producing thermonuclear reactor. *Proceedings of the Physical Society of London Section B*, 70(1):6–10, 1957.

[62] J R Gavaler. Superconductivity in Nb-Ge films above 22 K. *Applied Physics Letters*, 23(8):480–482, 1973.

[63] W L McMillan. Transition temperature of strong coupled superconductors. *Physical Review*, 167(2):331–344, 1968.

[64] C C Tsuei and J R Kirtley. Pairing symmetry in cuprate superconductors. *Reviews of Modern Physics*, 72(4):969–1016, 2000.

[65] C C Tsuei and J R Kirtley. Phase-sensitive evidence for d-wave pairing symmetry in electron-doped cuprate superconductors. *Physical Review Letters*, 85(1):182–185, 2000.

[66] T Timusk and B Statt. The pseudogap in high-temperature superconductors: an experimental survey. *Reports on Progress in Physics*, 62(1):61, 1999.

[67] P W Anderson, P A Lee, M Randeria, T M Rice, N Trivedi, and F C Zhang. The physics behind high-temperature superconducting cuprates: the 'plain vanilla' version of RVB. *Journal of Physics: Condensed Matter*, 16(24):R755, 2004.

[68] A S Alexandrov. Theory of high-temperature superconductivity in doped polar insulators. *EPL (Europhysics Letters)*, 95(2):27004, 2011.

[69] D J Scalapino. A common thread: The pairing interaction for unconventional superconductors. *Reviews of Modern Physics*, 84(4):1383–1417, 2012.

[70] J D Jorgensen, M A Beno, D G Hinks, L Soderholm, K J Volin, R L Hitterman, J D Grace, and I K Schuller. Oxygen ordering and the orthorhombic-to-tetragonal phase transition in $YBa_2Cu_3O_{7-x}$. *Physical Review B*, 36(7):3608–3616, 1987.

[71] A K Saxena. *High-Temperature Superconductors*. Springer, 2010.

[72] A Gauzzi, J Le Cochec, G Lamura, B J Jönsson, V A Gasparov, F R Ladan, B Plaçais, P A Probst, D Pavuna, and J Bok. Very high resolution measurement of the penetration depth of superconductors by a novel single-coil inductance technique. *Review of Scientific Instruments*, 71(5):2147–2153, 2000.

[73] T S Hutchison, G Ocampo, and G J C Carpenter. Crystal structure and morphology in commercial NbTi (46.5 wt % Ti) superconducting fibers. *Scripta Metallurgica*, 19(5):635–638, 1985.

[74] J W Ekin. *Experimental Techniques for Low-Temperature Measurements*. Oxford University Press, New York, 2007.

[75] D Zheng, A Campbell, J Johnson, J Cooper, F Blunt, A Porch, and P Freeman. Magnetic susceptibilities, critical fields, and critical currents of Co- and Zn-doped $YBa_2Cu_3O_7$. *Physical Review B*, 49(2):1417–1426, 1994.

[76] G M Wang, M J Raine, and D P Hampshire. The cause of 'weak-link' grain boundary behaviour in polycrystalline $Bi_2Sr_2CaCu_2O_8$ and $Bi_2Sr_2Ca_2Cu_3O_{10}$ superconductors. *Superconductor Science and Technology*, 31(2):19, 2018.

[77] S Mitra, J H Cho, W C Lee, D C Johnston, and V G Kogan. Magnetic field penetration depth of polycrystalline $(Y, Gd)\,Ba_2Cu_3O_7$, grain-aligned $YBa_2Cu_3O_7$, and single-crystal $Bi_2Sr_2CaCu_2O_8$. *Physical Review B*, 40(4):2674–2677, 1989.

[78] L Miu, P Wagner, U Frey, A Hadish, D Miu, and H Adrian. Vortex unbinding and layer decoupling in epitaxial $Bi_2Sr_2Ca_2Cu_3O_{10+\delta}$ films. *Physical Review B*, 52(6):4553–4558, 1995.

[79] D E Farrell, J P Rice, and D M Ginsberg. Experimental evidence for flux-lattice melting. *Physical Review Letters*, 67(9):1165–1168, 1991.

[80] D S Fisher, M P A Fisher, and D A Huse. Thermal fluctuations, quenched disorder, phase transitions, and transport in Type-II superconductors. *Physical Review B*, 43(1):130–159, 1991.

[81] Y Xu and M Suenaga. Irreversibility temperatures in superconducting oxides: the flux-line-lattice melting, the glass liquid transition, or the depinning temperatures. *Physical Review B*, 43(7):5516–5525, 1991.

[82] I J Daniel and D P Hampshire. Harmonic calculations and measurements of the irreversibility field using a vibrating sample magnetometer. *Physical Review B*, 61(10):6982–6993, 2000.

[83] Y Ando, G S Boebinger, A Passner, L F Schneemeyer, T Kimura, M Okuya, S Watauchi, J Shimoyama, K Kishio, K Tamasaku, N Ichikawa, and S Uchida. Resistive upper critical fields and irreversibility lines of optimally doped high-T_c cuprates. *Physical Review B*, 60:12475–12479, 1999.

[84] D E Farrell, B S Chandrasekhar, M R DeGuire, M M Fang, V G Kogan, J R Clem, and D K Finnemore. Superconducting properties of aligned crystalline grains of $Y_1Ba_2Cu_3O_{7-\delta}$. *Physical Review B*, 36(7):4025–4027, 1987.

[85] G W Crabtree, J Z Liu, A Umezawa, W K Kwok, C H Sowers, S K Malik, B W Veal, D J Lam, M B Brodsky, and J W Downey. Large anisotropic critical magnetization currents in single-crystal $YBa_2Cu_3O_{7-\delta}$. *Physical Review B*, 36(7):4021–4024, 1987.

[86] L F Schneemeyer, E M Gyorgy, and J V Waszczak. Magnetic characterization of rare-earth barium cuprate superconductors. *Physical Review B*, 36(16):8804–8806, 1987.

[87] J W Ekin, A I Braginski, A J Panson, M A Janocko, D W Capone, N J Zaluzec, B Flandermeyer, O F de Lima, M Hong, J Kwo, and S H Liou. Evidence for weak link and anisotropy limitations on the transport critical current in bulk polycrystalline $Y_1Ba_2Cu_3O_x$. *Journal of Applied Physics*, 62(12):4821–4828, 1987.

[88] D Dimos, P Chaudhari, J Mannhart, and F K LeGoues. Orientation dependence of grain-boundary critical currents in $YBa_2Cu_3O_{7-\delta}$ bicrystals. *Physical Review Letters*, 61(2):219–222, 1988.

[89] N F Heinig, R D Redwing, I Fei Tsu, A Gurevich, J E Nordman, S E Babcock, and D C Larbalestier. Evidence for channel conduction in low misorientation angle [001] tilt YBaCuO bicrystal flims. *Applied Physics Letters*, 69:577–580, 1996.

[90] H Hilgenkamp and J Mannhart. Grain boundaries in high-T_c superconductors. *Reviews of Modern Physics*, 74(2):485–549, 2002.

[91] Z G Ivanov, P Å Nilsson, D Winkler, J A Alarco, T Claeson, E A Stepantsov, and A Y Tzalenchuk. Weak links and dc squids on artificial nonsymmetric grain boundaries in $YBa_2Cu_3O_{7-\delta}$. *Applied Physics Letters*, 59:3030–3032, 1991.

[92] D Dimos, P Chaudhari, and J Mannhart. Superconducting transport properties of grain boundaries in $YBa_2Cu_3O_7$ bicrystals. *Physical Review B*, 41(7):4038–4049, 1990.

[93] J H Durrell and N A Rutter. Importance of low-angle grain boundaries in $YBa_2Cu_3O_{7-\delta}$ coated conductors. *Superconductor Science and Technology*, 22(1):013001, 2009.

[94] P G De Gennes. *Superconductivity of Metals and Alloys*. Perseus Books Group, Boulder, Colorado, 1999.

[95] National High Magnetic Field Laboratory. https://nationalmaglab.org/magnet-development/applied-superconductivity-center/plots. *Comparisons of critical and engineering current densities for superconductors available in long lengths*, 2018(02/04/2018):National High Magnetic Field Laboratory, 2017.

[96] Y Yamada, M Mogi, and K Sato. Examples and future prospects of high-temperature superconductor products. *Sei Technical Review*, 65:51–59, 2007.

[97] D C Larbalestier, J Jiang, U P Trociewitz, F Kametani, C Scheuerlein, M Dalban-Canassy, M Matras, P Chen, N C Craig, P J Lee, and E E Hellstrom. Isotropic round-wire multifilament cuprate superconductor for generation of magnetic fields above 30 T. *Nat Mater*, 13(4):375–381, 2014.

[98] Y Yuan, J Jiang, X Y Cai, D C Larbalestier, E E Hellstrom, Y Huang, and R Parrella. Significantly enhanced critical current density in Ag-sheathed $(Bi,Pb)_2Sr_2Ca_2Cu_3O_x$ composite conductors prepared by overpressure processing in final heat treatment. *Applied Physics Letters*, 84(12):2127–2129, 2004.

[99] P Chen, U P Trociewitz, D S Davis, E S Bosque, D K Hilton, Y Kim, D V Abraimov, W L Starch, J Jiang, E E Hellstrom, and D C Larbalestier. Development of a persistent superconducting joint between Bi-2212/Ag-alloy multifilamentary round wires. *Superconductor Science and Technology*, 30(2):025020, 2017.

[100] H Kitaguchi, K Takahashi, H Kumakura, T Hayashi, K Fujino, N Ayai, and K Sato. Performance of an over-pressure processed Bi-2223/Ag/SUS tape and a small layer-winding coil. *Superconductor Science Technology*, 22, 2009.

[101] F Kametani, J Jiang, M Matras, D Abraimov, E E Hellstrom, and D C Larbalestier. Comparison of growth texture in round Bi2212 and flat Bi2223 wires and its relation to high critical current density development. *Scientific Reports*, 5:8285, 2015.

[102] SuperPower-Furukawa. High quality joints for superpower 2G HTS wire. *http://www.superpower-inc.com/system/files/SP_2G+Wire+Joints_2013FEC_v2.pdf*, 2013.

[103] Haynes International. Hastelloy C-276 alloy. *http://haynesintl.com/docs/default-source/pdfs/new-alloy-brochures/corrosion-resistant-alloys/brochures/c-276.pdf*, 2018(16/03/2018).

[104] L S Yu, J M E Harper, J J Cuomo, and D A Smith. Alignment of thin films by glancing angle ion bombardment during deposition. *Applied Physics Letters*, 47(9):932–933, 1985.

[105] Fujikura. 2g high temperature superconductor. *https://www.fujikura.co.uk/products/energy-and-environment/2g-ybco-high-tempurature-superconductors/#productDescription*, 2018(03/12/2018).

[106] SuNam. Superconducitng wire. *http://i-sunam.com/home/en$_p$roduct*, 1, 3, 1, 1, 1, 2019.

[107] SuperOx. 2G HTS tape performance and specifications. *http://www.superox.ru/products/0001.pdf*, 2018.

[108] Bruker. YBCO 2G HTS. *https://www.bruker.com/products/superconductors-and-metal-composite-materials/superconductors/ybco-2g-hts-superconductors/learn-more.html*, 2018(03/12/2018), 2018.

[109] M Bauer, R Semerad, and H Kinder. YBCO films on metal substrates with biaxially aligned MgO buffer layers. *IEEE Transactions on Applied Superconductivity*, 9(2):1502–1505, 1999.

[110] THEVA. THEVA pro-line HTS wire: general properties. *https://www.theva.de/wp-content/uploads/2018/05/171218_THEVA_Broschuere_Pro-Line_generalproperties.pdf*, 2017.

[111] D P Norton, A Goyal, J D Budai, D K Christen, D M Kroeger, E D Specht, Q He, B Saffian, M Paranthaman, C E Klabunde, D F Lee, B C Sales, and F A List. Epitaxial $YBa_2Cu_3O_7$ on biaxially textured nickel (001): An approach to superconducting tapes with high critical current density. *Science*, 274(5288):755, 1996.

[112] X Li, M W Rupich, C L H Thieme, M Teplitsky, S Sathyamurthy, E Thompson, D Buczek, J Schreiber, K DeMoranville, J Lynch, J Inch, D Tucker, R Savoy, and S Fleshler. The development of second generation HTS wire at American Superconductor. *IEEE Transactions on Applied Superconductivity*, 19(3):3231–3235, 2009.

[113] Jeffrey T Cheung. *Chapter 5.4 - Pulsed Laser Deposition*, pages 694–710. Academic Press, San Diego, 1998.

[114] Y Ichino, R Honda, M Miura, M Itoh, Y Yoshida, Y Takai, K Matsumoto, M Mukaida, A Ichinose, and S Horii. Microstructure and field angle dependence of critical current densities in $REBa_2Cu_3O_y$ thin films prepared by PLD method. *IEEE Transactions on Applied Superconductivity*, 15(2):3730–3733, 2005.

[115] D M Feldmann, D C Larbalestier, T Holesinger, R Feenstra, A A Gapud, and E D Specht. Evidence for extensive grain boundary meander and overgrowth of substrate grain boundaries in high critical current density ex situ $YBa_2Cu_3O_{7x}$ coated conductors. *Journal of Materials Research*, 20(8):2012–2020, 2005.

[116] T G Holesinger, P N Arendt, R Feenstra, A A Gapud, E D Specht, D M Feldmann, and D C Larbalestier. Liquid mediated growth and the bimodal microstructure of $YBa_2Cu_3O_{7-\delta}$ films made by the ex situ conversion of physical vapor deposited BaF_2 precursors. *Journal of Materials Research*, 20(5):1216–1233, 2011.

[117] X Obradors, T Puig, S Ricart, M Coll, J Gazquez, A Palau, and X Granados. Growth, nanostructure and vortex pinning in superconducting $YBa_2Cu_3O_7$ thin films based on trifluoroacetate solutions. *Superconductor Science and Technology*, 25(12):123001, 2012.

[118] M W Rupich, W Zhang, X Li, T Kodenkanth, D T Verebelyi, U Schoop, C Thieme, M Teplitsky, J Lynch, N Nguyen, E Siegal, J Scudiere, V Maroni, K Venkataraman, D Miller, and T G Holesinger. Progress on MOD/RABiTS(TM) 2G HTS wire. *Physica C*, 412-414:877–884, 2004.

[119] V Selvamanickam, H G Lee, Y Li, J Reeves, Y Qiao, Y Y Xie, K Lenseth, G Carota, M Funk, K Zdun, J Xie, K Likes, M Jones, L Hope, and D W Hazelton. Scale up of high-performance Y-Ba-Cu-O coated conductors. *IEEE Transactions on Applied Superconductivity*, 13(2):2492–2495, 2003.

[120] R P Zhao, F Zhang, Q Liu, Y D Xia, Y M Lu, C B Cai, B W Tao, and Y R Li. The preparation of high-J_c $Gd_{0.5}Y_{0.5}Ba_2Cu_3O_{7-\delta}$ thin films by the MOCVD process. *Superconductor Science and Technology*, 29(6):065015, 2016.

[121] H-S Kim, S-S Oh, H-S Ha, D Youm, S-H Moon, J H Kim, S X Dou, Y-U Heo, S-H Wee, and A Goyal. Ultra-high performance, high-temperature superconducting wires via cost-effective, scalable, co-evaporation process. *Scientific Reports*, 4:4744, 2014.

[122] A V Pan, S Pysarenko, and S X Dou. Drastic improvement of surface structure and current-carrying ability in $YBa_2Cu_3O_7$ films by introducing multilayered structure. *Applied Physics Letters*, 88(23):232506, 2006.

[123] R Ramesh, A Inam, D M Hwang, T D Sands, C C Chang, and D L Hart. Surface outgrowth problem in *c*-axis oriented Y-Ba-Cu-O superconducting thin films. *Applied Physics Letters*, 58(14):1557–1559, 1991.

[124] C J van der Beek, M Konczykowski, A Abal'oshev, I Abal'osheva, P Gierlowski, S J Lewandowski, M V Indenbom, and S Barbanera. Strong pinning in high-temperature superconducting films. *Physical Review B*, 66(2):024523, 2002.

[125] A O Ijaduola, F List, H S Kim, S S Oh, and A Goyal. Robust critical current density in applied magnetic fields in 5 μm thick, $SmBa_2Cu_3O_{7\delta}$ based superconducting wires. *Physica C: Superconductivity and its Applications*, 517:1–4, 2015.

[126] T Yoshida, A Ibi, T Takahashi, M Yoshizumi, T Izumi, and Y Shiohara. Fabrication of $Eu_1Ba_2Cu_3O_{7-\delta} + BaHfO_3$ coated conductors with 141 A/cm-w under 3 T at 77 K using the IBAD/PLD process. *Physica C: Superconductivity and its Applications*, 504:42–46, 2014.

[127] D Zhu, J Huang, H Li, M Shen, and X Su. A new method to preserve the *c*-axis growth of thick $YBa_2Cu_3O_{7-\delta}$ films grown by pulsed laser deposition. *Physica C: Superconductivity and its Applications*, 469(22):1977–1982, 2009.

[128] B Maiorov, S A Baily, H Zhou, O Ugurlu, J A Kennison, P C Dowden, T G Holesinger, S R Foltyn, and L Civale. Synergetic combination of different types of defect to optimize pinning landscape using $BaZrO_3$-doped $YBa_2Cu_3O_7$. *Nature Materials*, 8:398, 2009.

[129] S Miura, Y Yoshida, Y Ichino, A Tsuruta, K Matsumoto, A Ichinose, and S Awaji. Vortex pinning at low temperature under high magnetic field in $SmBa_2Cu_3O_y$ superconducting films with high number density and small size of $BaHfO_3$ nanorods. *Superconductor Science and Technology*, 28(11):114006, 2015.

[130] R Teranishi, S Yasunaga, H Kai, K Yamada, M Mukaida, N Mori, T Fujiyoshi, A Ichinose, S Horii, K Matsumoto, Y Yoshida, R Kita, and S Awaji. Superconducting properties of ErBCO films with $BaMO_3$ nanorods (M = Zr and Sn) by pulsed laser deposition. *Physica C: Superconductivity*, 468(15):1522–1526, 2008.

[131] J Z Wu, J J Shi, F J Baca, R Emergo, J Wilt, and T J Haugan. Controlling $BaZrO_3$ nanostructure orientation in $YBa_2Cu_3O_{7-\delta}$ films for a three-dimensional pinning landscape. *Superconductor Science and Technology*, 28(12):125009, 2015.

[132] V Selvamanickam, Y Chen, T Shi, Y Liu, N D Khatri, J Liu, Y Yao, X Xiong, C Lei, S Soloveichik, E Galstyan, and G Majkic. Enhanced critical currents in $(Gd, Y)\,Ba_2Cu_3O_x$ superconducting tapes with high levels of zr addition. *Superconductivity Science and Technology*, 26:035006, 2013.

[133] A Xu, V Braccini, J Jaroszynski, Y Xin, and D C Larbalestier. Role of weak uncorrelated pinning introduced by $BaZrO_3$ nanorods at low-temperature in $(Y, Gd)\,Ba_2Cu_3O_x$ thin films. *Physical Review B*, 86(11):115416, 2012.

[134] A Xu, L Delgado, N Khatri, Y Liu, V Selvamanickam, D Abraimov, J Jaroszynski, F. Kametani, and D. C. Larbalestier. Strongly enhanced vortex pinning from 4 to 77 K in magnetic fields up to 31 T in 15 mol.% Zr-added (Gd, Y)-Ba-Cu-O superconducting tapes. *APL Materials*, 2(4):046111, 2014.

[135] A Llordés, A Palau, J Gázquez, M Coll, R Vlad, A Pomar, J Arbiol, R Guzmán, S Ye, V Rouco, F Sandiumenge, S Ricart, T Puig, M Varela, D Chateigner, J Vanacken, J Gutiérrez, V Moshchalkov, G Deutscher, C Magen, and X Obradors. Nanoscale strain-induced pair suppression as a vortex-pinning mechanism in high-temperature superconductors. *Nature Materials*, 11:329, 2012.

[136] A Xu, J Jaroszynski, F Kametani, and D Larbalestier. Broad temperature range study of J_c and H_{irr} anisotropy in $YBa_2Cu_3O_x$ thin films containing either Y_2O_3 nanoparticles or stacking faults. *Applied Physics Letters*, 106(5):052603, 2015.

[137] V Selvamanickam, A Xu, Y Liu, N D Khatri, C Lei, Y Chen, E Galstyan, and G Majkic. Correlation between in-field critical currents in zr-added $(Gd, Y)\,Ba_2Cu_3O_x$ superconducting tapes at 30 k and 77 k. *Supercond. Sci. and Technol.*, 27:055010, 2014.

[138] A Xu, L Delgado, M Heydari Gharahcheshmeh, N Khatri, Y Liu, and V Selvamanickam. Strong correlation between $J_c\,(T, H \parallel c)$ and $j_c\,(77\,K, 3\,T \parallel c)$ in Zr-added (Gd, Y) BaCuO coated conductors at temperatures from 77 down to 20 K and fields up to 9 T. *Superconductor Science and Technology*, 28(8):082001, 2015.

[139] V Mishev, M Zehetmayer, D X Fischer, M Nakajima, H Eisaki, and M Eisterer. Interaction of vortices in anisotropic superconductors with isotropic defects. *Superconductor Science and Technology*, 28(10):102001, 2015.

[140] L Civale, B Maiorov, A Serquis, S R Foltyn, Q X Jia, P N Arendt, H Wang, J O Willis, J Y Coulter, T G Holesinger, J L MacManus-Driscoll, M W Rupich, W Zhang, and X Li. Influence of crystalline texture on vortex pinning near the *ab*-plane in $YBa_2Cu_3O_7$ thin films and coated conductors. *Physica C: Superconductivity*, 412–414, Part 2:976–982, 2004.

[141] H Yamasaki, K Ohki, H Yamada, Y Nakagawa, and Y Mawatari. Strong flux pinning in $YBa_2Cu_3O_{7-\delta}$ thin films due to nanometer-sized precipitates. *Superconductor Science and Technology*, 21(12):125011, 2008.

[142] H Yamasaki, I Yamaguchi, M Sohma, W Kondo, H Matsui, T Manabe, and T Kumagai. Temperature dependence of magnetic-field angle dependent critical current density and the flux pinning in $YBa_2Cu_3O_7$ thin films. *Physica C-Superconductivity and Its Applications*, 478:19–28, 2012.

[143] H Yamasaki, K Ohki, I Yamaguchi, M Sohma, W Kondo, H Matsui, T Manabe, and T Kumagai. Strong flux pinning due to dislocations associated with stacking faults in $YBa_2Cu_3O_{7-\delta}$ thin films prepared by fluorine-free metal organic deposition. *Superconductor Science and Technology*, 23(10):105004, 2010.

[144] M Tachiki and S Takahashi. Anisotropy of critical current in layered oxide superconductors. *Solid State Communications*, 72(11):1083–1086, 1989.

[145] M Tachiki and S Takahashi. Strong vortex pinning intrinsic in high-T_c oxide superconductors. *Solid State Communications*, 70(3):291–295, 1989.

[146] L Civale, B Maiorov, J L MacManus-Driscoll, H Wang, T G Holesinger, S R Foltyn, A Serquis, and R N Arendt. Identification of intrinsic *ab*-plane pinning in $YBa_2Cu_3O_7$ thin films and coated conductors. *IEEE Transactions on Applied Superconductivity*, 15(2):2808–2811, 2005.

[147] T Sueyoshi, Y Iwanaga, T Fujioyoshi, Y Takai, M Mukaida, M Kudo, K Yasuda, and N Ishikawa. Angular behavior of J_c in gdbco-coated conductors with crossed columnar defects around *ab* plane. *IEEE Transactions on Applied Superconductivity*, 27(4):1–5, 2017.

[148] N Cheggour, J W Ekin, C C Clickner, D T Verebelyi, C L H Thieme, R Feenstra, and A Goyal. Reversible axial-strain effect and extended strain limits in y-ba-cu-o coatings on deformation-textured substrates. *Applied Physics Letters*, 83(20):4223–4225, 2003.

[149] N Cheggour, J W Ekin, C L H Thieme, Y-Y Xie, V Selvamanickam, and R Feenstra. Reversible axial-strain effect y-ba-cu-o coated conductors. *Superconductor Science Technology*, 18:S319–S324, 2005.

[150] A Gorospe, Z Bautista, H S Shin, H Oguro, and S Awaji. Characteristic irreversible critical strain limit of GdBCO-coated conductor tapes under various temperature and magnetic field conditions. *IEEE Transactions on Applied Superconductivity*, 27(4):1–5, 2017.

[151] K Osamura, S Machiya, H Suzuki, S Ochiai, H Adachi, N Ayai, K Hayashi, and K Sato. Mechanical behavior and strain dependence of the critical current of di-bscco tapes. *Superconductor Science and Technology*, 21:054010, 2008.

[152] K Osamura, S Machiya, Y Tsuchiya, and H Suzuki. Force free strain exerted on a ybco layer at 77 k in surround cu stabilized ybco coated conductors. *Superconductor Science and Technology*, 23(4):045020, 2010.

[153] K Osamura, M Sugano, S Machiya, H Adachi, S Ochiai, and M Sato. Internal residual strain and critical current maximum of a surrounded cu stabilized ybco coated conductor. *Superconductor Science and Technology*, 22:065001, 2009.

[154] K Osamura, S Machiya, and G Nishijima. Reversible stress and strain limits of the critical current of practical REBCO and BSCCO wires. *Superconductor Science and Technology*, 29(9):094003, 2016.

[155] H S Shin, K H Kim, J RC Dizon, T Y Kim, R K Ko, and S S Oh. The strain effect on critical current in ybco coated conductors with different stabilizing layers. *Superconductor Science Technology*, 18:S364–S368, 2005.

[156] D M J Taylor, S A Keys, and D P Hampshire. Reversible and irreversible effects of strain on the critical current density of a niobium-tin superconducting wire. *Cryogenics*, 42:109–112, 2002.

[157] A Grossmüller, V Zelizko, and M V Swain. Fatigue crack growth in ceramics using a compressive loading geometry. *Journal of Materials Science Letters*, 8(1):29–31, 1989.

[158] E Z Wang and N G Shrive. On the griffith criteria for brittle fracture in compression. *Engineering Fracture Mechanics*, 46(1):15–26, 1993.

[159] E Z Wang and N G Shrive. Brittle fracture in compression: Mechanisms, models and criteria. *Engineering Fracture Mechanics*, 52(6):1107–1126, 1995.

[160] J W Ekin. Strain dependence of the critical current and critical field in multifilamentary Nb_3Sn composites. *IEEE Transactions on Magnetics*, 15:197–200, 1979.

[161] M Sugano, K Osamura, W Prusseit, R Semerad, K Itoh, and T Kiyoshi. Tensile fracture behaviour of RE-123 coated conductors induced by discontinuous yielding in Hastelloy C-276 substrate. *Superconductor Science and Technology*, 18(12):S344, 2005.

[162] M Sugano, K Osamura, W Prusseit, R Semerad, T Kuroda, K Itoh, and T Kiyoshi. Reversible strain dependence of critical current in 100 A class coated conductors. *Ieee Transactions on Applied Superconductivity*, 15(2):3581–3584, 2005.

[163] A Villaume, A Antonevici, D Bourgault, L Porcar, J P Leggeri, and C Villard. Luders bands in coated conductors: an in situ strain and transport magneto-optical investigation. *Superconductor Science and Technology*, 20(10):1019–1025, 2007.

[164] A Godeke, M H C Hartman, M G T Mentink, J Jiang, M Matras, E E Hellstrom, and D C Larbalestier. Critical current of dense Bi-2212 round wires as a function of axial strain. *Superconductor Science and Technology*, 28(3):032001, Feb 2015.

[165] P Sunwong, J S Higgins, and D P Hampshire. Angular, temperature and strain dependencies of the critical current of DI-BSCCO tapes in high magnetic fields. *IEEE Transactions on Applied Superconductivity*, 21(3):2840–2844, 2011.

[166] B ten Haken, A Beuink, and H H J ten Kate. Small and repetitive axial strain reducing the critical current in BSCCO/Ag superconductors. *IEEE Transactions on Applied Superconductivity*, 7:2034–2037, 1997.

[167] J W Ekin. Relationships between critical current and stress in nbti. *IEEE Trans. Magn.*, 23(2):1634–1637, 1987.

[168] N Cheggour and D P Hampshire. Unifying the strain and temperature scaling laws for the pinning force density in superconducting niobium-tin multifilamentary wires. *Journal of Applied Physics*, 86:552, 1999.

[169] N Cheggour and D P Hampshire. The unified strain and temperature scaling law for the pinning force density of bronze-route Nb3Sn wires in high magnetic fields. *Cryogenics*, 42:299 – 309, 2002.

[170] J W Ekin. Strain scaling law for flux pinning in practical superconductors. part i: Basic relationship and application to Nb_3Sn conductors. *Cryogenics*, 20:611–624, 1980.

[171] J W Ekin. Unified scaling law for flux pinning in practical superconductors: I. separability postulate, raw scaling data and parameterization at moderate strains. *Superconductor Science Technology*, 23:083001, 2010.

[172] A Godeke, B ten Haken, H H J ten Kate, and D Larbalestier. A general scaling relation for the critical current density in Nb_3Sn. *Superconductor Science Technology*, 19:R100–R116, 2006.

[173] S A Keys and D P Hampshire. A scaling law for the critical current density of weakly and strongly-coupled superconductors, used to parameterise data from a technological Nb_3Sn strand. *Superconductor Science and Technology*, 16:1097–1108, 2003.

[174] X F Lu and D P Hampshire. The magnetic field, temperature and strain dependence of the critical current of a Nb_3Sn strand using a six free-parameter scaling law. *IEEE Transactions on Applied Superconductivity*, 19(3):2619–2623, 2009.

[175] X F Lu and D P Hampshire. The field, temperature and strain dependence of the critical current density of a powder-in-tube (pit) nb3sn superconducting strand. *Superconductor Science Technology*, 23:025002, 2010.

[176] X F Lu, S Pragnell, and D P Hampshire. Influence of longitudinal strain on the critical current of Nb_3Sn strands. Report EFDA/06-1524, Durham University, 2008.

[177] X F Lu, D M J Taylor, and D P Hampshire. Critical current scaling laws for advanced nb3sn superconducting strands for fusion applications with six free parameters. *Superconductor Science Technology*, 21(10):105016, 2008.

[178] D M J Taylor and D P Hampshire. The scaling law for the strain dependence of the critical current density in nb3sn superconducting wires. *Superconductor Science and Technology*, 18:S241–S252, 2005.

[179] Y Tsui and D P Hampshire. Critical current scaling and the pivot-point in Nb_3Sn strands. *Superconductor Science and Technology*, 25(5):054008, 2012.

[180] N Cheggour and D P Hampshire. A probe for investigating the effect of magnetic field, temperature and strain on transport critical currents in superconducting tapes and wires. *Review of Scientific Instruments*, 71:4521, 2000.

[181] J W Ekin, N Cheggour, M Abrecht, C C Clickner, M B Field, S Hong, J A Parrell, and Y Z Zhang. Compressive pre-strain in high-niobium-fraction Nb_3Sn superconductors. *IEEE Transactions on Applied Superconductivity*, 15(2):3560–3563, 2005.

[182] S Ochiai, K Osamura, and K Watanabe. Estimation of the strength distribution of Nb_3Sn in multifilamentary composite wire from change in superconducting current due to preloading. *Journal of Applied Physics*, 74(1):440–445, 1993.

[183] K Osamura, S Machiya, Y Tsuchiya, H Suzuki, T Shobu, M Sato, T Hemmi, Y Nunoya, and S Ochiai. Local strain and its influence on mechanical–electromagnetic properties of twisted and untwisted ITER Nb_3Sn strands. *Superconductor Science and Technology*, 25(5):054010, 2012.

[184] S Ochiai and K Osamura. Influence of cyclic loading at room-temperature on the critical current at 4.2 K of Nb_3Sn superconducting composite wire. *Cryogenics*, 32(6):584–590, 1992.

[185] D M J Taylor and D P Hampshire. Effect of axial strain cycling on the critical current density and n-values of ITER niobium-tin wires. *Physica C*, 401:40–46, 2004.

[186] N Cheggour, J W Ekin, and C Thieme. Magnetic-field dependence of the reversible axial-strain effect in y-ba-cu-o coated conductors. *IEEE Transactions on Applied Superconductivity*, 15:3577–3580, 2005.

[187] K Higashikawa, T Kiss, M Inoue, K Imamura, T Nakamura, S Awaji, K Watanabe, H Fukushima, Y Yamada, and Y Shiohara. Coupled analysis method for high-field magnet coil using coated conductor based on $j - e$ characteristics as a function of temperature, magnetic field vector and mechanical strain. *IEEE Transactions on Applied Superconductivity*, 19(3):1621–1625, 2009.

[188] H Shin, A Gorospe, Z Bautista, and M J Dedicatoria. Evaluation of the electromechanical properties in gdbco coated conductor tapes under low cyclic loading and bending. *Superconductor Science and Technology*, 29(1):014001, 2016.

[189] K Osamura, M Sugano, K Nakao, Y Shiohara, A Ibi, Y Yamada, N Nakashima, S Nagaya, T Saitoh, Y Iijima, Y Aoki, T Hasegawa, and T Kato. Reversible strain limit of critical currents and universality of intrinsic strain effect for REBCO-coated conductors. *Superconductor Science and Technology*, 22(2), 2009.

[190] H S Shin, M Dedicatoria, A Gorospe, J R Dizon, H Oguro, and S Awaji. Strain and magnetic field response of I_c in reinforced GdBCO coated conductor tapes at 77 K. *Advances in Cryogenic Engineering, Vol 60*, 1574:239–244, 2014.

[191] H S Shin, M J Dedicatoria, and A Gorospe. I_c strain performance of REBCO coated-conductor tapes under low magnetic field. *IEEE Transactions on Applied Superconductivity*, 26(4):1–4, 2016.

[192] H S Shin, M J Dedicatoria, A Gorospe, and S H Lee. Experimental measurement of characteristic $I_c(\varepsilon, \theta, B)$ response in $GdBa_2Cu_3O_\delta$ coated conductor tapes under low magnetic field at 77 K. *Review of Scientific Instruments*, 86(3):9, 2015.

[193] H S Shin, M J Dedicatoria, A Gorospe, H Oguro, and S Awaji. I_c response with high magnetic field, low temperature, and uniaxial strain in REBCO coated conductor tapes. *IEEE Transactions on Applied Superconductivity*, 26(4):1–4, 2016.

[194] H S Shin, A Gorospe, A R Nisay, M J Dedicatoria, K D Sim, S Awaji, and H Oguro. Macroscopic strain response of I_c under magnetic fields in differently stabilized REBCO CC tapes. *IEEE Transactions on Applied Superconductivity*, 25(3):1–4, 2015.

[195] M Sugano, T Nakamura, T Manabe, K Shikimachi, N Hirano, and S Nagaya. The intrinsic strain effect on critical current under a magnetic field parallel to the *c* axis for a MOCVD-YBCO-coated conductor. *Superconductor Science and Technology*, 21:115019, 2008.

[196] M Sugano, K Osamura, W Prusseit, R Semerad, K Itoh, and T Kiyoshi. Intrinsic strain effect on critical current and its reversibility for YBCO coated conductors with different buffer layers. *Superconductor Science and Technology*, 18(3):369–372, 2005.

[197] D Uglietti, B Seeber, V Abacherli, W L Carter, and R Flukiger. Critical currents versus applied strain for industrial Y-123 coated conductors at various temperatures and magnetic fields up to 19 T. *Superconductor Science and Technology*, 19:869–872, 2006.

[198] K Ilin, K A Yagotintsev, C Zhou, P Gao, J Kosse, S J Otten, W A J Wessel, T J Haugan, D C van der Laan, and A Nijhuis. Experiments and fe modeling of stress-strain state in rebco tape under tensile, torsional and transverse load. *Superconductor Science Technology*, 28(5):17, 2015.

[199] K Osamura, S Machiya, and D P Hampshire. Mechanism for the uniaxial strain dependence of the critical current in practical rebco tapes. *Superconductor Science and Technology*, 29(6):065019, 2016.

[200] D C van der Laan. YBCO coated conductor cabling for low ac-loss and high-field magnet applications. *Superconductor Science and Technology*, 22:065013, 2009.

[201] D C van der Laan, D Abraimov, A A Polyanskii, D C Larbalestier, J F Douglas, R Semerad, and M Bauer. Anisotropic in-plane reversible strain effect in $Y_{0.5}Gd_{0.5}Ba_2Cu_3O_{7-\delta}$ coated conductors. *Superconductor Science and Technology*, 24(11):115010, 2011.

[202] D C van der Laan, J F Douglas, L F Goodrich, R Semerad, and M Bauer. Correlation between in-plane grain orientation and the reversible strain effect on flux pinning in RE-$Ba_2Cu_3O_{7-\delta}$ coated conductors. *IEEE Transactions on Applied Superconductivity*, 22(1):8400707–8400707, 2012.

[203] D C van der Laan and J W Ekin. Large intrinsic effect of axial strain on the critical current of high-temperature superconductors for electric power applications. *Applied Physics Letters*, 90(5):052506, 2007.

[204] D C van der Laan, X F Lu, and L F Goodrich. Compact $GdBa_2Cu_3O_{7-\delta}$ coated conductor cables for electric power transmission and magnet applications. *Superconductor Science and Technology*, 24(4), 2011.

[205] C Zhou, K A Yagotintsev, P Gao, T J Haugan, D C van der Laan, and A Nijhuis. Critical current of various REBCO tapes under uniaxial strain. *IEEE Transactions on Applied Superconductivity*, 26(4):1–4, 2016.

[206] J S Higgins and D P Hampshire. Critical current density of $YBa_2Cu_3O_{7-\delta}$ coated conductors under high compression in high fields. *IEEE Transactions on Applied Superconductivity*, 21(3):3234–3237, 2011.

[207] P Sunwong, J S Higgins, Y Tsui, M J Raine, and D P Hampshire. The critical current density of grain boundary channels in polycrystalline HTS and LTS superconductors in magnetic fields. *Superconductor Science and Technology*, 26:095006, 2013.

[208] M Sugano, K Shikimachi, N Hirano, and S Nagaya. The reversible strain effect on critical current over a wide range of temperatures and magnetic fields for ybco coated conductors. *Superconductor Science and Technology*, 23:085013, 2010.

[209] D C van der Laan, J W Ekin, J F Douglas, C C Clickner, T C Stauffer, and L F Goodrich. Effect of strain, magnetic field and field angle on the critical current density of $YBa_2Cu_3O_{7-\delta}$ coated conductors. *Superconductor Science Technology*, 23:072001, 2010.

[210] W H Fietz, K P Weiss, and S I Schlachter. Influence of intrinsic strain on tc and critical current of high-t_c superconductors. *Superconductor Science Technology*, 18(12):S332–S337, 2005.

[211] U Welp, M Grimsditch, S Fleshler, W Nessler, J Downey, and G W Crabtree. Effect of uniaxial stress on the superconducting transition in $YBa_2Cu_3O_7$. *Physical Review Letters*, 69(14):2130, 1992.

[212] J Boutard, A Alamo, R Lindau, and M Rieth. Fissile core and tritium-breeding blanket: structural materials and their requirements. *Comptes Rendus Physique*, 9(3):287–302, 2008.

[213] K Tobita, H Utoh, C Liu, H Tanigawa, D Tsuru, M Enoeda, T Yoshida, and N Asakura. Search for reality of solid breeder blanket for DEMO. *Fusion Engineering and Design*, 85(7–9):1342–1347, 2010.

[214] S G Roberts, R Kemp, D Neely, S Lilley, L Morgan, A Widdowson, G Pintsuk, M Rieth, A Costley, and M Porton. Fusion DTN: Materials applications course. *Lecture course, http://www.fusion-cdt.ac.uk/training/materials/*, 2013.

[215] T Lauritzen, A Withop, and U E Wolff. Swelling of austenitic stainless steels under fast neutron irradiation at elevated temperatures. *Nuclear Engineering and Design*, 9(2):265–268, 1969.

[216] V de Castro, S Lozano-Perez, and M L Jenkins. Stability of nanoparticles in an oxide dispersion strengthened alloy. *Journal of Physics: Conference Series*, 241(1):012107, 2010.

[217] R L Klueh, J P Shingledecker, R W Swindeman, and D T Hoelzer. Oxide dispersion-strengthened steels: A comparison of some commercial and experimental alloys. *Journal of Nuclear Materials*, 341(2-3):103–114, 2005.

[218] A Kohyama, A Hishinuma, D S Gelles, R L Klueh, W Dietz, and K Ehrlich. Low-activation ferritic and martensitic steels for fusion application. *Journal of Nuclear Materials*, 233-237:138–147, 1996.

[219] R Lässer, N Baluc, J L Boutard, E Diegele, S Dudarev, M Gasparotto, A Möslang, R Pippan, B Riccardi, and B van der Schaaf. Structural materials for DEMO: The EU development, strategy, testing and modelling. *Fusion Engineering and Design*, 82(5):511–520, 2007.

[220] R Lindau, A Möslang, M Rieth, M Klimiankou, E Materna-Morris, A Alamo, A A F Tavassoli, C Cayron, A M Lancha, P Fernandez, N Baluc, R Schäublin, E Diegele, G Filacchioni, J W Rensman, B van der Schaaf, E Lucon, and W Dietz. Present development status of EUROFER and ODS-EUROFER for application in blanket concepts. *Fusion Engineering and Design*, 75-79:989–996, 2005.

[221] E Lucon, P Benoit, P Jacquet, E Diegele, R Lässer, A Alamo, R Coppola, F Gillemot, P Jung, A Lind, S Messoloras, P Novosad, R Lindau, D Preininger, M Klimiankou, C Petersen, M Rieth, E Materna-Morris, H C Schneider, J W Rensman, B van der Schaaf, B K Singh, and P Spaetig. The european effort towards the development of a DEMO structural material: Irradiation behaviour of the european reference RAFM steel EUROFER. *Fusion Engineering and Design*, 81(8):917–923, 2006.

[222] B van der Schaaf, F Tavassoli, C Fazio, E Rigal, E Diegele, R Lindau, and G LeMarois. The development of EUROFER reduced activation steel. *Fusion Engineering and Design*, 69(1):197–203, 2003.

[223] M Aleksa, P Pongratz, O Eibl, F M Sauerzopf, H W Weber, T W Li, and P H Kes. Tem observation of neutron-induced collision cascades in bi-2212 single crystals. *Physica C: Superconductivity*, 297(3):171–175, 1998.

[224] M C Frischherz, M A Kirk, J Farmer, L R Greenwood, and H W Weber. Defect cascades produced by neutron irradiation in $YBa_2Cu_3O_{7\delta}$. *Physica C: Superconductivity*, 232(3):309–327, 1994.

[225] A Nishimura, T Takeuchi, S Nishijima, H Oguro, K Ochiai, K Watanabe, and T Shikama. Fast neutron irradiation effect on superconducting properties of Nb_3Sn and Nb_3Al strands. *AIP Conference Proceedings*, 1435(1):217–224, 2012.

[226] T Baumgartner, M Eisterer, H W Weber, R Flükiger, C Scheuerlein, and L Bottura. Effects of neutron irradiation on pinning force scaling in state-of-the-art Nb_3Sn wires. *Superconductor Science and Technology*, 27(1):015005, 2014.

[227] T Baumgartner, M Eisterer, H W Weber, R Flükiger, C Scheuerlein, and L Bottura. Performance boost in industrial multifilamentary nb3sn wires due to radiation induced pinning centers. *Scientific Reports*, 5:10236, 2015.

[228] M Chudy, M Eisterer, and H W Weber. Asymmetric angular dependence of J_c in coated conductors prior to and after fast neutron irradiation. *Physica C-Superconductivity and Its Applications*, 470(20):1300–1303, 2010.

[229] M Chudy, R Fuger, M Eisterer, and H W Weber. Characterization of commercial YBCO coated conductors after neutron irradiation. *IEEE Transactions on Applied Superconductivity*, 21(3):3162–3165, 2011.

[230] M Chudy, Z Zhong, M Eisterer, and T Coombs. n-values of commercial YBCO tapes before and after irradiation by fast neutrons. *Superconductor Science and Technology*, 28(3):035008, 2015.

[231] M Eisterer, R Fuger, M Chudy, F Hengstberger, and H W Weber. Neutron irradiation of coated conductors. *Superconductor Science and Technology*, 23(1):014009, 2010.

[232] R Flükiger, T Baumgartner, M Eisterer, H W Weber, T Spina, C Scheuerlein, C Senatore, A Ballarino, and L Bottura. Variation of $(j_c/j_{c0})_{max}$ of binary and ternary alloyed rrp and pit Nb_3Sn wires exposed to fast neutron irradiation at ambient reactor temperature. *IEEE Transactions on Applied Superconductivity*, 23(3):8001404–8001404, 2013.

[233] R Fuger, M Eisterer, F Hengstberger, and H W Weber. Influence of neutron irradiation on high temperature superconducting coated conductors. *Physica C: Superconductivity*, 468(15-20):1647–1651, 2008.

[234] R Fuger, M Eisterer, and H W Weber. YBCO coated conductors for fusion magnets. *IEEE Transactions on Applied Superconductivity*, 19(3):1532–1535, 2009.

[235] S Haindl, M Eisterer, R Muller, R Prokopec, H W Weber, M Muller, H Kirchmayr, T Takeuchi, and L Bargioni. Neutron irradiation effects on a15 multifilamentary wires. *IEEE Transactions on Applied Superconductivity*, 15(2):3414–3417, 2005.

[236] A Nishimura, T Takeuchi, S Nishijima, G Nishijima, T Shikama, K Ochiai, and N Koizumi. Neutron irradiation effects on superconducting wires and insulating materials. *Fusion Engineering and Design*, 84(7):1425–1428, 2009.

[237] R Prokopec, D X Fischer, H W Weber, and M Eisterer. Suitability of coated conductors for fusion magnets in view of their radiation response. *Superconductor Science and Technology*, 28(1):014005, 2015.

[238] F M Sauerzopf. Anisotropic flux pinning in $YBa_2Cu_3O_{7-\delta}$ single crystals: The influence of defect size and density as determined from neutron irradiation. *Physical Review B*, 57(17):10959–10971, 1998.

[239] F M Sauerzopf, H P Wiesinger, W Kritscha, H W Weber, G W Crabtree, and J Z Liu. Neutron irradiation effects on critical current densities in single-crystalline $YBa_2Cu_3O_{7-\delta}$. *Physical Review B*, 43(4):3091–3100, 1991.

[240] A R Sweedler, D E Cox, and S Moehlecke. Neutron irradiation of superconducting compounds. *Journal of Nuclear Materials*, 72(1):50–69, 1978.

[241] J Emhofer, M Eisterer, and H W Weber. Stress dependence of the critical currents in neutron irradiated (re)bco coated conductors. *Superconductor Science Technology*, 26(3), 2013.

[242] K E Sickafus, J O Willis, P J Kung, W B Wilson, D M Parkin, M P Maley, F W Clinard, C J Salgado, R P Dye, and K M Hubbard. Neutron-radiation-induced flux pinning in Gd-doped $YBa_2Cu_3O_{7-x}$ and $GdBa_2Cu_3O_{7-x}$. *Physical Review B*, 46(18):11862–11870, 1992.

[243] K Osamura, S Machiya, Y Tsuchiya, and H Suzuki. Force free strain exerted on a ybco layer at 77 k in surround cu stabilized ybco coated conductors. *Superconductor Science and Technology*, 23:045020, 2010.

[244] B Pietrass. Effect of non-hydrostatic stress on the superconducting transition of a15 compounds with high critical temperature. *Physica Status Solidi (A)*, 60(2):441–450, 1980.

[245] M Weger, B G Silbernagel, and E S Greiner. Effect of stress on the superconducting transition temperature of V_3Si. *Physical Review Letters*, 13(17):521–523, 1964.

[246] P Sunwong, J S Higgins, and D P Hampshire. Probes for investigating the effect of magnetic field, field orientation, temperature and strain on the critical current density of anisotropic high-temperature superconducting tapes in a split-pair 15 T horizontal magnet. *Rev. Sci. Instrum.*, 85(6):065111, 2014.

[247] Z Mei, H Holder, and H A Vander Plas. Low-temperature solders. *Hewlett-Packard Journal*, page 10, 1996.

[248] A Preuss, W H Fietz, F Immel, S Kauffmann-Weiss, and M J Wolf. Critical current degradation of coated conductors under soldering conditions. *IEEE Transactions on Applied Superconductivity*, 28(4):1–5, 2018.

[249] A Godeke, M Dhallé, A Morelli, L Stobbelaar, H van Weeren, H J N van Eck, W Abbas, A Nijhuis, A den Ouden, and B ten Haken. A device to investigate the axial strain dependence of the critical current density in superconductors. *Review of Scientific Instruments*, 75(12):5112–5118, 2004.

[250] D C van der Laan, H J N van Eck, J Schwartz, B ten Haken, and H H J ten Kate. Interpretation of the critical current in $Bi_2Sr_2Ca_2Cu_3O_x$ tape conductors as parallel weak-link and strong-link paths. *Physica C*, 372-376:1024–1027, 2002.

[251] B L Brandt, D W Liu, and L G Rubin. Low temperature thermometry in high magnetic fields. vii cernoxtm sensors to 32 t. *Review of Scientific Instruments*, 70:104–110, 1999.

[252] M J Raine, S A Keys, and D P Hampshire. *Characterisation of the Transport Critical Current Density for Conductor Applications*. Accepted by Taylor and Francis, 2017.

[253] C R Walters, I M Davidson, and G E Tuck. Long sample high sensitivity critical current measurements under strain. *Cryogenics*, 26:406–412, 1986.

[254] T Boutboul, V Abaecherli, G Berger, D Hampshire, J Parrell, M Raine, P Readman, B Sailer, K Schlenga, M Thoener, E Viladiu, and Y Zhang. European Nb_3Sn superconducting strand production and characterization for ITER tf coil conductor. *IEEE Transactions on Applied Superconductivity*, 26(4):1–4, 2016.

[255] D M J Taylor and D P Hampshire. Relationship between the n-value and critical current in nb3sn superconducting wires exhibiting intrinsic and extrinsic behaviour. *Superconductor Science and Technology*, 18:S297–S302, 2005.

[256] D M J Taylor, S A Keys, and D P Hampshire. $E - J$ characteristics and n-values of a niobium-tin superconducting wire as a function of magnetic field, temperature and strain. *Physica C*, 372:1291–1294, 2002.

[257] C P Poole, H A Farach, and R J Creswick. *Superconductivity*. Academic Press Inc, San Diego, California, 1995.

[258] Y Tsui, M J Raine, and D P Hampshire. Extended charachterisation of ITER strands - (MS-MG) TARSIS. Report, Durham University, 2014.

[259] D P Hampshire, H Jones, and E W J Mitchell. An in-depth characterisation of $(nbta)_3$ sn filamentary superconductor. *IEEE Transactions on Magnetics*, 21:289–292, 1985.

[260] M N Wilson. *Superconducting Magnets*. Oxford University Press, Oxford, UK, 1986.

[261] D R Tilley and J Tilley. *Superfluids: An Introduction*, page 18. IOP publishing Ltd., Bristol, 3rd edition, 1990.

[262] G J Carty and D P Hampshire. Visualising the mechanism that determines the critical current density in polycrystalline superconductors using time-dependent ginzburg-landau theory. *Physical Review B*, 77:172501, 2008.

[263] I G Hughes and T P A Hase. *Measurements and their Uncertainties: a practical guide to modern error analysis*. OUP, New York, USA, 2010.

[264] D Uglietti, N Bykovsky, K Sedlak, B Stepanov, R Wesche, and P Bruzzone. Test of 60 kA coated conductor cable prototypes for fusion magnets. *Superconductor Science and Technology*, 28(12):124005, 2015.

[265] J P McEvoy. Effect of uniaxial stress on the superconducting transition temperature of monocrystalline Nb_3Sn. *Physica*, 55:540–544, 1971.

[266] S Machiya, K Osamura, T Shobu, K Kiriyama, M Sugano, and K Tanaka. Macroscopic elastic constant analysis and strain behavior of crystal on the YBCO layer in a YBCO-coated conductor. *Teion Kogaku*, 46(5):233–238, 2011.

[267] T Suzuki, S Awaji, H Oguro, and K Watanabe. Applied strain effect on superconducting properties for detwinned (Y, Gd) BCO coated conductors. *IEEE Transactions on Applied Superconductivity*, 25(3):1–4, 2015.

[268] D S Easton, D M Kroeger, W Specking, and C C Koch. A prediction of the stress state in nb3sn superconducting composites. *Journal of Applied Physics*, 51(5):2748–2757, 1980.

[269] L Rossi. Superconductivity: its role, its success and its setbacks in the large hadron collider of cern. *Superconductor Science and Technology*, 23:034001, 2010.

[270] M Sborchia, E Barbero Soto, R Batista, B Bellesia, A Bonito Oliva, E Boter Rebollo, T Boutboul, Bratu E, J Caballero, M Comelis, J Fanthome, R Harrison, M Losasso, A Portone, H Rajainmaki, P Readman, and P Valente. Overview of ITER magnet system and european contribution. *IEEE/NPSS 24th Symposium on Fusion Engineering*, pages 1–8, 2011.

[271] L Shlyk, G Krabbes, G Fuchs, K Nenkov, and B Schupp. Flux pinning and magnetic relaxation in melt-processed $YBa_2Cu_3O_{7-\delta}$ doped with Li. *Journal of Applied Physics*, 96(6):3371–3378, 2004.

[272] S Awaji, T Suzuki, H Oguro, K Watanabe, and K Matsumoto. Strain-controlled critical temperature in $REBa_2Cu_3O_y - coatedconductors. Scientific Reports, 5 :$ 11156, 2015.

[273] G De Marzi, L Morici, L Muzzi, A della Corte, and M B Nardelli. Strain sensitivity and superconducting properties of Nb_3Sn from first principles calculations. *Journal of Physics: Condensed Matter*, 25(13):135702, 2013.

[274] L R Testardi. *Elastic behaviour and structural instability of high-temperature A-15 structure superconductors*, volume 10, page 193. Academic, New York, 1973.

[275] A T van Kessel, H W Myron, and F M Mueller. Electronic-structure of Nb_3Sn. *Physical Review Letters*, 41(3):181–184, 1978.

[276] D O Welch. Alteration of the superconducting properties of A15 compounds and elementary composite superconductors by nonhydrostatic elastic strain. *Advances in Cryogenic Engineering*, 26:48–65, 1980.

[277] G R Barsch and Z P Chang. Shear-mode anomaly, precursor effects, and pressure dependence of the structural phase transformation in Nb_3Sn. *Physical Review B*, 24(1):96–104, 1981.

[278] A Godeke. A review of the properties of nb3sn and their variation with a15 composition, morphology and strain state. *Superconductor Science Technology*, 19:R68–R80, 2006.

[279] J Zhou, Y Jo, Z H Sung, H Zhou, PJ Lee, and D C Larbalestier. Evidence that the upper critical field of Nb_3Sn is independent of whether it is cubic or tetragonal. *Applied Physics Letters*, 99:122507, 2011.

[280] P F Carcia and G R Barsch. Elastic properties and superconductivity of V_3Si at high pressure. *physica status solidi (b)*, 59(2):595–606, 1973.

[281] G W Cullen and J P McEvoy. Field and angular dependence of critical currents in Nb_3Sn. *Physical Review*, 132:577–580, 1961.

[282] A Godeke, A Nijhuis, B Ten Haken, and H H J Ten Kate. Angular dependence of critical current versus magnetic field in Nb_3Sn wires at 9 - 15 t. *IoP J Conference Series*, pages 917–920, 1997.

[283] T Y Hsiang and D K Finnemore. Superconducting critical currents for thick, clean superconductor-normal-metal-superconductor junctions. *Physical Review B*, 22(1):154–163, 1980.

[284] J W Ekin, N Cheggour, L Goodrich, J Splett, B Bordini, and D Richter. Unified scaling law for flux pinning in practical superconductors: Ii. parameter testing, scaling constants, and the extrapolative scaling expression. *Superconductor Science and Technology*, 29(12):38, 2016.

[285] J Ekin. Compendium of practical Nb_3Sn conductor properties and data.

[286] L Civale. Angular-dependent vortex pinning mechanisms in $YBa_2Cu_3O_7$ coated conductors and thin films. *Applied Physics Letters*, 84:2121, 2004.

[287] A K Jha, K Matsumoto, T Horide, S Saini, P Mele, A Ichinose, Y Yoshida, and S Awaji. Tailoring the vortex pinning strength of ybco thin films by systematic incorporation of hybrid artificial pinning centers. *Superconductor Science Technology*, 28(11), 2015.

[288] F Rizzo, A Augieri, A Angrisani Armenio, V Galluzzi, A Mancini, V Pinto, A Rufoloni, A Vannozzi, M Bianchetti, A Kursumovic, J L MacManus-Driscoll, A Meledin, G van Tendeloo, and G Celentano. Enhanced 77 k vortex-pinning in $YBa_2Cu_3O_{7x}$ films with $Ba_2Y\,TaO_6$ and mixed $Ba_2Y\,TaO_6$ + $Ba_2Y\,NbO_6$ nanocolumnar inclusions with irreversibility field to 11 T. *APL Materials*, 4(6):061101, 2016.

[289] H Yamasaki, K Ohki, H Yamada, Y Nakagawa, and Y Mawatari. Strong flux pinning in $YBa_2Cu_3O_{7-\delta}$ thin films due to nanometer-sized precipitates. *Supercond. Sci. Technol.*, 21:125011, 2008.

[290] A Antonevici and C Villard. On the link between critical temperature and critical current as a function of strain in coated conductors. *Superconductor Science & Technology*, 21(7), 2008.

[291] P Branch, Y Tsui, K Osamura, and D P Hampshire. Multimodal strain dependence of the critical parameters in high-field technological superconductors. *Submitted to Super. Sci and Tech.*, 2018.

[292] G Blatter, M V Feigelman, V B Geshkenbein, A I Larkin, and V M Vinokur. Vortices in high-temperature superconductors. *Reviews of Modern Physics*, 66(4):1125–1388, 1994.

[293] J R Greenwood, E Surrey, and D P Hampshire. Biaxial strain measurements of J_c on a (RE) BCO coated conductor. *IEEE Transaction on Applied Superconductivity*, 28(4), 2018.

[294] C Scheuerlein, B Fedelich, P Alknes, G Arnau, R Bjoerstad, and B Bordini. Elastic anisotropy in multifilament Nb_3Sn superconducting wires. *IEEE Transactions on Applied Superconductivity*, 25(3):1–5, June 2015.

[295] C Scheuerlein, G Arnau, P Alknes, N Jimenez, B Bordini, A Ballarino, M Di Michiel, L Thilly, T Besara, and T Siegrist. Texture in state-of-the-art Nb_3Sn multifilamentary superconducting wires. *Superconductor Science and Technology*, 27(2):025013, jan 2014.

[296] S Awaji, T Suzuki, H Oguro, K Watanabe, S Machiya, M Sugano, M Sato, T Koganezawa, and K Matsumoto. Control of residual strain and twin boundary by annealing under strain. *Superconductor Science and Technology*, 26(6):065013, 2013.

[297] B N Sorbom, J Ball, T R Palmer, F J Mangiarotti, J M Sierchio, P T Bonoli, C Kasten, D A Sutherland, H S Barnard, C B Haakonsen, J Goh, C Sung, and D G Whyte. ARC: A compact, high-field, fusion nuclear science facility and demonstration power plant with demountable magnets. *Fusion Engineering and Design*, 100:378–405, 2015.

[298] A Sykes, A E Costley, C G Windsor, O Asunta, G Brittles, P Buxton, V Chuyanov, J W Connor, M P Gryaznevich, B Huang, J Hugill, A Kukushkin, D Kingham, A V Langtry, S McNamara, J G Morgan, P Noonan, J S H Ross, V Shevchenko, R Slade, and G Smith. Compact fusion energy based on the spherical tokamak. *Nuclear Fusion*, 58(1):016039, 2018.